Thermal Laser Epitaxy: From Fundamental Physics to the Growth of Novel Thin Films

von der Fakultät Mathematik und Physik
der Universität Stuttgart
zur Erlangung der Würde eines Doktors der
Naturwissenschaften (Dr. rer. nat.) genehmigte Abhandlung

Vorgelegt von

Thomas James Smart

aus Chesterfield, UK

Hauptberichter:	Prof. Dr. Jochen Mannhart
Mitberichter:	Prof. Dr. Sebastian Loth
Prüfungsvorsitzende:	Prof. Dr. Maria Daghofer

Tag der mündlichen Prüfung: 21. März 2023

Max-Planck-Institut für Festkörperforschung

2023

Acknowledgements

No work like this can be accomplished alone, therefore I have many people to thank for their continuous support. I would like to thank my supervisors at the Max Planck Institute for Solid State Research: Dr. Wolfgang Braun and Prof. Dr. Jochen Mannhart, for their guidance, encouragement and support.

In regards to the simulation work within this thesis, I am sincerely grateful for the help of Prof. Bilen Emek Abali for his aid in the construction and testing of these models. Additional thanks are also in order for Fabian Felden for his help collecting deposition data for various elemental sources.

I would also like to thank Dr. Sander Smink, Dr. Dong Yeong Kim and Ms. Lena Majer for their help and guidance in the growth of epitaxial sapphire that forms the last chapter of this thesis.

Finally I wish to thank my family and friends for their continuous love and support (even if they didn't understand what I was talking about half of the time). You are the ones who kept me going.

Thomas J. Smart,
Stuttgart,
April 2022.

Abstract/ Zusammenfassung

Thin films have many different applications in the modern world, from computer chips to optical coatings. There is an increasing demand for the growth of thin film heterostructures composed of a variety of different chemical elements to explore novel quantum effects, which poses a challenge to many existing thin film growth technologies.

Based on fundamental scientific principles, a new technique for epitaxial growth of thin films, thermal laser epitaxy (TLE), is presented. In TLE, lasers are used to vaporize free-standing sources of material, which are then deposited on a substrate. It has been successfully demonstrated that TLE can be used to deposit all solid, non-radioactive elements of the entire periodic table. Due to the localized heating emanating from a laser source, a liquid phase can be present on the source during deposition at the location of the laser spot, i.e., the source acts as its own crucible. In this way, ultra-clean thin films can be prepared without contamination from external crucibles. When the growth rate of a material is plotted as a function of laser power, an Arrhenius-like dependence is seen for each element tested. This Arrhenius-like dependence was observed for the growth rate in the deposition of Al over seven orders of magnitude. This Arrhenius-like dependence can be explained by the different temperature dependencies of the radiation, evaporation, and attenuation of the source laser

by the evaporating species.

When using a visible-light laser, the required laser power for a bespoke deposition could be reduced due to the lower reflection of the light. The required laser power is a direct measure of the temperature-dependent optical properties of the starting material. Stabilization of the deposition can be achieved by using motors that continuously shift the relative position of the laser on the source. Basically, the output power of the laser will slowly increase. In the case of Si, this results in deposition stability superior to other epitaxial techniques. For the growth of compounds, especially oxides, a gas atmosphere can be introduced into the TLE chamber, as shown in this work for the growth of Al_2O_3. I show that the Arrhenius-like dependence of the growth rate of Al in ultrahigh vacuum is distorted by the catalytic role of oxygen in the laser-heated Al-O system. By gaining further insight into the evaporation of Al in an oxygen atmosphere, I successfully establish that homoepitaxy of Al_2O_3 in TLE is possible, which is of great importance for future applications of TLE, especially for quantum applications.

It is concluded that TLE is ideally suited for the growth of many different epitaxial material systems, with a particular future perspective for devices. It is shown that high-purity epitaxial thin films of various elements and their oxides can be successfully grown with TLE. Nitrides are also possible, as shown by the successful growth of AlN. Other compounds such as fluorides, chlorides, or carbides may be able to be grown with TLE, but this needs to be further investigated on a case-by-case basis.

The finite element simulations presented in this work allow for modeling of the evaporation behavior of each solid element, which has a large impact on the range of different compounds that can be grown with TLE. These simulations can lead to a better understanding of the heating process of sources in TLE,

This can be used to optimize fast heating and cooling rates, which has profound implications for the growth of heterostructures or sharp interfaces.

Dünne Schichten haben in der modernen Welt viele verschiedene Anwendungen, von Computerchips bis zu optischen Beschichtungen. Es besteht eine steigende Nachfrage nach dem Wachstum von Dünnschicht-Heterostrukturen, die aus einer Vielzahl verschiedener chemischer Elemente bestehen, um neuartige Quanteneffekte zu erforschen, was eine Herausforderung für viele bestehende Dünnschicht-Wachstumstechnologien darstellt.

Auf der Grundlage grundlegender wissenschaftlicher Prinzipien wird eine neue Technik für das epitaktische Wachstum von Dünnschichten, die thermische Laserepitaxie (TLE), vorgestellt. Bei der TLE werden Laser eingesetzt, um freistehende Materialquellen zu verdampfen, die dann auf einem Substrat abgeschieden werden. Es wurde erfolgreich demonstriert, dass sich mit TLE alle festen, nicht radioaktiven Elemente des gesamten Periodensystems abscheiden lassen. Aufgrund der lokalen Erwärmung, die von einer Laserquelle ausgeht, kann sich während der Abscheidung an der Stelle des Laserspots eine flüssige Phase auf der Quelle befinden, d. h. die Quelle fungiert als ihr eigener Schmelztiegel. Auf diese Weise können ultra-saubere dünne Schichten ohne Verunreinigung durch externe Tiegel hegestellt werden. Wird die Wachstumsrate eines Materials als Funktion der Laserleistung aufgetragen, zeigt sich für jedes getestete Element eine Arrhenius-ähnliche Abhängigkeit. Diese Arrhenius-ähnliche Abhängigkeit wurde für die Wachstumsrate bei der Abscheidung von Al über sieben Größenordnungen hinweg beobachtet. Diese Arrhenius-ähnliche Abhängigkeit lässt sich durch die unterschiedlichen Temperaturabhängigkeiten der Strahlung, der Verdampfung und der Abschwächung des Quelllasers durch die verdampfenden Spezies erklären.

Bei Verwendung eines Lasers mit sichtbarem Licht konnte die erforderliche Laserleistung für eine besstimmte Abscheidung aufgrund der geringeren Reflektion des Lichts reduziert werden. Die erforderliche Laserleistung ist ein direktes Maß für die temperaturabhängigen optischen Eigenschaften des Ausgangsmaterials. Eine Stabilisierung der Abscheidung kann durch den Einsatz von Motoren erreicht werden, die die relative Position des Lasers auf der Quelle kontinuierlich verschieben. Zwätzlich wird die Ausgangsleistung des Lasers langsam erhöhen. Im Falle von Si führt dies zu einer Abscheidungsstabilität, die anderen Epitaxietechniken überlegen ist. Für das Wachstum von verbindiengen, insbesondere oxiden, kann eine Gasatmosphäre in die TLE-Kammer eingeführt werden, wie in dieser Arbeit für das Wachstum von Al_2O_3 gezeigt wird. Ich zeige, dass die Arrhenius-ähnliche Abhängigkeit der Wachstumsrate von Al im Ultrahochvakuum durch die katalytische Rolle von Sauerstoff im laserbeheizten Al-O-System verzerrt wird. Indem ich weitere Einblicke in die Verdampfung von Al in einer Sauerstoffatmosphäre gewinne, stelle ich erfolgreich fest, dass Homoepitaxie von Al_2O_3 in TLE möglich ist, was für zukünftige Anwendungen der TLE, insbesondere für Quantenanwendungen, von großer Bedeutung ist.

Es wird gefolgert, dass TLE ideal für das Wachstum vieler verschiedener epitaktischer Materialsysteme geeignet ist, mit einer besonderen Zukunftsperspektive für Bauelemente. Es wird gezeigt, dass hochreine epitaktische Dünnschichten aus verschiedenen Elementen und ihren Oxiden erfolgreich mit TLE gezüchtet werden können. Auch Nitride sind möglich, wie das erfolgreiche Wachstum von AlN zeigt. Andere Verbindungen wie Fluoride, Chloride oder Carbide können möglicherweise mit TLE gezüchtet werden, dies muss jedoch von Fall zu Fall noch genauer untersucht werden.

Die in dieser Arbeit vorgestellten Finite-Elemente-Simulationen erlauben eine Modellierung des Verdampfungsverhaltens jedes festen Elements ermöglichen, was einen großen Einfluss auf die Bandbreite der verschiedenen Verbindungen hat, die mit TLE gezüchtet werden können. Diese Simulationen können zu einem besseren Verständnis des Erhitzungsprozesses von Quellen in TLE führen, Damit können schnelle Heiz- und Kühlraten optimiert werden, was tiefgreifende Auswirkungen auf das Wachstum von Heterostrukturen oder scharfen Grenzflächen hat.

Contents

1

Introduction

Thin films are layers of material with a thickness ranging from a monolayer (a layer of atoms) to several micrometers. Thin films are ubiquitous in the modern world. They exist in virtually every aspect of modern life and play an important role in many applications, from computer chips and camera lenses to medical devices and potato chip packages. For example, two major applications of thin films within physics are solar cells and superconducting films on sapphire for applications in quantum computing. In a thin film solar cell, extremely little material is required in order to reach high solar cell efficiencies and significant photocurrents. For example, only a micron thick film of Si on a substrate of 1 cm^2 is required to achieve cell efficiencies of over 65 % and photocurrents of 26.3 $\mathrm{mA/cm}^2$.[1] In comparison, superconducting thin films are often used within Josephson junctions, which are key components for qubits and quantum computing. The construction of said junctions as thin films allow them to be embedded in devices or to have techniques like electron beam lithography to be easily performed upon them to easily design the desired device.[2]

A further selection of the applications of thin films is illustrated in Fig. 1.1. Thin films are present both as single elements, and as chemical compounds. Their abundance in applications results from the fact that thin films are endlessly tunable to any desired scenario. The physical properties of many bulk materials are changed when the material is present as a thin film or exists at

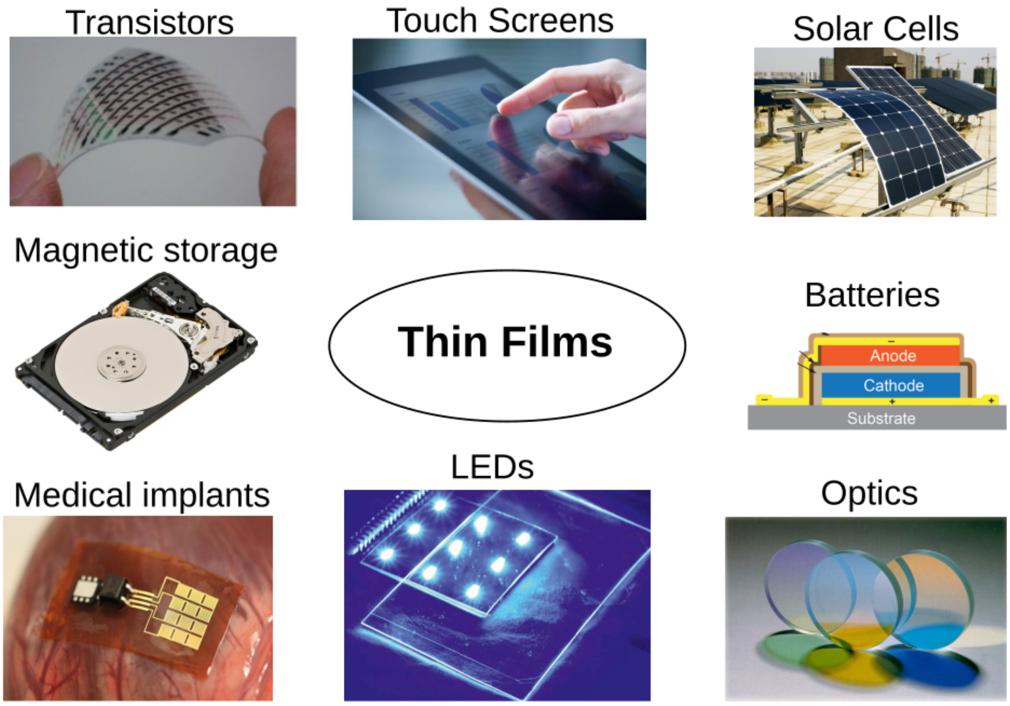

Figure 1.1: Examples of the applications of thin films within the modern world.

an interface with another material. Therefore, thin films serve as an ideal template with which many unique physical effects can be studied and applied to the modern world in the myriad of devices illustrated in Fig. 1.1.

Within a thin film, the crystal structure often plays a key role in determining its physical properties. Examples of common crystal structures can be seen in Fig. 1. The crystal structure of an element emerges from its electronic properties leading to a wide variety of physical properties that favor the use of different elements for specific applications. For example, the metals in Group IB (consisting of Cu, Au, and Ag) are all extremely good electrical and thermal conductors due to their electronic structure.

Thin films are often deposited within a vacuum and there are many techniques to accomplish this such as molecular beam epitaxy, pulsed laser depo-

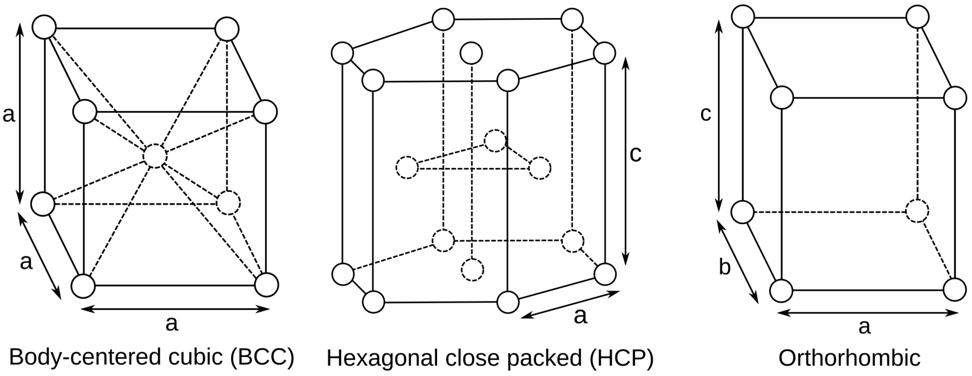

Figure 1.2: Common crystal structures present in nature: body-centered cubic (BCC), hexagonal close packed (HCP) and orthorhombic crystal structures. The lattice constants *a*, *b* and *c*, referring to the dimensions of the unit cell are indicated for each structure.

sition, sputtering and chemical vapor deposition. For this thesis, molecular beam epitaxy (MBE) is the most relevant.

1.1 Molecular Beam Epitaxy

The term "epitaxy" refers to a form of crystal growth, often in the form of a thin film, in which, under the right conditions, the in-plane crystalline orientation of the thin film matches that of the crystalline base or substrate to which the film has been grown.

MBE usually relies on the use of beams of elemental atomic vapors to deposit atoms upon a substrate as illustrated in Fig. 1.3.[3] With the addition of a substrate heater, the growth conditions can be tuned in order to ensure that the grown thin film are of high crystalline quality. *In-situ* measurements such as reflection high-energy electron diffraction (RHEED) present the opportunity to monitor the composition and crystalline quality of the deposited film to be observed in real time. The effusion cells that generate the elemental atomic

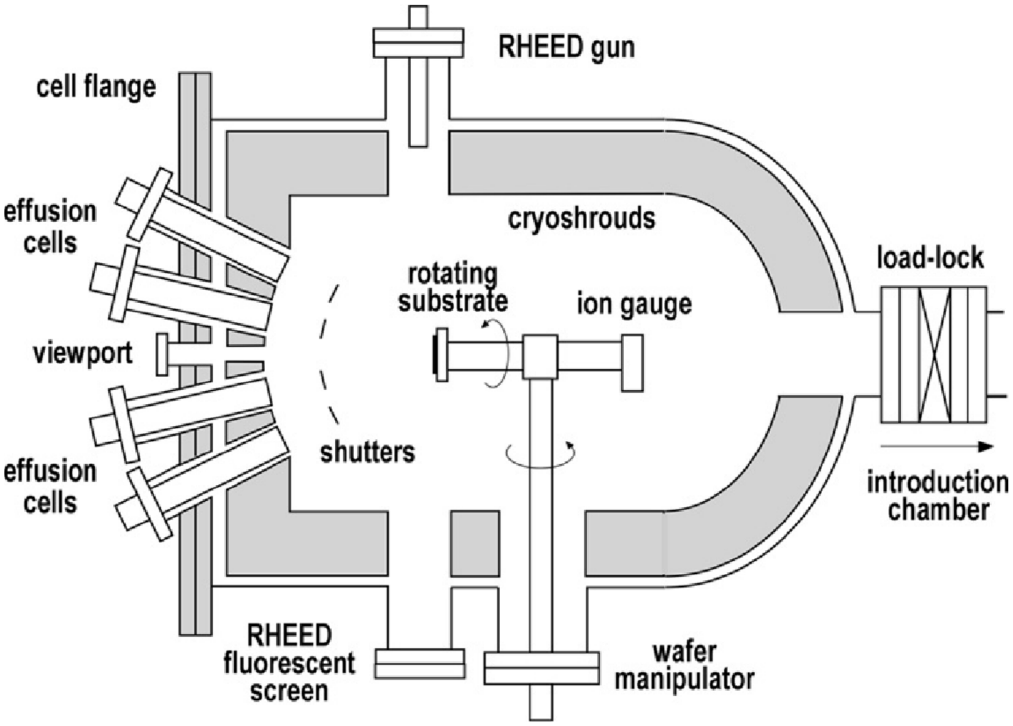

Figure 1.3: Diagram of an MBE growth chamber (cross-section). Typical MBE systems are on the scale of a meter across. Figure taken from Ref. [4].

vapors (see below) use closed-loop control to achieve temperature stability on the order of tenths of a degree, allowing for high flux stability over time. [4]

1.1.1 The effusion cell

The primary method for generating atomic fluxes in MBE is to evaporate a source of material in a heated vessel or crucible. The typical design for evaporation hardware is based on Ohmic heating, also known as resistive heating or Joule heating. By wrapping a wire around a container or crucible containing the desired source and then passing a current through that wire, the source is indirectly heated to produce a vapor. Alternatively, the crucible itself may be made of a resistive material through which the current is passed directly.

The use of Joule heating for thin film deposition dates back to Nahrwold and Kundt in 1887 and 1888, respectively.[5] This technique was refined by Knudsen in the early twentieth century and led to the effusion cell.[6] The cell is essentially an isothermal cavity containing a hole through which the evaporating medium exits. The cell behaves like a small-area source and exhibits a $\cos(\theta)$ vapor distribution, as shown in Fig. 1.4:

$$\Phi_P = \frac{\Phi_e}{\pi r_p^2} \cos(\theta) \cos(\theta + \phi), \tag{1.1}$$

where Φ_P is the flux that reaches a point P on the substrate and Φ_e is the flux that passes through the orifice of the effusion cell. The parameter r_p represents the distance between the orifice and the point P on the substrate and ϕ represents the angle between the normal vectors of the effusion cell and the substrate as shown in Fig. 1.4.[4] To fully optimize the deposition of a given element, its evaporation behavior must be fully considered, specifically the required temperature for a desired evaporation rate. Evaporation is characterized by the vapor pressure of the evaporating material.

1.1.2 Vapor pressure and enthalpy

The vapor pressure, p_{vap} of a material is defined as the pressure exerted by a vapor when it is in thermodynamic equilibrium with its condensed state within a closed system.[7] The parameter p_{vap} at a given temperature is related to the evaporation rate of the material in vacuum Γ, via the Hertz-Knudsen equation:[8]

$$\Gamma = \sqrt{\frac{m}{2\pi k_b T}} p_{\text{vap}}(T), \tag{1.2}$$

where m is the mass of an evaporated particle, k_b is the Boltzmann constant and $p_{\text{vap}}(T)$ is the vapor pressure of the material in Pa at a temperature T. The

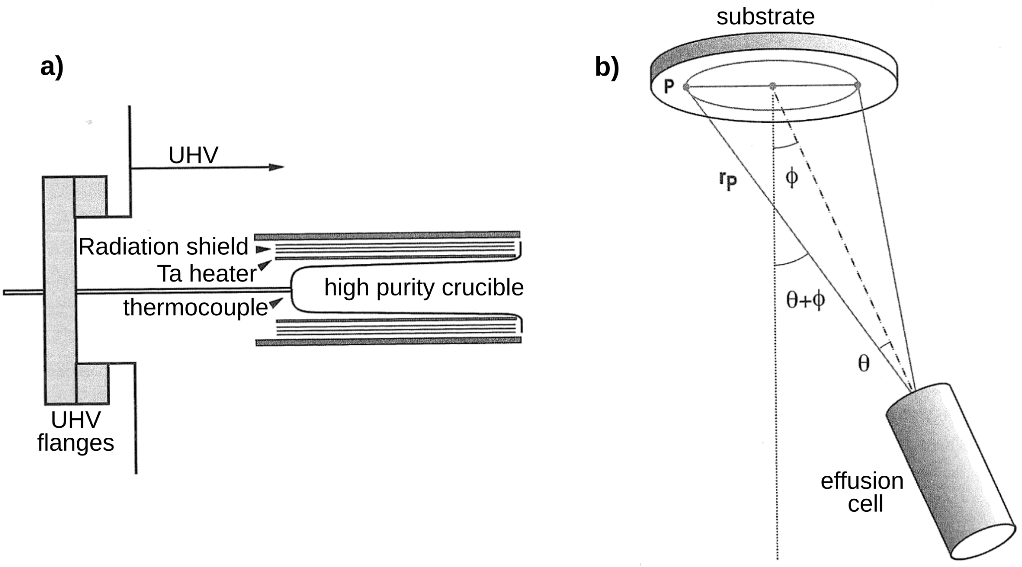

Figure 1.4: a) shows a diagram of typical effusion cell that uses resistive heating from a coil to generate an atomic flux during deposition. A diagram of the cosine flux distribution from the Knudsen cell is shown in b). Both diagrams were adapted from Ref. [4].

vapor pressures of various elements as a function of temperature are shown in Fig. 1.5.[9] From this equation, Γ is directly proportional to p_{vap}, therefore we can determine the relative evaporation rate of a material from its vapor pressure. From Fig. 1.5, it can clearly be seen that elements with higher vapor pressures at a given temperature evaporate faster than materials with lower vapor pressures. A high vapor pressure implies that little energy is required to liberate an atom from the condensed phase. If said condensed phase is a solid, then the energy required to liberate an atom is given by the enthalpy of sublimation ΔH_{sub}. This is the sum of the energy to change its state from a solid to a liquid, the enthalpy of fusion ΔH_{fus} and the energy required to change the material from a liquid to a vapor, the enthalpy of vaporization, ΔH_{vap}. From Fig. 1.5, it is evident that higher vapor pressures correspond to low values of ΔH_{atom}, which is consistent with the known relationship between p_{vap} and the enthalpy of transition in the form of the Clausius-Clapeyron Equation:[10]

$$\frac{d}{dT}\ln(p_{\mathrm{vap}}) = \frac{\Delta H}{RT^2}, \tag{1.3}$$

For Eqn. 1.3, ΔH can be quoted as either ΔH_{sub} or ΔH_{vap} depending on whether the source of material exists as a solid or a liquid at a given temperature. Higher values of ΔH emerge from greater bond strengths between atoms within the solid or liquid. For example, W possesses the lowest vapor pressure of all transition metals due to the high number of strong covalent bonds between the $5d$ electrons. It should be noted that in reality, ΔH_{vap} is a function of temperature, eventually reaching zero at the critical temperature of a material where the liquid and gaseous phases are indistinguishable.[11] This explains why the vapor pressure of most elements is continuous as the melting point is passed. Since the Clausius-Claperyon equation is often assumed to have a constant ΔH, empirical equations for p_{vap} as a function of temperature such as the Antoine equation are used to account for the additional temperature dependence of ΔH.[10]

1.1.3 Challenges of MBE

Despite the tremendous success of MBE with effusion cells, there are limitations to their effectiveness. First, effusion cells are inherently limited by the temperature range of the heating elements and the crucible. Above 1800 K, many crucible materials such as pryolytic boron nitride (PBN) and Al_2O_3 break down into their consistent components, compromising their structural integrity and introducing impurities into the source material and thus into the final layer. Therefore, evaporation of extremely low vapor pressure materials such as W or Ta is often performed using e-beam evaporation, which uses an electron beam to heat a material source, but is technically complex. At high temperatures, eutectic reactions often occur between the crucible material and the source, as well as diffusion of impurities from the crucible into the source. In addition, the use of corrosive background gases is limited due to the resistive substrate heaters commonly used in MBE. This limits the type of compounds that can be easily grown in MBE.

As eluded to earlier, MBE is not the only technique available for depositing thin films. Another widely used epitaxy technique that does not utilize effusion cells or thermal evaporation from a crucible is sputtering.

1.2 Sputtering

In sputtering, a source of material is placed inside of a vacuum chamber that is filled with gas at low pressure, such as Ar, Xe or O_2. In the case of DC sputtering, a voltage is applied between the source and the substrate, causing them to act as a cathode and an anode respectively. A plasma is then created in a self-sustaining manner and can be shaped using magnetic fields. The positively charged ions in the plasma collide with the negatively charged cathode source and initiate collisions in the source.

Sputtering can be used to deposit elements with very high melting points such as W or Ta as uniform thin films.[13] However, sputtering is not suitable for all thin films and substrates because, for example, damage from ultraviolet radiation, X-rays or high-energy particle bombardment can affect the quality of the deposited film.[14, 15]

Ideally, we wish to avoid the issues of low growth rates and substrate damage while also avoiding the issues associated with the use of an effusion cell. To accomplish this, we can directly irradiate the source material with a laser beam.

1.3 The (very) basics of laser physics

In 1917, Albert Einstein theoretically derived the basis for the laser by rederiving Max Planck's law of radiation for the absorption, spontaneous emission and stimulated emission of electromagnetic radiation. The concept of stimulated emission, in which an excited state of an atom can be perturbed by an incoming photon, causing the atom to transition to a lower energy level and produce an identical photon, was confirmed by R. Ladenburg in 1928.[16, 17] The first laser was constructed by T. H. Maiman in 1960. It built on the principle of the maser, the microwave analog of the laser, which was constructed by C. H. Townes in 1953.[18, 19]

The laser operates on the principle of stimulated emission of radiation as shown in Fig. 1.6. In this scenario, an excited state of an atom is perturbed by incident radiation with a photon energy equal to the difference between the energies of the excited state and the ground state, ΔE:

$$E_2 - E_1 = \Delta E = h\nu, \tag{1.4}$$

where E_1 and E_2 are the energies of the ground and excited state respectively. This perturbation by the incident photon causes the atom to emit a photon with the same frequency and phase as the original, leaving the atom in its ground state. When multiplied over many interactions, this creates a beam of coherent photons with the same wavelength and phase. The rate at which stimulated emission occurs is directly proportional to the number of atoms in the excited state, N_2:

$$\frac{\partial N_2}{\partial t} = -\frac{\partial N_1}{\partial t} = -B_{21}\rho(\nu)N_2, \tag{1.5}$$

where N_1 is the number of atoms in the ground state and B_{21} is the Einstein coefficient of induced emission for a given transition and $\rho(\nu)$ represents the density of incident radiation with a frequency ν. To achieve stimulated emission, these interactions must take place in a gain medium, as shown in Fig. 1.7, in which a two-level system can be realized and population inversion can be achieved. Examples of such gain media are crystals such as yttrium aluminum garnet ($Y_3Al_5O_{12}$) or YAG for short and sapphire (Al_2O_3), gases such as He and Ne, or organic dyes such as rhodamine 6G. [20, 21] This gain medium is contained in an optical resonator where the radiation bounces back and forth and is amplified with each pass. An external pump such as an arc lamp is used to create the population inversion within the gain medium necessary to creating the lasing effect. Lasing can then be induced either by waiting for spontaneous emission or via the use of a seed laser to stimulate the emission of photons.[20]

Two laser types that are particularly relevant for this thesis are the CO_2 laser and the disk laser. The CO_2 laser was among one of the first types of lasers to be used in applications during the 1960s.[22, 23] As illustrated in Fig. 1.7a, it utilizes a mix of gases including N_2, CO_2 and He, with the rotational transitions of the $\Sigma_u{}^+$ - $\Sigma_g{}^+$ vibrational band of CO_2 at around $\lambda = 10.4\,\mu$m and $\lambda = 9.4\,\mu$m serving as the lasing transitions.[24] The CO_2 laser is extremely advantageous for heating substrates as its laser wavelength is absorbed by many common oxide substrate materials, allowing for the possibility of substrate preparation via thermal annealing.[25]

The disk laser utilizes a thin, solid-state active medium attached to a heat sink which is then irradiated by a pump laser as illustrated in Fig. 1.7b. Whilst many prototypes of the disk laser were developed during the latter half of the twentieth century,[26] a major advancement was made in 1994 at the University of Stuttgart with the use of a Yb doped YAG crystal as the active medium.[27] Due to the large area of the disk and the high power densities upon it, the disk laser is now widely used for high power lasers in many different applications.[28] Due to these properties, we used disk lasers as the heating device for the evaporation sources within this thesis.

With a laser acting as a direct heater of a source of material, we need to consider how light interacts with said material in order to have a more complete understanding of the evaporation process.

1.3.1 Light-matter interactions

When light interacts with the surface of a solid, it is either transmitted, reflected or absorbed. From this, the only energy from the light that is transformed into heat in the solid comes from the absorbed light. There are two primary processes for the absorption of light within a material: damped free-electron oscillations and interband transitions.

Both mechanisms are temperature dependent and therefore change the optical properties of the material as a function of T.[30, 31] For most materials, each absorption mechanism is dominant for different incident photon energies. At low energies (e.g., in the infrared region), the free electrons in the material oscillate in response to the incident electromagnetic field of light. Damping of these oscillations is caused, for example, by scattering between electrons and phonons, which are quantized oscillations of the crystal lattice. This damping leads to absorption in this range of photon energy. Conversely, at high photon energies, the photon has enough energy to excite electrons from an occupied state in the valence band to an unoccupied state in the conduction band. The energy is then converted to heat by the emission of phonons during the relaxation of the excited electron to the band edge. Later in this thesis, the temperature dependence of these two processes will play an important role in determining how the optical properties of a material change at elevated temperatures (Chap. 4).

The high power density of a laser combined with the direct absorption of light is a compelling argument for using a laser to heat and vaporize elemental material sources without the disadvantages of an indirect heating mechanism. Because of the high power densities possible with a laser, high-purity thin films can be produced with unlimited source temperatures. It turns out that this is not a completely new concept and the use of a laser for thermal evaporation has been performed before...

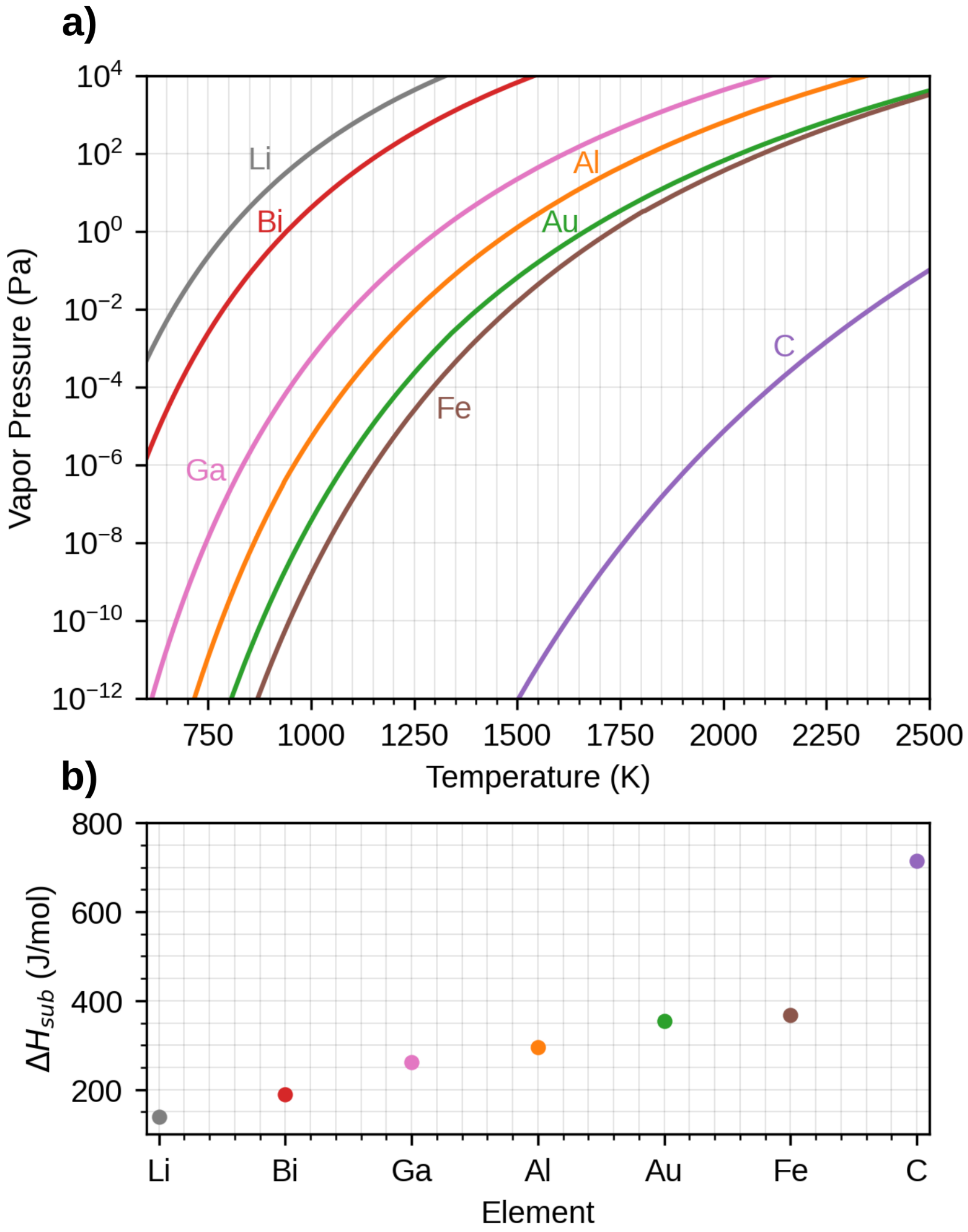

Figure 1.5: Vapor pressure of various elements as a function of temperature.[9] The corresponding values of the enthalpy of atomization, ΔH_{sub} are shown in the bottom graph.[12] At a given temperature, higher vapor pressures correspond to lower ΔH_{sub} values as less energy is required to remove an atom from the condensed phase of the material.

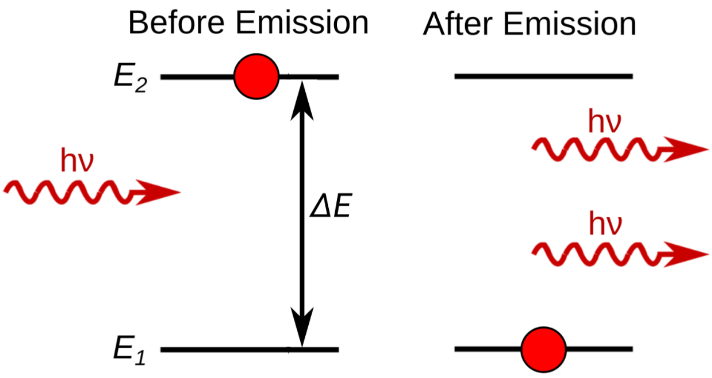

Figure 1.6: Illustration of stimulated emission. An incident photon with energy $h\nu$ perturbs an atom which is in its excited state with an excitation energy $\Delta E = h\nu$, causing the atom to release a photon with the same energy $h\nu$ and same phase as the original photon. The original photon is not absorbed during this process.

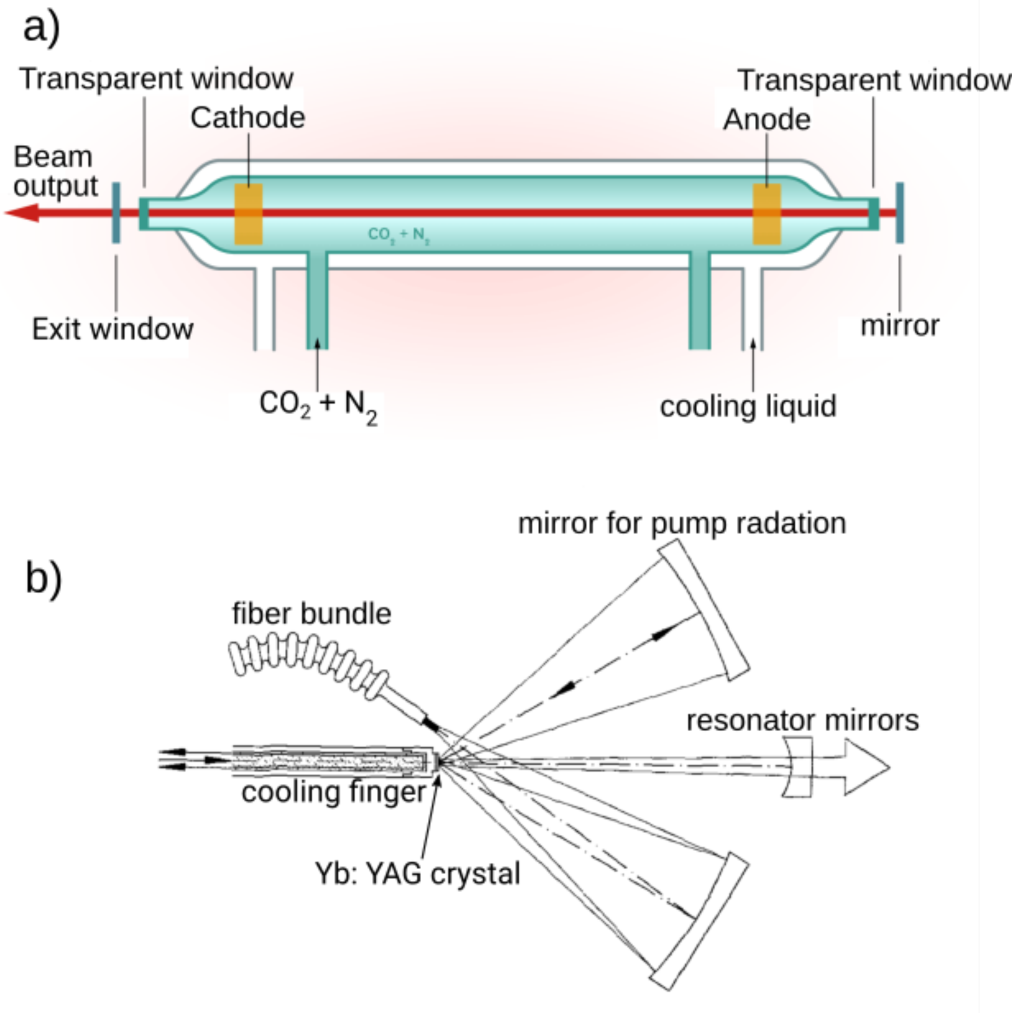

Figure 1.7: Diagrams of two different types of lasers (cross section); the CO_2 laser (a) and the disk laser (b). a) is taken from Ref. [29] and b) is taken from Ref. [27]

2

Introduction to thermal laser epitaxy

2.1 The history of the use of lasers for evaporation

The use of lasers for thermal evaporation emerged shortly after the invention of the laser which occurred in 1960.[18] The first documented use of a laser for vaporization occurred in 1962 by Breech and Cross, where a pulsed ruby laser was used to vaporize and excite atoms from solid surfaces.[32] In 1965, Smith and Turner demonstrated that "many materials can be vaporized in vacuum by a directed laser beam and condensed on substrates" using a pulsed ruby laser. [33] However, it was noted that for the growth of InAs thin films from a powdered source, the stoichiometry of the source was not replicated in the deposited film. The final film contained around 35 times more As compared to In due to As being preferentially evaporated. This lead to the conclusion that "success in [the growth of] stoichiometric films may depend on controlled laser-power operating conditions." [33] The growth of thin films from powder sources using pulsed laser evaporation was found to be possible for some compounds, as reported in 1968 by Zavitsanos and Sauer for GaAs,[34] and Schwarz and Tourtellotte for $BaTiO_3$ and $SrTiO_3$ also in 1968.[35]

The deposition of thin films with a continuous wave (CW) CO_2 laser was first reported by Groh in 1969. The use of a CW laser resulted in temperatures of over 3000 K measured at the laser focus. This allowed not only deposition rates in the range of 100 Å/s for compounds such as SiO and PbF_2, but also the successful deposition of refractory ceramics such as Al_2O_3 and TiO_2, however their stoichiometry was not reported.[22] Successful deposition of SiO_2 films with a CW CO_2 laser was also reported by Hass and Ramsey in 1969.[23]

In 1970, Ban and Kramer compared the thin films grown with a CW CO_2 laser and a pulsed ruby laser using the simple deposition system shown in Fig. 2.1.[36] These studies used powder sources contained inside a stainless steel (S.S.) sample holder. They identified groups of materials (namely the III-V materials such as GaAs) that exhibit congruent evaporation when heated with a laser. Congruent evaporation is defined as when the plume of evaporated material has the same composition or stoichiometry as the original material source. Incongruent evaporation is said to occur in the opposite case, when the composition of the evaporating plume differs from that of the original source material. From their attempts to deposit III-V and II-VI (eg. ZnS) compounds, Ban and Kramer concluded that "stoichiometric deposition resulting from the [pulsed] ruby laser-solid interaction could be utilized in the preparation of thin films which normally evaporate incongruently", whereas the results of the CW CO_2 laser were reminiscent of "the attempts to prepare these materials with conventional evaporation" with "the resulting films containing a large excess of the more volatile compound".[36]

Depending on the length of the pulse, evaporation or ablation is possible using a pulsed laser. For the case of very short pulse lengths, ablation occurs when a small volume of the source is completely ablated and the resulting plume of material is congruent. The congruent ablation of many compounds with a pulsed laser with short pulse lengths results from the rapid heating rates in each laser pulse, which lead to the complete ablation of a very small volume of the source. In comparison, long laser pulses result in evaporation which displays

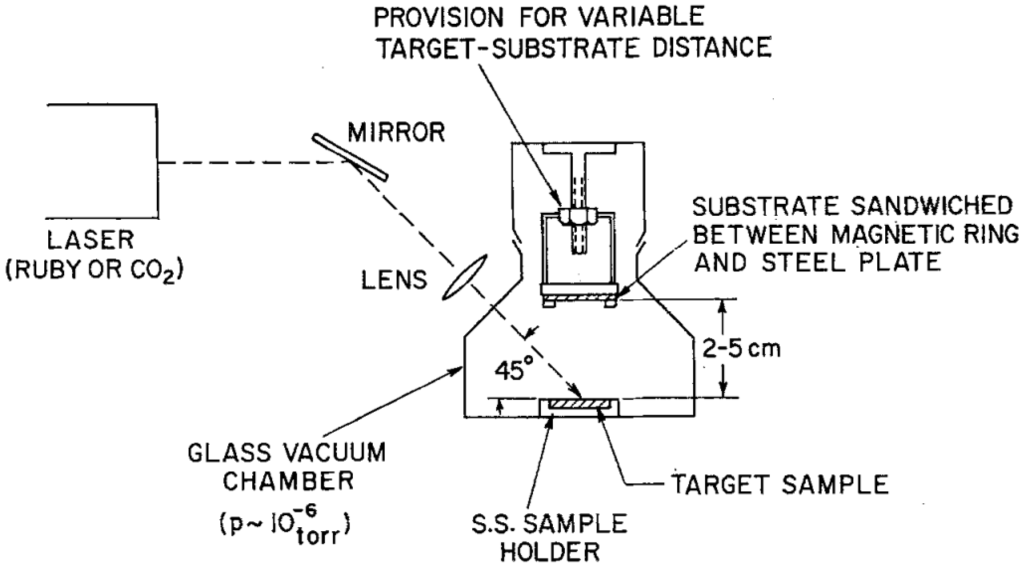

Figure 2.1: Cross-section of the apparatus used for the laser evaporation experiments conducted by Ban and Kramer. Figure taken from Ref. [36]

incongruent evaporation because the temperatures are lower due to the lower power densities and the heat flux is distributed over the entire source instead of being highly localized as in ablation using a pulsed laser.[36]

The experiments using pulsed lasers for ablation paved the way for pulsed laser deposition (PLD), which grasped the attention of the scientific community in 1987, when Dijkkamp *et al.* used a pulsed KrF eximer laser to successfully deposit $YBa_2Cu_3O_{7-x}$, a high T_c superconductor.[37] Since then, PLD has been extremely successful in the growth of complex oxide thin films and is widely used today.

Concurrently with the development of pulsed laser evaporation, experiments with CW lasers were reported occasionally. Pt was successfully deposited using a CW $YtAlO_3$ laser by Hess and Milkosky in 1972,[38] whilst PbF_2 was successfully deposited by Sankur using a CW CO_2 laser in 1986 replicating the results performed by Groh nearly two decades previously.[39, 22] Trujillo *et al* were also successful in epitaxially growing crystalline CdS films using a CW Nd:YtAlO$_3$ laser in 1993.[40] Despite these successes, the problem of incongruent evaporation and non-stoichiometric films remained for many compounds, which, combined with the successes of PLD, led the scientific community to pursue PLD as the epitaxial technique of choice.

Within the modern world, there is an increased demand for the epitaxial growth of ultra-pure thin film heterostructures composed of a wide variety of dissimilar elements from across the periodic table, both for research and applications. The recent availability of high power CW lasers allow for the possibility of uniting the distinct techniques of MBE and laser evaporation, by using lasers to locally heat individual sources of material with the resulting vapor condensing upon a substrate. This is particularly appealing for the growth of oxides since within PLD, the purity of deposited oxide film relies on the purity of the compound source. The purity of these oxide sources is always limited due to these sources being made from powders with large surface areas exposed to air, which poses a problem for the properties of heterostructures designed to study elusive quantum effects. By contrast, CW laser evaporation may allow for the growth of an ultra-pure oxide by evaporating metallic sources in an O_2 or O_3 atmosphere. In addition, CW laser evaporation uses power densities far lower than PLD, meaning the deposition process is thermal in nature. These lower energies prevent any high energy plasmas or ionic species from being generated by CW laser evaporation, a factor that is advantageous for the growth of ultra-pure, defect-free films.[41] The higher energies available from modern lasers permit the use of metals with high melting points and low vapor pressures as sources, whereas prior attempts primarily used pressed powder targets due to the low laser energies available at the time.

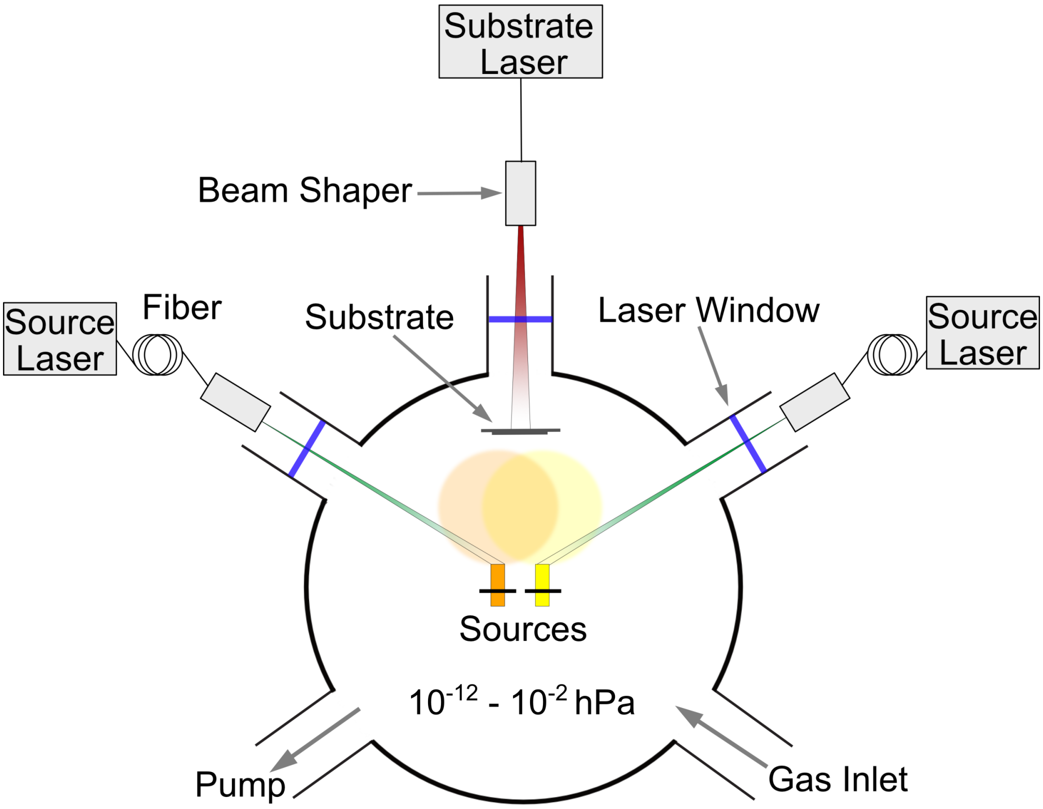

Figure 2.2: Cross-sectional cut of a TLE chamber. Without breaking the vacuum, both the substrate and the sources are exchangeable via a load-lock. With the addition of a gas inlet, a gaseous atmosphere may be to be present inside the chamber. Without any atmosphere, this chamber operates at UHV pressures. The pale colored regions represent the approximate flux distributions from the sources. Figure taken from Ref. [43].

Since CW laser evaporation is very promising for the epitaxial growth of high-purity thin films, it was reinvented and refined as an optimized process in 2018-2019. This deposition process is now called "thermal laser epitaxy".[42]

2.2 Thermal laser epitaxy

Thermal laser epitaxy (TLE) uses CW lasers to locally heat free-standing elemental sources and generate a flux of a desired atomic species, as shown in Fig. 2.2. This vapor is then deposited onto a substrate, which is heated to a specific temperature to produce high-quality, crystalline thin films. Substrate heating can be achieved using another laser, for example: a $\lambda = 10.2\,\mu$m CO_2 laser.[25, 44] Long wavelength lasers are useful for heating oxide substrates, but many metals possess low reflectivities within the visible to ultraviolet spectrum. The use of a source laser with a visible wavelength will be discussed in Chap. 4. In many cases, the use of a visible light laser is expensive so a source laser with a peak wavelength in the near infrared is usually used. To avoid contamination from the laser optics and the technological challenges of electrical feedthroughs, all lasers are located outside the chamber. This results in a compact, minimal chamber design. Consequently, growth configurations with small distances between source and substrate are easy to realize.

The design of the free-standing sources combined with the local heating generated by the source laser results in large thermal gradients within the source. This can create small liquid melt-pools, while the remainder of the source remains solid, as shown in Fig. 2.3 for the case of a Si source. The source then effectively acts as its own crucible, which offers major advantages over the use of an external crucible. The ductile nature of metals combined with the lack of a mismatch in the thermal expansion coefficients between the "crucible" and the "contents" avoids the issue of crucible failure due to thermally-induced strain. The absence of an external crucible also avoids reactions between the source and the crucible, since the solid-liquid interface remains in the source itself. This prevents contamination from the crucible in the deposited film. The desired physical properties of an "ideal" TLE source and the effects of changes in

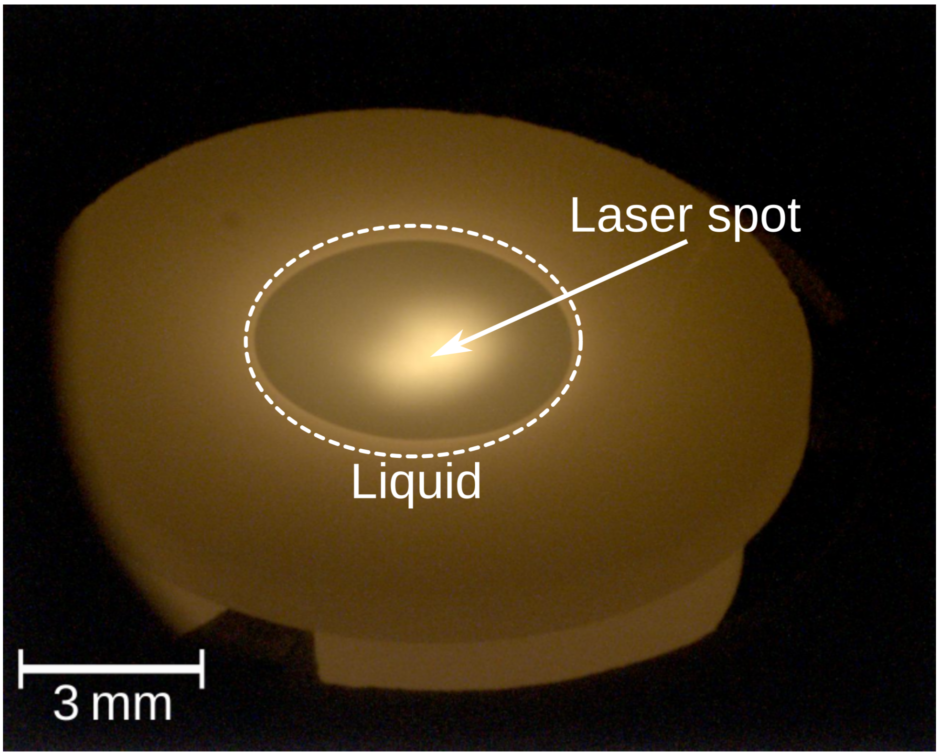

Figure 2.3: Photograph of a free-standing Si source (12.7 mm in diameter and 4 mm thick) during deposition. A liquid phase can be seen on the surface of the source, indicating a surface temperature of at least 1687 K[9] . During this deposition, the average deposition rate was 5.2 Å/s, resulting from 400 W supplied by a $\lambda = 1030$ nm laser.

the size and surface morphology of the source are discussed in the next chapter. The diameter of the free-standing sources was determined by the chamber geometry, with the minimum source diameter set at 2 mm and the maximum diameter at 12.7 mm. Unless specifically stated, the length of each cylindrical source was 8 mm.

With the use of multiple source lasers, co-evaporation of multiple free-standing sources enables the growth of chemical compounds as thin films. By varying the incident laser power at each source, a correspondingly variable composition can be achieved. The small working distances resulting from the compact design of the TLE chamber enables efficient use of the source material. An additional gas inlet can be used to introduce an atmosphere into the chamber that enables the growth of compounds, such as oxide or nitride films.[45]

Within this thesis, I shall primarily focus on the physics behind the CW laser evaporation of sources in an ultra high vacuum (UHV) environment. The aim is to replicate the desired properties of an epitaxial growth technique, while demonstrating many of the unique advantages of TLE compared to existing techniques. In the final chapter, I shall combine all the prior findings of this thesis to investigate how the evaporation of elemental sources is affected in the presence of an O_2 atmosphere with a brief aside regarding epitaxial growth using a laser substrate heater. The use of a laser substrate heater and an oxidizing atmosphere in TLE is not fully unique to this thesis and has been studied by some of my colleagues within the group.[46, 45]

2.3 Investigation of source evaporation in thermal laser epitaxy

Most experiments reported within this thesis were performed inside a simplified TLE test chamber, shown schematically in Fig. 2.4. This chamber shares many similarities with the test chamber used by Ban and Kramer in 1970 shown in Fig. 2.1. This chamber was the first TLE chamber ever constructed and was consequentially quite simple in its design. Due to its basic design, typical background pressures inside the chamber operated around UHV levels (10^{-8} - 10^{-9} hPa) whereas a more refined chamber can reach far lower pressures. The test chamber was left at ambient temperatures and operated without any intentional substrate heating. Any substrate heating that occured originated from irradiation from the thermal radiation from the hot source.

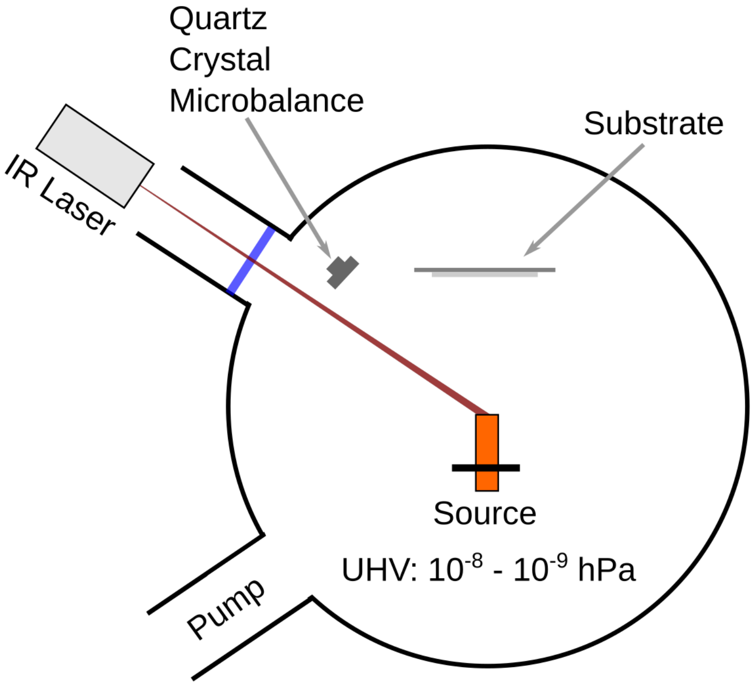

Figure 2.4: Cross-section of the TLE test chamber. Infrared radiation from the source during operation heated the substrates.

Initially, only one source laser was used and was provided by a $\lambda = 1030\,\mathrm{nm}$ fiber-coupled disk laser with a peak power of 2 kW. Within this chamber, the distance between the source and the focal point of the laser was 130 mm. The aforementioned laser was incident at 45° to the surface of the source, illuminating an area of approximately $1\,\mathrm{mm}^2$ on the surface of the source with an approximate Gaussian intensity profile. During the course of the thesis, many modifications were made to the chamber to investigate specific phenomena, resulting in the final configuration shown in Fig. 2.5. The relevant modifications from the basic design shown in Fig. 2.4 are discussed within later chapters.

Within this test chamber, 0.27 mm thick Si (111) wafers with a diameter of

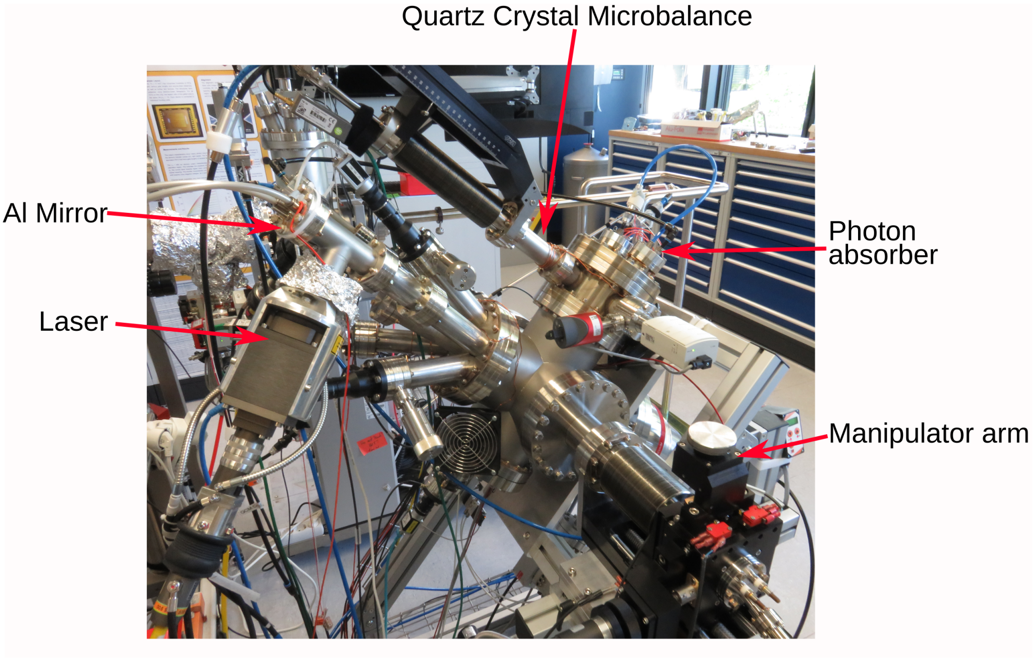

Figure 2.5: Photograph of the final configuration of the TLE test chamber.

2" were used as the substrate of choice due to their ease of acquisition and widespread use within epitaxy. As shown in Fig. 2.6, the substrate was centered 60 mm vertically above the source, with the temperature of the substrate being monitored by a type C W/Re thermocouple.

The sources were composed of free-standing cylinders of the desired material inserted into a Ta ring, which itself was supported by three Ta pins, as shown in the inset of Fig. 2.6. The cylinder of material was suspended from a Ta wire cage welded to the Ta ring. The cylindrical design was chosen due to the axi-symmetric nature of the laser heating process and because of the ease of acquisition of source materials. The choice of the diameter of the cylindrical sources for a given source element will be detailed in the next chapter. The use of a Ta cage results in the thermal conduction from the source to the manipulator arm being minimized. This reduces the heat loss from the source during operation, allowing for higher evaporation rates to be achieved with lower incident laser power densities.

The evaporation of the source was monitored using a water-cooled quartz crystal microbalance (QCM), which consists of a piezoelectric crystal whose oscillation frequency is altered by the addition of mass due to deposition. From this shift in the resonant frequency of the quartz crystal, the thickness of the deposited material can be determined. These thickness measurements are then multiplied by a tooling factor to convert the QCM measurement to the actual thickness determined by scanning electron microscopy (SEM) measurements. The QCM is sensitive to temperature so it was cooled by a cooling water circuit, however the temperature of the water oscillates over time due to the temperature control of the cooling water. This causes the QCM signal to oscillate at a base frequency; this oscillating signal is used to calculate the average deposition rate for a given laser power.

As shown in Fig. 2.7, a vertical and horizontal shift is introduced into the data from the QCM to align the oscillatory signal before and after deposition. By dividing the value of the vertical offset by the deposition time, an average growth rate for the incident laser power value is extracted. Variations in the phase and the amplitude of the oscillations, caused by instability in the temperature control of the cooling water introduces uncertainty into the extracted growth rate. This uncertainty is particularly relevant for the deposition stability that will be discussed in Chap. 5.

An additional source of uncertainty in TLE is coating of the optical components, namely the laser viewport and the laser mirror, the latter of which is present in a modified version of the TLE test chamber discussed in Chap. 5. To reduce the coating of the optical components, a pinhole aperture was mounted at the focal point of the laser. For a UHV system, TaC is an ideal pinhole material due to its refractive thermal properties, which can be rapidly produced *in situ* by fixing a Ta pinhole, similar in size to the beam width at the focal point of the laser during the deposition of C. The heating of pinhole by the Gaussian laser beam combined with the C flux creates the necessary conditions for the formation of TaC.

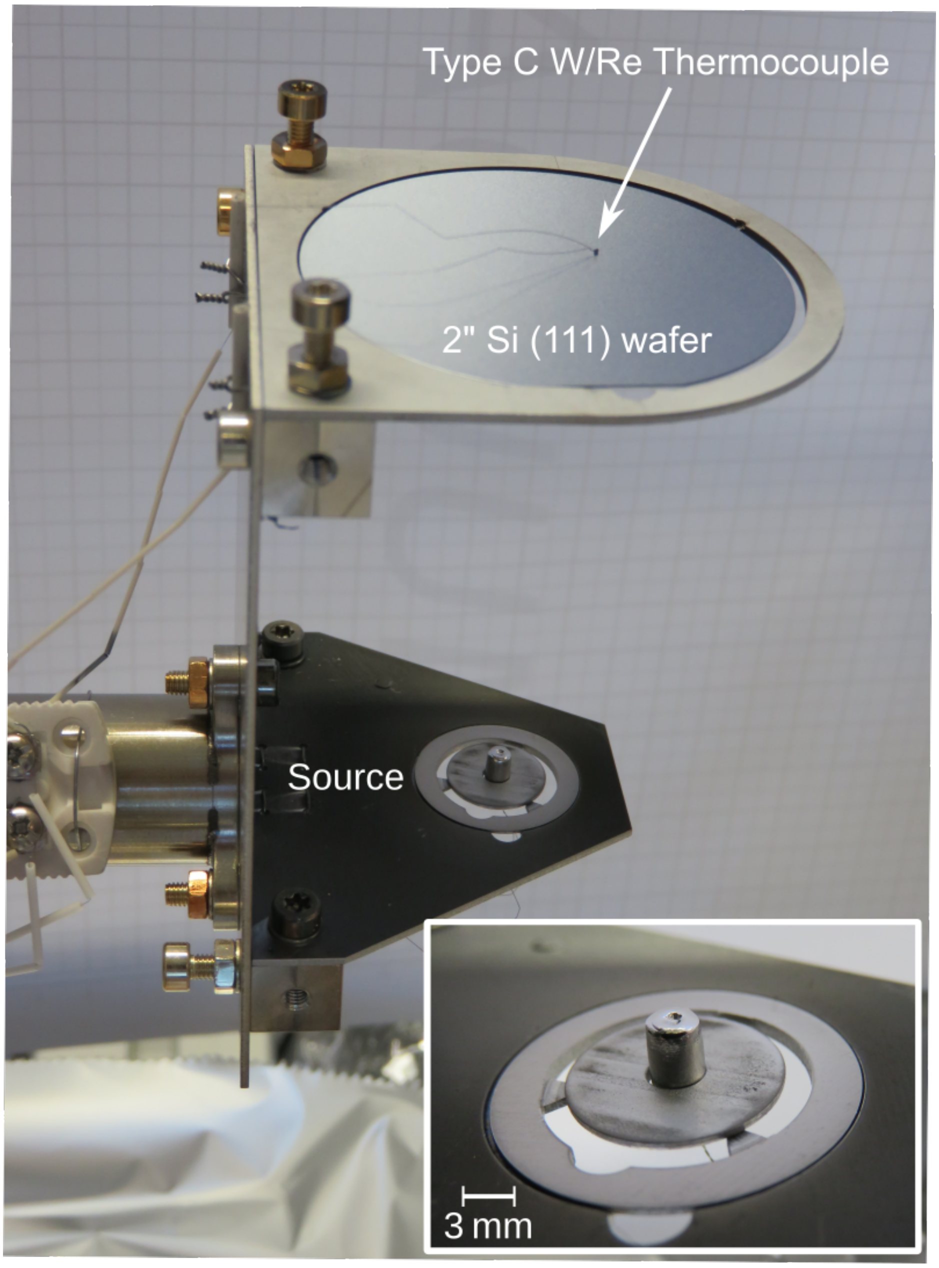

Figure 2.6: Photograph of source-substrate configuration. The source presented is a Ti cylinder with a diameter of 3 mm and a length of 8 mm. The substrate is located 60 mm above the source. The inset shows a photograph of the Ti source after deposition. The surface has melted, creating a dip at the location of the laser spot. The structural integrity of the source has nevertheless remained intact.

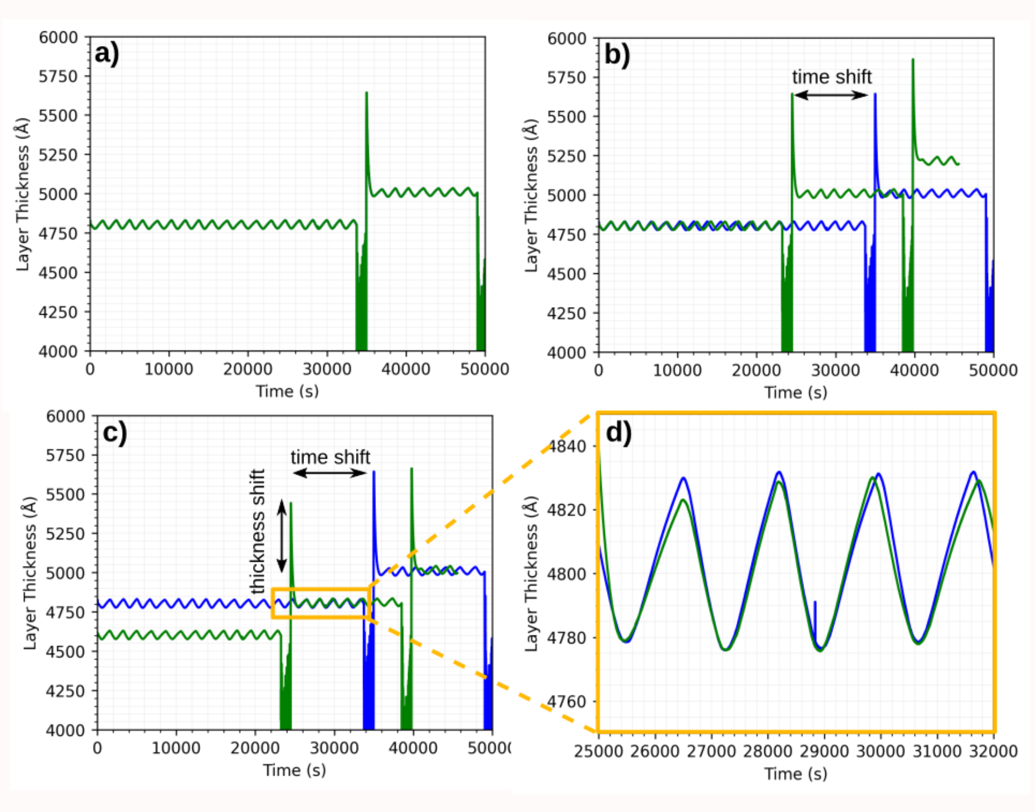

Figure 2.7: Illustration demonstrating how the average growth rate is extracted using the oscillatory signal from the QCM. Panel a) shows the film layer thickness given by the QCM as a function of time. The step at $t \sim 35000$ s indicates when deposition occurred. The small oscillations in the film layer thickness result from the oscillating temperature of the cooling water of the QCM. Panel b) shows a copy of the same signal (in blue) that has been shifted in time in order to align the oscillatory signal before and after the step at $t \sim 35000$ s. Panel c) shows the original signal (green) and the shifted signal (blue) aligned via the introduction of a offset in the thickness. This vertical offset is the divided by the deposition time to obtain the average deposition rate. Panel d) shows a zoomed-in section of panel c) shown in yellow, demonstrating the alignment of the original and shifted signal. Variations in the amplitude and the phase caused by instability in the temperature control of the cooling water of the QCM introduce uncertainty into the value of the thickness offset and therefore the average growth rate.

3

Deposition of elements from across the periodic table by thermal laser epitaxy

The first question I want to explore in this thesis is: Which elements from the periodic table can be deposited with TLE? The purpose of this question is obvious: the more elements that can be deposited with TLE, the broader the range of potential applications that TLE can offer. For example, if Sr and Ti can be successfully deposited as single metallic thin films, it means that the growth of $SrTiO_3$ (STO) is feasible in an oxygen atmosphere. STO is a popular substrate for the epitaxial growth of thin films.[47]

To study the deposition of the different elements, the TLE chamber introduced in Chap. 1 was used. The individual elements were deposited as thin films upon the Si wafers described above. The films were then examined with a scanning electron microscope (SEM) to determine the properties of the deposited film on the substrate. To ensure that dense and uniform films will be deposited, the evaporation behavior of the elements and the resulting evaporation parameters under UHV conditions need to be determined to ensure efficient deposition. To do this, we split the elements into three different groups depending on their evaporation properties.

3.1 Relationship between vapor pressure and melting point

We can divide the solid elements into those that sublimate and those that melt in UHV at elevated temperatures. Elements which exist as a liquid or a gas in UHV or those that are radioactive are not considered in the following discussion. To do this, the temperature required for each element to reach a given vapor pressure was calculated from the vapor pressure curve for the corresponding element.[9] The pressures chosen were 0.1 hPa and 1 hPa, since these vapor pressures are in the upper range of elemental flux from effusion sources in MBE. The required temperature for each vapor pressure value versus the corresponding melting point is shown in Fig. 3.1 as a function of element number.

The results presented in Fig. 3.1 allow us to divide the elements into three categories. The first category of materials "Sublimating", refers to elements where the melting point does not have to be reached to obtain the desired vapor pressure. For these elements, the diameter of the source can be reduced until it matches the dimensions of the Gaussian laser beam, since sublimation mainly originates from the location of the laser spot. This ensures efficient use of material without compromising the structural integrity of the source itself.

The second category labeled "Free-standing", refers to elements where temperatures above the melting point of the material must be reached to achieve the required vapor pressure or growth rate. However, an upper limit was set for the temperature difference between the evaporation temperature T_{evap} and the melting point T_{melt}. This limit was set such that T_{evap} - $T_{melt} \leq$ 500 K. This limit is present due to the thermal gradients present within the source during deposition between the center and the edge of the source. Within the "Free-

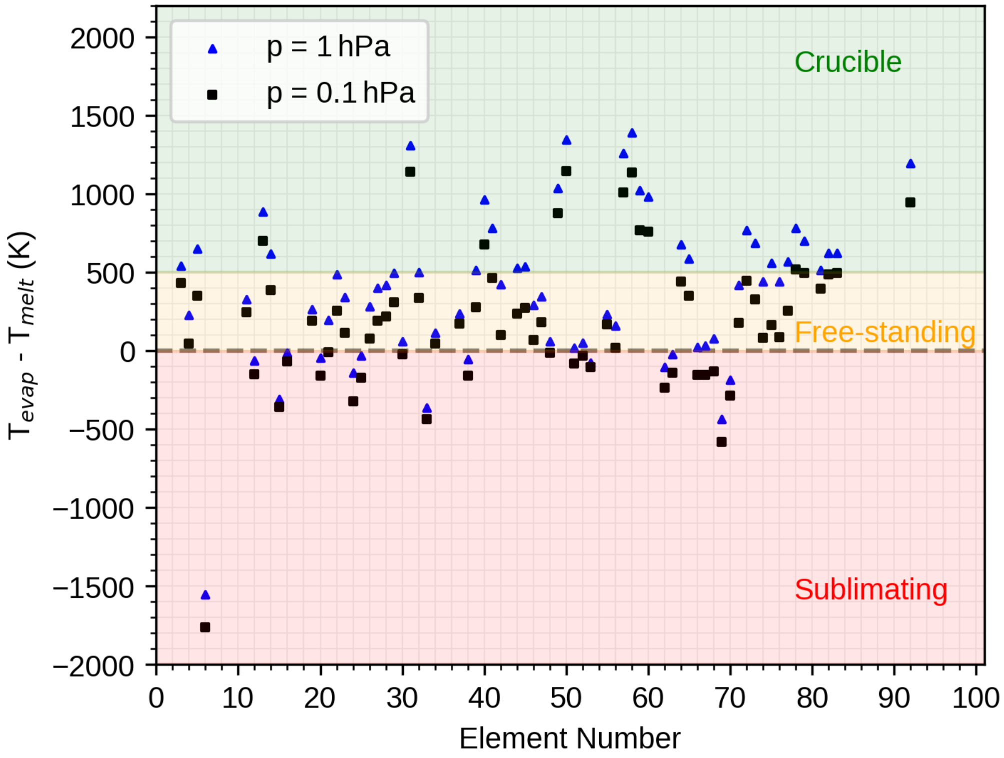

Figure 3.1: Calculated temperature to reach a fixed vapor pressure relative to the melting point, as a function of element number for all solid elements in the periodic table.[9] Elements were only included if vapor pressure data was available. From this, we can broadly split the elements into three categories: "Sublimating", "Free-standing" and "Crucible".

standing" class of materials, a source acts as its own crucible and like the sublimating elements, is ideally suited for depositing ultra-pure thin films using TLE.

If the required evaporation temperature of the source is more than 500 K above the melting point of the source material, these element were evaporated using granular sources held in crucibles. These elements are classified within the third category of materials, labeled as "Crucible". To avoid wetting between the source and the crucible and avoid the formation of eutectic alloys, Al_2O_3 crucibles were used within this thesis unless explicitly stated.

Importantly, in experimental practice, individual elements may differ from their theoretically assigned class due to their thermal conductivities or other physical properties. For example, Ag has the highest thermal conductivity of any element in the periodic table at room temperature, with a value of 430 W/m K. This results in very flat temperature gradients in the source. As a consequence, the structural integrity of a free-standing Ag source will be compromised by the required evaporation temperature for a vapor pressure of 0.1 hPa, therefore crucibles are required for successful deposition of Ag. For similar elements, marginal growth rates on the order of 0.01 Å/s were still possible with freestanding sources of 12.7 mm diameter for Au, Pt, and Zr, but a crucible was required to achieve significant growth rates due to the structural failure of the freestanding sources.

With all this being considered, Table 3.1 shows how all solid, non-radioactive elements divide into the three classes.

Sublimating	C, Tm, As, P, Cr, Yb, Sm, Mn, Sr, Ca, Ho, Dy, Mg, Eu, Er, I, Sb, S, Te, Zn, Cd, Sc
Free-standing	Ba, Be, Se, Pd, Fe, W, Os, Mo, V, Re, Cs, Rb, Lu, Co, K, Ni, Ru, Na, Ti, Ir, Rh, Y, Cu, Ta, Ge, Tb, B, Si, Tl, Li, Gd, Hf, Nb, Bi
Crucible	Pb, Au, Pt, Zr, Al, Nd, Pr, Ag, In, La, Ce, Ga, Sn

Table 3.1: Evaporation behavior of different solid elements in TLE. Radioactive and gaseous elements have been omitted.

3.2 Achievement of deposition of elements from across the periodic table

Using the classes introduced, the deposition of a range of different elements from across the periodic table can be attempted. The deposited elements were limited to solid, non-radioactive elements which were not heavily toxic, nor produced a highly toxic oxide. Successful deposition was defined to have been accomplished when a growth rate greater than 0.1 Å/s was reached. With the exception of Bi, Ce, Sc, Cr, Ca, Yb, and Mn, all elements were locally heated using the aforementioned $\lambda = 1030\,\mathrm{nm}$ disk laser. For the highlighted elements, deposition occurred with a $\lambda = 1070\,\mathrm{nm}$ fiber laser which had the same approximate spot size on the source of $1\,\mathrm{mm}^2$. Photographs of the deposited films were taken after deposition, a selection of which are shown in Fig. 3.2. The associated SEM cross-sections and average film thicknesses are also shown in Fig. 3.2.

Deposition was particularly successful for the metals. Uniform, dense layers with the characteristic columnar structure formed for deposition on an unheated substrate. Since the substrates were not intentionally heated, the layers

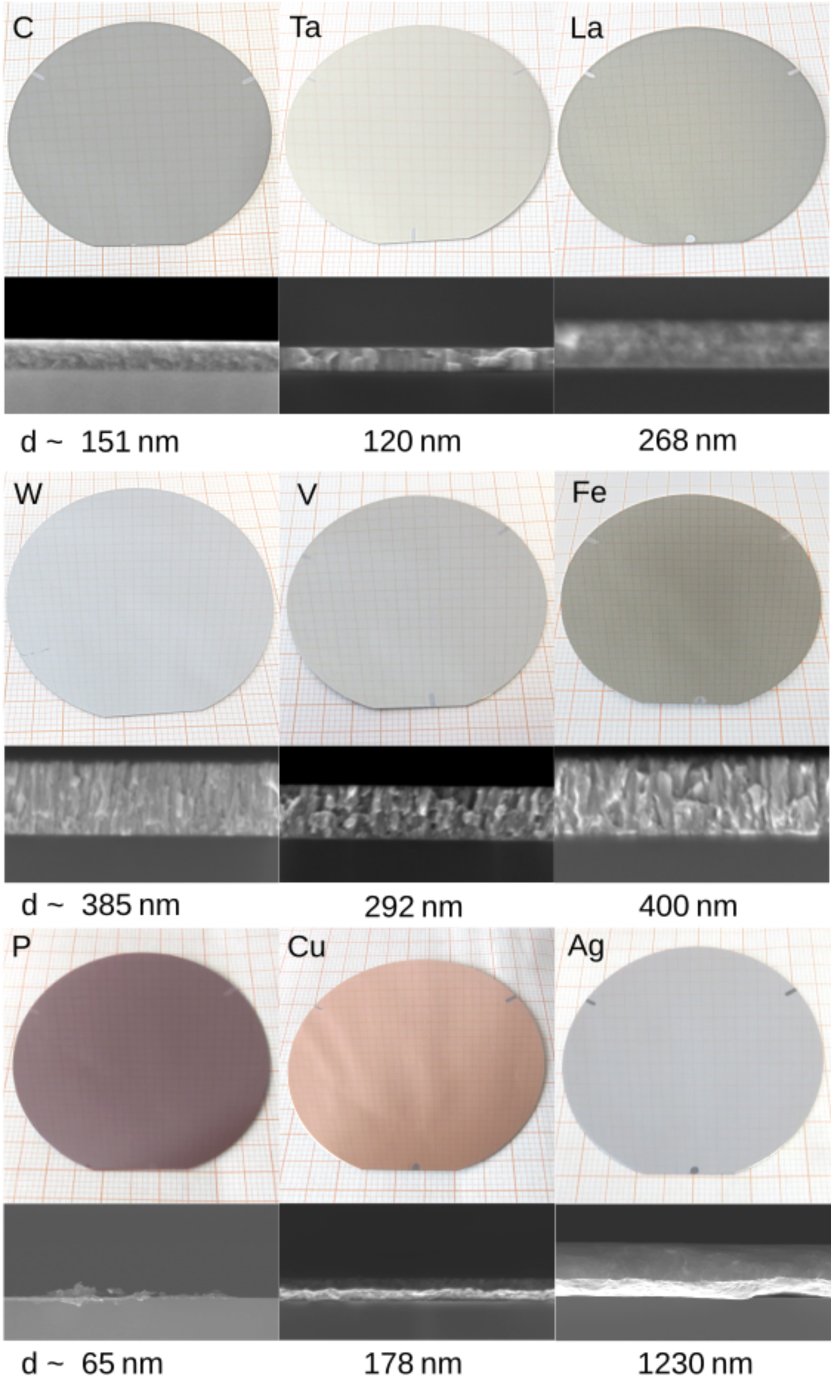

Figure 3.2: Photographs of various elemental films deposited by TLE on 2" Si substrates. The corresponding cross-sectional SEM images are shown below each wafer, along with the average thickness of the deposited layers. The lattice patterns on the wafer surfaces are created by optical reflections. Pin marks from the Ta support pins can be seen on each wafer.

were polycrystalline. On average, the thickness of the films decreased by 10-20 % between the center and the edge of the substrate, which is consistent with the ~14.8 % thickness variation expected due to the $\cos^2(\theta)$ flux distribution across the wafer relative to the normal of the source surface. Some materials, such as S and P, exhibited highly non-uniform layers with a significant number of clusters in the final films. However, other materials are more encouraging: the fact that refractory metals such as W and Ta can be deposited as thin films with TLE is a promising first step for broader application as these materials are challenging to deposit with other epitaxy techniques.

Due to the extreme temperatures that the source can reach during deposition, measuring the temperature of the source with conventional instruments is impossible. For the refractory metals, evaporation temperatures in excess of 3000 K can easily be reached, which is well outside the operating range of most temperature measurement instruments. Therefore, the easily measurable output laser power was used as the variable against which the growth rate was measured. The laser power value could simply be recorded from the output of the laser. Technically, the laser power incident on the source is the parameter that matters here and the output laser power does not necessarily match the incident laser power due to coating of the laser optics. Unless explicitly stated, we will assume that the difference between these two values is small and that the output laser power and the incident laser power are equal. The growth rate as a function of incident laser power for various refractory metals is shown in Fig. 3.3 and over a much larger range of incident laser powers for different elements in Fig. 3.4. For most of the refractory metals in Fig. 3.3, growth rates exceeding 1 Å/s were achieved with less than 500 W of incident laser power. These results represent the first successful deposition of W, C and Ta by thermal evaporation induced by a CW laser.

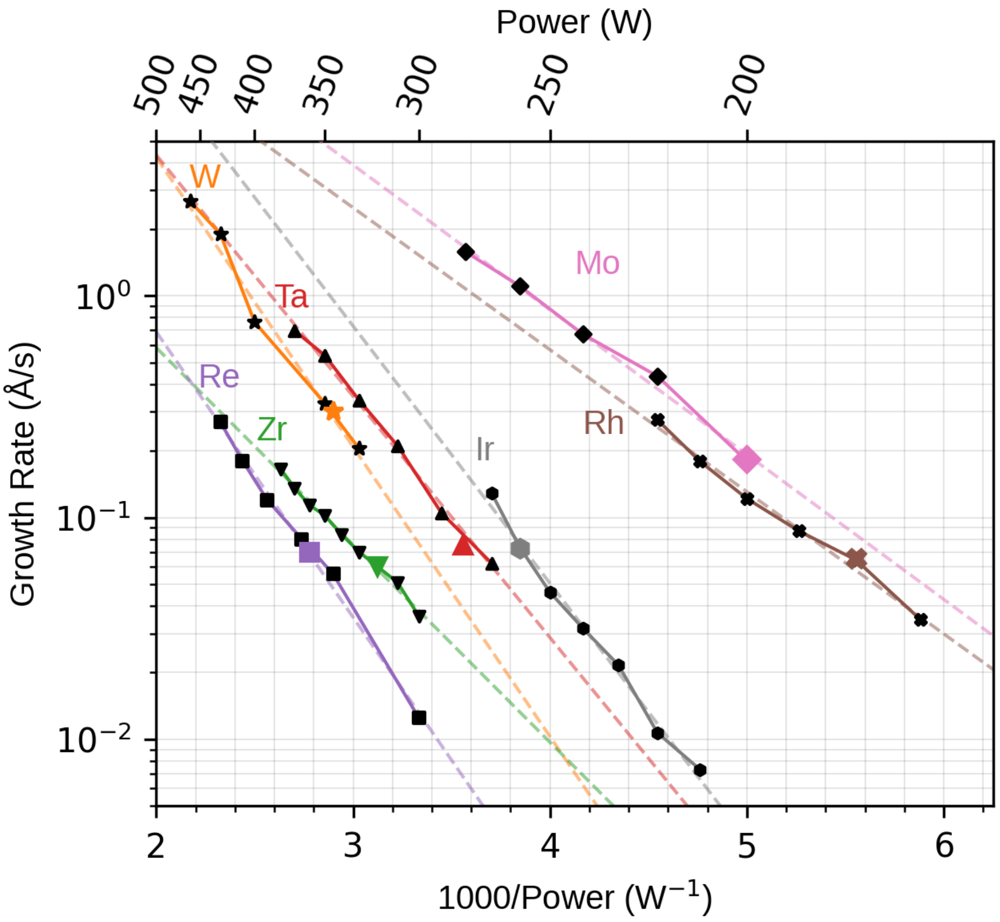

Figure 3.3: Measured growth rates as a function of incident laser power for a range of refractory metals. The dotted line associated with each data set represents an Arrhenius-like dependence fitted to the data. The colored symbols represent the observed melting points of each element. The laser wavelength was $\lambda = 1030$ nm, the source-substrate distance was fixed at 60 mm and the focal distance of the laser was 500 mm.

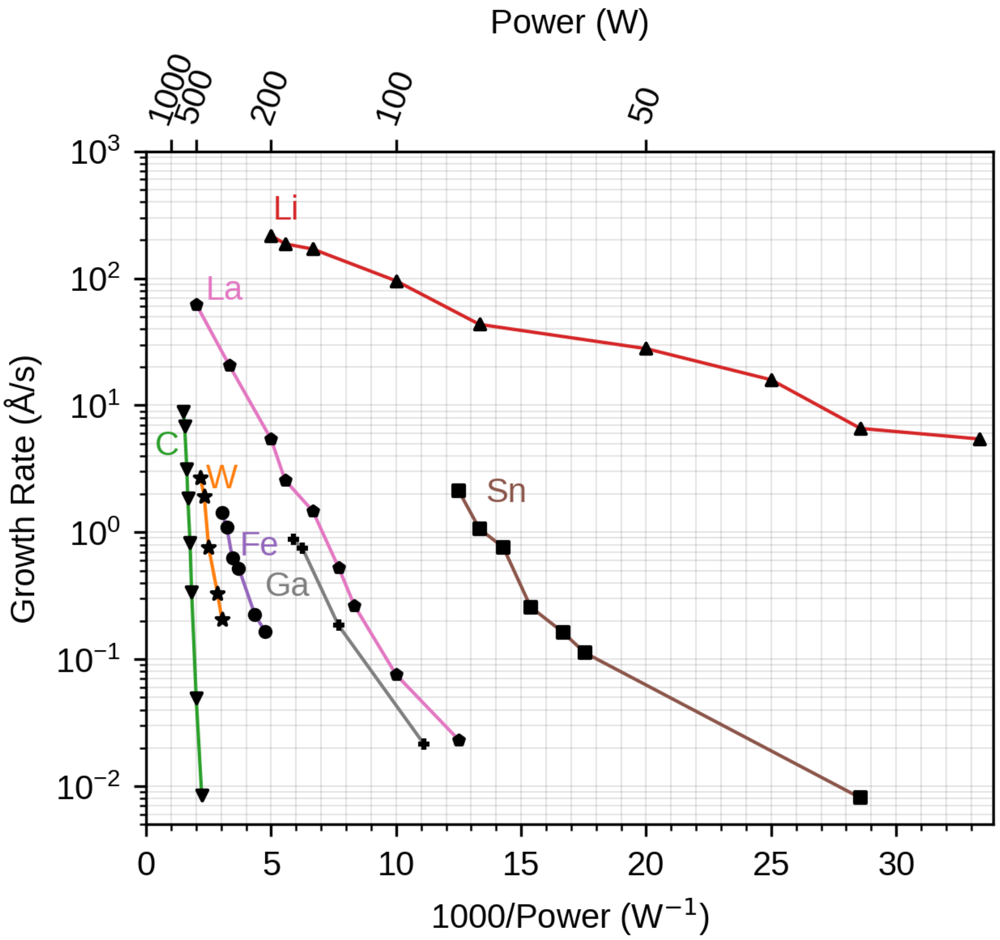

Figure 3.4: Measured growth rates as a function of incident laser power for a number of different elements from the entire periodic table. The laser wavelength was λ = 1030 nm, the source-substrate distance was fixed at 60 mm and the focal distance of the laser was 500 mm.

For each element, the growth rate as a function of incident laser power appears to follow a functional dependence similar to an Arrhenius equation that characterizes the temperature dependence of reaction rates in physical chemistry and whose functional form appears often within the natural sciences.[48] An Arrhenius equation $y(x)$ has the form:

$$y = ae^{-\frac{b}{x}}, \tag{3.1}$$

where a and b are fit constants. In the plots shown in Fig. 3.3 and Fig. 3.4, an Arrhenius-like dependence manifests as a straight line. The experimental Arrhenius-like fits for the growth rate, R_G as a function of laser power, P shown in Fig. 3.3 have the form:

$$R_G = ae^{-\frac{b}{P}}, \tag{3.2}$$

where a and b are fit constants. This form is not unexpected as it is well established that the growth rate of a material upon a substrate is directly proportional to its vapor pressure.[49] To a first-order approximation, the vapor pressure follows an Arrhenius dependence in the Clausius-Clapeyron equation (Eqn. 1.3).[7] If one equates Eqn. 3.2 and the Clausius-Clapeyron equation, an approximate relation can be found between P and the source temperature, T.

$$\frac{1}{T} = \frac{A}{P} + B, \tag{3.3}$$

where A and B are material properties determined by fitting the data. The physics behind this dependence and its consequences will be discussed in Chap. 6.

The successful deposition of many different elements from across the periodic table raises the question of whether TLE can be applied to any solid element in the periodic table. To answer this question, we specifically studied the growth of elements with extreme physical parameters. For example, the ability to readily evaporate W, which has the lowest vapor pressure of any element in the periodic table and a melting point of 3695 K, suggests that TLE is not limited by evaporation temperature. Similarly, the successful deposition of the Group IB elements (Cu, Ag, and Au), all of which have reflectance values close to one at 1030 nm, indicates that reflectivity is not a barrier to TLE. High and low values of thermal conductivity are also not a problem, as both Ag and S were successfully evaporated. Ag also holds the distinction of being especially challenging due to its high reflectivity, high thermal conductivity and low vapor pressure. The fact that this material can be successfully deposited helps us form the argument that TLE can be applied to all solid elements in the periodic table. All the elements that have been successfully deposited via TLE are shown in Fig. 3.5. At the time of writing, we have successfully deposited 51 out of 68 (75%) of all solid, non-radioactive elements either from a free-standing source, or from a crucible.

3.3 Selecting an appropriate source diameter

Finally, we can turn our attention to the class of "Free-standing" materials. Elements within this class may be deposited from a range of source diameters ranging from 2 mm to 12.7 mm diameter. The selection of an appropriate source diameter is therefore critical to optimizing the required incident laser power for the desired growth rate. Optimizing the source diameter can result in a significant increase in the growth rate achieved for a fixed laser power density. As shown in Fig. 3.6, in the case of Ta, increasing the diameter of the source at a fixed laser power leads to a decreasing growth rate. This is due to the fact that

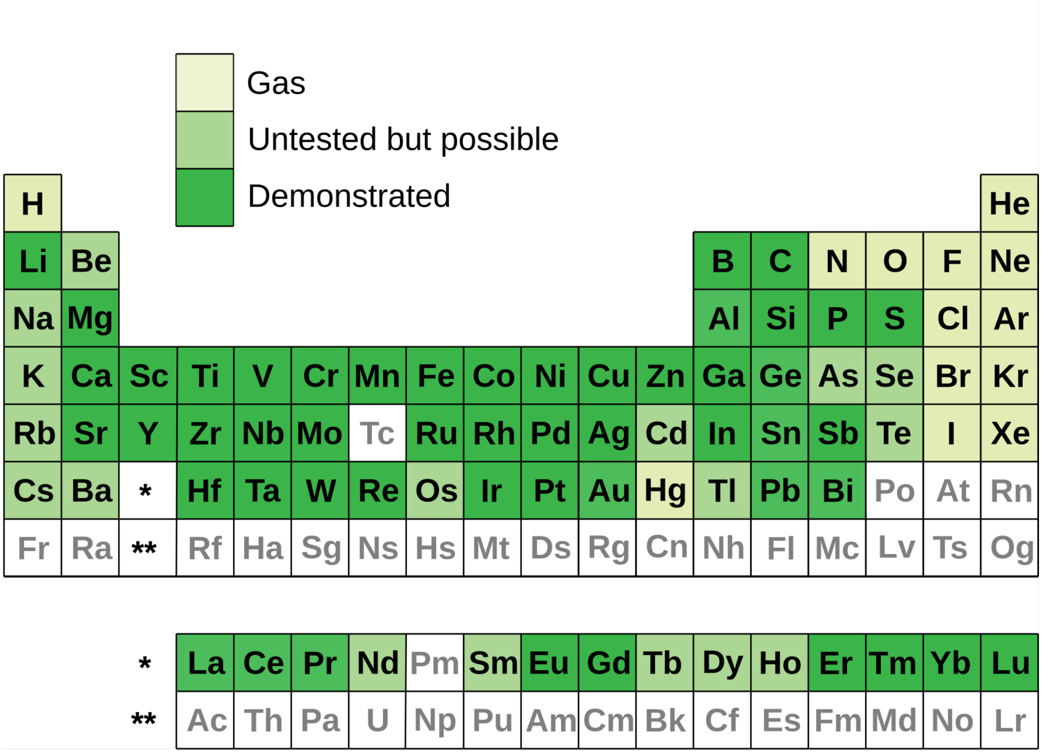

Gas

Untested but possible

Demonstrated

H																	He
Li	Be											B	C	N	O	F	Ne
Na	Mg											Al	Si	P	S	Cl	Ar
K	Ca	Sc	Ti	V	Cr	Mn	Fe	Co	Ni	Cu	Zn	Ga	Ge	As	Se	Br	Kr
Rb	Sr	Y	Zr	Nb	Mo	Tc	Ru	Rh	Pd	Ag	Cd	In	Sn	Sb	Te	I	Xe
Cs	Ba	*	Hf	Ta	W	Re	Os	Ir	Pt	Au	Hg	Tl	Pb	Bi	Po	At	Rn
Fr	Ra	**	Rf	Ha	Sg	Ns	Hs	Mt	Ds	Rg	Cn	Nh	Fl	Mc	Lv	Ts	Og
		*	La	Ce	Pr	Nd	Pm	Sm	Eu	Gd	Tb	Dy	Ho	Er	Tm	Yb	Lu
		**	Ac	Th	Pa	U	Np	Pu	Am	Cm	Bk	Cf	Es	Fm	Md	No	Lr

Figure 3.5: Periodic table showing in dark green the range of elements that have been successfully deposited at substantial growth rates using free-standing sources and crucibles at the time of writing. Light green elements represent those elements that have not yet been experimentally tested but are found to be possible to deposit using TLE. Elements that have been grayed out are radioactive.

the temperature of the source decreases as the diameter of the source increases due to the energy loss per unit time. The energy loss due to radiation and evaporation is directly proportional to the surface area of the cylindrical source, so increasing this surface area results in a greater energy loss per unit time. This greater energy loss results in a feedback loop where greater surface areas result in lower temperatures which then reduces the energy lost due to the temperature dependence of radiation and evaporation. Therefore the amount of energy lost is an interplay between the surface area of the source and the temperature dependence of each loss mechanism. Strictly speaking, this interpretation is only valid at low evaporation rates, as further elaborated on in Chap. 6. Regardless, these results show that minimizing the diameter of the source increases the growth rate at a fixed laser power density.

However, there are limits to the diameter of the source, especially for materials belonging to the "Free-standing" class mentioned earlier. The growth rate can be adversely affected if the laser power is too high for a given source diameter. To demonstrate this, we again turn to the example of a Ta source with a diameter of 3 mm in Fig. 3.7, wherein increasing the incident laser power results in the localized liquid Ta expanding, eventually hitting the rim of the source. Once this occurs, the high surface tension of liquid Ta causes the formation of a spherical bulb on top of the source.[50] This leads to a wider angular distribution in the flux from the source, causing a rapid decline in the growth rate. In the case of Ta shown in Fig. 3.7, a notable curvature formed at ~ 350 W but the growth rate continued to increase until ~ 370 W which seems to contradict the previous argument regarding the wider angular distribution of the flux. We speculate that this is because the projected spot size of the laser increases due to the curved surface of the liquid Ta, resulting in a larger area of the surface with a higher temperature and increasing the growth rate. Another problem

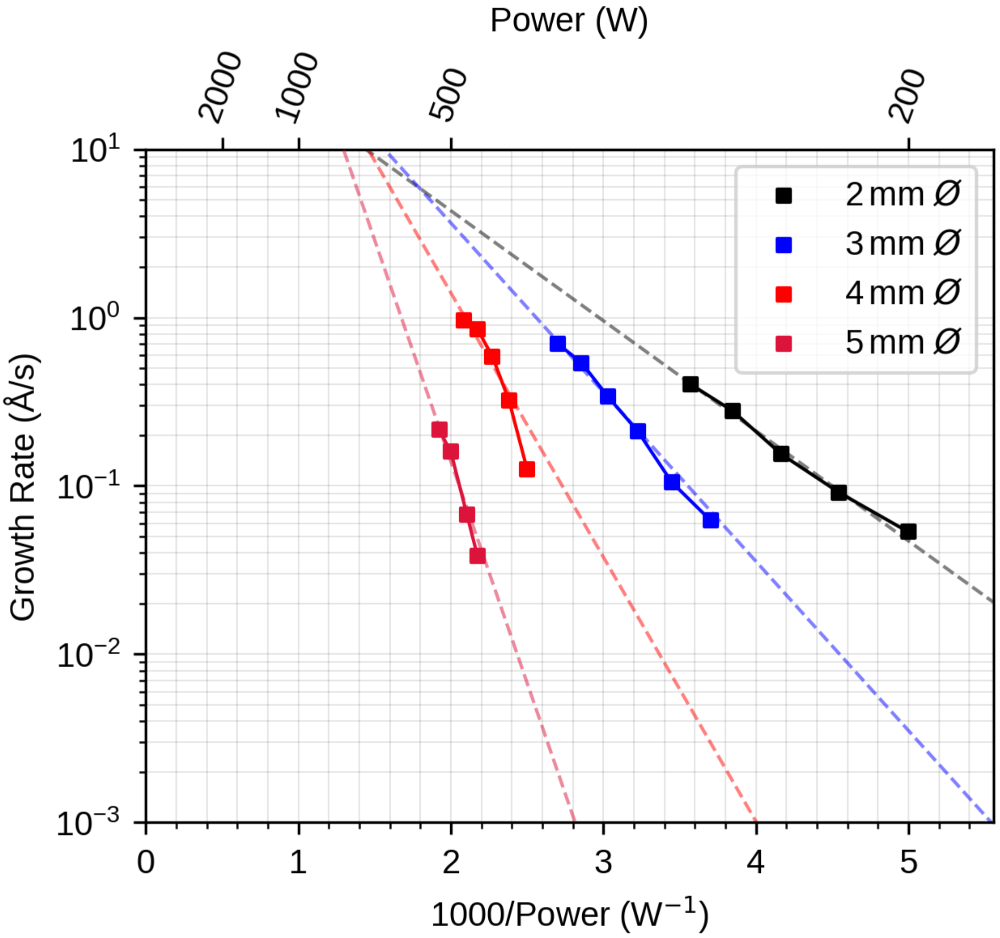

Figure 3.6: Measured growth rate data of Ta as a function of laser power for different source diameters. The dashed lines show Arrhenius-like fits for each data set according to Eqn. 3.2. Increasing the diameter of the source for a fixed laser power results decreases the growth rate due to the increased energy loss caused by the larger surface area of the source. The laser wavelength was $\lambda = 1030$ nm, the source-substrate distance was fixed at 60 mm and the focal distance of the laser was 500 mm.

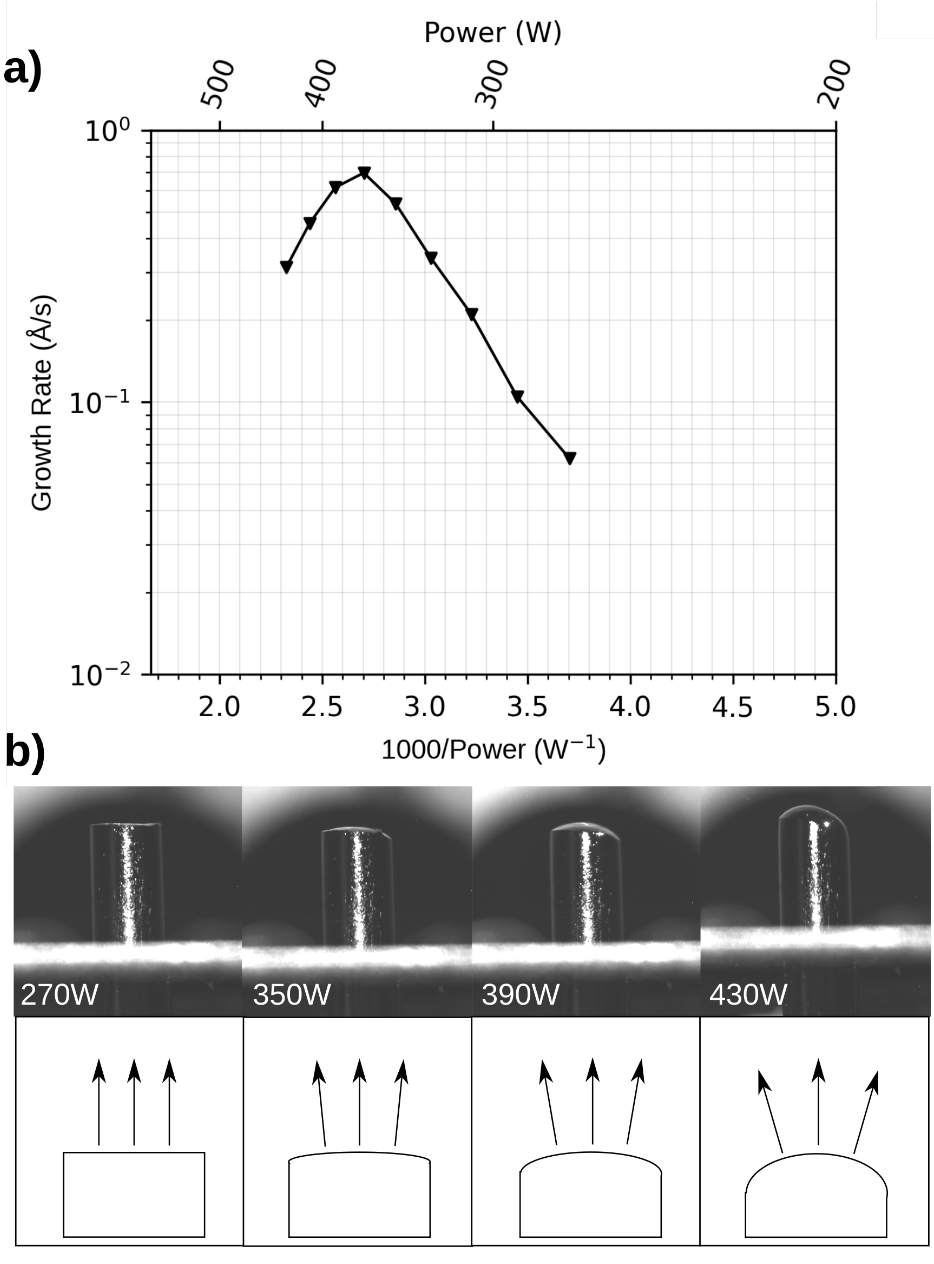

Figure 3.7: a) Growth rate of a Ta source with a diameter of 3 mm as a function of output laser power. The accompanying photos in b) show a side view of the Ta source with a diameter of 3 mm after 10 minutes of deposition at the indicated laser power. An illustration of the flux distribution for each laser power is included with each photo. Increasing the laser power eventually causes the entire surface to become a liquid and form a spherical bulge due to surface tension. This leads to a scatter in the flux distribution, resulting in a decrease in the growth rate measured with the QCM. The laser wavelength was λ = 1030 nm, the source-substrate distance was fixed at 60 mm and the focal distance of the laser was 500 mm.

with using a laser power that is too high for the source geometry is structural failure, where a large portion of the source melts without the rest of the source remaining intact. These factors must be considered when choosing an appropriate source size.

In summary, it has been shown that TLE is capable of depositing all solid, non-radioactive elements from the entire periodic table with a relatively simple experimental setup. Elements that are difficult to deposit with other epitaxy techniques, such as the refractory metals, can be readily deposited with TLE. Most metals deposited as thin films with TLE exhibit uniform, dense films on a 2" Si substrate. When we study the vapor pressure of the elements, we can divide the elements into three classes based on their evaporation behavior in a vacuum chamber. These include a group of materials that can be deposited from free-standing element sources without the need for a crucible. By optimizing the diameter of the cylindrical free-standing sources used in TLE, the growth rate can be increased at a fixed laser power, although flux scattering or structural failure can occur if the incident laser power is too high.

4

Utilizing the optical properties of metals to increase the deposition efficiency of TLE

Most of the elements are metals. Due to the wavelength dependence of light-matter interactions within metals, the reflectivity of a metal drops significantly moving from the infrared to the ultraviolet range. This change in the reflectivity $\mathscr{R}$ is shown for a selection of metals using the results of room temperature optical spectroscopic ellipsometry measurements in Fig. 4.1. The experimental data is compared to literature values from bulk samples of the indicated element.[51, 52] To make the relation to the absorption of light more explicit, the ellipsometry data in Fig. 4.1 is given in terms of the absorptivity $\mathscr{A}$, assuming the transmissivity of the samples are zero:

$$\mathscr{R} + \mathscr{A} = 1, \tag{4.1}$$

therefore within this system we can assume that $\mathscr{R}$ and $\mathscr{A}$ are functionally equivalent. Within this system, the transmissivity $\mathscr{T}$ is defined as the ratio of the intensity of light transmitted through the entire sample I_t and the intensity of the incident radiation upon the sample I_0:

$$\mathscr{T} = \frac{I_t}{I_0}, \tag{4.2}$$

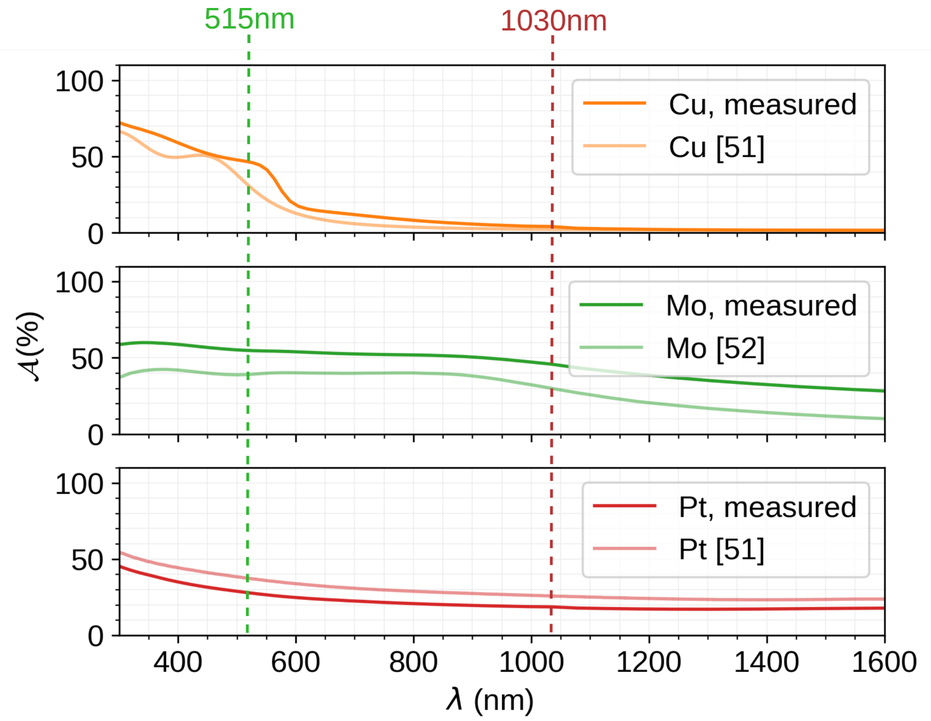

Figure 4.1: Measured absorptivity spectra for Cu, Mo and Pt thin films grown via TLE compared to literature values for bulk samples.[51, 52] The wavelengths of the visible and infrared lasers used in this thesis are indicated. Transmission is assumed to be zero.

Assuming that $\mathcal{T}$ is zero means that no light is transmitted through the entire sample, which is a valid assumption for macroscopic metallic samples irradiated with infrared to visible radiation.

Within Fig. 4.1, a rapid increase in visible light absorptivity is observed within the spectra of Cu, indicating a significant increase in the fraction of visible light absorbed by Cu compared to infrared wavelengths. A similar increase in absorbance at visible wavelengths is also observed for the other elements in Group IB: Ag and Au, resulting in each element having a characteristic color. The presence of a wavelength dependence in the optical properties of an element presents an opportunity to increase the efficiency of the laser evaporation process. With the availability of high power visible wavelength disk lasers, the use of a visible light laser for source evaporation in TLE becomes feasible. This is particularly interesting for refractory metals, which require very high laser powers to achieve high growth rates with an infrared laser (see Chap. 3).[43]

To investigate the effects of using visible laser light for source evaporation in TLE, two different fiber-coupled disk lasers were compared: a $\lambda = 1030\,\mathrm{nm}$ laser with a peak power of 2 kW and a $\lambda = 515\,\mathrm{nm}$ laser with a peak power of 850 W.[28] As detailed previously, the laser beams were incident at 45° relative to the surface of the source with a distance of 62 mm between the source and focal point of each laser. Both lasers illuminated an area of approximately 1 mm^2 on the source with a Gaussian intensity profile. If incident laser power values below the minimum stable CW power were required (~30 W for both lasers), the lasers could be pulsed to achieve the desired average power values. Due to the high heat capacity of many metals, the temperature may take tens of seconds to drop significantly when the laser is switched off, therefore during an appropriate duty cycle, the change in the temperature in between laser pulses can be assumed to be minimal. Given that pulsing the lasers is only required for materials that have high vapor pressures and consequentially require low evaporation temperatures, the energy loss via evaporation which scales as T^4 is minimal. The example of a source of Zn with a diameter of 3 mm heated to 670 K can be used. This temperature corresponds to a vapor pressure of $\sim$ 0.1 hPa. From finite element simulations discussed in more detail in Chap. 6, we can estimate that within 0.5 seconds of the laser switching off, the temperature drops by $\sim$ 15 K from 670 K to 655 K. This temperature drop reduces the vapor pressure by a factor of $\sim$ 2. The change in the vapor pressure during the temperature drop may explain some of the instability and jitter observed in the growth rate for elements that were irradiated using a pulsed laser, however for this thesis, I deem that the error bars from this jitter are acceptable. Two different duty cycles were used during the course of this thesis: a 10 % duty cycle with a pulse length of 10 ms and a repetition rate of 10 Hz and a 1 % duty cycle with a pulse length of 1 ms and a repetition rate of 10 Hz.

For each element, the Arrhenius-like dependence of the growth rate as a function of the incident laser power was used to estimate an error bar for the required power to reach a given growth rate.

To determine the wavelength dependence of the evaporation efficiency, the incident power required to achieve a desired growth rate was determined. For other epitaxial techniques, the typical range of growth rates for thin film growth is from 0.01 Å/s to 1 Å/s.[53, 54] Therefore, our comparison point was set at 0.1Å/s. Further comparisons were made at 0.01 Å/s and 1 Å/s to investigate a possible dependence of the efficiency on the incident laser power.

The incident laser powers required to achieve 0.1 Å/s for both the $\lambda = 515$ nm and the $\lambda = 1030$ nm lasers are shown in Fig. 4.2. Zn and Eu required incident laser powers below the minimum stable CW laser power (~ 30 W), necessitating the lasers to be operated on a pulsed duty cycle. These elements possess high vapor pressures and relatively high reflectivity values, resulting in a minimal amount of incident laser power being required to achieve the desired growth rate.[9] It should be noted that the relative uncertainty in the required power values for these elements becomes more significant due to the lasers operating in a pulsed duty cycle. During operation in this pulsed duty cycle, jitter in the pulse widths adds to the CW fluctuations of the output laser power, thereby increasing the noise in the data.

As shown in Fig. 4.2, a majority of the elements tested required approximately 20-30% lower laser power values with the $\lambda = 515$ nm compared to the $\lambda = 1030$ nm laser. For the visible light laser, this results in growth rates exceed-

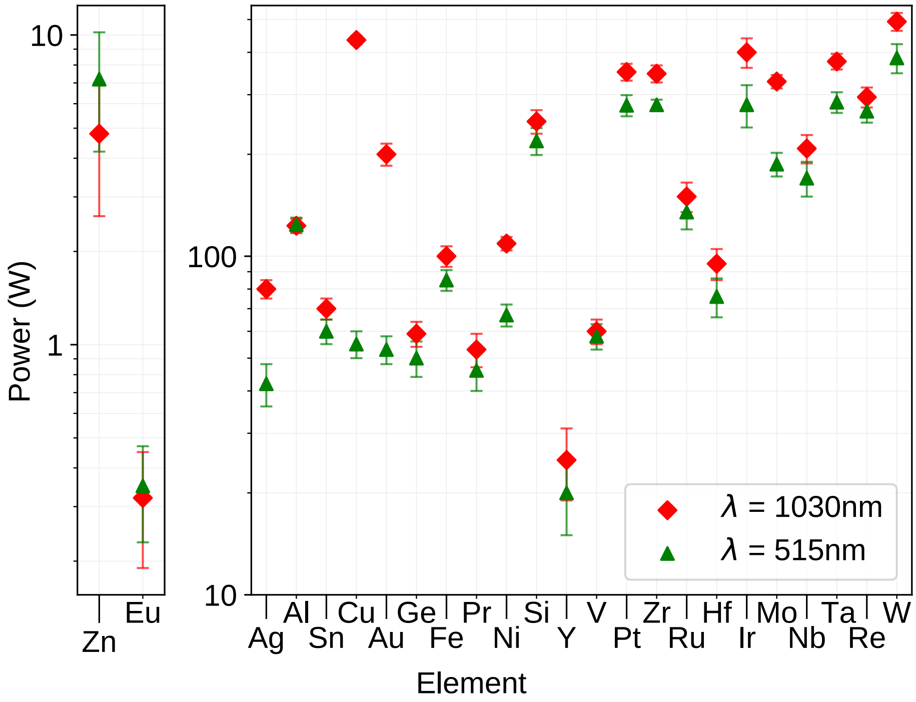

Figure 4.2: Output laser power required to achieve a growth rate of 0.1 Å/s using 515 and λ = 1030 nm laser light for a variety of elements. Apparently missing error bars are smaller than the given marker size. The left-hand panel shows the elements that required the lasers to operate in pulsed mode. The source-substrate distance was fixed at 60 mm and the focal length of both lasers were 500 mm.

ing 0.1 Å/s being achieved with less than 400 W of incident laser power for all elements tested. By optimizing the size of the source, as described in Chap. 3, the required power will likely be reduced further.

By comparing the relative reductions in laser power directly, the ratio of the required powers for both lasers, $\alpha = P_{1030\text{nm}}/P_{515\text{nm}}$ was calculated. These values are plotted in Fig. 4.3. Values of α greater than unity were obtained for nearly all elements tested, except for Zn and Eu. This is likely the result of uncertainty in the incident laser power caused by the pulsed duty cycle. Where available, the corresponding values of α are also shown for 1 Å/s and 0.01 Å/s.

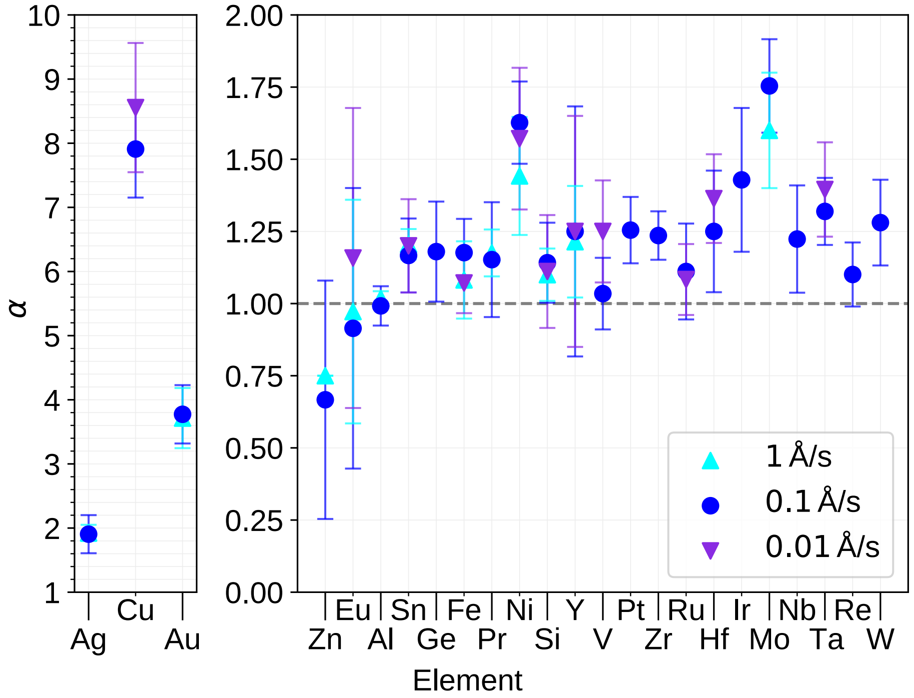

Figure 4.3: Measured ratio of the required powers, α to achieve indicated growth rates for a variety of elements as calculated from Fig. 4.2. The left panel presents the elements with $\alpha > 1.8$.

Significant values of α were observed for Ag, Cu and Au equal to 1.9 ± 0.2, 3.8 ± 0.4 and 8.1 ± 1.1 respectively. The uncertainty values in Fig. 4.3 were extracted from Fig. 4.2 calculating the error by using uncertainty propagation.

4.1 Relating efficiency to physical properties

Previous literature detailing the heating of metals via a Gaussian laser concludes that for a semi-infinite plane of metal, the maximum temperature, T_{max} of the metal is given by:[55]

$$T_{\text{max}} = \frac{(1-\mathscr{R}) I_0 w \sqrt{\pi}}{2k}, \tag{4.3}$$

Where w is the full-width-at-half-maximum of the intensity of the laser beam, and k is the thermal conductivity. Therefore to achieve the same T_{max} , a change in I_0 must be matched by a corresponding change in $\mathscr{R}$. From this, I define the parameter $\mu = (1-\mathscr{R}_{515\text{nm}})/(1-\mathscr{R}_{1030\text{nm}})$. To see how this value relates to α, it must be stated that we wish for two different laser wavelengths to possess the same T_{max} for the same material:

$$\frac{T_{\text{max},1}}{T_{\text{max},2}} = 1, \tag{4.4}$$

where the indices 1 and 2 indicate the two different laser wavelengths, This equation is then equal to:

$$\frac{\frac{(1-\mathscr{R}_1)I_{0,1}w\sqrt{\pi}}{2k}}{\frac{(1-\mathscr{R}_2)I_{0,2}w\sqrt{\pi}}{2k}} = \frac{(1-\mathscr{R}_1)I_{0,1}}{(1-\mathscr{R}_2)I_{0,2}} = \frac{(1-\mathscr{R}_1)P_1}{(1-\mathscr{R}_2)P_2}, \tag{4.5}$$

where we have assumed that both lasers illuminate the same spot size, so the denominators of the intensity terms cancel, leaving behind the laser power values for each wavelength P_1 and P_2. If we let index 1 represent $\lambda = 1030\,\text{nm}$ and index 2 represent $\lambda = 515\,\text{nm}$, we can insert our previous definitions of α and μ:

$$\frac{\alpha}{\mu} = \frac{T_{\text{max},1030\,nm}}{T_{\text{max},515\,nm}} = 1, \tag{4.6}$$

which reduces to:

$$\alpha = \mu. \tag{4.7}$$

Therefore, α and μ are equivalent to one another if Eqn. 4.3 holds. α emerges from our experimentally measured values of the required laser power while μ comes from the literature values of $\mathscr{R}$ for each laser wavelength. The comparisan between α and the temperature dependent values of μ are shown in Fig.

4.5.

4.1.1 Temperature dependence of the optical properties of a material

The temperature dependence of $\mathscr{R}$ emerges from the dielectric function, $\epsilon(T) = \epsilon_r(T) + i\epsilon_i(T)$. The dielectric function describes the polarization of a material in response to an electric field: ϵ_r characterizes the linear polarization response of a material whilst ϵ_i describes the dielectric losses within the material, typically as a result of absorption or scattering. The components of the dielectric function are related to the reflectivity, $\mathscr{R}$ via: [56]

$$\mathscr{R} = \frac{(1-n)^2 + k^2}{(1+n)^2 + k^2}, \tag{4.8}$$

where

$$n = \frac{1}{\sqrt{2}}\sqrt{\sqrt{\epsilon_r^2 + \epsilon_i^2} + \epsilon_r}, \tag{4.9}$$

$$k = \frac{1}{\sqrt{2}}\sqrt{\sqrt{\epsilon_r^2 + \epsilon_i^2} - \epsilon_r}. \tag{4.10}$$

$\mathscr{R}$ as a function of ϵ_r and ϵ_i is plotted in Fig. 4.4, with overlaid values of the dielectric function at a given laser wavelength for individual elements extracted from literature.[57, 58, 59, 60] Given the limited availability of data for the dielectric function for all temperature values, the colored arrows only indicate the change from room temperature values to the value of the dielectric function at the indicated temperature. Regardless, this serves as an indication of the temperature dependent behavior of the dielectric function and therefore of the reflectivity for the given elements. Further insight may be gained from this data by considering the origin of the temperature dependent optical properties. As previously discussed in Chap. 1, the primary absorption mechanisms of light within a material are via plasma oscillations and interband transitions, each of which has their own temperature dependence. The temperature dependent effects can therefore be traced back to interactions between the electrons themselves and between the electrons and the crystalline lattice. For plasma oscillations, which are the dominant absorption mechanism at low photon energies, the temperature dependence emerges from the damping of these oscillations by electron-phonon scattering. In the case of Cu, by increasing the temperature to 920 K, the increase in the electron-phonon scattering rate causes the reflectivity of Cu at 1030 nm to drop from around 97.1% to around 93.7%, increasing the amount of radiation absorbed by a factor of ~ 2.[57]

Conversely, the temperature dependence of interband transition rates for pure metals emerges from the thermal broadening of the electron Fermi-Dirac distribution and from the thermal expansion of the crystalline lattice which changes the inter-atomic distance and the crystalline potential.[61] The thermal broadening of the Fermi-Dirac distribution broadens the transition level and thus affects the energy of the given interband transition.[62] Returning to the case of Cu, these effects move the onset energy for interband absorption from ~ 2.13 eV at room temperature to 2.08 eV at 700 K.[57] Broadening of the energy levels caused by electron-phonon interactions plays a role but this can often be neglected.[63, 62] In comparison to the free-electron oscillations, the temperature dependence of the interband transitions has a minor effect on the reflectivity. For Cu, this equates to a reduction in the reflectivity at 515 nm from 58.7% to 56.9% by increasing the temperature from room temperature to 920 K.[57] This temperature dependence increases the amount of radiation absorbed at $\lambda = 515$ nm by a factor of 1.04.

Whilst these temperature dependencies have been studied experimentally for many metals,[64, 57, 65] the change in the optical properties past their melting points have not been readily studied experimentally, and theoretical values of the optical properties for liquid metals vary between different studies.[30, 31, 66] This is a gap that the experimentally measured values of α may be able to help alleviate.

4.2 Required laser power for evaporation in TLE as a measure of the optical properties of a material at high temperatures.

One can take the temperature dependent reflectivity values calculated from the literature and use them to calculate temperature dependent values of μ. From the argument presented, a direct comparison between the values of μ and the experimentally derived values of α can be made. Such a direct comparison is made in Fig. 4.5 where the dashed line indicates a linear dependence between α and μ.

Whilst one is limited by the availability of data for the temperature dependent optical constants, a conclusion can be made that μ and α are not exactly linear due the scatter away from the $\alpha = \mu$ line in Fig. 4.5 This contradicts the assumption of the semi-infinite thermodynamic model in Eqn. 4.3, which is logical due to the radiative boundaries present in the real source compared to the semi-infinite model. However, more data points are required to make a definite conclusion. A secondary comparison between μ and α can be made by extracting temperature values for each α value were extracted by noting that the growth rate and the vapor pressure of an element are proportional to each other along with the required laser power to observe the melting point of said element.[49] In discussing the temperature dependence of the optical proper-

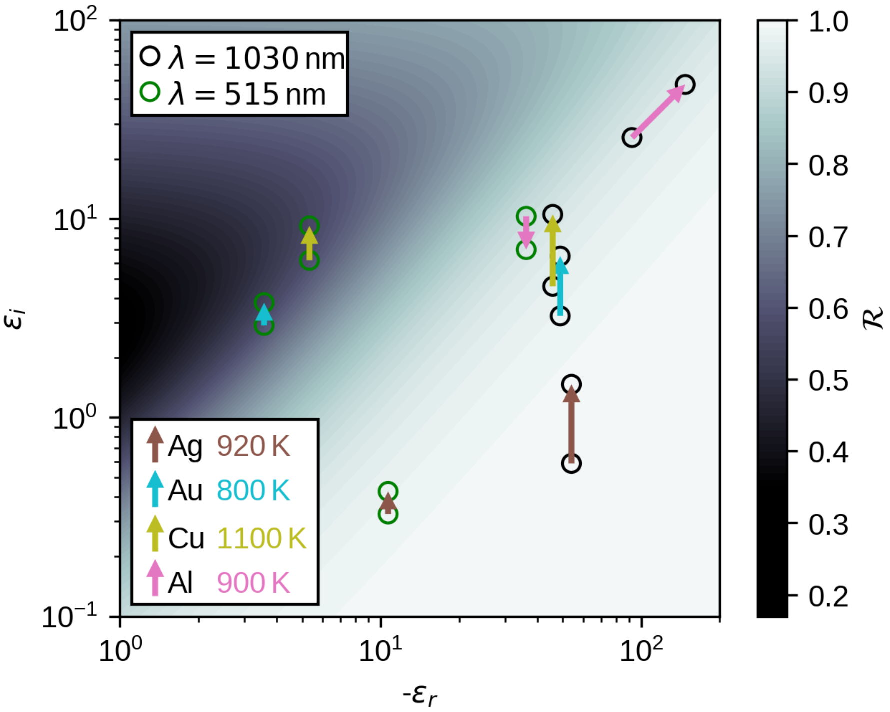

Figure 4.4: Plot of reflectivity as a function of the components of the dielectric function. Individual points for each laser wavelength are shown with the associated colored arrow indicating the element in question. These points were taken from literature values.[57, 58, 59, 60] The arrows indicate the change in the dielectric function and thus the reflectivity when the temperature dependence is of the dielectric function is explicitly considered.

ties, I will primarily focus upon the group IB metals (Cu, Au and Ag) as their temperature dependent properties have been widely studied in literature and I found these elements to exhibit the largest values of α during the experiments that provided the data of Fig. 4.3.

Cu, Au and Ag possess fully filled d-bands ($3d^{10}$, $4d^{10}$ and $5d^{10}$, respectively), and each has a single valence electron in its respective s-band. The maxima of the d-bands lie ~ 2.1, 2.4 and 3.8 eV below the Fermi level.[67] This results in the onset of interband transitions between the filled d-band and the

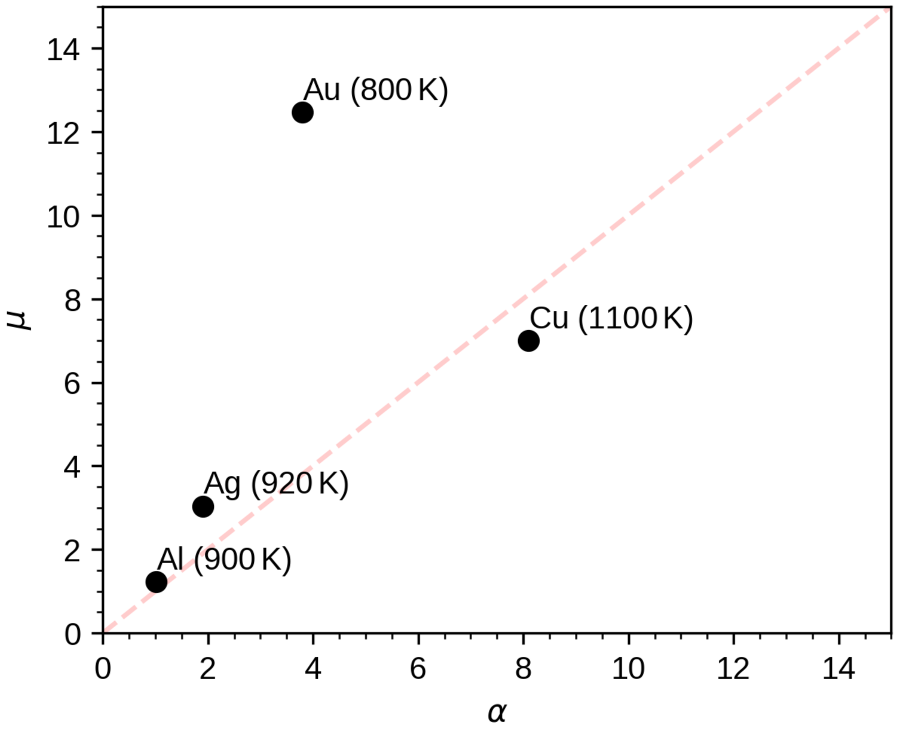

Figure 4.5: Comparison between the experimentally measured values of α and the temperature dependent values of μ derived from literature.[57, 58, 59, 60] The dashed line indicates the $\alpha = \mu$ dependence.

s-band occurring within the visible spectra. At the $\lambda = 515\,\text{nm}$ laser photon energy, some interband transitions occur within Cu and Au due to the proximity to the respective interband transition threshold energy. This produces the large observed values of α seen in Fig. 4.3. A significant difference remains between the photon energy of $\lambda = 515\,\text{nm}$ (2.4 eV) and the interband transition threshold for Ag. I conclude that this enhancement in the efficiency for Ag does not emerge from interband transitions, but rather is a plasmonic effect, as demonstrated by the near unity value of the reflectivity of Ag at both 515 nm and $\lambda = 1030\,\text{nm}$.[68]

Values of μ as a function of temperature are shown in Fig. 4.6. Both litera-

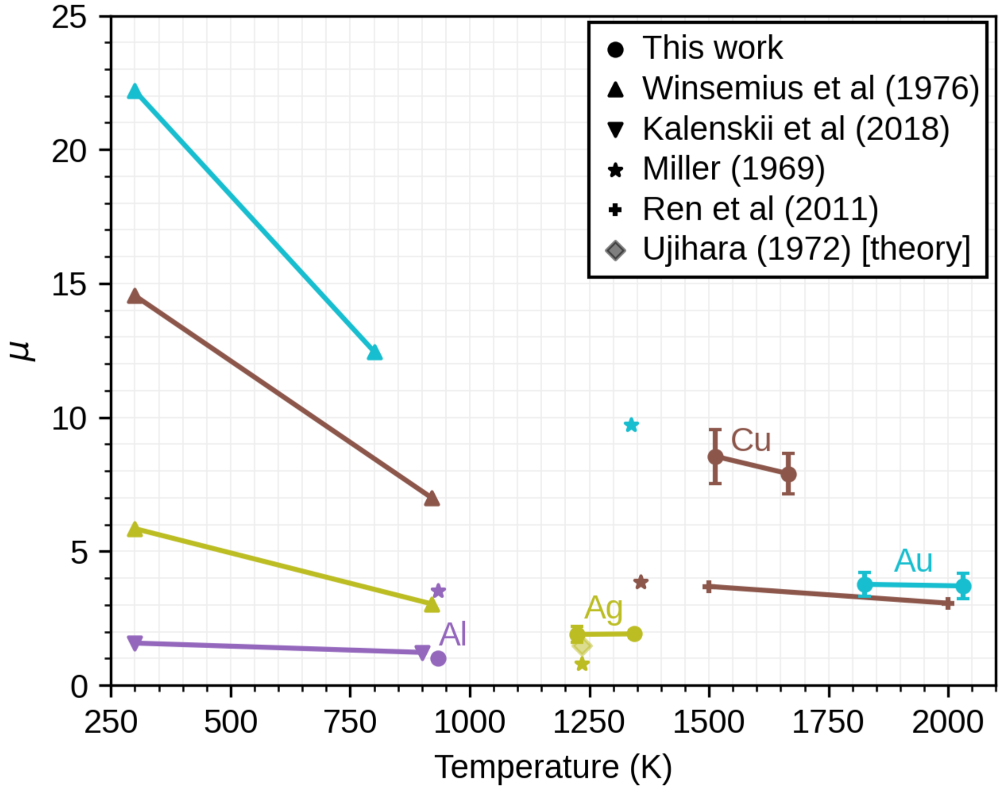

Figure 4.6: Values of μ at various temperatures for a selection of elements. Our values were derived from the equivalence between α and μ discussed previously, using required laser power density to achieve melting, then extracting the source temperature from the corresponding vapor pressure.[9] Values of μ derived from experimental and theoretical literature values are also shown.[57, 69, 66, 70, 30]

ture values and our experimental values taken from the corresponding values of α are shown together. Taken together, these values help elucidate the temperature dependence of the μ and thus the optical properties as a whole and are consistent with prior literature. This is particularly apt for Cu and Au as the threshold of interband transitions lies in between the photon energies from the $\lambda = 1030\,\text{nm}$ laser and the $\lambda = 515\,\text{nm}$ laser. The primary absorption mechanism is different at each wavelength and given the very weak temperature dependence of interband transitions, the dependence of μ on temperature can be viewed as mimicking the temperature dependence of the plasma oscillations for the given material.[57, 63]

In summary in this chapter, I have shown that for practically all elements investigated here, using green laser light in thermal laser epitaxy reduces the required laser power by approximately $20-30\%$. Greater reductions of the required power values were observed for Ag, Au and Cu, namely factors of 1.9 ± 0.2, 3.8 ± 0.4 and 8.1 ± 1.1, respectively. From the optical properties of a source, the required laser power for a given growth rate can be determined as a function of temperature, opening up the possibility of using TLE for the study of the optical properties of metals at elevated temperatures.

5

Physical aspects behind deposition stability in TLE

It has been shown that TLE can deposit a wide range of different elements. However, this is only one piece of the overall puzzle as far as the success of TLE as an epitaxial technique is concerned. Another important piece of the puzzle is how stable the deposition of a given material actually is over time, that is by how much does the growth rate vary over time. The deposition process should be fully controllable, particularly for the potential application of TLE to fabricate devices with sharp interfaces. Therefore, a study of the stability of the deposition of different elements with TLE was performed, identifying the sources of instability, and applying methods to counteract the instability and obtain stable deposition processes.

Two distinct cases for the behavior of elements in UHV were investigated: The elements that have a localized liquid phase during deposition at significant growth rates belonging to the "Free-standing" class of materials introduced in Chap. 3, and the elements that sublimate in UHV belonging to the "Sublimation" class of materials. Examples of these two cases are shown in Fig. 5.1 for Si and C, respectively. As C sublimates in UHV at elevated temperatures, a hole quickly forms in the surface of the source oriented in the direction of the incident laser beam. At the location of the laser spot, the surface changes rapidly due to sublimation, which in turn changes the resulting flux distribution. In comparison, Si forms a large melt pool at the site of the laser spot. The melt pool has a flat surface, resulting in a locally flat region at the site of the laser spot. In addition, Marangoni convection currents contribute to a uniform temperature distribution on the liquid surface, making the melt pool the dominant source of outgoing atomic flux.

The different evaporation behavior of these materials poses an interesting test for stable deposition in TLE. In both cases, it is important to maintain a flat surface profile to ensure the same flux distribution and thus the stability of the deposition. One way to achieve this is to continuously move the relative position of the laser beam on the surface of the source to constantly expose the laser beam to a new surface area. A similar technique is sometimes used in PLD, where the laser is usually scanned across the surface of the source to ensure a uniform surface morphology.[71]

The design of the TLE chamber used to investigate the stability of deposition is shown in Fig. 5.2. The laser used was a λ=515 nm disk laser with a peak power of 850 W. Linear motors were attached to the x and y directions of the manipulator arm to ensure the relative position of the laser on the source could be continuously changed following a circular track with a chosen radius.

To avoid problems with the coating of the laser viewport during repeated deposition, a water-cooled Al mirror was used to reflect the laser radiation on to the source. However, as shown by Fig. 5.3, this mirror became coated over time, reducing its reflectivity. The mirror remained specular, as the rectangular grid reflected within the mirror in Fig. 5.3 can still be clearly seen in the coated region of the mirror. As a consequence, the coated mirror could still be used, but required increasing the output laser power over time. Within the experiments presented within this thesis, only the growth rate stability between depositions was examined as in-flight measurements of the flux stability during

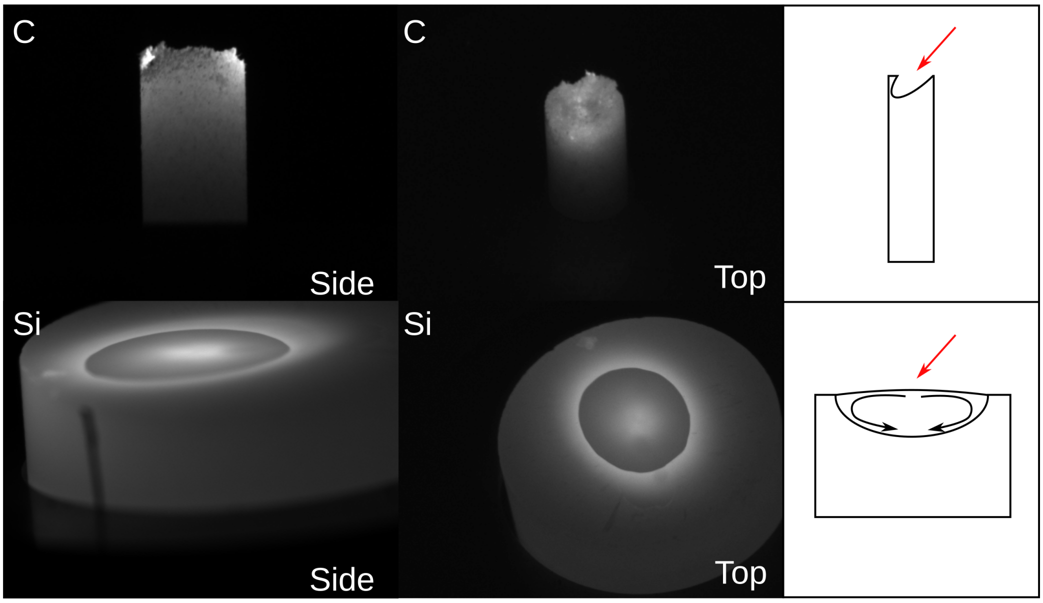

Figure 5.1: Comparison of C and Si during deposition, with photographs of the side profile and the top of the source. For C, the images were taken at 400 W of incident laser power from a $\lambda = 1030$ nm laser and for Si, the images were taken with 500 W of incident laser power from the same laser. Diagrams of the surface morphology for each case are shown with the red arrow indicating the incident direction and angle of the incoming laser. For C, the source sublimates which forms a cavity orientated towards the direction of the incoming laser. Si forms a large, localized melt-pool with convection currents creating a large locally flat region at the location of the laser spot. The C source had a diameter of 3 mm and the Si source had a diameter of 12 mm.

deposition were not possible with the current chamber geometry.

From this chamber design, one can conclude that for a given material source there are two main causes of growth rate instability over time, namely the constantly changing surface morphology of the source and the coating of the Al laser mirror. By moving the laser spot around the source and increasing the laser power over time, these points of instability can hopefully be eliminated.

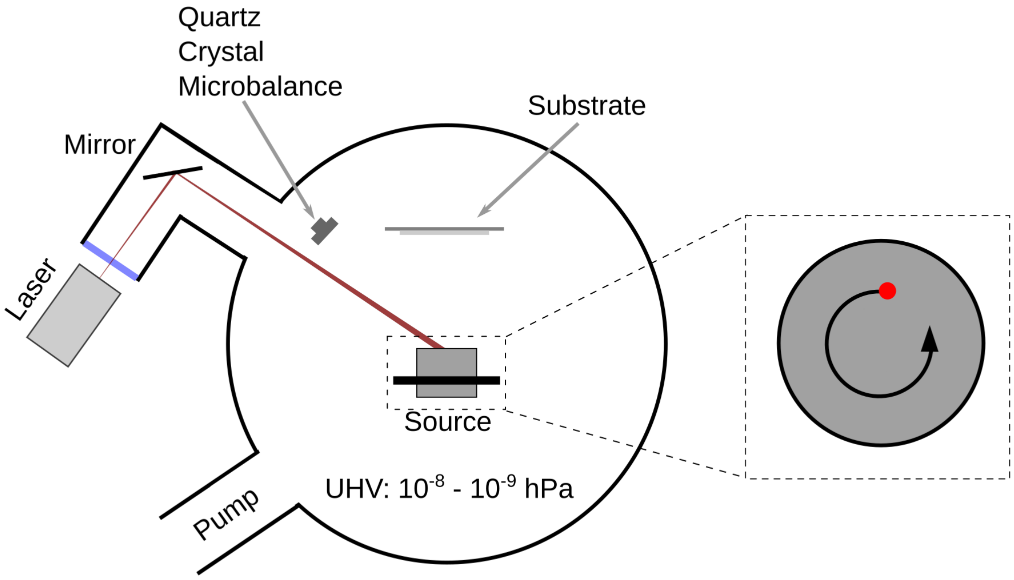

Figure 5.2: Cross-section of the TLE chamber used to study the deposition stability. The source was moved on a circular path by a pair of motors fixed to the manipulator arm on which the source rested. The laser was scanned on the surface on a circular path or on a spiral path depending on the source material.

5.1 Selection of elements for stability investigation

For a free-standing source, Si was chosen for the evaporation stability measurements, because it is one of the most important and widely used elements in the modern world. Si forms the basis of most electronic circuits, especially transistors and semiconducting chips. Therefore, studying the stability of Si deposition possibly has profound implications for the applications of TLE.

Si has another property which makes it an interesting case to study. Like water, the liquid phase of Si has a higher density than the solid phase.[72, 73] This density difference leads to the formation of sharp tips during the rapid freezing of liquid Si, as shown in Fig. 5.4.[74] Due to this effect, it is challenging to reproduce the same surface between depositions, particularly if the output laser power is continuously changed. This effect can be alleviated by slowly re-

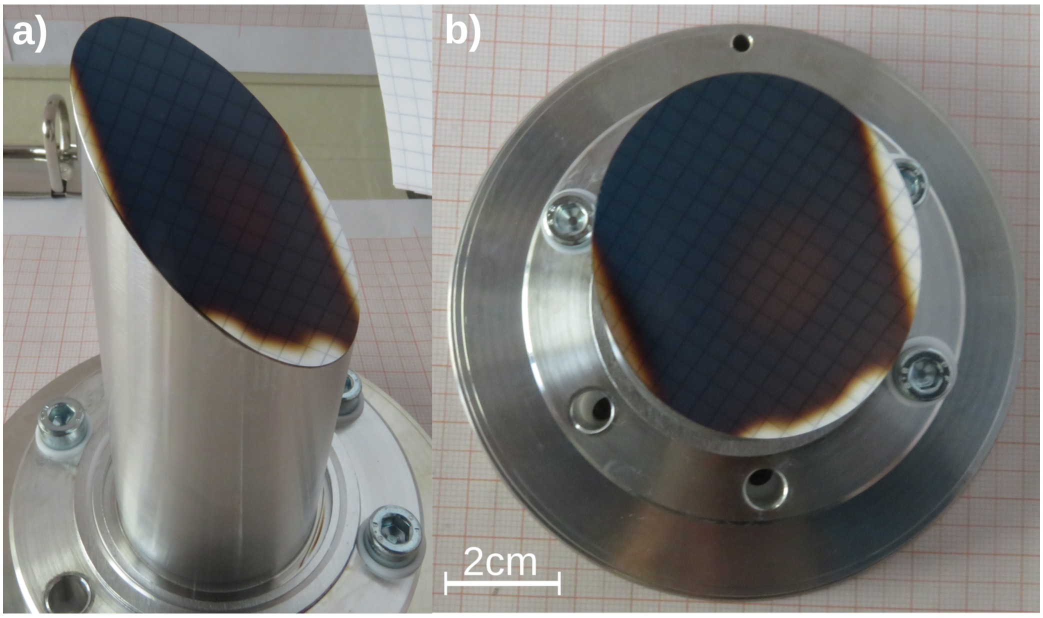

Figure 5.3: Photographs of an Al mirror strongly coated after approximately six months of operation. Panels a) and b) show the mirror at different viewing angles. Despite its heavily coated surface, the mirror remains specular for the laser light, such that the laser can still be used by increasing the output laser power over time to account for the decreasing reflectivity of the mirror.

ducing the output laser power after deposition whilst moving the source along a circular path to smooth the surface of the source.

Zn was chosen as the material of the sublimating source because of its widespread use in semiconductor electronics and optics. Of particular interest are the zinc chalcogenides (ZnS, ZnSe, ZnTe), all of which are II-VI semiconductors that are extensively used in solar cells, blue LEDs, and laser gain mediums.[75, 76] Similar to the case of Si, being able to successfully achieve deposition stability with Zn would have significant insight for the growth of II-VI semiconductors using TLE.

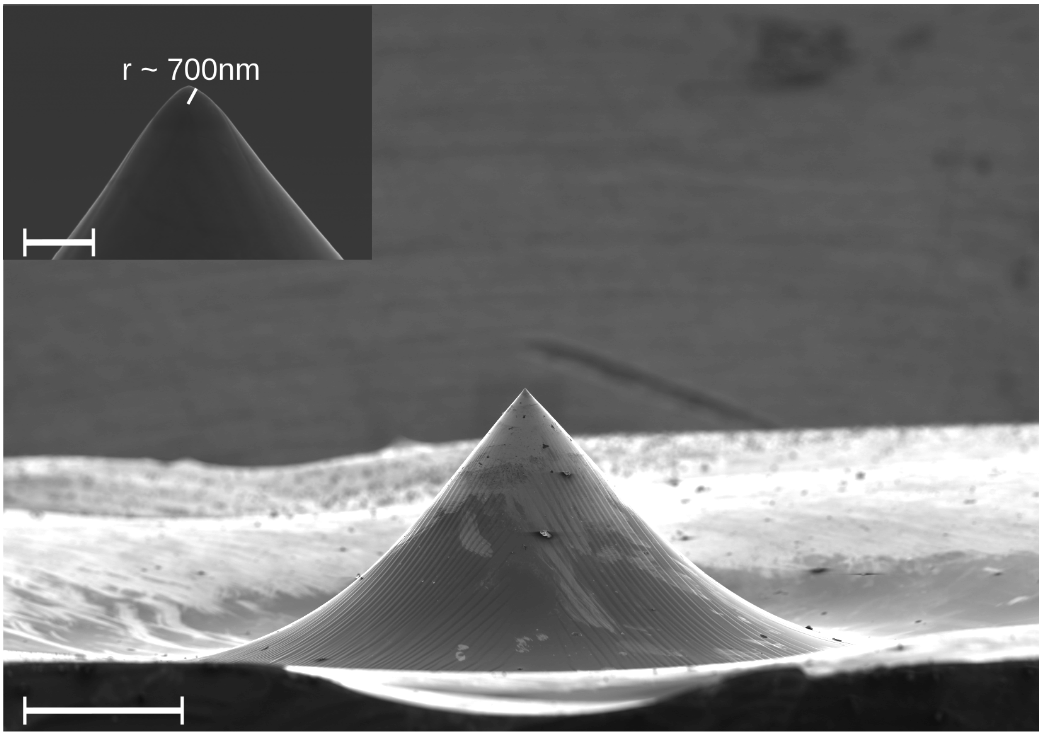

Figure 5.4: SEM images of the tip formed in Si during freezing. The scale bars represent 750 μm in the main image and 3 μm in the inset. The radius of the conical tip is indicated in the inset image.

5.2 Calculation of laser ramp rates

As described earlier, how the Al mirror is coated over time needs to be determined along with how this affects the growth rate of a particular material. The effect on the growth rate is shown in Fig. 5.5 for Si at 400 W of constant laser power. In this case, a clear downward trend of the deposition rate is observed due to the coating of the laser mirror with Si. To remove the influence of the changing surface morphology, the source was moved on a circular path of a radius of 2 mm to ensure that any change in the growth rate over time would be dominated by the coating of the laser mirror. The change in growth rate over time can be converted to a change in incident laser power using the Arrhenius-like dependence of the growth rate as a function of the laser power for the given

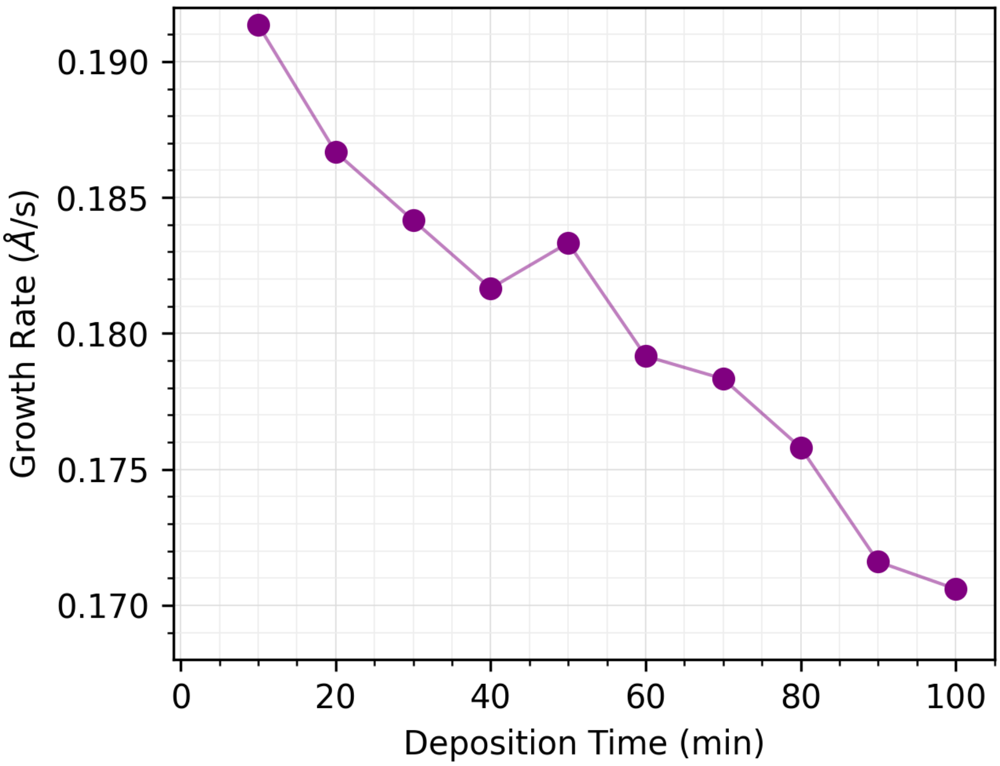

Figure 5.5: The measured growth rate over time for a Si source with a 12 mm diameter with a constant output laser power of 400 W. Motor movement was active so the decrease in the growth rate over time is a consequence of the laser mirror being coated.

source. Neglecting other sources of optical losses such as losses within the optical fiber, the relation between the output laser power from the laser itself P_{out} and the incident laser power on the source P_{in} is related by the reflectivity of the laser mirror $\mathscr{R}_{\text{mirr}}$,

$$P_{\text{in}} = \mathscr{R}_{\text{mirr}} P_{\text{out}}. \tag{5.1}$$

Therefore, a change in incident laser power results from a corresponding change in the reflectivity of the mirror at a constant output laser power if the other optical losses are constant as a function of time. To maintain a constant incident laser power, the output laser power must be increased over time to compensate for the decreasing reflectivity caused by the coating of the mirror. The incident laser power P_{in} can be estimated by inverting the Arrhenius-like dependence of the growth rate, R_G on P_{in}:

$$R_G = ae^{-\frac{b}{P_{\text{in}}}} \quad \Rightarrow \quad P_{\text{in}} = \frac{b}{\ln(a) - \ln(R_G)} \tag{5.2}$$

From the extracted mirror reflectivity as a function of time, the resulting data was fit to an exponential dependence as a function of time. This dependence is suggested by the Beer-Lambert law in which the electromagnetic field of light inside a material decays exponentially.[77] The coating of the mirror results in its reflectivity changing from bare Al to that of the coating material, with the total reflectivity being a function of the thickness of the coating; however, this interpretation neglects any reactions or eutectic alloys that could form between the different coating layers during repeated deposition. For a heavily coated mirror like the one in Fig. 5.3, reactions between the coating layers further reduced the reflectance, making it difficult to determine the saturation value of the reflectance of the mirror. The extracted reflectance of the mirror is fitted to the following equation:

$$\mathscr{R}_{\text{mirr}}(t) = Ae^{-Bt} + C, \tag{5.3}$$

where A, B and C are fit constants. From this fit, shown in Fig. 5.6 for Si, the required output laser power and the required laser ramp rate have been derived in order to keep the incident laser power upon the source constant.

5.3 Results: Silicon

The results of the stability measurements for Si evaporation are shown in Fig. 5.7 for a sequence of 20 minute long depositions, where the growth rate was measured from the QCM after each deposition. The error bars for this data set emerge from the temperature instability of the QCM signal discussed in Chap. 2. A pause occurred in the deposition to test the effect of exchanging to a new Si source on the growth rate stability. During this pause, further experiments with Si were performed that are not relevant for these stability measurements. By continuing deposition with the appropriate power values extrapolated from the required laser power given in Fig. 5.6, the stability of deposition was maintained. This behavior shows that the history of the source is not relevant for deposition stability, rather it is the history of the mirror that determines the deposition stability.

The total deposition stability of Si was determined to be ± 0.3 % over a time period of 560 minutes containing a set of 25 runs, giving an average growth rate of 0.1802 ± 0.0005 Å/s. Shown in Fig. 5.7, a stability goal was set at ± 1 % as this is the typical stability range for MBE effusion cells.[78] It is particularly difficult to deposit Si at high growth rates by MBE because Si is extremely reactive with many crucible materials at high temperatures, limiting its use to a range below the melting point and affecting the available growth rates.[79] The fact that the deposition stability for Si was achieved by TLE with a relatively simple chamber geometry is remarkable.

5.4 Results: Zinc

To reduce the uncertainty in the growth rate resulting from the temperature instability within the QCM, the water-cooling line of the QCM was attached to a chiller with a temperature stability of 0.01 °C. The addition of this chiller significantly reduced the error bars for each growth rate value extracted from the QCM. Unless explicitly shown, the uncertainty in the growth rate can be assumed to be smaller than the marker size within the relevant figures (Fig. 5.8 and Fig. 5.9). Due to Zn belonging to the "Sublimating" class of materials, as discussed in Chap. 3, the source was moved upon a spiral path with an outer radius of 4 mm, to ensure that the surface remained flat and that no holes or trenches formed from repeated deposition.

The high vapor pressure of Zn implies that significant growth rates are achievable with small incident laser power values. Due to the heavy coating of Zn on the mirror during deposition, the deposited Zn oxidizes to ZnO as soon as the chamber is opened and exposed to atmospheric conditions. This oxidation occurs each time the source is replaced in the TLE test chamber, which occurred prior to each series of deposition stability measurements. This led to a transition phase in which the newly formed ZnO layer on the mirror was slowly covered by Zn, allowing the deposition rate to stabilize due to the motion of the motors and the continuously increasing laser power.

Three separate series of stability experiments were performed with Zn, and in each case an initial transition in growth rate was observed. Each experiment within a series was performed over 10 minutes. During this transition period, the growth rate is initially high, but slowly decreases over time until it reaches a near-constant value. This indicates that the reflectivity of ZnO coated mirror was greater than that of the Zn-coated one. With this transient period removed, the average deposition stability across all three series was calculated to be ± 2.11%. The stability of each deposition series with Zn is plotted in Fig. 5.8. The average growth rates and error bars for each deposition series with Zn is given in Table 5.1. Within Fig. 5.8, "Series #1" has the largest number of

Series #	**Average growth rate (Å/s)**	**Average stability (%)**
1	4.549 ± 0.10	2.192
2	4.051 ± 0.083	2.046
3	6.649 ± 0.180	2.710

Table 5.1: Average growth rate and stability of each deposition series of Zn.

data points and is therefore the most statistically significant. For this reason, the stability of deposition is plotted for "Series #1" in Fig. 5.9 where the initial transient has been ignored to focus on the stability regime.

Unlike the case for Si, deviations from the average growth rate begin to become more significant as deposition continues, leading to a downward trend in two of the three datasets at greater total deposition times as shown in Fig. 5.8. Within each dataset, it was assumed that the reflectivity of the mirror follows Eqn. 5.3, leading to diminishing changes in the output laser power as deposition continues. As seen in Fig. 5.9, as the laser power begins to saturate towards a constant value, the growth rate begins to drop. One must conclude that for the case of Zn, the exponential form of the reflectivity of the mirror given in Eqn. 5.3 is insufficient. It may be possible that higher order terms exist that can account for the secondary effects of mirror coating such as thermal expansion and eutectic formation, but to fully determine the required form, the reflectivity of the laser mirror needs to be accurately measured *in-situ*. This remains a technical challenge for the further improvement of TLE.

5.5 Effect of each instability source on the overall deposition stability

For the results presented previously, a question emerges regarding the effect of each source of instability on the overall deposition stability. Turning to the example of Si irradiated with a constant laser power, the effect of moving the source upon a circular path can be examined. The results of this are shown in Fig. 5.10. Without any motor movement and a constant output laser power of 600 W, the deposition stability was approximately ± 6.18 %. Instability was reduced further with the addition of motor movement to a value of ± 2.7 % for a constant output laser power of 510 W. When both motor movement and a constantly increasing laser power are utilized, the instability is reduced to ± 0.3 % as shown in Fig. 5.7.

From these results, an argument can be made for the coating of the laser mirror being the dominant source of instability in the growth rate of Si inside a typical TLE system. A reduction in the instability by a factor of ~3 was observed with motor movement compared to the reduction in the instability in the growth rate by a factor of ~10 going from a constant output laser power to a continuously increasing output laser power. The prior discussion with Zn supports the conclusion that the coating of the laser mirror dominates due to the remaining instability with a Zn source with rastering of the laser across the surface of the source. Therefore, it is the history of the laser mirror rather than the source itself that determines the stability of deposition. This supports the conclusion made previously after the Si source was exchanged for a new piece of Si.

5.6 Enhancing deposition stability with an absorber of the reflected light

A potential path towards greater deposition stability emerges when considering the laser light reflected from the source in TLE. If the incident laser power upon the source remained constant, one would expect the reflected laser power to also remain constant, providing that the source remains at the same temperature to ensure the same reflectivity. If a photon absorber is placed in the path of the reflected beam, the steady-state temperature of the photon absorber can be used as an indicator of the reflected power and thus the growth rate.

To investigate this hypothesis, a water-cooled Al photon absorber was placed at 45° to the surface of the source, in the path of the reflected laser beam. This absorber was split into four quadrants with a W/Re Type C thermocouple embedded in each quadrant, allowing for the temperature of each segment to be measured. As previously stipulated, if the reflected beam remains focused upon the absorber and the reflectivity of the source remains constant, the stability of the temperature of the absorber may be used as a measure of the stability of the growth rate. This assumes that we have an ideal absorber that can respond quickly to short-term fluctuations which is not the case for a practical absorber due to the finite specific heat capacity and thermal conductivity. The irradiated surface of the absorber was sand-blasted to increase its absorptivity.

The temperature of each quadrant was monitored during the stability experiments with Si and recorded the temperature of each. Each quadrant took approximately 10 minutes to reach a steady state temperature due to the large thermal mass of the absorber. The uncertainty in each temperature value emerges from the variation in the steady state temperature of each quadrant. The results of this are shown in Fig. 5.11. It is found that the temperature of each quadrant remains relatively stable with an upward trend visible for the "Left" quadrant over time. I attribute this to the gradual movement of the reflected laser beam towards the "Left" quadrant on the absorber caused by slow changes in the surface morphology.

From the results shown in Fig. 5.11, one could conclude that the use of a photon absorber is a viable technique to control the growth rate stability. However there are challenges with the use of said absorber in the current chamber geometry. Firstly, if the surface of the source is heavily scattering. For example, if the source is heavily sublimating, then the reflected laser beam will be distributed all around the chamber. Due to this scattering the resulting temperatures upon the absorber may fluctuate significantly due to the scattering from the source, presenting a challenge to the notion that a constant absorber temperatures equals a constant growth rate. Secondly, the large thermal mass of the absorber limits its use as an *in-situ* control mechanism for deposition stability as it takes a significant amount of time for the temperature of the absorber to respond to changes in the output laser power.

The ideal scenario for the use of a photon absorber is for it to be used in a control loop (such as a PID controller), where the desired temperature for each quadrant would be set and the output laser power would adjust accordingly until this set point is reached. However, given the large thermal mass of the current photon absorber, such a mechanism is impractical with the current design. In addition, the W/Re thermocouples used within the photon absorber are ill-suited to applications at low temperature compared to their typical operating range due to their inherent uncertainty, however this point along with the discussion regarding the large thermal mass of the photon absorber remain engineering challenges that can be improved upon for further iterations of TLE.

Within this chapter, it has been shown that deposition stability can be attained in TLE by accounting for the two primary sources of instability in the growth rate within a typical system. These sources are changes in the surface morphology of the source and the coating of the mirror which couples laser radiation into the chamber. This was done by moving the source along a circular track and by slowly increasing the output laser power to keep the incident laser power upon the source constant. Two elements, Si and Zn were chosen for investigation due to their differing physical behavior in vacuum conditions and their wide variety of applications within semiconducting electronics. For the case of Si, the stability in the growth rate was found to be ± 0.3 %, which is below the ± 1 % value that is typical of many MBE systems. The large liquid melt-pool around the location of the laser spot kept the surface of the Si source flat and the specular quality of the coated mirror allowed for the output laser power to be easily adjusted to ensure the incident laser power upon the source remained constant.

Conversely, Zn sublimates in UHV conditions so the laser was moved in a spiral pattern across the surface of the source to ensure a constant surface morphology is maintained. Zn proved to be more unstable than Si, averaging a stability value of ± 2.49 %. From this, one can conclude that the original assumption of an exponentially falling mirror reflectivity is not fully accurate and that at high mirror coating rates, second order effects such as eutectic formation and thermal expansion may play a significant role in how the reflectivity of the mirror drops over time during deposition. A possible successor to the current stability algorithm could be to measure the reflected laser power via the temperature of a photon absorber and use this temperature within a closed feedback system, however, this remains the subject of further research.

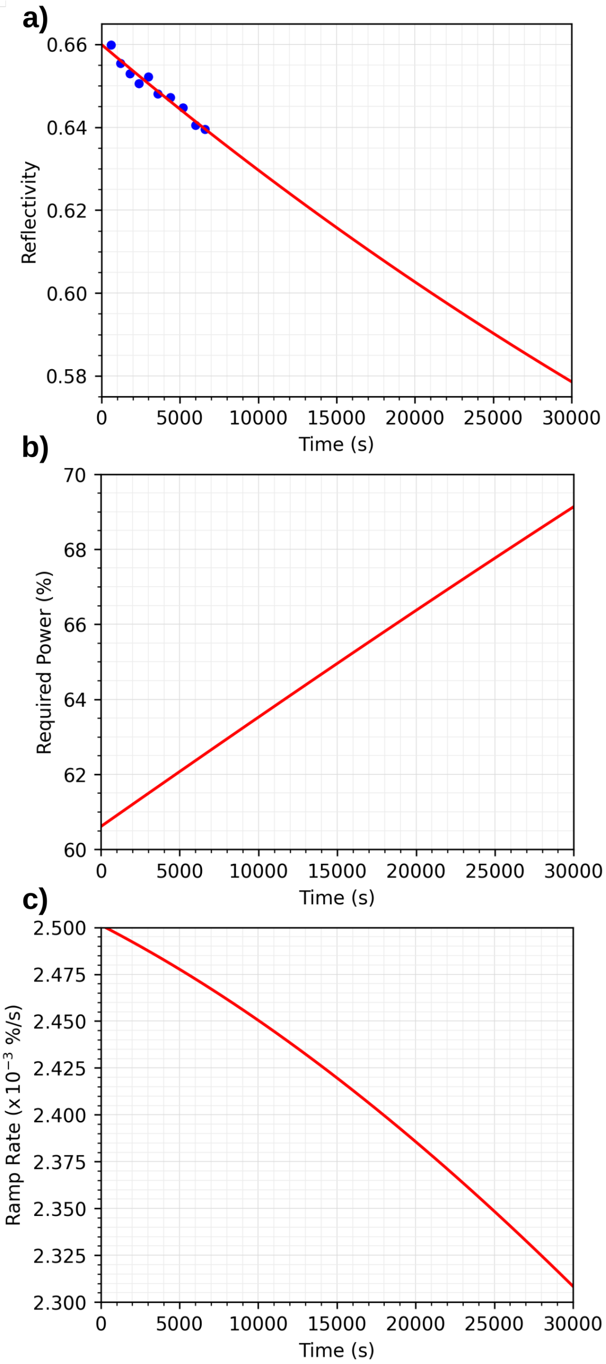

Figure 5.6: a) The reflectivity of the laser mirror calculated for the laser mirror over time. The decreasing value of the reflectivity is the result of coating by Si during deposition. The data points (blue) are fit to an exponential dependence as given in Eqn. 5.3 and shown by the red line. Panel b) shows the required output laser power as a function of time to keep the incident laser power upon the source constant, as calculated from the data in panel a). The data is given in terms of the percentage of the maximum laser power from the $\lambda = 515\,\mathrm{nm}$ laser. Panel c) shows the required rate at which the output laser power has to be increased in terms of %/s.

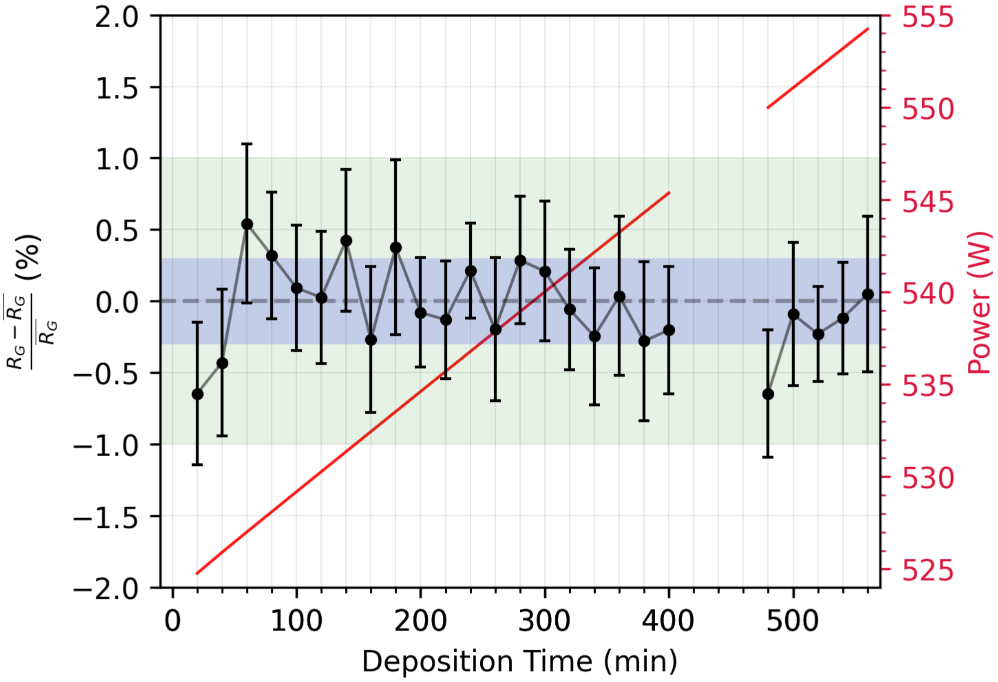

Figure 5.7: Stability of deposition with Si for a sequence of 20 minute long depositions. The output laser power is shown on the secondary axis. The blue rectangle represents the standard deviation of the growth rate over time, equal to a standard deviation of ± 0.3 %. The green rectangle represents an uncertainty of ± 1 %. The uncertainty in the stability measurements results from temperature instabilities within the QCM itself, cause a deviation in the oscillatory signal. The gap in the data represents a period of time where Si was not deposited inside the chamber, then a new Si source was placed inside and deposition continued. The average growth rate was 0.1802 ± 0.0005 Å/s.

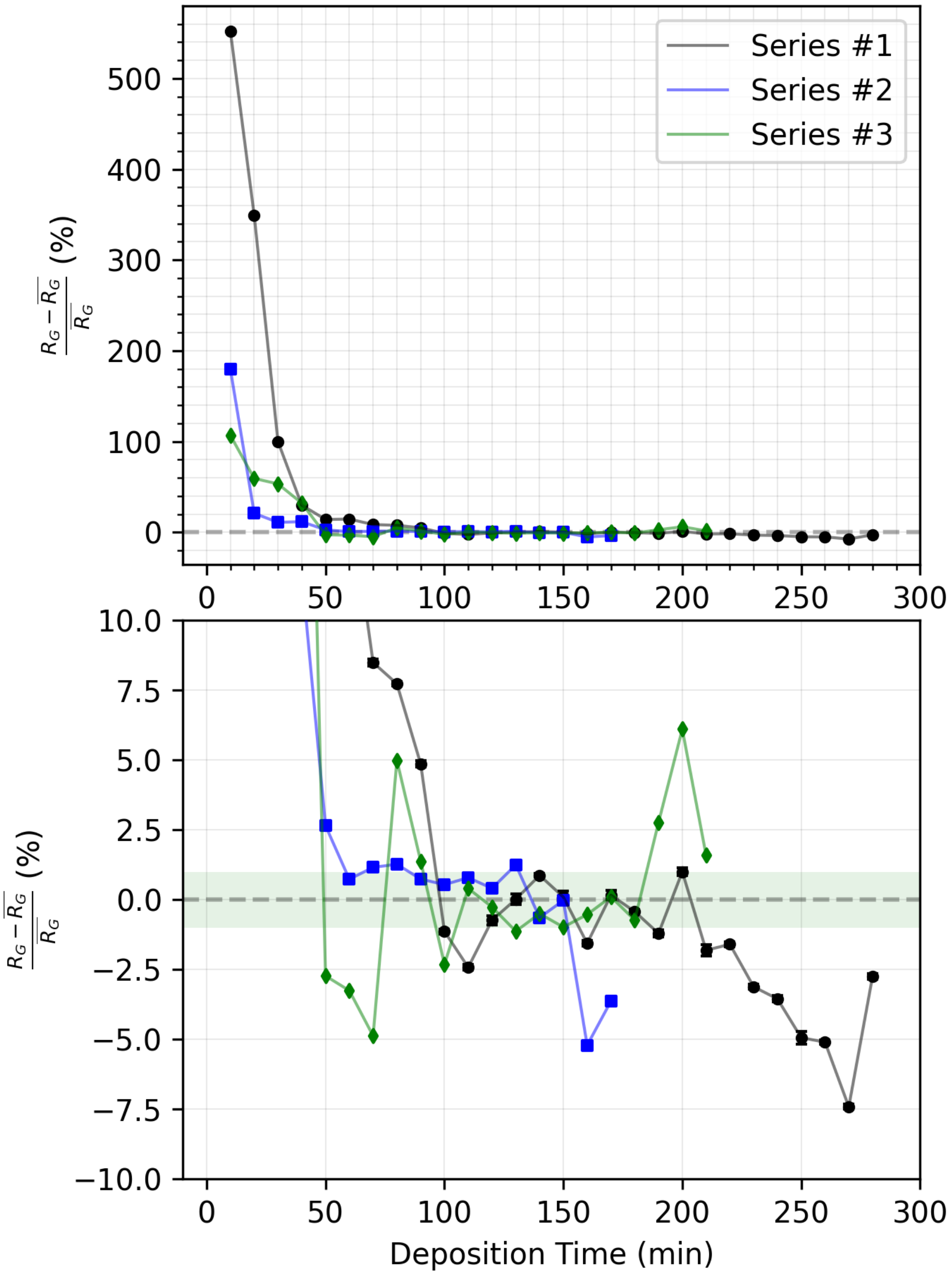

Figure 5.8: Series of deposition experiments with Zn. Panel a) shows the initial transient phase caused by the formation of ZnO upon the laser mirror whilst panel b) shows the stability regime. The green rectangle in panel b) represents a deposition uncertainty of ± 1 %.

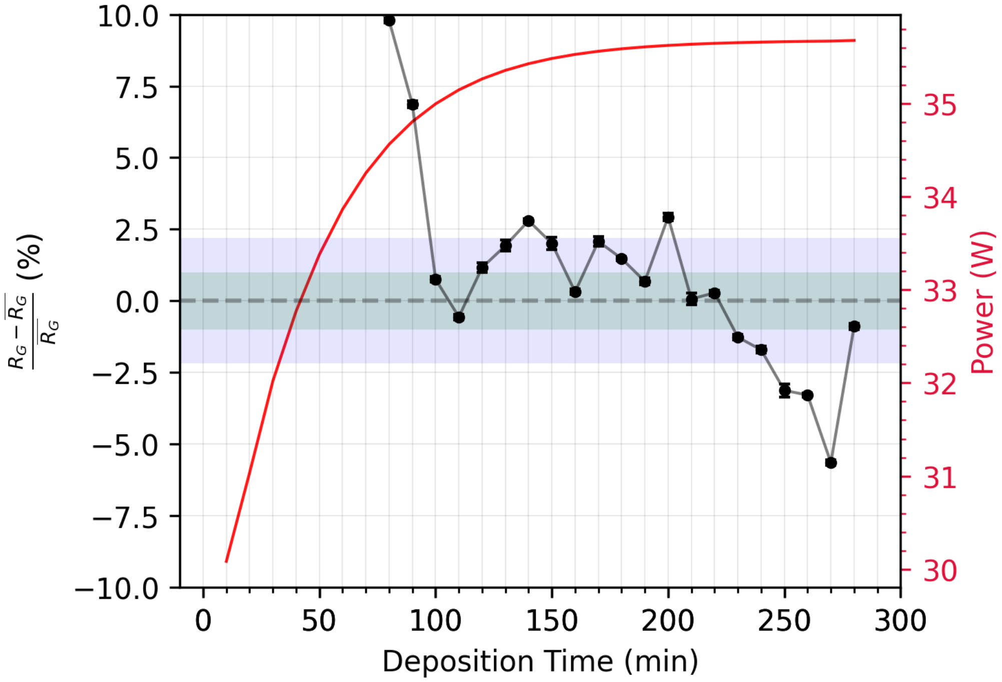

Figure 5.9: Stability of deposition with Zn for a sequence of 10 minute long depositions. This corresponds to the dataset of "Attempt #1" as shown in Fig. 5.8. The output laser power is shown on the secondary axis. The blue rectangle represents the standard deviation of the growth rate over time, equal to a standard deviation of ± 2.71 %. The green rectangle represents an uncertainty of ± 1 %. The average growth rate was 4.636 ± 0.221 Å/s. The laser wavelength was λ = 515 nm, the source-substrate distance was 60 mm and the focal length of the laser was 500 mm.

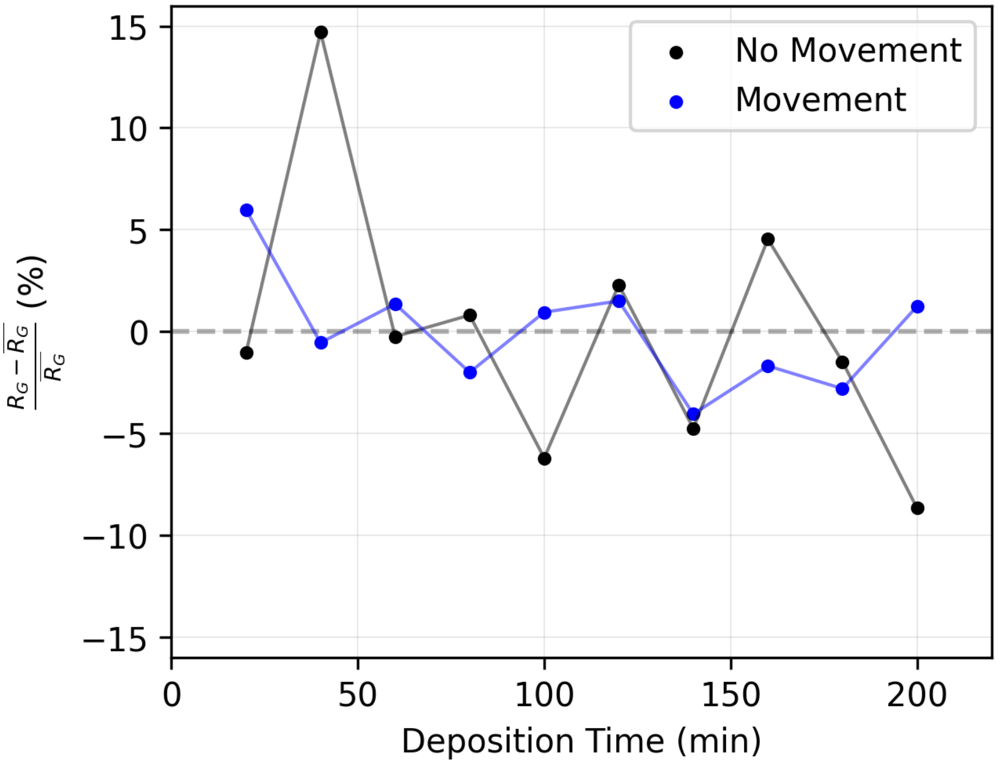

Figure 5.10: Comparison between the experimental stability data for Si with a stationary source and 600 W of output laser power ("No Movement") and with a moving laser position on the source and 510 W of output laser power ("Movement"). The stability of the "No Movement" data set was ± 6.18 % and the "Movement" set was ± 2.7 %. The laser wavelength was $\lambda = 515$ nm, the source-substrate distance was 60 mm and the focal length of the laser was 500 mm. The average growth rate for the "No Movement" data set was 0.960 ± 0.059 Å/s and the average growth rate for the "Movement" data set was 0.1817 ± 0.0049 Å/s.

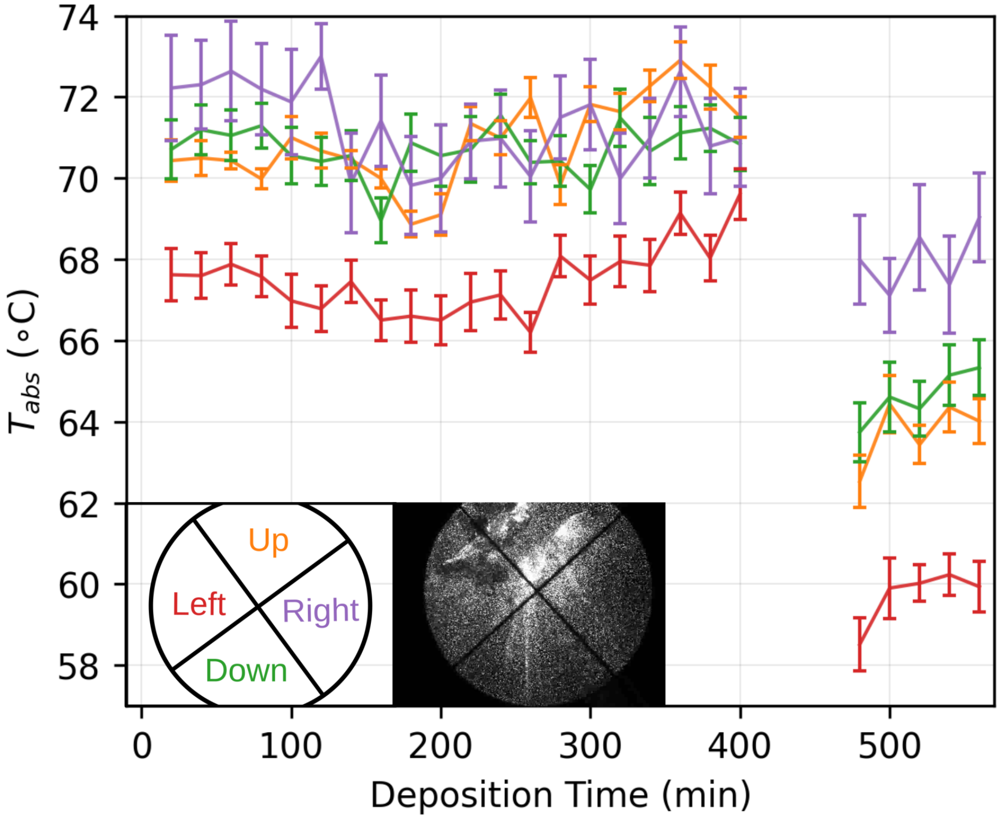

Figure 5.11: Measured temperatures of the quadrant photon absorber for the stability measurements with Si shown in Fig. 5.7. The inset shows a sketch of the face of the photon absorber with each color denoting a given quadrant. The photograph shows as an example of how the reflected laser beam upon the photon absorber looks like during the deposition.

6

Energy balance within laser-induced evaporation

To make the evaporation process in TLE as efficient as possible, the thermodynamics of the laser-induced heating of the source must be examined in detail. For efficient evaporation, the majority of the incident energy flux into the source must transformed into evaporation energy, a process which is determined by the energy balance inside the source. The energy balance is crucial to maximizing evaporative losses and achieving efficient deposition. For a system in a steady state, the energy entering the system must be the same as the energy leaving the system.

Within TLE, the energy entering the system comes from the incoming laser beam. The main sources of energy dissipation leaving the system are conduction, radiation and evaporation. Maximizing evaporation requires that the energy lost by the other channels be minimal. For a system with negligible conduction, evaporation will become dominant over radiation as the primary dispersion mechanism at a specific temperature, θ. This results from the differing temperature dependences of the energy removal mechanisms, shown in Fig. 6.1. Radiation scales with $\sim T^4$ as given by the Stefan-Boltzmann law and evaporation scales as $\sim \frac{e^{-1/T}}{\sqrt{T}}$ for the removal of atoms from the condensed phase with an additional dependence of $\sim \sqrt{T}e^{-1/T}$ for the kinetic energy distribution of the evaporant.[7] With increasing T, the evaporation process becomes more and more efficient. Conduction can be neglected within this argument due to the small size of the source along with its free-standing design. This ensures that minimal conduction occurs throughout the source and that a negligible amount of conduction occurs between the source and the manipulator arm on which the source rests.

Laser-induced heating has previously been modeled to produce high evaporation efficiencies due to the high evaporation temperatures attainable with the use of a laser.[81, 82] In Chap. 3, it was concluded that TLE is capable of depositing the refractory metals with rapid growth rates, implying the high source temperatures have been obtained. Thus, TLE serves as an ideal platform to reach temperatures where evaporation dominates the energy balance and the proportion of incident energy on the source that is dissipated as evaporation tends towards 100%.

Within this chapter, I experimentally demonstrate that evaporation is the dominant energy dissipation mechanism at elevated T for a set of materials. I do this by varying the incident laser power density, varying the evaporation rate by many orders of magnitude. From the evaporation rate data, I extract the temperature of the source as a function of laser powers and find a highly nonlinear dependence. With the aid of a finite element simulation of the laser evaporation process, it is shown that this nonlinear temperature dependence can be explained by the increasing influence of evaporation as an energy removal mechanism, resulting in the evaporation efficiency tending towards 100 % for increasing evaporation rates.

For the sources, it was required that the elements belong to the "Crucible" class of materials discussed in Chap. 3. This is so that the laser-induced evaporation process can be investigated over a wide range of incident laser power densities without any concern as to the structural integrity of a free-standing

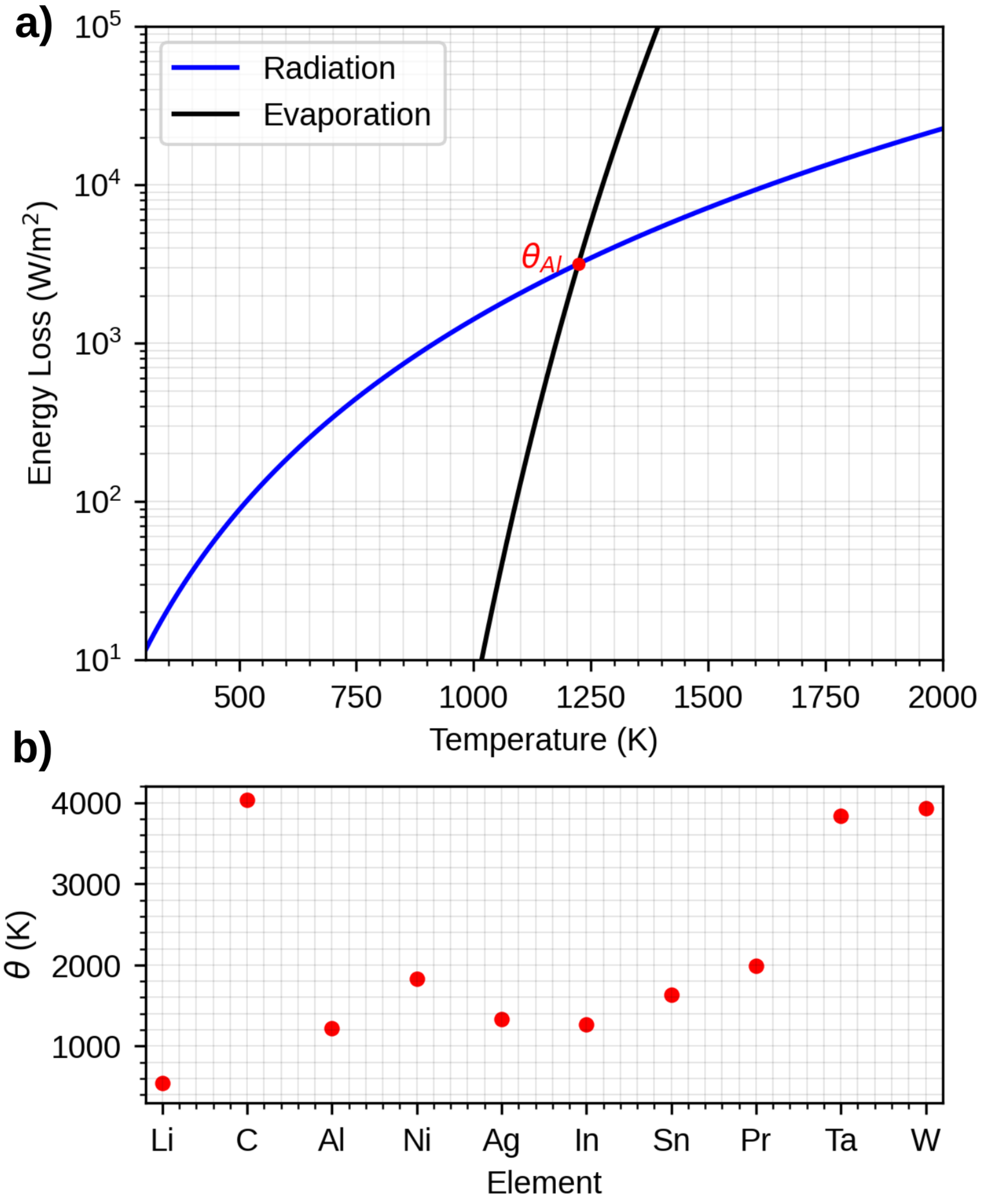

Figure 6.1: a) Diagram of energy removal from the source via evaporation and radiation as a function of temperature for Al.[80, 7] The cross-over point, θ_{Al} where energy removal via evaporation dominates is indicated. Panel b) shows the approximate value of θ calculated for various elements. Conduction has not been considered here due to its negligible effect.

source. Due to these factors, Al and Ag were chosen. Both Al and Ag are used extensively within quantum circuitry and nanoscience, making their study appealing for wider applications of TLE. [83, 84] Both elements were placed in frustum-shaped Al_2O_3 crucibles with an upper diameter of 12 mm as shown in the inset of Fig. 6.2.

These experiments utilized a modified version of the test chamber described in Chap. 2, shown in Fig. 6.2. To prevent coating of the laser window, the incoming laser radiation was reflected off a water-cooled Al mirror, with an initial reflectivity of around 95% at $\lambda = 1030\,\text{nm}$. The sequence of depositions alternated between high and low laser powers in order to minimize the effect of the absorption of laser radiation by the mirror on the growth rate data. The high reflectivity of Al and Ag at 1030 nm ensured that mirror remained highly reflective even after coating. For all experiments, the laser parameters of the disk laser were not altered, except for the output laser power.

The crucible was weighed before and after each experiment to determine the mass of the evaporated material. The calculated mass was then divided by the duration of the evaporation to give an average mass evaporation rate for the given laser power value. The crucible was then refilled and placed back into the vacuum chamber. Once the deposition series of Al was complete, the source was exchanged to Ag. The same experimental procedure was repeated for Ag, except that the evaporation rates were not directly measured due to experimental constraints. Instead the growth rates were scaled by a constant factor which was derived by comparing the evaporation rate and growth rate for Al. This conversion factor is independent of the material in question and solely depends upon the chamber geometry.[49] This factor was used to scale the Ag growth rate data to obtain the mass evaporation rate, calculated to be 361 Å/mg.

The growth rate of Al and Ag upon the Si substrate as a function of output

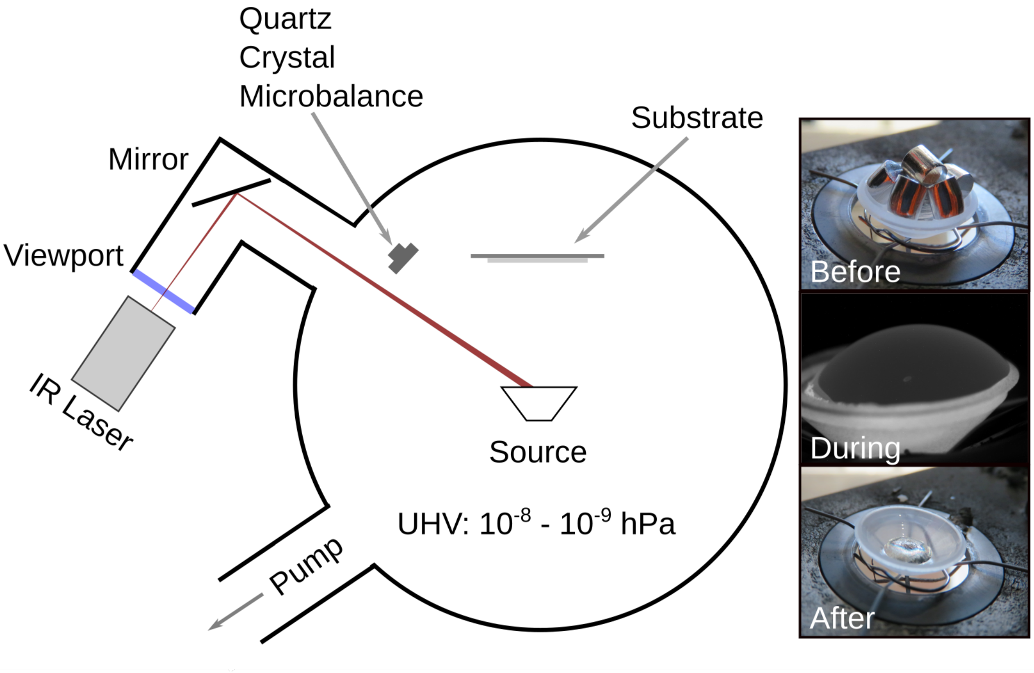

Figure 6.2: Cross-section of TLE system used for studying the deposition of Al and Ag. This chamber was connected to a λ = 1030 nm disk laser with a peak power of 2 kW. The inset shows photographs of the Al source before deposition, during deposition with 500 W of incident laser power and after deposition. The white shadow on the lower left of the liquid Al source in the middle photograph is a reflection of the crucible. The upper diameter of each crucible is 12 mm.

laser power serves as an indication of the evaporation behavior of the source.[49] Figure 6.3 shows the growth rate and mass evaporation rate data for both elements as a function of incident laser power. Error bars were estimated by comparing the surface area of the metallic source inside the Al_2O_3 crucible before and after deposition. At high temperatures with high evaporation rates, evaporation is the main source of energy removal,[85, 7] and thus the energy removal is proportional to the area of the evaporating surface. Given that the source was illuminated with a fixed laser power, a change in the evaporating surface area must be compensated by an increased evaporation rate to ensure the same energy removal. By comparing the surface area of the metallic source before and after deposition for high incident laser powers, an uncertainty value in the evaporation rate can be calculated which is shown in Fig. 6.3.

For each element, both datasets follow the exponential Arrhenius-like dependence as a function of laser power, described previously in Chap. 3. These are shown as dashed lines in Fig. 6.3. Both datasets adhere to this Arrhenius-like dependence over a wide range of incident laser powers, resulting in the Arrhenius-like dependence spanning seven orders of magnitude in growth rate for Al. To fully understand the thermodynamics within the source and thus the origin of the Arrhenius-like dependence, the value of the temperature of the source needs to be known. One can extract source temperatures using the mass evaporation rate data and the laser power at which the melting point was observed. Via the Hertz-Knudsen equation (Eqn. 1.2), it is established that the evaporation rate and vapor pressure are proportional to each other, so that the relative change in evaporation rate can be converted into a relative change in vapor pressure, which in turn is converted into a source temperature via the corresponding vapor pressure curve. This first-order estimate neglects the $\sqrt{T}$ factor present in Eqn. 1.2, but this is acceptable due to the dominance of the ex-

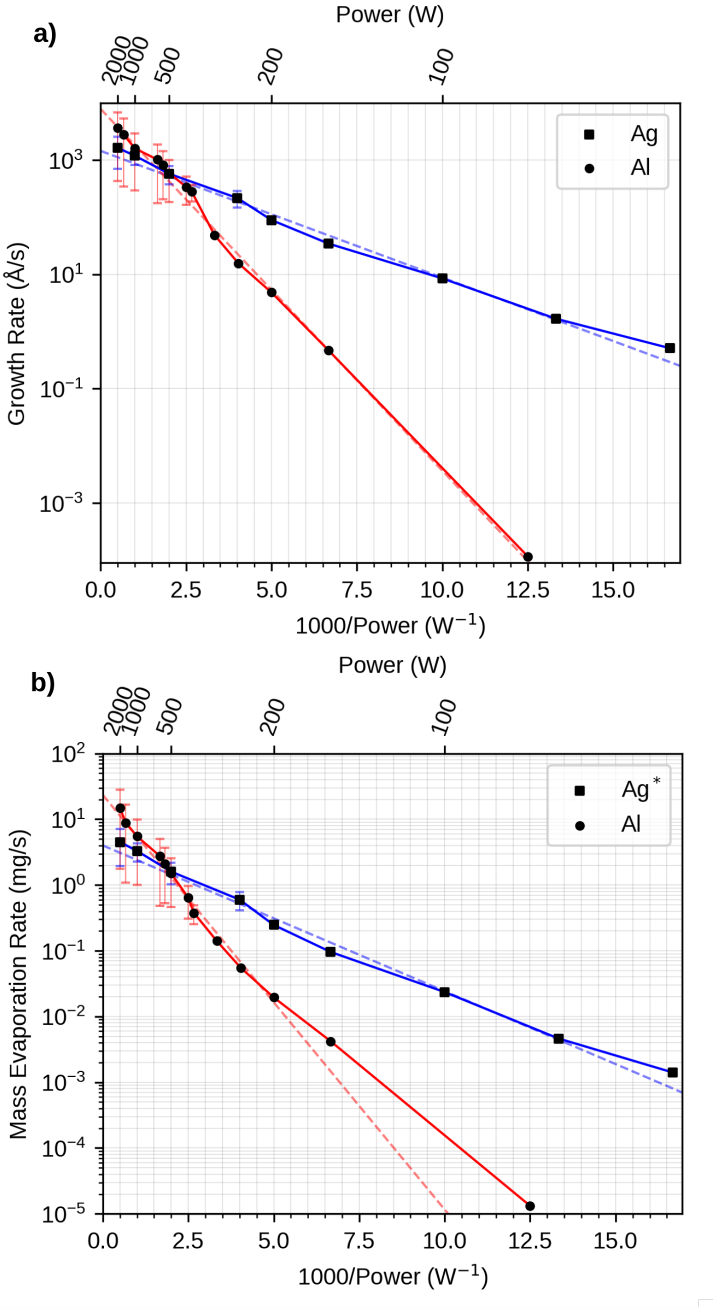

Figure 6.3: Measurements of the a) growth rate and b) mass evaporation rate of Al and Ag as a function of laser power, displayed on an Arrhenius-type plot. In both plots, dashed lines represent an Arrhenius-like exponential fit. Evaporation rate data is not measured for Ag, the growth rate is therefore scaled by a constant factor of 361 Å/mg since growth rate and evaporation rate are proportional.[49] This factor is geometry dependent and is calculated by comparing the growth rate data and mass evaporation rate data for Al . This scaled data is labeled in b) as Ag^*. The laser used was a $\lambda = 1030$ nm disk laser with a peak power of 2 kW and the source-substrate distance was fixed at 60 mm.

ponential dependence of the vapor pressure on temperature compared to the factor of $\sqrt{T}$.

The temperature of the Al and Ag sources as a function of output laser power are shown in Fig. 6.4. For a steady state, the amount of energy entering the source must be the same as the amount of energy leaving it. Therefore, Fig. 6.4 serves as an indication of the energy balance within the source. For both datasets, the rate of change of temperature with output laser power decreases rapidly with increasing output laser power, indicating a rapid increase in the energy lost at higher laser powers. This follows from the exponential dependence of the energy lost via evaporation as a function of temperature shown in Fig. 6.1, implying that within TLE, the evaporation-dominated temperature regime is reached.

The hyperbolic-like dependence of the source temperature on the output laser power is consistent with the Arrhenius-like dependence of the growth rate and mass evaporation rate as a function of laser power. Within the Arrhenius-like dependence, increasing the laser power must result in diminishing changes in the evaporation rate, which is consistent with the temperature dependence seen in Fig. 6.4. If this Arrhenius-like dependence continues to hold at greater laser power densities, evaporation rate saturation is present, which cannot be explained via evaporation and radiation alone. To fully understand this, the energy balance within TLE must be simulated.

6.1 The energy balance

In collaboration with Prof. Dr. Bilen Emek Abali from Uppsala University, the CW laser-induced heating of the source was simulated using finite element analysis (FEA). This simulation was constructed in Python using FEniCS, an

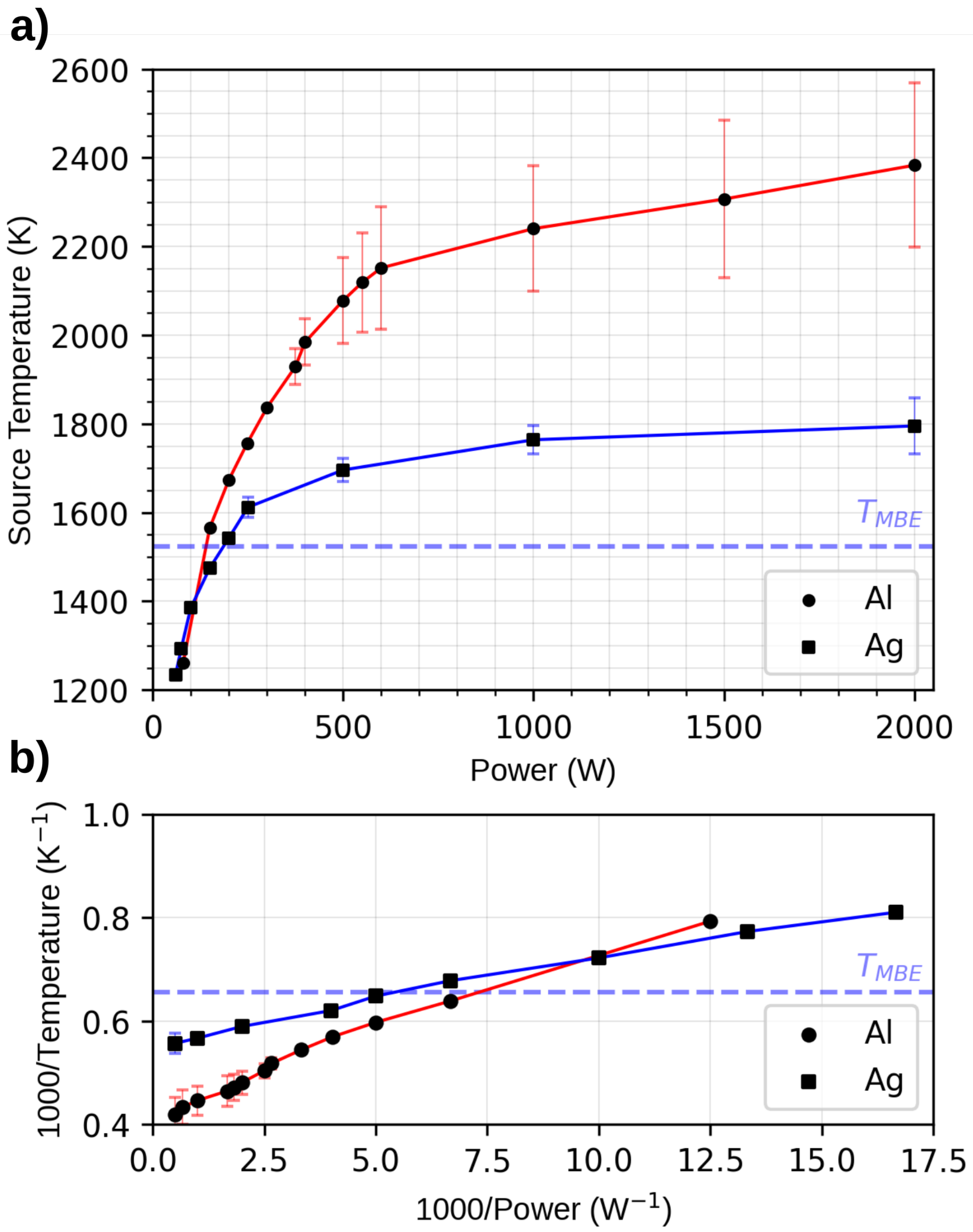

Figure 6.4: Panel a): The source temperature as a function of laser power extracted from the growth rate of Al and Ag. The maximum operating temperature in MBE for Al and Ag, T_{MBE} which is around 1250 °C is indicated [86]. Panel b) shows the same data but plotted as a function of inverse temperature and inverse power to emphasize the hyperbolic nature of the obtained data. For both Al and Ag, it is obvious that the rate of temperature change rapidly decreases with increasing laser power, strongly deviating from the linear dependence assumed in prior literature.[43, 55] This trend indicates a shift from energy removal dominated by radiation to energy removal dominated by evaporation.

open-source computing platform designed to solve partial differential equations. [87] The simulation used a Newton-Raphson nonlinear solver combined with the backward Euler method for time discretization and the Galerkin finite element procedure for space discretization in order to compute the temperature distribution in space and time.[88] The time dependence was explicitly considered, with the simulation modeling the system until it reaches a steady-state condition where the heat losses leaving the source equaled the incoming heat flux. FEA requires a mesh over which the partial differential equations are solved. At each node on the mesh, the system of equations is iteratively solved, allowing for a full solution to be determined across the whole mesh, as shown in Fig. 6.5. The mesh was composed of approximately 10^5 first-order continuous tetrahedral elements auto-generated in SALOME by using NETGEN algorithms.[89, 90]

Within this simulation, four primary methods of energy removal were modeled within the physical system:[7]

- energy removal via conduction within the source ($\sim \nabla^2 T$)
- energy removal via radiation ($\sim \epsilon_{\text{eff}} T^4$)
- energy removal via evaporation including the enthalpy of vaporization ($\sim \frac{e^{-1/T}}{\sqrt{T}}$) and the kinetic energy distribution of the evaporant ($\sim \sqrt{T} e^{-1/T}$).
- energy removal due to the attenuation of the laser beam by absorption and scattering from the evaporating species ($\sim e^{-\tau}$).

Secondary sources of heat transfer such as convection within the liquid metal and changes in the mass of the source were neglected to improve the simplicity of the model. An effective emissivity ϵ_{eff}, was used for the system as explicitly accounting for the effects of surface roughness and the interface between the

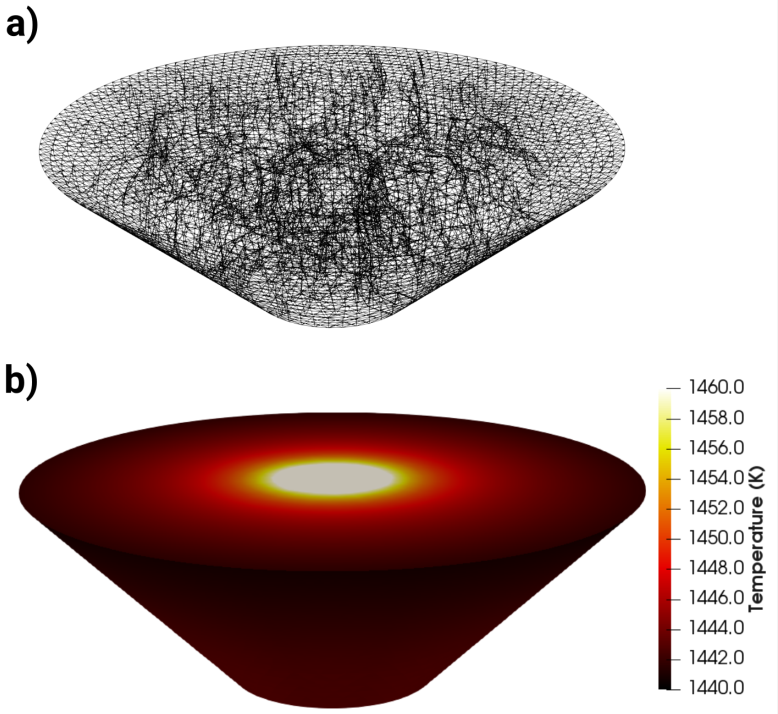

Figure 6.5: a) Wire mesh model of the crucible used for FEA. b) Steady state solution produced by FEA simulation of an Al crucible.

liquid source and the crucible would increase the complexity of the model. This would be detrimental to both computational time and the models' simplicity. For Al, this effective emissivity was calculated from the temperature dependent emissivity of Al $\epsilon_{Al}(T)$: [80]

$$\epsilon_{\text{eff, Al}}(T) = \epsilon_{Al}(T) + \epsilon_{+,\text{Al}}, \tag{6.1}$$

where $\epsilon_{+,Al}$ is a constant value that is discussed later. In the case of Ag, temperature dependent emissivity data was not readily available above ~ 1200 K, therefore the effective emissivity of Ag is fixed at 0.03. This value was extrapolated from the room temperature emissivity for Ag.

To account for the attenuation of the laser beam by the evaporating species close to the evaporating surface, an optical depth τ was calculated from a modified version of the Beer–Lambert law.[77] Given that the evaporation flux follows an inverse square law with distance from the surface of the source x, and that the outward mass flux is emitted in a cosine distribution[91], τ was calculated via:

$$\tau = \int \frac{\mu M p(T)}{\sqrt{2}\rho R T} \frac{1}{x^2} dx, \tag{6.2}$$

where the expression for the density of the vapor is derived from the ideal gas law. μ represents the linear attenuation coefficient of the laser wavelength by the evaporating species, M is the molar mass of the evaporant and $p(T)$ is the vapor pressure of the evaporant at a given temperature, T. Because the optical properties of many metallic gases could not be found in the literature, the value of μ was used as a free parameter with which the simulation was tuned. However, one could place limits on its value. For a solid metal, the optical depth is governed by the absorption coefficient (generally given in the range of 10^7-10^8 m^{-1} for visible/ near IR wavelengths).[92] Therefore it would be reasonable if the value of μ also fell within this range because μ characterizes both absorption and scattering within the vapor. The functional form of the heat equation used for these simulations is discussed in Appendix A.

To test the validity of the model, the evaporation rates at each node on the mesh of the irradiated surface of the source were extracted using the Hertz–Knudsen equation. These values were then integrated across the entire surface to obtain simulated mass evaporation rate data to compare with our experimental values as seen in Fig. 6.3b. By iteratively changing the values of the free parameters, μ and ϵ, I fit the simulated mass evaporation rate data to the experimental data for both Al and Ag. From this, I determined the ideal values for these free parameters to be $\mu \sim 9\,\mathrm{x}\,10^7\,\mathrm{m}^{-1}$ and $\epsilon_+ \sim 0.18$ for Al and $\mu \sim 8\,\mathrm{x}\,10^7\,\mathrm{m}^{-1}$ and $\epsilon(T) \sim 0.03$ for Ag .

To examine the effects of the three primary energy removal mechanisms assumed previously, the effects of each heat loss mechanism is simulated for each material. These different physical scenarios are shown in Fig. 6.6 and represent energy removal due to radiation only (blue), evaporative cooling only (purple), radiation and evaporative cooling (red) and from laser beam attenuation, evaporative cooling and radiation (black). It is apparent that the attenuation of the laser beam due to the evaporating species close to the surface may account for growth rate saturation in both systems. Energy removal due to radiation dominates at low laser powers whereas evaporative cooling becomes dominant at high values due to the high evaporation rates achieved. The overall slope of the Arrhenius-like dependence is formed by the transition between radiation and evaporation as the primary energy removal mechanism. Each curve depends on different physical constants, such as the emissivity and the enthalpy of vaporization, which also affects the location of this cross-over point. The location of this cross-over point does not match the theoretically predicted value

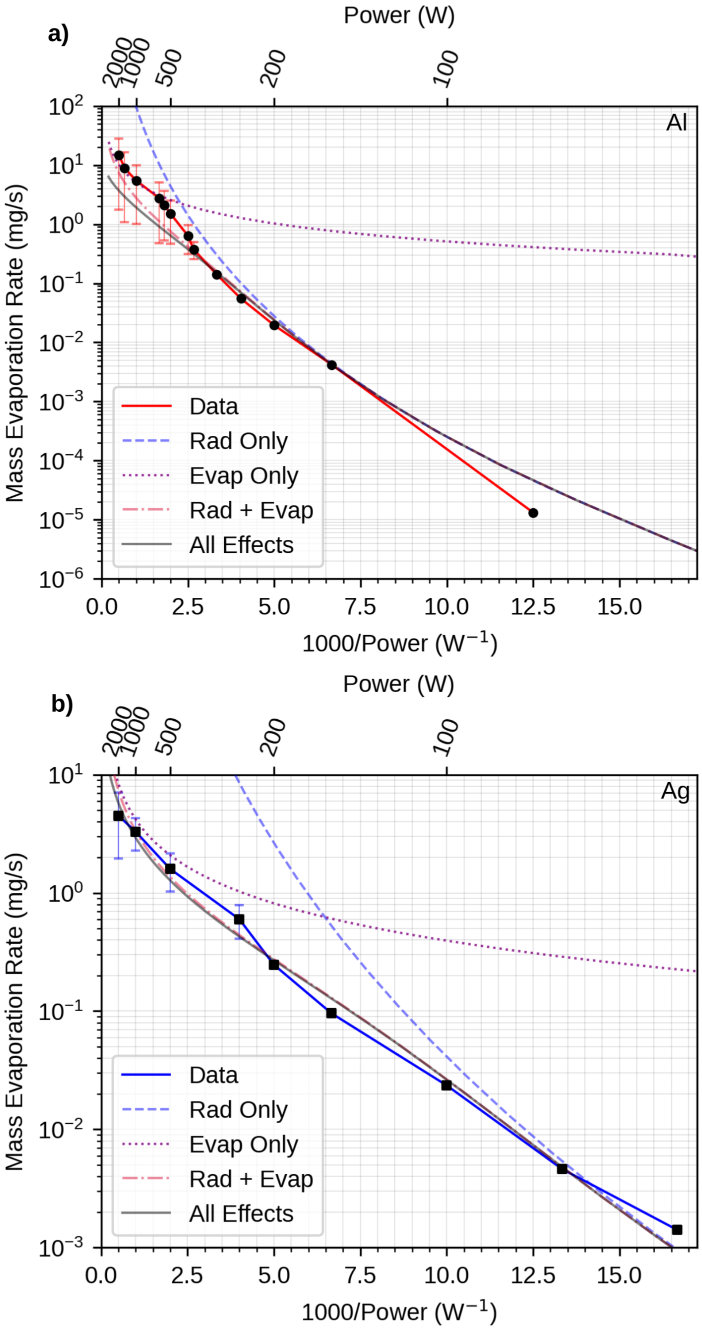

Figure 6.6: Experimental evaporation rate data for Al (a) and Ag (b) as a function of laser power with simulated evaporation data for four different physical scenarios for heat loss: radiation only (blue), evaporative cooling only (purple), radiation and evaporative cooling (red) and radiation, evaporative cooling and attenuation of the laser by the evaporating species (black). For these simulations, the values of $\mu = 9 \, \mathrm{x} \, 10^7 \, \mathrm{m}^{-1}$ and $\epsilon_+ = 0.18$ are used for Al and $\mu = 8 \, \mathrm{x} \, 10^7 \, \mathrm{m}^{-1}$ and $\epsilon = 0.03$ for Ag.

of θ for Ag and Al since the simulation includes finite temperature gradients and temperature-dependent physical constants. In addition, while evaporation only occurs on one surface boundary of the domain, radiation is present on all domain boundaries.

It is clear from these simulations that CW laser evaporation allows for the evaporation-dominant regime to be easily accessed due to the high temperatures possible via laser-induced heating. The Arrhenius-like dependence of the mass evaporation rate as a function of output laser power is an indicator of this, as its shape is formed by the energy balance moving from radiation to evaporation as the primary loss mechanism. Growth rate saturation at high laser powers can be explained via attenuation of the incident laser beam by the evaporating species. However, the strength of this attenuation needs to be experimentally verified.

Error bars for the evaporation rate are present at high laser powers due to the high evaporation rates relative to the mass of the source. As a consequence, the mass of the source rapidly diminishes, causing the temperature of the source to increase due to a decreasing thermal mass and surface area. This phenomena leads to the evaporation rate increasing with time, reflected in the average mass evaporation rate of Al deviating from simulations at $\sim 400\,\mathrm{W}$.

6.2 Exploring the dominance of the evaporation energy in the energy balance

From the results of the finite element analysis simulations, the dominance of evaporation in the energy balance can be investigated. This can be determined by calculating the required energy input for a given evaporation rate and comparing this value with the energy absorbed by the source from the laser beam.

This evaporation dominance ratio, χ is given by:

$$\chi = \frac{\Delta H_{\mathrm{vap}}\Gamma}{M(1-\mathscr{R})P}, \tag{6.3}$$

where ΔH_{vap} is the enthalpy of vaporisation, Γ is the mass evaporation rate at a given P and $\mathscr{R}$ represents the reflectivity of the source at the laser wavelength. The experimental and simulated values of χ for Al and Ag are shown in Fig. 6.7. There is a source of uncertainty regarding the value of $\mathscr{R}$ due to its temperature dependence. By taking the reported values of $\mathscr{R}$ for both elements in their liquid phases, an uncertainty value can be calculated by comparing the high temperature reflectivities with their room temperature values.[31] From the data in Fig. 6.7, it is evident that as the incident power density increases for a fixed laser spot size, the amount of energy lost by evaporation as a proportion of the total energy lost within the source tends towards 100 %, indicating the domination of evaporation as the primary energy removal mechanism.

The attenuation of the incident laser beam by the evaporating species does not have any noticeable effect on the dominance of evaporation in the energy balance. This is logical as attenuation does not change how the incident energy flux is distributed across different energy removal mechanisms, rather it reduces the incident energy flux. As shown in Fig. 6.4, at high laser powers, temperature saturation is present. Therefore, reducing the incident energy flux has a minimal effect on the temperature distribution of the source and thus does not significantly change the value of χ for the present system.

Given that a wide array of different elements have been observed to exhibit a similar Arrhenius-like dependence of growth rate on the incident laser power, it is natural to wonder if the value of χ also increases with increasing laser power for these other elements.[43] As a first order approximation, it is assumed that the geometrical scaling factor of 361 Å/mg is the same across different mate-

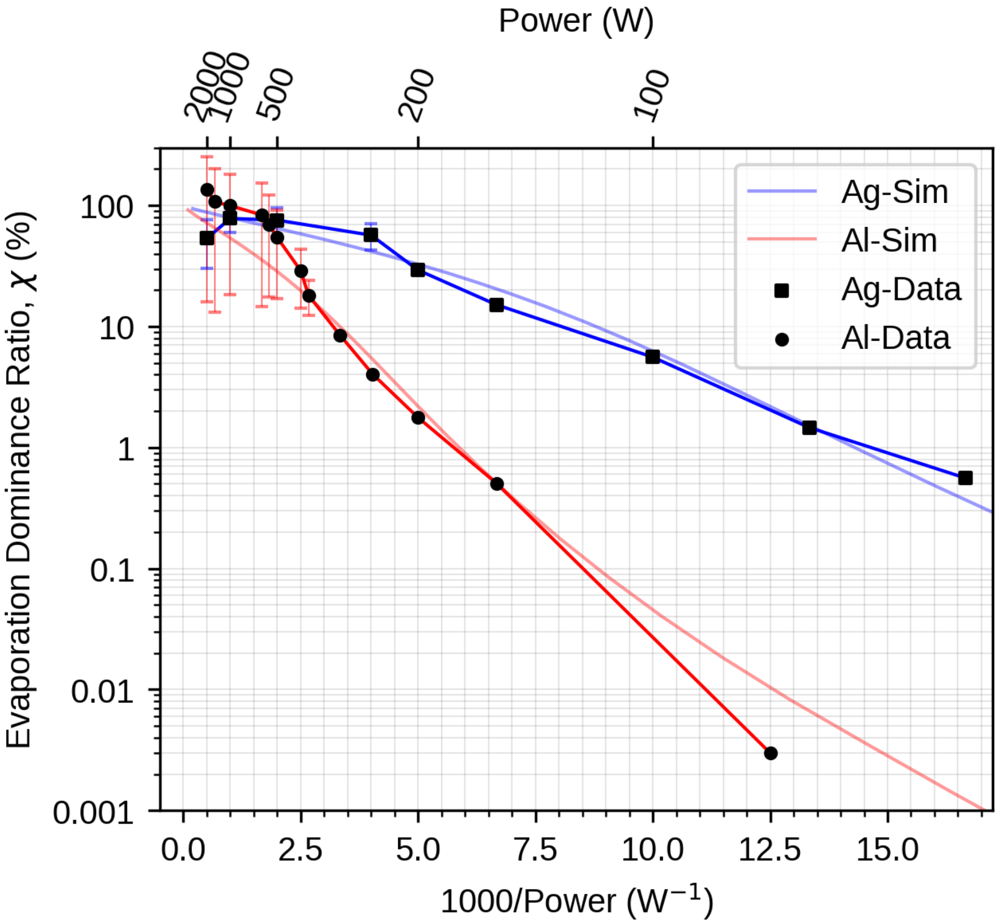

Figure 6.7: Values of the evaporation dominance ratio χ, calculated from experiment and simulation for both Al and Ag. Error bars emerge from the uncertainty in the evaporation rate and the temperature dependent reflectivity of each element. The laser used was a $\lambda = 1030$ nm disk laser with a peak power of 2 kW. The source-substrate distance was fixed at 60 mm and the focal length of the laser was 500 mm.

rials and the growth rate is multiplied by said factor to obtain the evaporation rate data for a range of elements. Using Eqn. 6.3, values of χ as a function of laser power emerge, plotted in Fig. 6.8. Each element within this figure was deposited from a Al_2O_3 crucible as performed with Ag and Al.

By extracting the source temperature as a function of incident laser power for the elements shown in Fig. 6.8, the values of θ for each element as estimated in Fig. 6.1 are plotted. These are shown by colored "X" symbols in Fig. 6.8. In the case of Li, the corresponding power value of θ was $\sim 10\,\mathrm{W}$ and was not plotted for visual clarity. It is clear that TLE allows for the evaporation dominated regime to be easily accessed with relatively low incident laser power densities. As the laser power increases, χ begins to approach 100% for all shown elements, implying that adherence to an Arrhenius-like dependence of growth rate as a function of laser power results from the transition to evaporation as the dominant energy removal mechanism in the energy balance.

In terms of the source temperatures available and extremely high growth rates, the closest competitor to TLE is e-beam deposition. This is an extremely versatile technique that heats a source of material via bombardment by a beam of electrons.[7, 93] However, at high e-beam currents, bremsstrahlung and secondary electron emission can become significant sources of energy loss within an e-beam system.[94, 95] The flux of both these loss mechanisms can be considered as linear in temperature.[85] However, TLE uses photons rather than electrons as their source of energy so bremsstrahlung and second electron emission does not occur.

The tendency of evaporation to dominate the energy balance in TLE at high incident laser power densities begs the question of what the total efficiency of TLE is. In this case, one is primarily limited by the reflectivity of the source material, which for many metals exceeds 90% at $\lambda = 1030\,\mathrm{nm}$ and by the energy

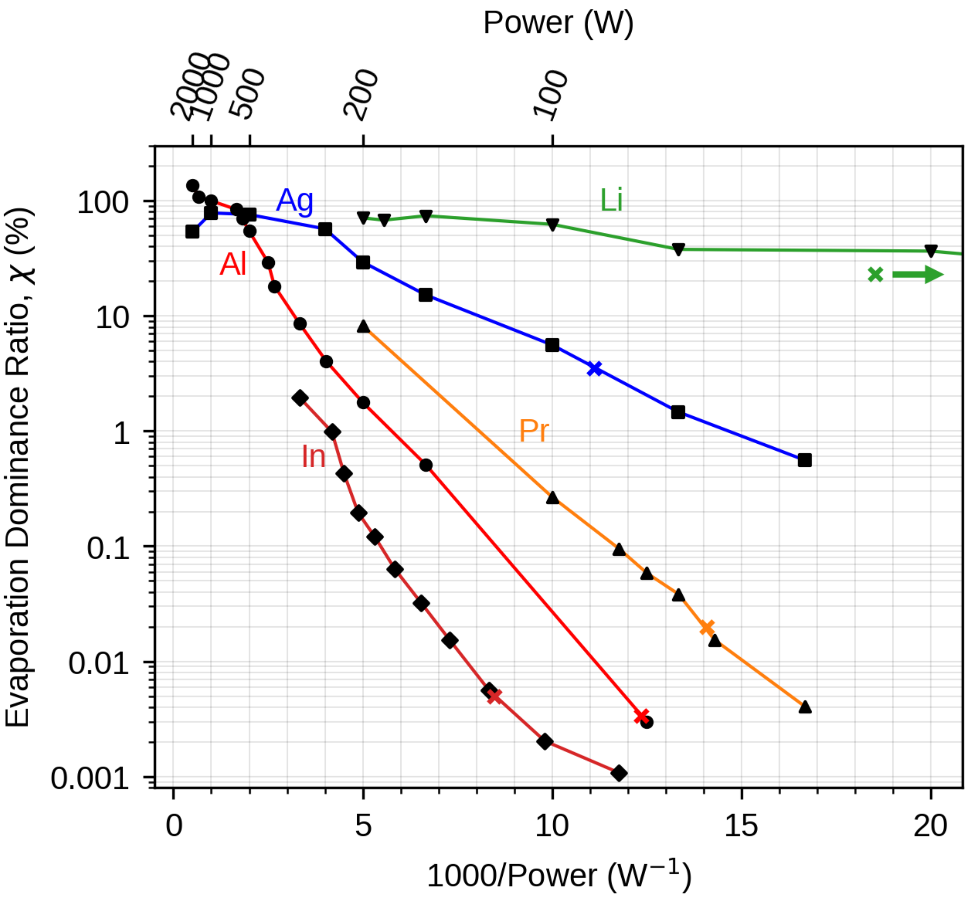

Figure 6.8: Values of the evaporation dominance ratio χ, calculated from the growth rate of various elements. The Arrhenius-like dependence of the growth rate as a function of the laser power is an indication of evaporation dominance in the energy balance of the corresponding source at high laser power densities. Each colored "X" represents the corresponding power value where the source temperature is approximately equal to the cross-over temperature, θ. In the case of Li, the corresponding power value lay outside of the range of the figure. The laser used was a λ = 1030 nm disk laser with a peak power of 2 kW. The source-substrate distance was fixed at 60 mm and the focal length of the laser was 500 mm.

conversion ("wall plug") efficiency of the laser. This "wall plug" efficiency typically lies around 35% for disk lasers.[28] Therefore the overall efficiency of the evaporation process in TLE lies around 30% for complete evaporation domination in the energy balance. The reflectivity of many metals decreases when moving from the infrared through to the ultraviolet due to the presence of interband transitions.[96] Therefore, as efficient high power lasers with wavelengths within the blue/ultraviolet range become available on the market, TLE using these lasers will result in a higher overall efficiencies than have been reported here.

6.3 Effect of the Arrhenius-like dependence of the growth rate as a function of laser power on area scaling

The final point to be discussed is in regards to the Arrhenius-like dependence of the growth rate as a function of the laser power itself. It has been shown that for the case of Al and Ag, an Arrhenius-like dependence can capture the behavior of the growth rate as a function of laser power over the range of output laser powers investigated for each element. However the question remains if this dependence is valid for all laser power values. If this is the case, then growth rate saturation must be present at high laser powers due to the attenuation of the incident laser beam by the evaporating species. As captured by Fig. 6.4, with an increasing laser power, the source temperature begins to saturate towards a constant value; therefore increasing the laser power results in diminishing increases of the growth rate.

Since the growth rate is proportional to the area of the evaporating surface as given by Eqn. **??**, it is relevant to investigate the effect of increasing the heated surface area of the source and how this effects the growth rate. This is done by introducing a scaling factor n which is a multiplicative factor that scales the surface area of the source by a factor n. This modifies the existing Arrhenius-like dependence into a new, area-scaled version for the growth rate R_G as a function of laser power P,

$$R_G = nae^{\frac{bn}{P}}. \tag{6.4}$$

Due to the greatest temperatures upon the source being located at the position of the laser spot, increasing the value of n can be viewed as being equivalent to increasing the laser spot size and thus reducing the laser power density. The effect of scaling the value of n for Al and Ag is shown in Fig. 6.9 and Fig. 6.10, respectively.

From this data, one can determine two distinct regions of growth rate scaling. At low laser powers, increasing the value of n results in a diminishing total growth rate since the growth rate has not saturated. As a result, reducing the laser power density results in a significant reduction in the overall growth rate, indicating that the growth rate within this regime is primarily medicated by the laser power. Conversely, at high laser powers, there is a regime when the growth rate has begun to saturate towards a constant value. By increasing the value of n, the overall growth rate increases due to the dominance of the effect of the evaporating surface area over the influence of the laser power on the overall growth rate.

There is a distinct transition point at which the growth rates goes from being mediated by the laser power at low laser powers to it being mediated by the surface area of the evaporating surface at high laser powers. The envelope of these transition points for adjacent values of n is shown by the red lines in both Fig.

6.9 and Fig. 6.10. This transition from a power-mediated to an area-mediated growth rate regime has profound implications for large scale applications of TLE.

For example, if one wished to achieve growth rates in the tens of μm/s range for uses in industrial coating of Al, simply increasing the laser power would not give the desired results. Instead, as Fig. 6.9 illustrates, increasing the value of n which increases the size of the evaporating surface would result in greater growth rates which exceed what could be achieved by simply increasing the laser power while keeping the surface area of the source constant. This provides a method to overcome the growth rate saturation resulting from the Arrhenius-like growth rate dependence. However, to experimentally prove this for Ag and Al, the required laser powers would exceed the peak power of the $\lambda = 1030\,\text{nm}$ laser used, leaving this idea of growth rate scaling to be the subject of future research.

Within this chapter, it has been successfully shown that using TLE allows for the thermodynamics behind CW laser evaporation of materials to be investigated. Due to the large range of possible source temperatures in TLE, evaporation becomes the dominant energy removal mechanism at relatively low laser power densities. The Arrhenius-like dependence of the growth rate as a function of the incident laser power results from the gradual shift from radiation to evaporation as the dominant energy removal mechanism. The growth rate saturation observed at high laser power densities can then be explained by the attenuation of the source laser beam by the evaporating species. As the energy dissipated by the evaporating species dominates in the energy balance in TLE, a majority of the incident energy goes into the evaporation process, tending towards 100% with increasing laser power. This means that the overall efficiency of TLE is limited by the "wall plug" efficiency of the laser and the reflectivity of the source. However, this will likely improve further with advancements in laser technology. It was also demonstrated that if the Arrhenius-like dependence of the growth rate as a function of laser power holds for all laser power values, then the growth rate saturation at high laser powers can be overcome by scaling the area of the evaporating surface.

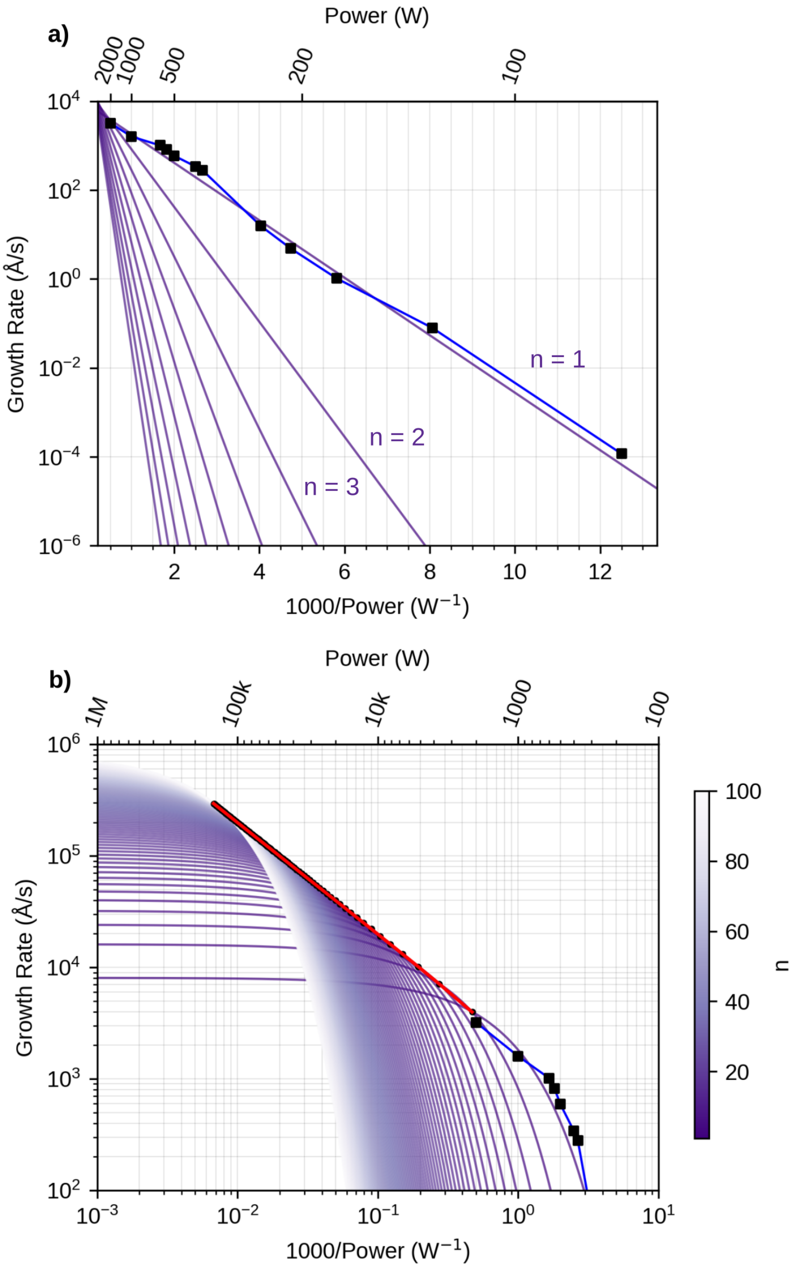

Figure 6.9: Measured and calculated growth rates as a function of laser power on an Arrhenius plot for a liquid Al source inside a Al_2O_3 crucible. The Arrhenius-like dependence given in Eqn. 6.4, is shown from n = 1 to n = 10 in **a)** and from n = 1 to n = 100 for **a)**. **a)** shows the laser power mediated regime and **b)** shows the surface area mediated regime. The red line in **b)** shows the envelope of the family of curves produced by varying the value of n.

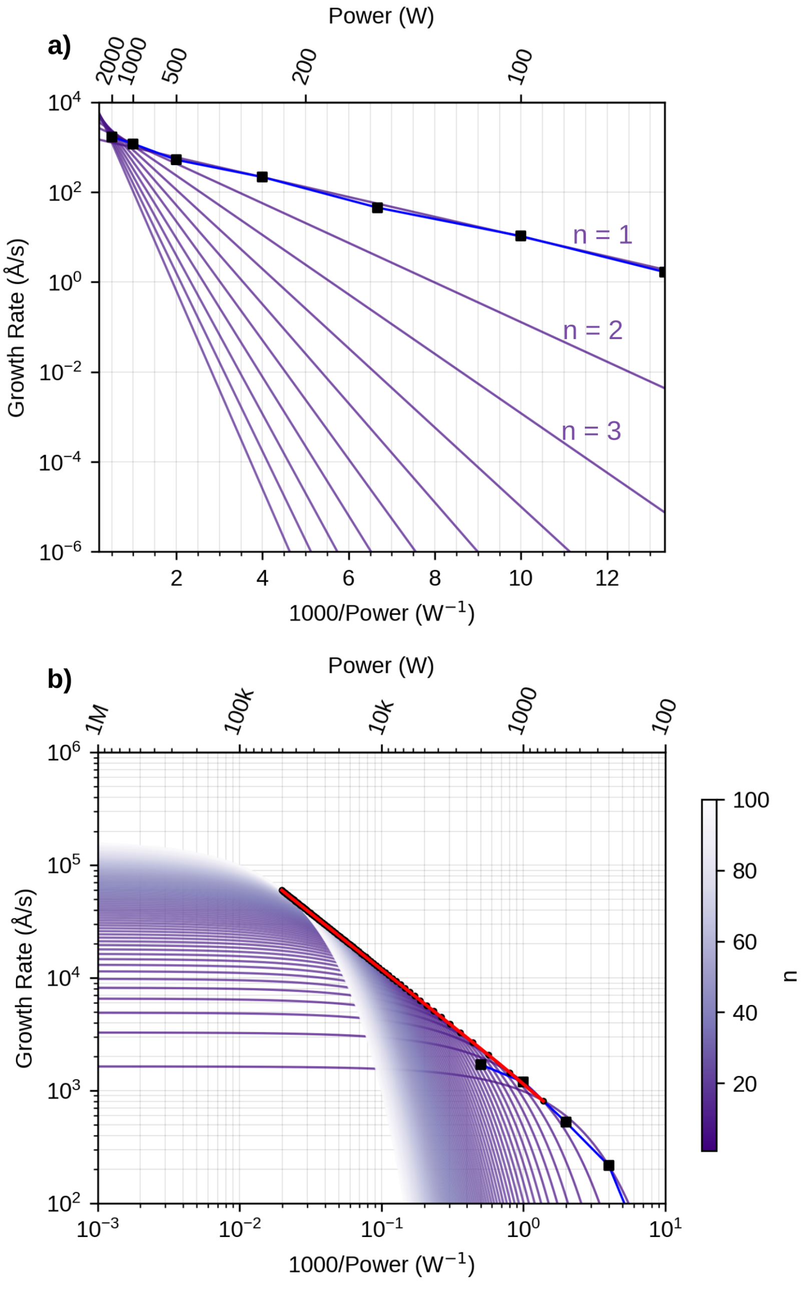

Figure 6.10: Measured and calculated growth rates as a function of laser power on an Arrhenius plot for a liquid Ag source inside a Al_2O_3 crucible. The Arrhenius-like dependence given in Eqn. 6.4, is shown from $n = 1$ to $n = 10$ in **a)** and from $n = 1$ to $n = 100$ for **a)**. **a)** shows the laser power mediated regime and **b)** shows the surface area mediated regime. The red line in **b)** shows the envelope of the family of curves produced by varying the value of n.

7

Example: Exploration of the Al-O system for homoepitaxy of Al_2O_3

In the previous chapters, it has been successfully demonstrated that TLE is a promising technique for the growth of thin film heterostructures and is well suited to meet the requirements of modern condensed matter physics. One area that remains to be explored in this work is the growth of oxides, which is of particular interest for the development of electronic devices. A major advantage of TLE over current epitaxy techniques is the absence of wire heaters as commonly used in effusion cells. The lack of wire heaters allows the use of reactive background gases within the TLE chamber without any damage to heating filaments that can be a problem in other epitaxial growth techniques. This makes TLE an ideal technique for the growth of complex oxides where the use of these background gases are critical.[97]

It is instructive to study source evaporation in the presence of an oxidizing atmosphere as a function of incident laser power, as the presence of an atmosphere can drastically change the evaporation behavior and composition of the deposited film.[45] It has been previously established that the behavior of the surface of the source is of major importance for deposition stability. Therefore, determining the behavior of a metallic source during deposition for a range of incident laser powers and O_2 pressures would be informative. It may be possible for example, that the same physical laws that produced the wide range of growth rates obtained for the Al system in UHV, as demonstrated in Chap. 6, may allow for the ultra-fast growth of an Al oxide in the presence of an oxidizing atmosphere.

Al_2O_3 is a particularly important oxide within condensed matter physics due to its use as a common substrate material for epitaxy and for electronics, particularly for quantum circuits. Its prevalence in electronics is only set to increase; in 2022, the total market value of the sapphire wafer industry sits around $ 638 million, expected to increase to $ 884 million by 2028.[98] Extremely high substrate temperatures are required to achieve epitaxial growth of Al_2O_3, making it an intriguing challenge for epitaxy using laser substrate heating in TLE.[25]

Recently, Kim *et al.* have successfully deposited a variety of oxides as thin films with TLE. However, the growth rate of these oxide thin films as a function of incident laser power have not been studied in detail, nor has the evaporation behavior of a metallic source in an oxidizing atmosphere at TLE. A better understanding of the evaporation process in an O_2 atmosphere could enable stable and reproducible deposition of oxide films.

In this chapter, as an example the evaporation behavior of Al in an O_2 atmosphere is investigated in greater detail with the goal of studying the homoepitaxy of Al_2O_3 via TLE. The experiments performed in this chapter were carried out in collaboration with Dr. Sander Smink, Dr. Dong Yeong Kim, and Ms. Lena N. Majer, all from the Max-Planck Institute for Solid State Research.

7.1 Experimental Setup

These experiments were performed in two separate TLE chambers with a unified geometry but with different physical characteristics. One chamber was used to study the evaporation behavior of Al in an O_2 atmosphere whilst the other was used to study the homoepitaxial growth of Al_2O_3 upon a heated substrate. Cross-sections of both these chambers are shown in Fig 7.1. Fig 7.1a shows the cross-section of the chamber used to investigate the evaporation of Al in an O_2 atmosphere. This chamber consisted of a water-cooled Al chamber with a $\lambda = 1075\,\text{nm}$ fiber laser with a peak power of 500 W providing the source heating. The chamber was cooled with water to ensure that the reflected laser radiation was rapidly transported out of the chamber. Driven by motors, the source could be moved upon a circular track with a chosen radius. Deposition was performed on 10 mm x 10 mm x 0.5 mm Si (111) substrates with a working distance of 60 mm between the substrate and the source. This chamber included the option for substrate heating via a defocused $\lambda = 1075\,\text{nm}$ fiber laser but this was not used. A photograph of this chamber is included in Fig. 7.2.

For each O_2 pressure value, the incident laser power was adjusted and the thickness of the deposited film was measured with a profilometer to determine the growth rate obtained for a given laser power. The measured thickness was then divided by the duration of the deposition experiment to obtain the average growth rate. For each O_2 pressure value, a new source was used, which was first melted with $\sim$ 30 W incident laser power under UHV conditions to remove any surface oxides or impurities in and on the source.

Conversely, Fig 7.1b shows the cross-section of the chamber used to investigate the homoepitaxial growth of Al_2O_3 that will be discussed later within this thesis. Substrate heating was provided by a $\lambda = 10\,\mu\text{m}$ CO_2 laser with a peak power of 1 kW. The substrates used were 10 mm x 10 mm x 1 mm Al_2O_3 (0001) with a source-substrate distance of 60 mm. In both chambers, the source laser was incident at 45° to the surface of the source with a working distance of 130 mm between the focal point of the laser and the source. This created a spot size of ~ 1 mm^2 on the surface of the source with an approximately Gaussian intensity profile. Within both chambers, the O_2 pressure was varied between 10^{-4} and 10^{-1} hPa via a gas inlet.

Since Al belongs to the class of "Crucible" materials introduced in Chap. 3, the granular Al source was placed in an Al_2O_3 crucible. Another reason for using an Al_2O_3 crucible to hold liquid Al in an O_2 atmosphere is based on the idea that the crucible will be replenished if it cracks due to thermal stress or suffers a thermally induced change in its stoichiometry.

7.2 Deposition of Al in an O_2 atmosphere

To fully understand the dynamics of the evaporating Al-O system, experiments were first performed with a stationary source and then a second set of data was collected over a larger range of O_2 pressures and with the Al source moving on a circular path with a radius of 1 mm as driven by the motor system. These data sets are plotted in Fig. 7.3 and 7.4 respectively. For the data taken with a circular motion of the source, both a regular and an Arrhenius plot are included to clearly show the evaporation behavior at different extremes of laser power. The experiments without motors served as an indicator of system behavior, while the measurements with motors served to stabilize the surface configuration and to study the Al-O system in more detail. Both data sets with and without motors show two different deposition regimes: a nearly flat growth rate dependence as a function of laser power at low laser powers and an Al-like deposition regime at high laser powers. To fully understand this system, both domains must be individually considered.

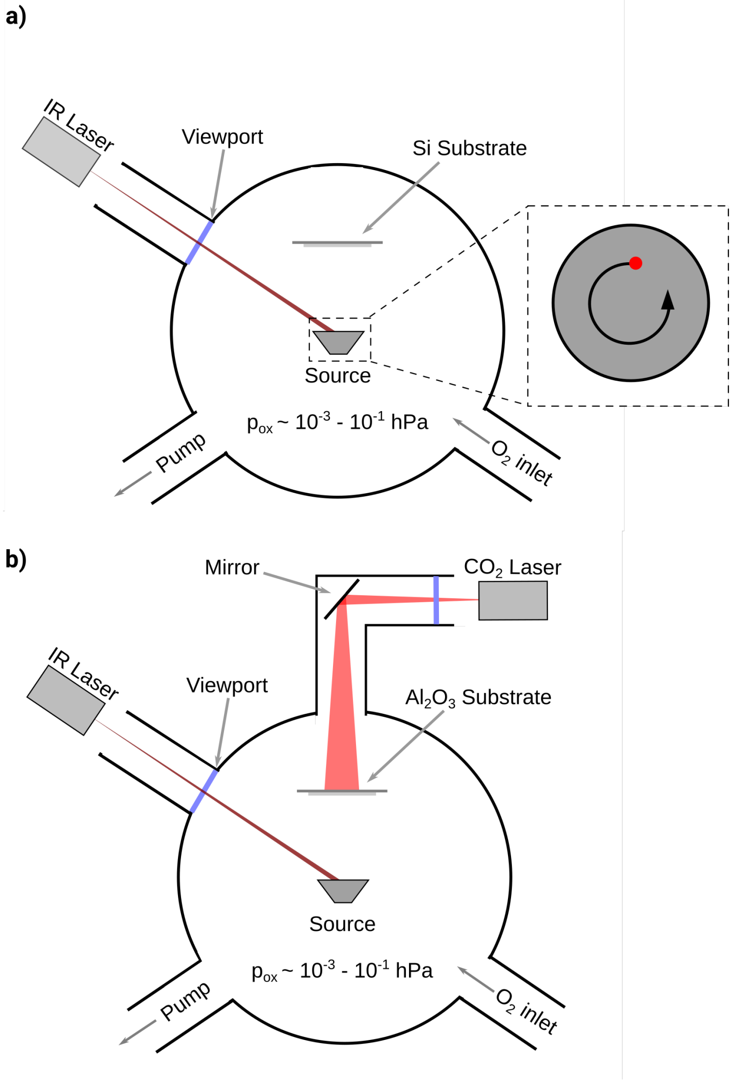

Figure 7.1: a) Cross-section of the TLE chambers used to investigate the evaporation behavior of Al in an O_2 atmosphere. This chamber included the option for substrate heating via a defocused $\lambda = 1075\,\text{nm}$ fiber laser although this option was not used. Via the use of motors, the source could be moved upon a circular track. b) Cross-section of the chamber used to study the homoepitaxial growth of Al_2O_3. Substrate heating could be provided by a CO_2 laser. For both chambers, O_2 could be fed into the chamber via a gas inlet.

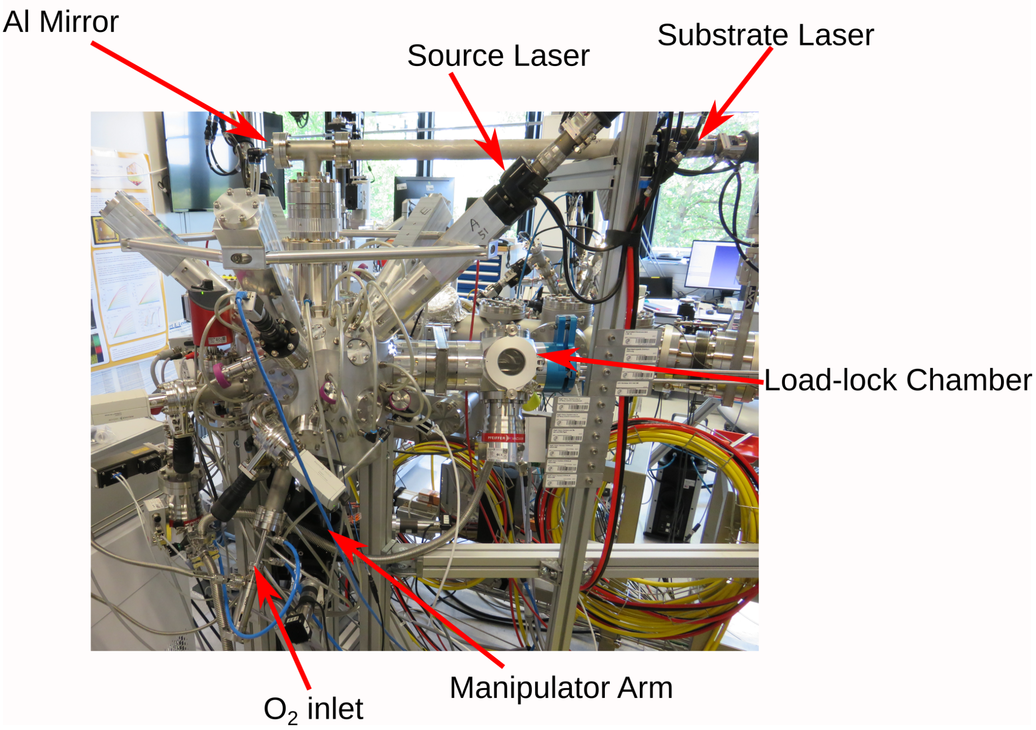

Figure 7.2: Photograph of the TLE chamber in which the study of the Al-O system was performed.

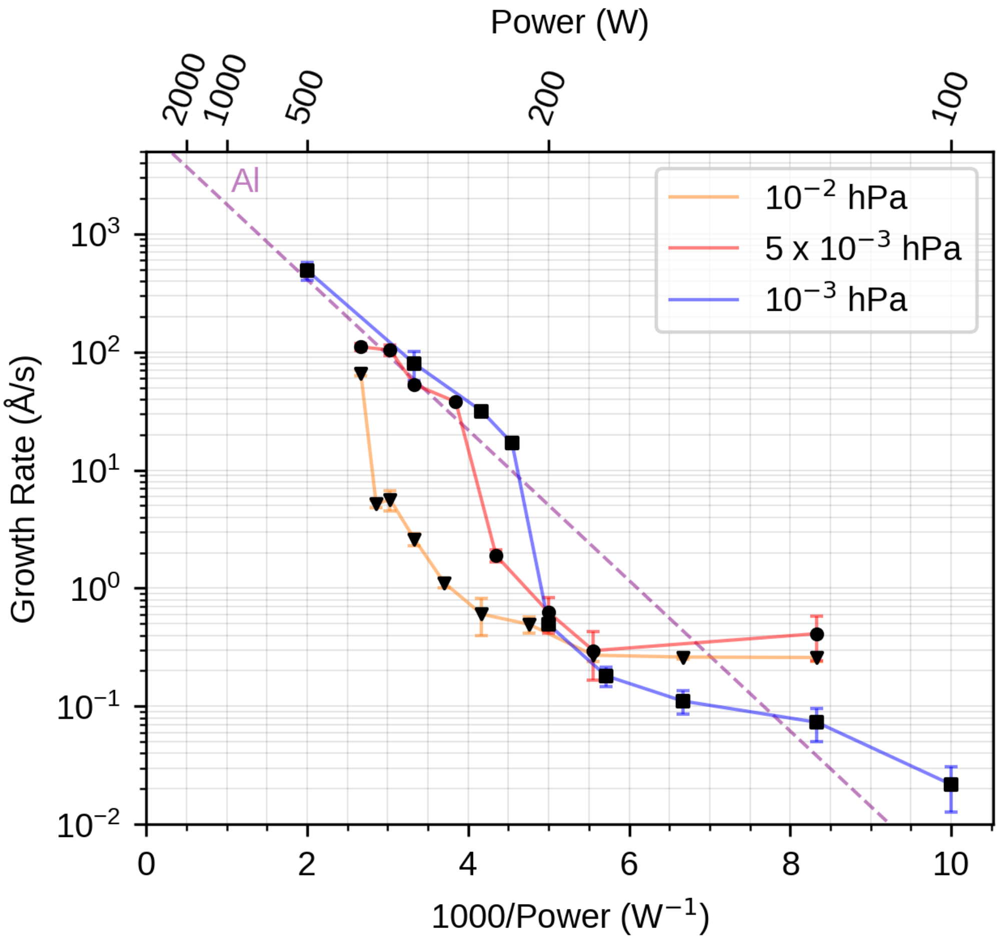

Figure 7.3: Growth rate of AlO_x as a function of laser power for different O_2 pressures. The dotted line indicates the associated Arrhenius-like dependence for the growth of Al in UHV. For each O_2 pressure, a clear jump can be seen between 200 W and 500 W, moving towards higher laser powers with increasing O_2 pressure.

7.2.1 Deposition at $P \lesssim 200\,W$

At low laser powers, the Al source coalesces into a sphere due to the strong surface tension and intermolecular interactions within the liquid metal and the large contact angle with the oxygen-terminated Al_2O_3 surface.[99] Usually, as the Al source heats up, the contact angle of the Al source to the Al_2O_3 crucible

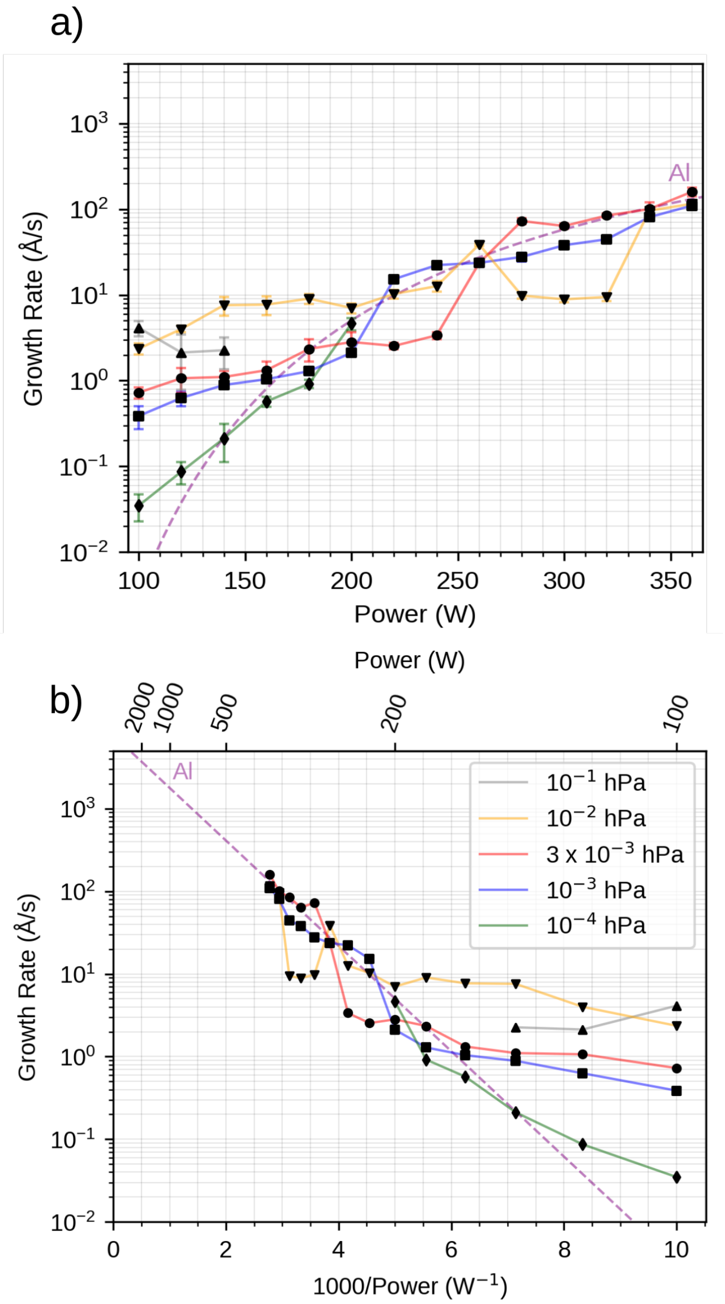

Figure 7.4: Growth rate of AlO_x as a function of laser power for different O_2 pressures with the source moving on a circular track with a radius of 1 mm. The data is plotted on a regular (a) and Arrhenius plot (b) in order to clearly show the deposition behavior at different extremes of laser power. The dotted lines indicates the associated Arrhenius-like dependence for the growth of Al in UHV.

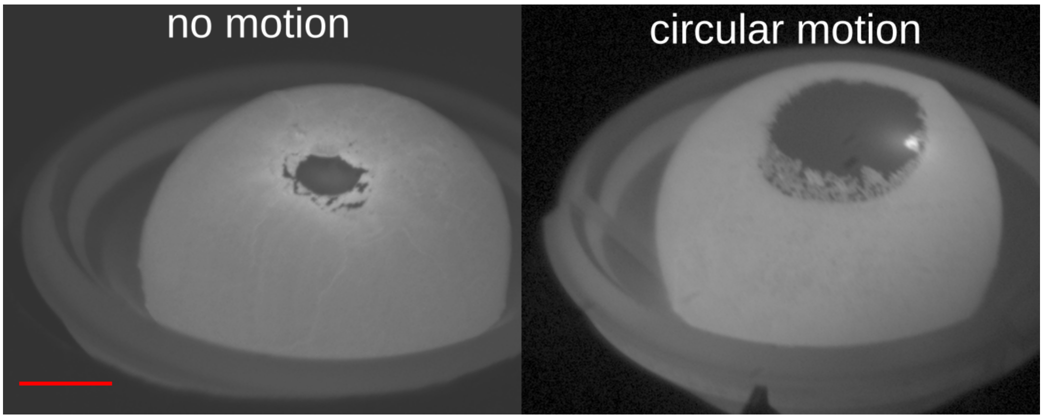

Figure 7.5: Comparison between an oxidized source of Al with and without motor movement for 120 W of incident laser power at an oxygen pressure of 10^{-3} hPa. By moving the source, the hole within the crust expands, increasing the growth rate. The scale bar represents 2 mm.

would decrease due to the decreasing surface tension of the Al source.[100] However, the formation of an AlO_x crust prevents the equilibrium contact angle between the Al source and the Al_2O_3 crucible from being reached. The crust formation therefore maintains the spherical shape of the Al source inside the Al_2O_3 crucible.

At the location of the laser spot, as seen in the left panel of Fig. 7.5, the AlO_x crust was removed due to the high temperatures obtained, leaving a hole within the crust and exposing the liquid Al beneath. The geometry appears stable for low laser powers, indicating that a steady state has been reached between the oxidation and adsorption of the AlO_x crust. The size of this hole can be widened by moving the laser position on the source by the motors to remove more of the AlO_x crust. The widening of this hole creates an increased flux of Al from the source, enhancing the growth rate obtained with motor movement compared to without motor movement. As demonstrated in Fig. 7.6, this steady state source geometry with the liquid patch at the location of the laser spot appears physically unaffected by changes in the surrounding O_2 pressure with only the

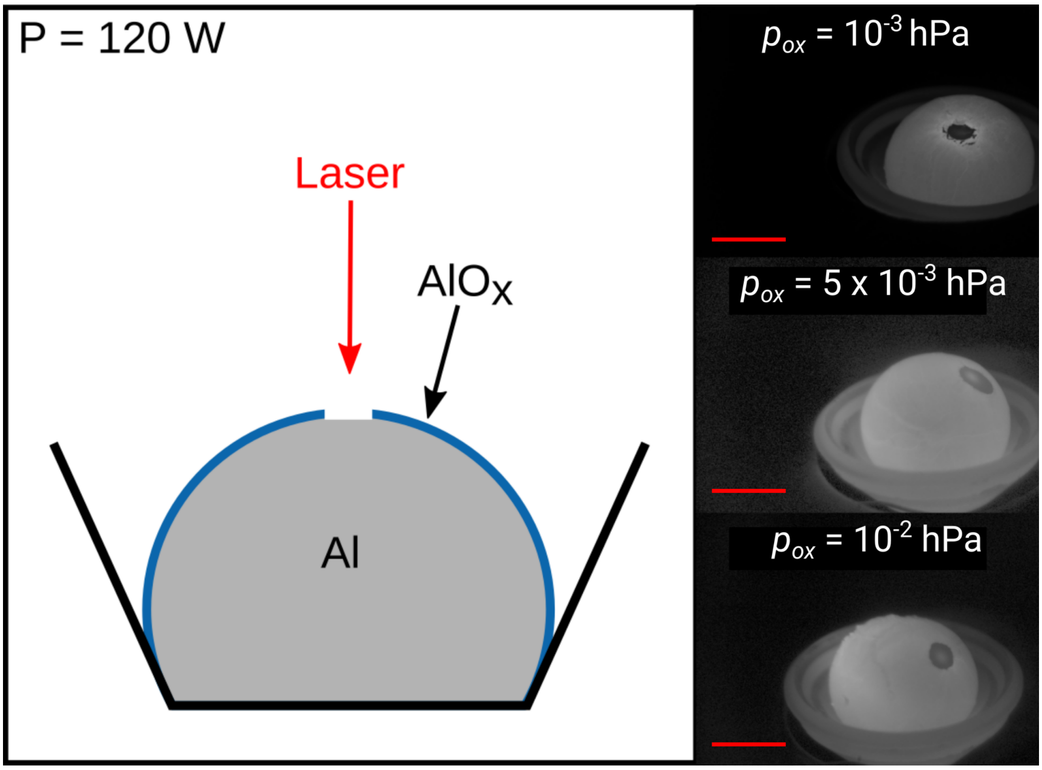

Figure 7.6: Sketch and photographs illustrating the behavior of an Al source in the presence of an O_2 atmosphere at low laser powers with no motor movement. The liquid Al source remains as a droplet due to its high surface tension. The surface of the liquid Al is covered by a thin AlO_x layer which is locally removed in the region of the laser spot. Photographs of individual Al sources at 120 W for various O_2 pressures are shown, all exhibiting similar behavior. The scale bar in each photograph represents 4 mm.

thickness of the AlO_x crust increasing with O_2 pressure.

Within the Al-O system, the evaporating species are produced by the following reactions:[101, 102]

$$Al_{(l)} = Al_{(g)} \tag{7.1}$$

$$4Al_{(l)} + 3O_{2\,(g)} = 2Al_2O_{3\,(s)} \tag{7.2}$$

$$4Al_{(l)} + Al_2O_{3\,(s)} = 3Al_2O_{(g)} \tag{7.3}$$

We can also add an additional reaction that is not discussed within literature:

$$4Al_{(l)} + O_{2\,(g)} = 2Al_2O_{(g)} \tag{7.4}$$

Therefore, the evaporating species will be a mix of Al vapor and Al_2O suboxide from the location of the laser spot, Al_2O_3 may also be formed during the time-of-flight of the evaporating species or upon the substrate but this needs to be experimentally verified with the use of a mass spectrometer. As the vapor pressure of Al_2O_3 is significantly lower than the vapor pressure for Al and Al_2O, the relative proportion of Al_2O_3 that is evaporated directly from the source is minimal.

The relative fluxes of Al_2O and Al are dependent on the temperature of the source due to their varying vapor pressures demonstrated in Fig. 7.7. From this, one would expect the growth rate to be lower than from the Al source in UHV due to the lower volatility of the oxidized Al source. However, when the motors are active, it is observed that the growth rate is greater than what would be obtained for an Al source in UHV. This increase in the growth rate is proportional to the size of the Al hole within the AlO_x crust. This supports the presence of a catalytic reaction (Eqn. 7.4) which affects the rate of formation of Al_2O that oxidizes further into Al_2O_3 upon reaching the substrate. This presence of this catalytic reaction is further supported by the observation of a proportional increase in the growth rate with increasing O_2 pressure indicating that it is the impingement rate of O_2 upon the liquid Al surface that determines the growth rate of Al_2O_3 by the formation of Al_2O suboxide. By this logic, widening the hole increases the number of impinging O_2 molecules on the Al surface which leads to an increased growth rate.

With the current experimental setup, gaining further insight into the behavior of the evaporant is difficult. The addition of a mass spectrometer would

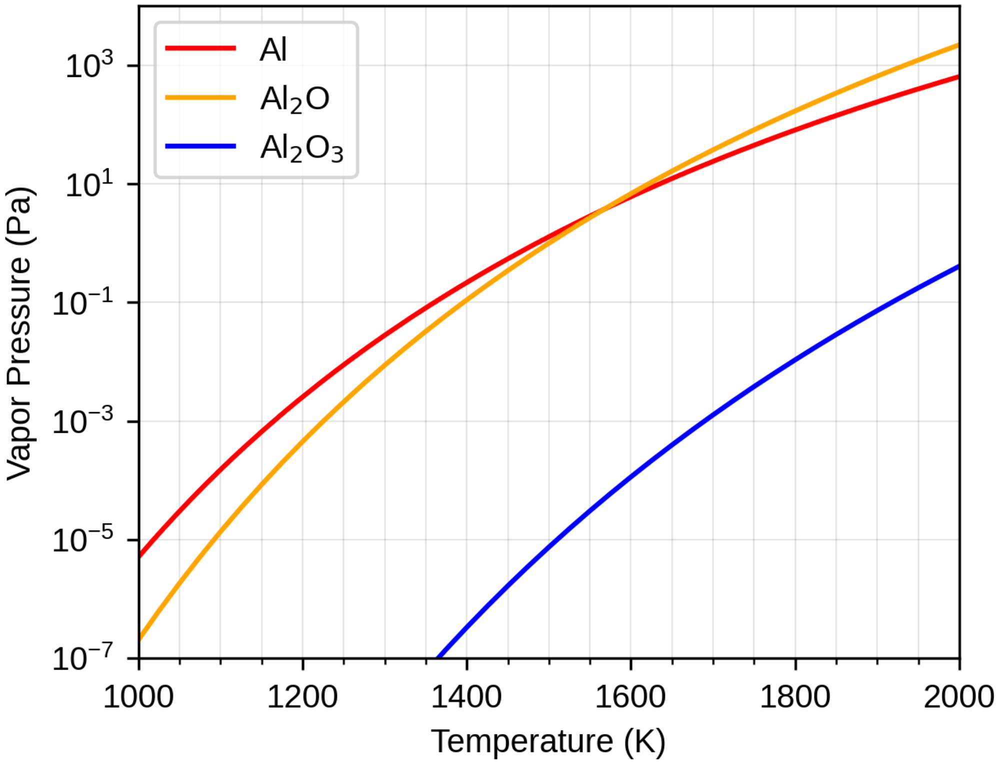

Figure 7.7: Vapor pressure curves for Al, Al_2O and Al_2O_3.[9, 103, 104]

allow for the composition of the evaporant to be determined.

One can further conclude that the evaporant is dominated by the suboxide Al_2O due to the adherence of the data to the power law dependence of the growth rate as a function of O_2 pressure. As shown in Fig. 7.8, the growth rate can be fit to the following dependence for a fixed laser power:[105, 45]

$$R_G \sim p_{\text{ox}}^n \tag{7.5}$$

Where p_{ox} is the O_2 pressure. The resulting fits obtained for $n = 0.904$ for $P = 100\,\text{W}$ and $n = 0.796$ for $P = 120\,\text{W}$ are shown in Fig. 7.8. At a steady state, the oxidation rate of Al equals the evaporation rate of Al_2O and the oxidation rate follows the aforementioned power law given in Eqn. 7.5. Therefore the

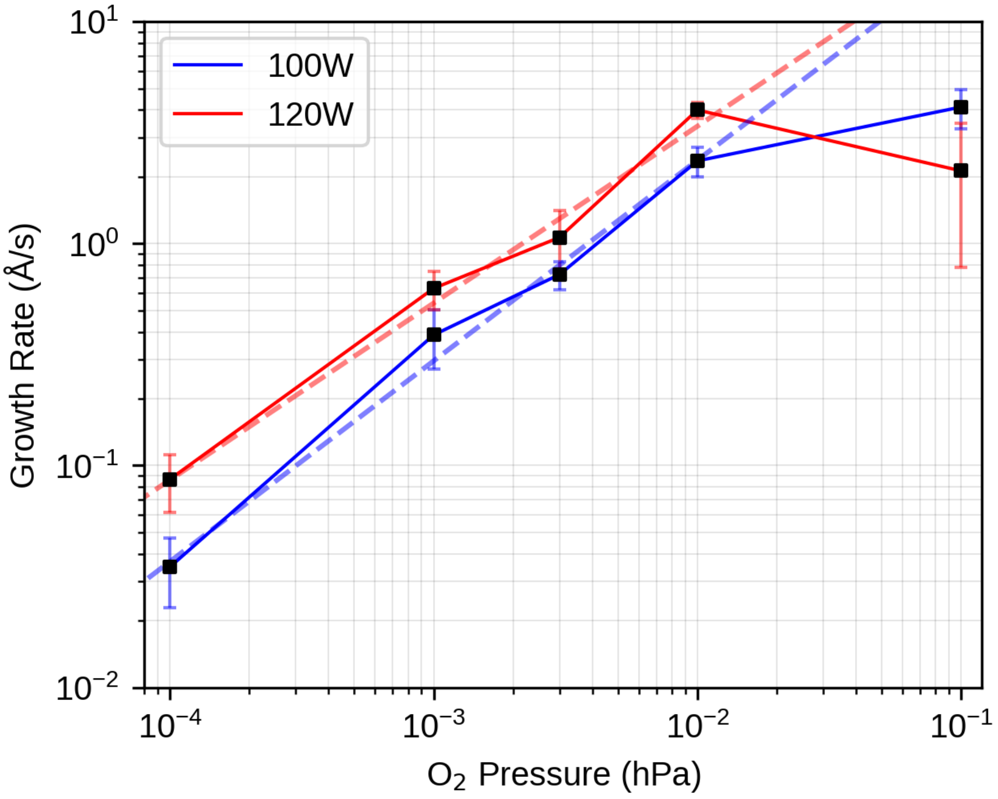

Figure 7.8: Growth rate of AlO_x as a function of O_2 pressure for 100 W and 120 W of incident laser power for the deposition of AlO_x. The dotted lines indicate fits to a power law given in Eqn. 7.5. The laser used was a $\lambda = 1075$ nm fiber laser with a peak power of 500 W and a spot size of ~ 1 mm^2. The source-substrate distance was fixed at 60 mm and the focal length of the laser was 500 mm. For 100 W, $n = 0.904$ and for 120 W, $n = 0.796$.

deposition rate increases with p_{ox}, providing that the oxide has a higher vapor pressure than the bare metal.

At $P \sim 200$ W, jumps are observed in the growth rate as shown in Fig. 7.3, going from the near-flat growth rate dependence as a function of laser power to the Arrhenius-like dependence for Al in UHV. These jumps can be explained by considering the evaporation rate of Al_2O as given by its vapor pressure. Once the vapor pressure of Al_2O exceeds the pressure of the O_2 atmosphere, the AlO_x

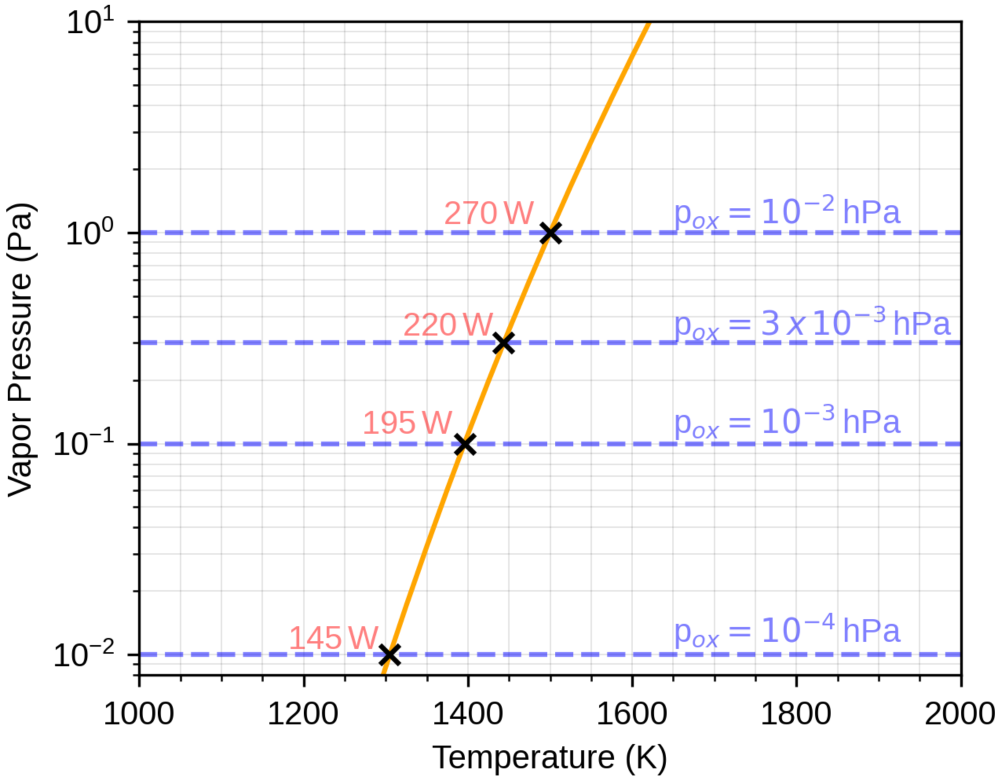

Figure 7.9: Vapor pressure curve of Al_2O with the different oxidizing atmospheres indicated. The vapor pressure curve was taken from Ref. [103]. The corresponding laser powers for each intersection point extracted from finite element simulations are indicated.

crust is rapidly removed exposing the bare Al beneath. These intersection points are shown in Fig. 7.9 for each O_2 pressure used in Fig. 7.4. The corresponding power values were extracted from the FEA simulations performed in Chap. 6 for Al in UHV. These intersection points are consistent with the results obtained within Fig. 7.3 and Fig. 7.4. However, the size of the jumps obtained with active motor movement are greatly diminished due to the greater evaporation rate obtained in the catalytic like regime. The origin of these jumps align nicely with the total removal of the AlO_x crust, recovering the bare liquid Al source and significantly increasing the formation of Al_2O suboxide.

7.2.2 Deposition at $P \gtrsim 200\,W$

At high laser powers, the AlO_x crust is fully removed and the contact angle between the Al source and the Al_2O_3 crucible is reduced. The transition temperature for wetting of the liquid Al/Al_2O_3 system has been measured in prior literature at around 1150 K, so the rapid onset of wetting after the removal of the AlO_x crust is consistent with the temperature measurements obtained in Fig. 7.9.[106]

Unlike the situation with low laser powers, within the high power regime, the growth rate of AlO_x follows the Arrhenius-like dependence obtained for Al in UHV conditions, indicated by the dotted line in Fig. 7.3 and Fig. 7.4. However it is curious to note that at high O_2 pressures, the growth rate undershoots the Arrhenius-like dependence of the growth rate as a function of laser power for Al. This implies that the growth rate of AlO_x is somehow suppressed. It may be possible that the formation of Al_2O as given in Eqn. 7.4 requires energy which acts as a dissipation mechanism for energy to leave the source and thus reduce its temperature compared to an Al source in UHV. This effect would also be more significant at high O_2 pressures, which is consistent with the greater undershoots of the UHV Al curve seen in 7.4. However, this is left as a topic for future investigation.

Once the AlO_x crust is removed, the O_2 flux is no longer high enough for Al_2O to be the dominant species in the evaporating flux, rather Al becomes the dominant species and the growth rate dependence as a function of laser power follows the Al curve in UHV.

Al may condense upon the cooler rim of the Al_2O_3 crucible, leading to the formation of Al_2O_3 on the Al-Al_2O_3 interface. Figure 7.10 shows how the growth of this new Al_2O_3 crust evolves with increasing O_2 pressure, with little to no growth observed at $p_{ox} = 10^{-3}$ hPa to significant growth at $p_{ox} = 10^{-2}$ hPa. Since

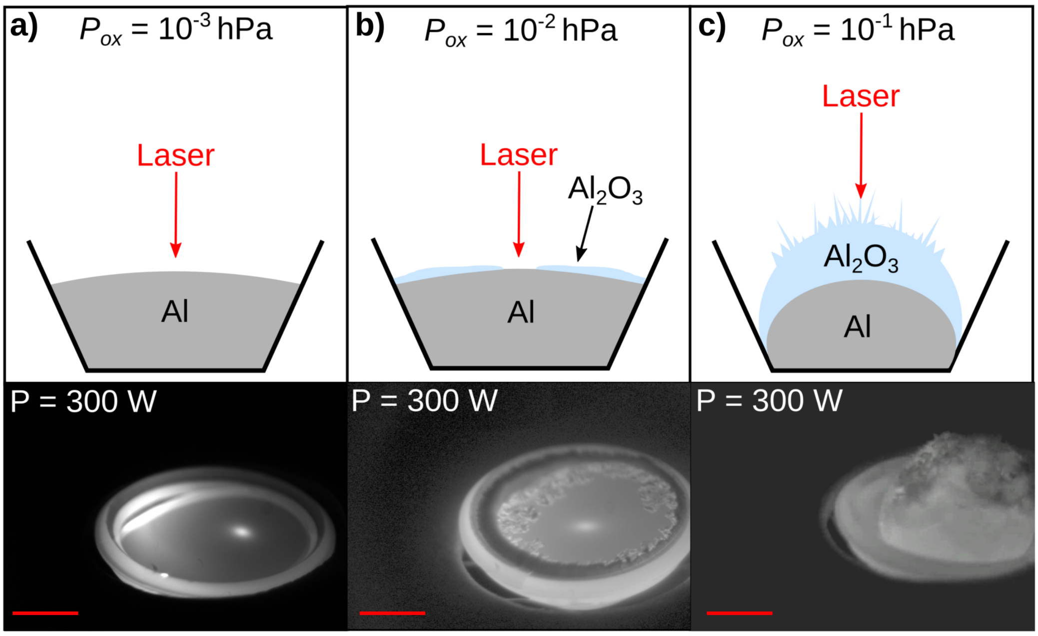

Figure 7.10: Behavior of an Al source in the presence of an O_2 atmosphere at high laser powers for no source motion. At lower O_2 pressures, the AlO_x crust seen in Fig. 7.6 is removed, leaving a metallic source. With increasing O_2 pressure, Al_2O_3 nucleates at the Al-crucible boundary causing larger proportions of the source to be converted from liquid Al to Al_2O_3. At $P_{ox} = 10^{-1}$ hPa, the entire surface of the source is converted to single crystal Al_2O_3. Photographs of individual Al sources at 300 W for various O_2 pressures accompany the corresponding diagram. The scale bar included in each photograph represents 4 mm.

this crust primarily forms on the rim of the crucible and grows inwards, its temperature is lower than the surrounding liquid Al, exemplified by its duller emission in the source photographs in Fig. 7.10.

The extreme case of this scenario occurs at high O_2 pressures where the temperatures obtained at the location of the laser spot do not produce high enough vapor pressures to overcome the oxidation rate of the source. At $p_{ox} = 10^{-1}$ hPa, an Al_2O_3 crust forms almost immediately upon heating the source. At the location of the laser spot, dendrite growth of Al_2O_3 is induced, an image of which is shown in Fig. 7.11. Similar dendrite growth has been observed

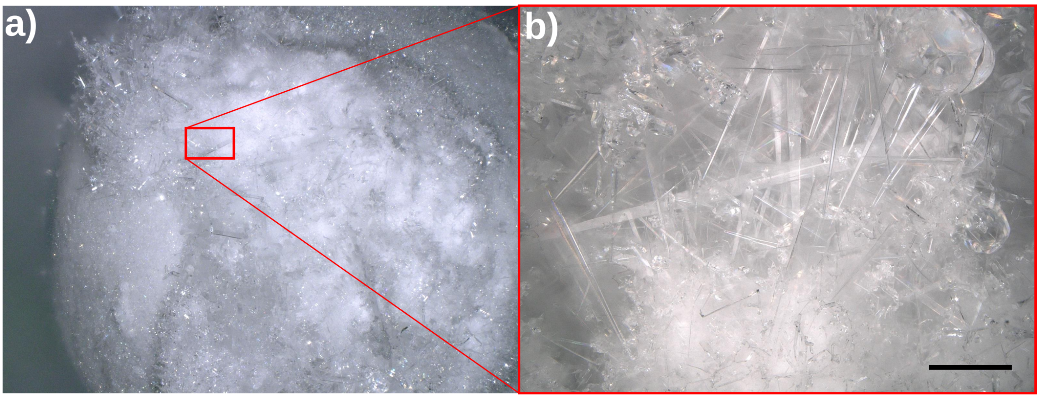

Figure 7.11: Optical microscopy images of a heavily oxidized Al source after ten minutes of deposition with 300 W of incident laser power and $p_{ox} = 10^{-1}$ hPa. Single crystal dendrites of Al_2O_3 can clearly be seen on the surface of the source. The black scale bar represents 100 μm.

within the Al-O system for high O_2 pressures and temperatures ~ 1500 K.[101] At 300 W with no motor movement, the obtained growth rate at $p_{ox} = 10^{-1}$ hPa was around 0.04 Å/s, around three orders of magnitude lower than what is expected from the Arrhenius-like dependence of Al. However, this is consistent with the difference in the vapor pressures between Al_2O and Al_2O_3 indicating that Al_2O_3 is evaporated from the heavily oxidized source.

Whilst growth rates exceeding 10 Å/s can be easily achieved with laser powers greater than 200 W, there is still uncertainty regarding the nature of the deposited AlO_x thin films. In order to reach the goal of rapid homoepitaxy of Al_2O_3, We must take the knowledge gained with respect to the Al-O system and apply it to epitaxy on a substrate of Al_2O_3 which is heated to a desired temperature via a laser.

7.3 Homoepitaxy of Al_2O_3 in TLE

To increase the crystalline quality of the deposited films, the substrate must be heated to increase the surface mobility and promote single crystal growth of a given material. For homoepitaxy, the deposited material is the same as that of the substrate with the same crystalline properties. For the case of Al_2O_3, this means that the deposited films must be grown with the corundum crystalline structure.

To achieve homoepitaxy of Al_2O_3, the CO_2 laser heater was used to thermally anneal an Al_2O_3 substrate at 1700 °C for 200 s in order to prepare it for deposition and improve the quality of the final thin film.[25] The substrate was then held at $T_{\mathrm{sub}} = 1100\,^\circ\mathrm{C}$ for 600 s with $p_{\mathrm{ox}} = 10^{-2}$ hPa and $P = 100$ W. The Al source remained stationary during deposition.

The deposition process was monitored in real time using reflection high-energy electron diffraction (RHEED). In RHEED, an electron gun generates a beam of electrons that strike the surface of the sample at a very shallow angle relative to the surface of said sample. The electrons then diffract from atoms at the surface of the sample, interfering constructively at certain angles to form a regular intensity pattern on the detector, which is usually a fluorescent screen.[107] The RHEED images of a thermally prepared Al_2O_3 substrate and the same sample after deposition of Al in an O_2 atmosphere are shown in Fig. 7.12.

Both images look similar, with both reconstructions of the Al_2O_3 surface present due to the symmetric nature of both images around their central axes. Kikuchi lines are visible in both images, indicating the high crystalline quality of both the thermally prepared substrate and the deposited sample. Since no obvious difference is present in the RHEED images before and after deposition, one needs to examine the surface morphology of the deposited thin film by atomic force microscopy (AFM) to search for further possible differences.

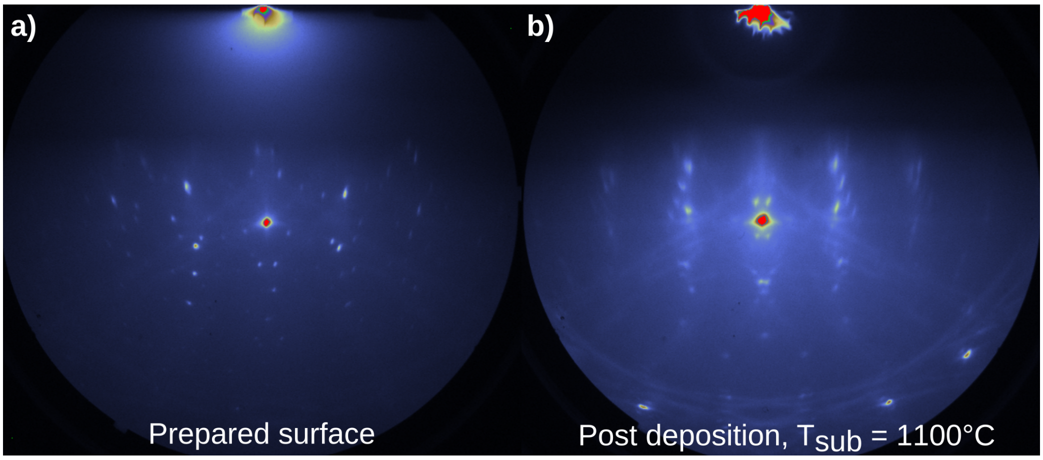

Figure 7.12: RHEED images of the thermally prepared Al_2O_3 surface and the grown Al_2O_3 surface after deposition at $p_{ox} = 10^{-3}$ hPa. The substrate was held at $T_{sub} = 1100\,°C$ for 600 s. Both images were taken along the (10-10) direction of the Al_2O_3 film.

AFM uses a cantilever with a sharp probe tip upon the end of it which is scanned across the surface of the sample.[108] When the probe is brought close to the sample, the canitilever is deflected by forces from the sample (for example: electromagnetic forces, van der Waals forces,etc.).[109] This displacement is kept at a low, constant level with the use of a feedback mechanism.[108]

The AFM image of the deposited Al_2O_3 film is shown in Fig. 7.13 and is the same film as what is shown in the RHEED image in Fig. 7.12. What immediately stands out here is the presence of multi-level islands with an approximately triangular shape, the orientation of which flips with each layer. The thickness of each layer Δy, as illustrated in the profile trace in Fig. 7.13 equals ~ 0.28 nm. Since the lattice constant c is equal to 1.299 nm for Al_2O_3, the corresponding distance between adjacent O layers is ~ 0.22 nm, which is consistent with the experimentally measured value of Δy. Step sizes equal to ~ 0.4 nm are also present within the deposited film, corresponding to the distance between alternating O layers. The observation of triangular islands indicates that epi-

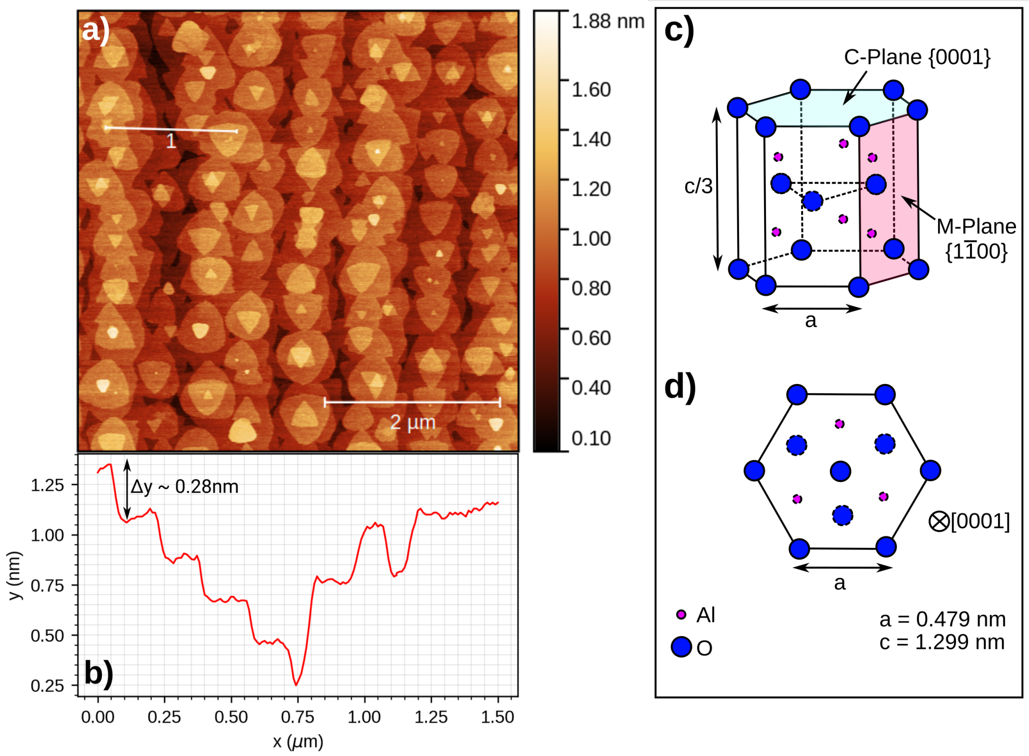

Figure 7.13: Panel a) shows an AFM image of the surface of the grown Al_2O_3 film at T_{sub} = 1100 °C. The height profile along the line "1" is shown with the single step height, Δy indicated in panel b). Panels c) and d) show the crystalline structure of Al_2O_3 The triangular islands emerge from the alternating orientation of the Al and O layers as shown in the crystalline structure of Al_2O_3.

taxy has been achieved for Al_2O_3 since these islands correspond to a HCP crystalline structure as illustrated in Fig. 7.13 and have been observed before for the perovskite oxide, $NiFeO_3$ on Ru (0001).[110] These islands are not present in a thermally prepared Al_2O_3 substrate, thus the presence of such islands implies growth has occurred.

One question that remains elusive here is the role of T_{sub} on the growth rate. For the ultra-fast growth of corundum Al_2O_3, it is required that both T_{sub} and the growth rate remain high enough to allow for step flow growth, where the deposited atoms diffuse to naturally-occurring step edges between adjacent atomic planes to form an atomically-smooth plane. To investigate this, the deposited thickness of each Al_2O_3 film was measured via a profilometer at shadowed areas under the support pins of the substrate to extract the growth rate as a function of T_{sub} for two different laser powers and O_2 pressures. The results of this are shown in Fig. 7.14 illustrating a rapid drop in the growth rate with increasing T_{sub}. Whilst this data has a fairly low resolution, two regions of interest arise. At $T_{sub} < 900\,^{\circ}C$, the growth rate drops slowly with increasing T_{sub}. We speculate that this drop is the result of Al_2O desorption from the deposited film. Beyond $T_{sub} = 900\,^{\circ}C$, there is a rapid drop in the growth rate of over an order of magnitude. We hypothesize that within this temperature regime, adsorption controlled growth is present, with excess Al incorporated into the final film being rapidly being removed from the surface. However, this remains the subject of future study as a more in-depth analysis is required.

It has been shown within this chapter that there are three key parameters in TLE that each have a strong effect on the growth procedures of the deposited film. These are the laser power, the pressure of the surrounding atmosphere and the substrate temperature. The laser power affects the growth rate of the deposited film and allows for all solid, non-radioactive elements in the periodic table to be grown as shown in Chap. 3. The gas pressure also has a significant effect on the growth rate of a given material, perhaps even serving a catalytic-like role in some material systems like Al_2O_3. The substrate temperature determines the crystalline quality as well as the growth rate of a given material. Each parameter has secondary effects on quantities such as the growth rate stability and stoichiometry of the deposited film. The exact role of each parameter on TLE remains the topic of future research.

In conclusion, the deposition behavior of an Al source in various O_2 pressures has been examined as a function of laser power. Two distinct regions

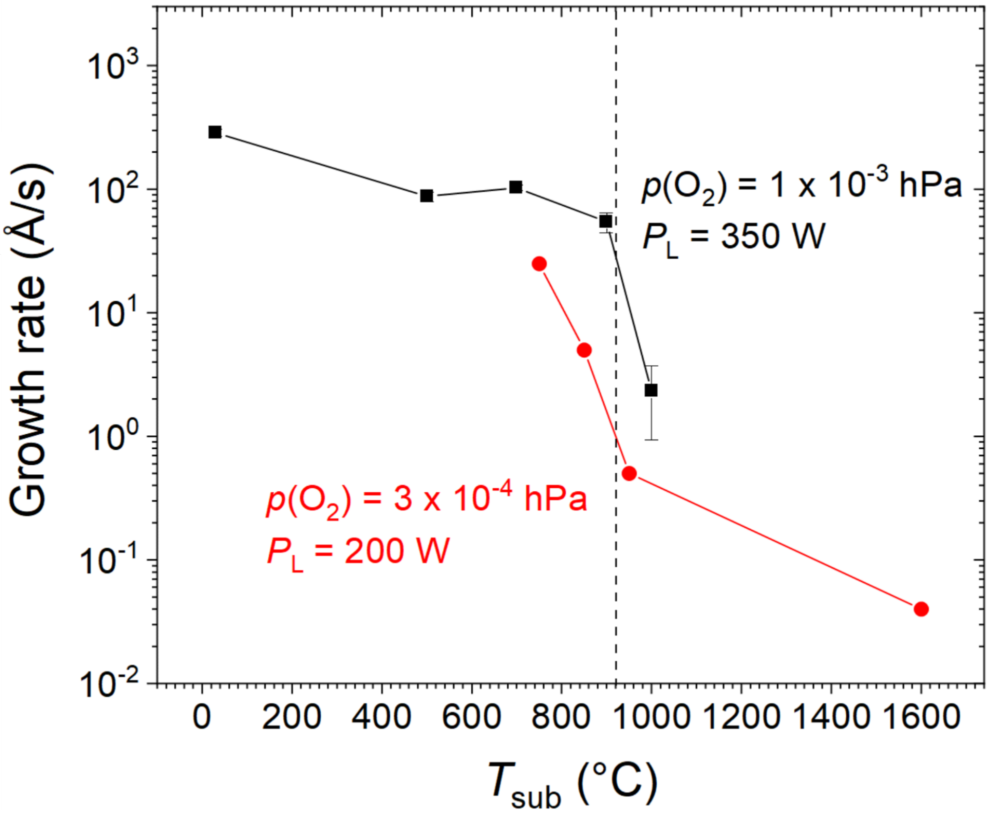

Figure 7.14: Growth rate of AlO_x as a function of substrate temperature T_{sub} for two different laser powers P_L and oxygen pressures $p(O_2)$. From this broad data set, there appears to be two regions of interest, a region of suboxide desorption at low T_{sub} and adsorption controlled growth at high T_{sub}. The laser used was a $\lambda = 1075$ nm fiber laser with a peak power of 500 W and a spot size of $\sim 1\,mm^2$. The source-substrate distance was fixed at 60 mm and the focal length of the laser was 500 mm. Figure taken from Ref. [111].

of interest were observed: one where the laser power has a minimal effect on the growth rate with a catalytic-like role of O_2 and one where deposition follows the Arrhenius-like dependence of Al in UHV. By examining the behavior of the source as a function of O_2 pressure and laser power, I was able to successfully explain the observations made during experiments. With the addition of a substrate heater, homoepitaxy of Al_2O_3 by TLE was demonstrated, with the growth of multi-level islands observed at T_{sub} = 1100 °C. Increasing T_{sub} for a fixed O_2 pressure and laser power causes the growth rate to drop significantly which I speculate is the result of suboxide desorption and adsorption controlled growth.

8

Summary and Outlook

Based on fundamental scientific principles, I have shown that TLE is uniquely suited to meet the challenges and requirements of modern condensed matter physics. Because of the highly localized heating provided by the source lasers, free-standing sources can be used for many elements of the periodic table, eliminating the need for crucibles and allowing ultra-pure films to be deposited. Deposition of all solid, non-radioactive elements of the periodic table is possible with TLE. The process is particularly successful for refractory metals such as W and Ta, which are difficult to deposit using other epitaxy techniques.

With the simple test chamber geometry used in this work, growth rates greater than 1 Å/s can be achieved for all elements tested with less than 500 W of incident laser power from a $\lambda = 1030$ nm disk laser and a laser spot size of $\sim 1\,\mathrm{mm}^2$. By changing the physical dimensions of the material source, the required laser power could be further adjusted as the amount of energy lost through radiation, evaporation, and conduction changes. Going from a $\lambda = 1030$ nm to a $\lambda = 515$ nm disk laser can reduce the required laser power for a given growth rate, and a significant reduction was observed for Group IB metals (Cu, Au, and Ag). The increased absorption of laser light at elevated temperatures observed for these materials is consistent with results found in the literature, suggesting that TLE may be a valid method for studying the optical properties of an element at high temperatures.

Due to changes in the surface of the source during deposition and the coating of the laser mirror used to couple the laser radiation into the chamber, stability of the growth rate in TLE is not immediately guaranteed. However, by continuously moving the relative position of the laser on the source and slowly increasing the output laser power, growth rate stability can be maintained. Two elements were investigated as candidates for stable deposition: Si and Zn. Si exhibited a growth rate stability of ± 0.3 % due to the large melt-pool formed during deposition and the relatively low rate of mirror coating. This value of ± 0.3 % is particularly remarkable as Si is challenging to deposit by MBE due to the high reactivity of Si with common crucible materials at elevated temperatures. For Zn, a stability value of ± 2,5 % was obtained, suggesting that second-order effects affect the coating of the mirror, such as thermal expansion and eutectic formation, may introduce additional terms into the assumed exponential dependence of the reflectivity of the mirror over time. By using a photon absorber, a closed feedback loop has been implemented by which the temperature of the absorber is directly related to the output laser power. This would allow the stability of the deposition to be improved even further than was possible with the basic algorithm shown in this work. However, there are still some technical challenges that will be the subject of future research.

An Arrhenius-like dependence of the growth rate as a function of laser power was observed experimentally for every element successfully deposited with TLE, as shown in the database of all tested elements given in Appendix B. The Arrhenius-like dependence can be explained by the different energy loss mechanisms in TLE. At low laser powers, radiation is the dominant source of energy loss, while evaporation becomes the dominant energy loss mechanism as laser power increases. To ensure saturation of the growth rate associated with an Arrhenius-like dependence at high laser powers, the incident laser beam must be attenuated by the evaporating material. Since evaporation becomes the primary energy dissipation mechanism at high laser powers, evaporation dominates the energy balance of TLE and ensures that an increasing fraction of the incident laser power goes directly to source evaporation. This ratio, called the evaporation dominance ratio, tends toward 100 % at infinite laser power, implying that the adherence to an Arrhenius-like dependence of the growth rate as a function of laser power results from the transition to evaporation as the dominant energy loss mechanism in the energy balance.

Finally, I explored an example of an oxide system in TLE: the Al-O system. I demonstrated that AlO_x can be successfully deposited as thin films in TLE, but that the oxidizing atmosphere has a significant effect on the deposition behavior of the Al source. At laser powers below around 200 W, the growth rate has a minimal dependence on the laser power, but it increases proportionally to the pressure of the surrounding O_2 atmosphere. A catalytic effect of the oxygen on the growth rate may be able to explain the behavior of this system with the impingement rate of oxygen upon the Al source being the driving factor. If a well-defined threshold is exceeded for a given O_2 pressure, the crust of AlO_x on the source is rapidly removed, exposing the Al source beneath. At this point, the growth rate follows the Arrhenius-like dependence of Al in UHV conditions, implying that Al is dominant in the outgoing flux from the source. With the addition of substrate heating provided by an additional CO_2 laser, I successfully demonstrated homoepitaxy of Al_2O_3 via TLE, with the growth of triangular multi-level islands observed at a substrate temperature of 1100 °C.

The future applications of TLE seem truly limitless. One can envision TLE being used to grow superlattices or heterostructures both of compound materials and of single elemental films. Such superlattices and heterostructures have many applications within transparent conducting oxides and the study of two dimensional electron gases.[112] The field of complex oxides is similarly ripe for exploration with TLE, notably the perovskites which possess a myriad of properties including colossal magnetoresistance, metal-to-insulator transitions and insulator-to-superconductor transitions for strongly correlated materials.[113] The ultra-high purity of the films deposited by TLE will likely enhance the physical effects that are sensitive to the purity of the heterostructures, potentially uncovering new and exciting physics. The work performed within this thesis has already lead to the epitaxial growth of ultra-pure thin films besides the case of Al_2O_3 discussed in Chap. 7. Examples of these thin films are shown in Fig. 8.1 and include Ru, Si and RuO_2. The successful epitaxial growth of Ru further opens up the possibility of TLE being used for functional coatings since Ru deposited on graphene has potential applications for anti-icing coatings.[114] Ultra-pure epitaxial films of superconducting elements such as Ta and Nb grown via TLE may also be applied within superconducting devices like Josephson Junctions. These Josephson Junctions lie at the heart of many modern quantum computing approaches which form the backbone of the current quantum revolution within science.[2]

Not only the epitaxial growth of oxides is possible, but the same logic can also apply for a similar class of materials: the nitrides. Successful deposition of AlN is shown in Fig. 8.2 via x-ray diffraction (XRD) for AlN. This presents the possibility of using TLE for the growth of transition metal nitrides which has a range of properties including high hardness, high electrical conductivity and high melting point.[115] I can extend the logic for the oxides and nitrides and conclude that with the appropriate chamber design, TLE is capable of depositing further compounds such as fluorides, chlorides and carbides, although this has to be investigated on a case-by-case basis.

I have successfully being able to model the Arrhenius-like dependence of the growth rate as a function of laser power for Ag and Al, therefore this model maybe used to determine the evaporation behavior of more elements. Alternatively, the model could be combined with a fluid simulation to accurately account for the effect of convection if a liquid phase is present around the location of the laser spot. This work will hopefully lead to greater understanding regarding the heating of sources in TLE, which maybe further applied to achieve rapid heating and cooling rates of the sources to achieve sharp interfaces in heterostructures.

TLE is capable of overcoming many obstacles that prove challenging for other epitaxy techniques allowing for the ultra-pure growth of any solid, non-radioactive element from across the periodic table as a thin film. These films can then be using in a wide range of future applications from optical coatings to quantum circuits to solar cells. TLE has the potential to become adopted as a go-to epitaxy technique for the growth of many thin film systems that will lead to many exciting physical systems and applications within the wider world.

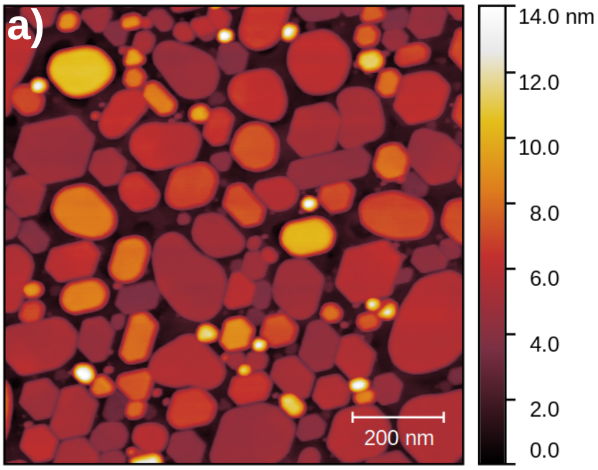

Ru on Al_2O_3 (0001)

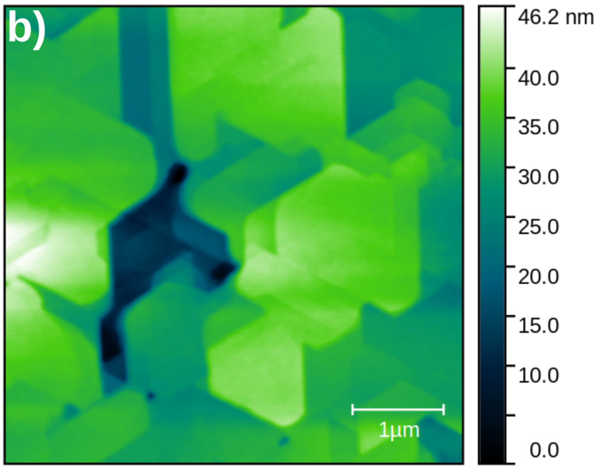

Si on Al_2O_3 (0001)

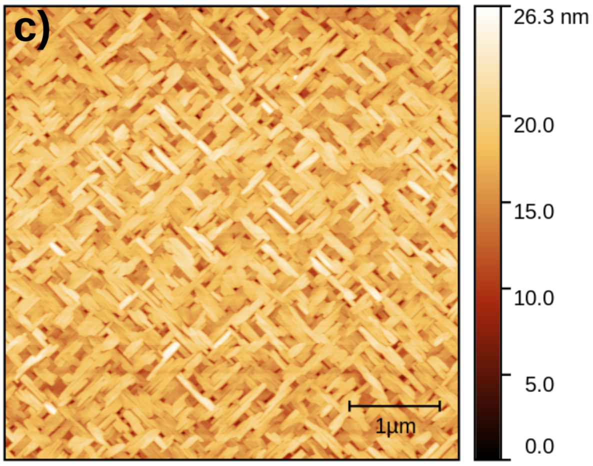

RuO_2 on MgO (001)

Figure 8.1: AFM micrographs of several epitaxial films that have been successfully grown via TLE. The Ru film was grown by Ms. Lena N. Majer and the Si and RuO_2 films were grown by Dr. Dong Yeong Kim. The Ru film had a thickness of $\sim$ 13 nm and the Si and RuO_2 films had thicknesses of $\sim$ 1.3 μm and $\sim$ 56 nm respectively.

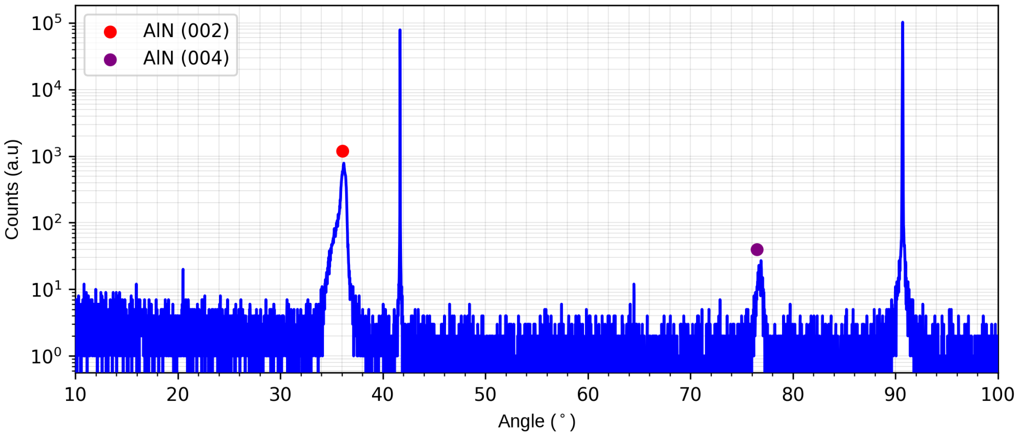

Figure 8.2: XRD spectra for a 90 nm thick AlN film on Al_2O_3 (0001) grown via TLE. The position of the AlN (002) and AlN (004) peaks are indicated by the colored circles. The AlN sample was grown by Dr. Dong Yeong Kim.

Appendices

A

Notes on FEA Simulation

All simulation work reported herein was performed in collaboration with Prof. Dr. Bilen Emek Abali from Uppsala University. The FEA simulation used to model the heat transfer processes within TLE was constructed in Python using FEniCS, an open-source computing platform designed to solve partial differential equations.[87] In this simulation, a nonlinear Newton-Raphson solver with a backward Euler method for time discretization was used, and the Galerkin method was used for the spatial discretization to calculate the temperature distribution in space and time.[88] After a while, the system reached an equilibrium state where the total heat loss across all boundaries equals the incoming heat flux, resulting in a constant temperature. The meshes were composed of approximately 10^5 first-order continuous tetrahedral elements auto-generated in SALOME by using NETGEN algorithms.

The problem solved by FEA simulation consisted of three different equations in the system of partial differential equations. These equations denoted different domains on the source: the bulk volume of the source (B), the outer surfaces of the source (S) and the upper circular face of the source which is directly irradiated by the laser (TS). The system of equations for temperature as a function of time and space, $T(\mathbf{x}, t)$ that we wished to solve are:

$$
\begin{aligned}
\mathrm{B}:\quad & \rho c_p \frac{\mathrm{d}T}{\mathrm{d}t} = -\kappa \Delta T && \forall \mathbf{x} \in \Omega \\
\mathrm{S}:\quad & \frac{1}{A_s}\frac{\mathrm{d}T}{\mathrm{d}t} = -\epsilon_{\mathrm{eff}}\sigma(T^4 - T^4_{\mathrm{amb}}) && \forall \mathbf{x} \in \partial\Omega_{\mathrm{S}} \\
\mathrm{TS}:\quad & \frac{1}{A_s}\frac{\mathrm{d}T}{\mathrm{d}t} = \frac{(1-\mathscr{R})Pe^{-\tau}}{\pi w^2} e^{-\frac{(x^2+y^2)}{w^2}} - \epsilon_{\mathrm{eff}}\sigma(T^4 - T^4_{\mathrm{amb}}) \\
& -\left(\frac{\Delta H_{\mathrm{vap}}}{M} + \frac{3N_{\mathrm{A}}k_b T}{2M}\right)\sqrt{\frac{m}{2\pi k_b T}}\, p(T) && \forall \mathbf{x} \in \partial\Omega_{\mathrm{TS}}
\end{aligned}
\tag{A.1}
$$

Where the symbols are the following:

- ρ - mass density [kg/m^3]
- c_p - specific heat capacity [J/kg K]
- A_s - surface area [m^2]
- N_{A} - Avogadro constant [mol^{-1}]
- κ - thermal conductivity [W/m K]
- ΔT - Laplacian of T, $\frac{\partial^2 T}{\partial x_i \partial x_j}$
- T_{amb} - Ambient temperature of the chamber (assumed to be 300 K)
- ϵ - hemispherical emissivity
- σ - Stefan-Boltzmann constant [W/m^2 K^4]
- $\mathscr{R}$ - reflectivity of element at the laser wavelength
- P - laser power [W]
- w - radius of Gaussian laser beam where the intensity falls to 1/e^2 of its axial value [m]

- k_b - Boltzmann constant [$m^2 kg/s^2 K$]
- ΔH_{vap} - enthalpy of vaporization of element [J/mol]
- R - ideal gas constant [J/mol K]
- m - mass of evaporated particle, assumed to be the atomic mass of Al/Ag [kg]
- M - molar mass of element [kg/mol]
- $p(T)$ - vapor pressure [Pa]

While radiative losses occur at all surfaces, we have assumed that evaporation (represented by the final term on the ’TS’ equation) only occurs from the surface directly irradiated by the laser.

This system of equations is then converted into the required weak form [116]

$$\begin{aligned}\text{Form} = &\int_{\Omega} \Big(\rho c_p \frac{(T - T_0)}{\delta t} V - \kappa \frac{\partial T}{\partial x_i}\frac{\partial V}{\partial x_i}\Big) dv + \int_{\partial\Omega} \epsilon_{\mathrm{eff}} \sigma (T^4 - T^4_{\mathrm{amb}}) V da \\ &+ \int_{\partial\Omega_t} \Big(\Big(\frac{\Delta H_{\mathrm{vap}}}{M} + \frac{3 N_{\mathrm{A}} k_b T}{2M}\Big)\sqrt{\frac{m}{2\pi k_b T}} p(T) \\ &- \frac{(1-\mathscr{R}) P e^{-\tau}}{\pi w^2} e^{-\frac{(x^2+y^2)}{w^2}}\Big) V da = 0\end{aligned} \tag{A.2}$$

Where δt is a time interval, T_0 is the temperature value at the prior time step, and V is a test function that is required for the finite element method.[117]

Within the simulation, the temperature dependence of the density, ρ, specific heat capacity, c_p, thermal conductivity, κ and emissivity, ϵ are all replicated for a given material.[80, 118, 119, 120, 121, 122] If the data was found to be lacking, the data was interpolated using a polynomial spline between existing data points to form a continuous function for each thermophysical property as shown in Fig. A.1. The temperature dependence for ΔH_{vap} and $\mathscr{R}$ are neglected in order to simplify the model.

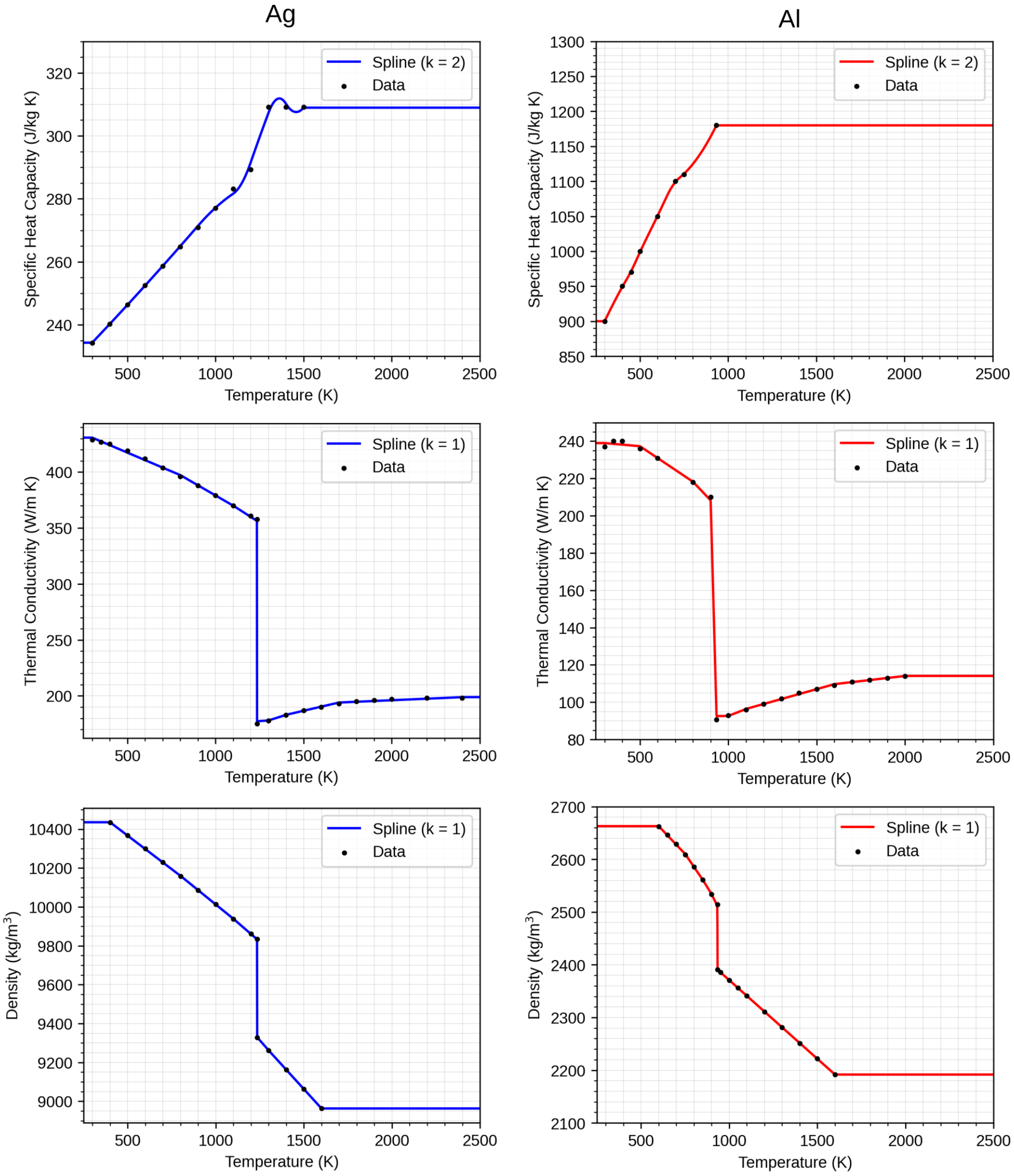

Figure A.1: Splines of different thermophysical data for Ag and Al with the indicated polynomial order, k with the corresponding temperature dependent data from literature. [80, 118, 119, 120, 121, 122]

B

Growth rate database of all tested elements

This appendix covers the database of all elements tested during the course of this thesis. Growth rate data any observations regarding growth are all given. Relevant Physical properties of the source material are also quoted. All growth rate data includes an Arrhenius-like fit to the equation:

$$R_G = ae^{-\frac{b}{P}} \tag{B.1}$$

Values of a and b are quoted for each element. If the reflectivity spectra could not be found, the field was left blank. The values for the thermal conductivity and the melting point for each element were taken from Ref. [12]. All crucibles that were used for deposition had an upper diameter of 12 mm and a height of 4 mm. Al_2O_3 was used as the crucible material unless explicitly stated. The source-substrate distance was held fixed at 60 mm and the focal distance of the laser was 500 mm.

Lithium (Li)

Physical properties

Thermal Conductivity (W/mK)	85
Enthalpy of Vaporization (kJ/mol) [123]	145.92
Reflectivity at laser wavelength[92]	0.89
Melting point (K)	453.65
Material Class	Crucible
Source Diameter (mm)	N/A

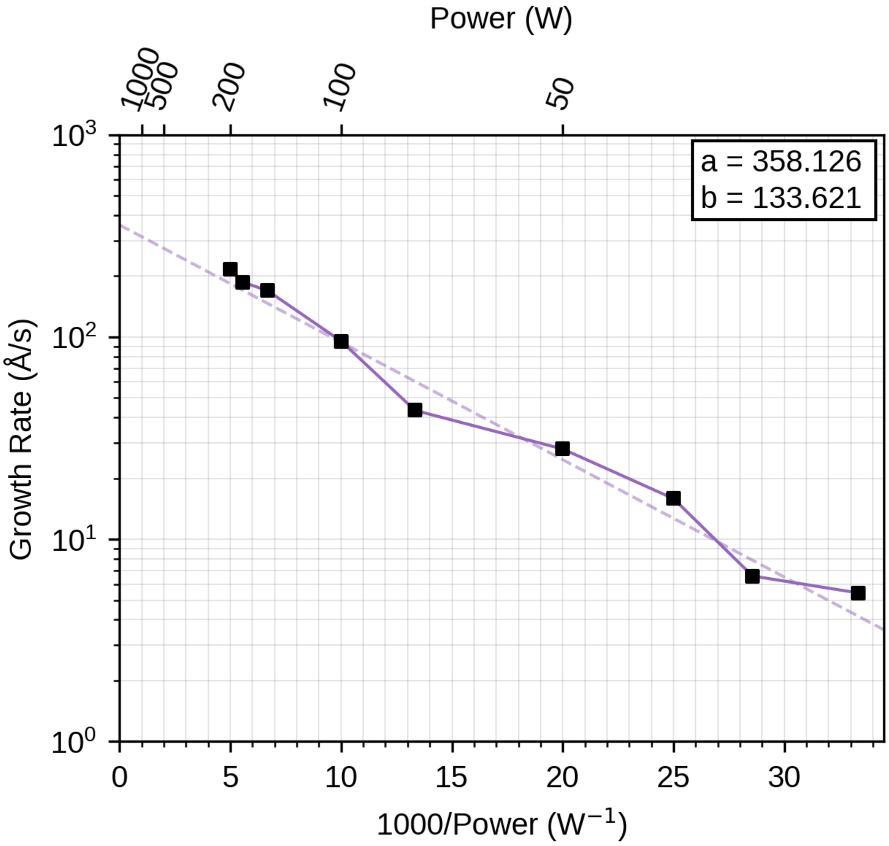

Figure B.1: Growth rate of Li as a function of incident laser power. Values of the fit parameters, *a* and *b* are quoted. Incident laser wavelength was $\lambda = 515$ nm.

Boron (B)

Physical properties

Thermal Conductivity (W/mK)	27.4
Enthalpy of Vaporization (kJ/mol)[123]	508
Reflectivity at laser wavelength[92]	0.3
Melting point (K)	2349
Material Class	Free-standing
Source Diameter (mm)	3mm

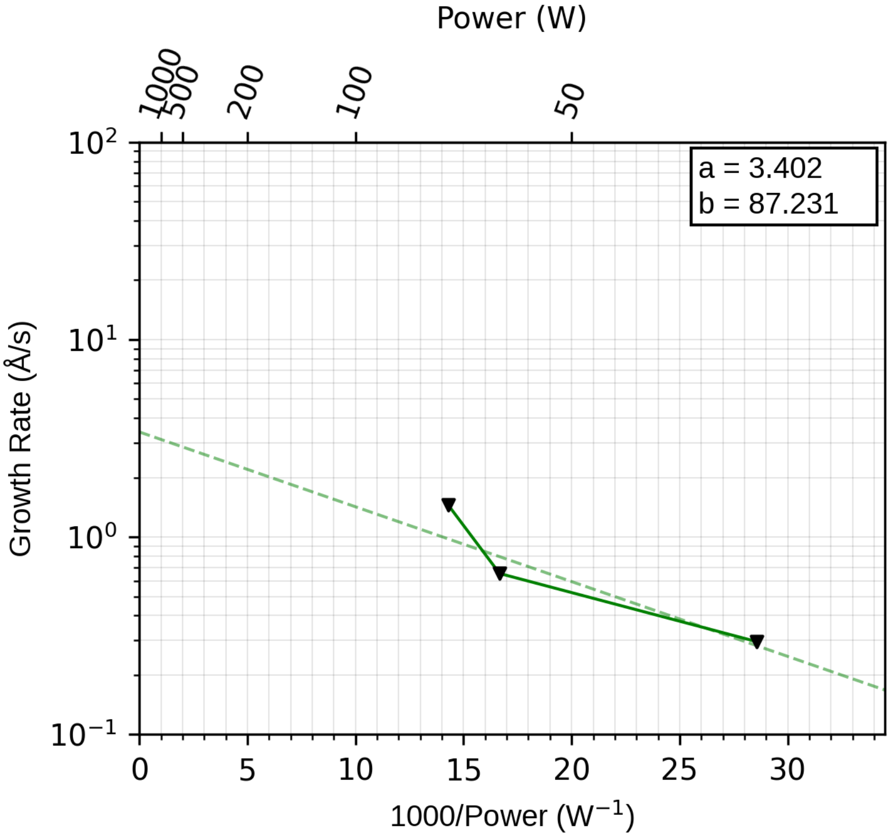

Figure B.2: Growth rate of B as a function of incident laser power. Values of the fit parameters, a and b are quoted. Incident laser wavelength was $\lambda = 515$ nm.

Carbon (C)

Physical properties

Thermal Conductivity (W/mK)	27.4
Enthalpy of Vaporization (kJ/mol)[123]	(sublimation) 715
Reflectivity at laser wavelength[92]	0.23
Melting point (K)	(high pressure) 3823
Material Class	Free-standing
Source Diameter (mm)	2mm

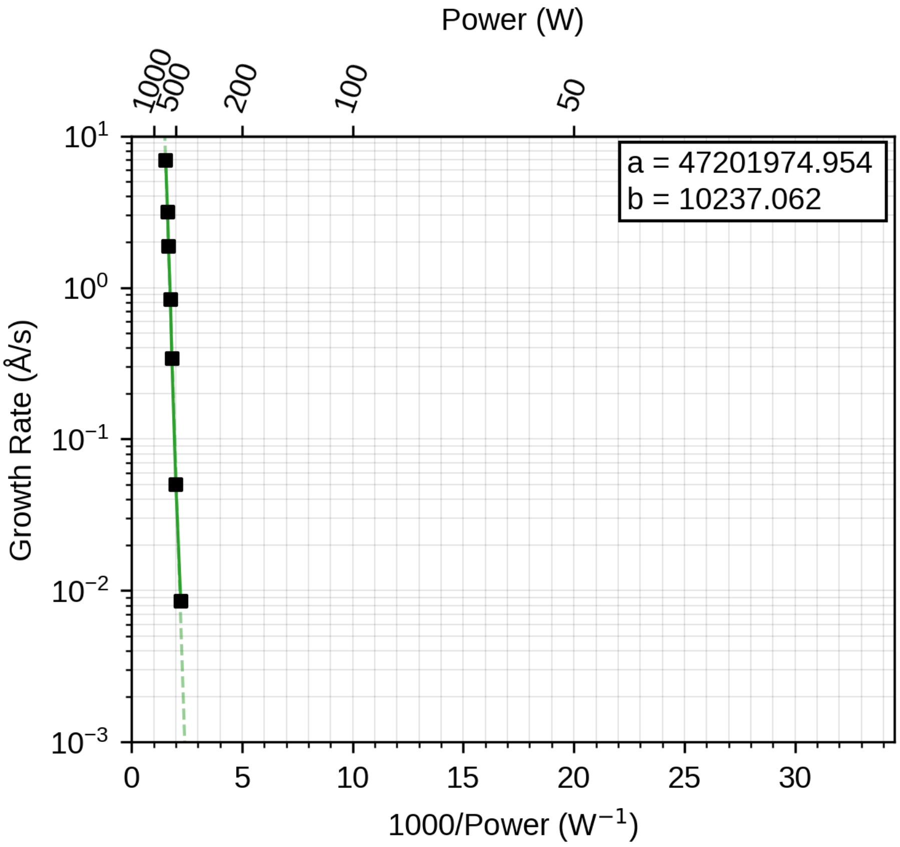

Figure B.3: Growth rate of C as a function of incident laser power. Values of the fit parameters, *a* and *b* are quoted. Incident laser wavelength was $\lambda = 1030\,\text{nm}$.

Magnesium (Mg)

Physical properties

Thermal Conductivity (W/mK)	156
Enthalpy of Vaporization (kJ/mol)[123]	132
Reflectivity at laser wavelength[92]	0.93
Melting point (K)	923
Material Class	sublimating
Source Diameter (mm)	2mm

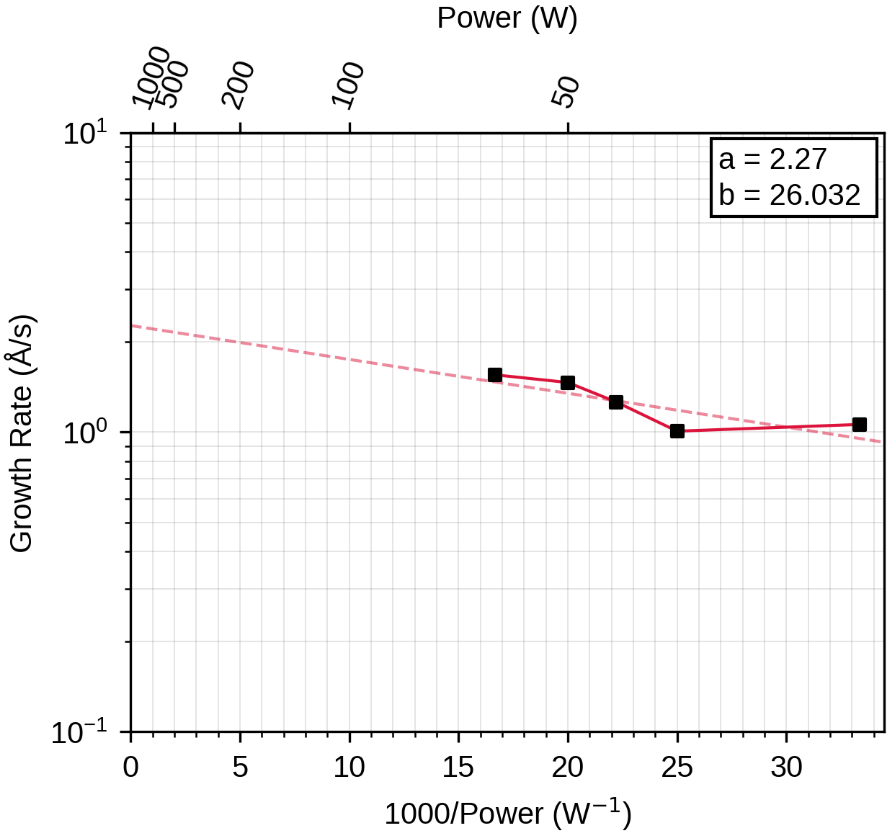

Figure B.4: Growth rate of Mg as a function of incident laser power. Values of the fit parameters, a and b are quoted. Incident laser wavelength was $\lambda = 1030$ nm.

Aluminum (Al)

Physical properties

Thermal Conductivity (W/mK)	237
Enthalpy of Vaporization (kJ/mol)[123]	284
Reflectivity at laser wavelength[92]	0.23
Melting point (K)	933.47
Material Class	Crucible
Source Diameter (mm)	N/A

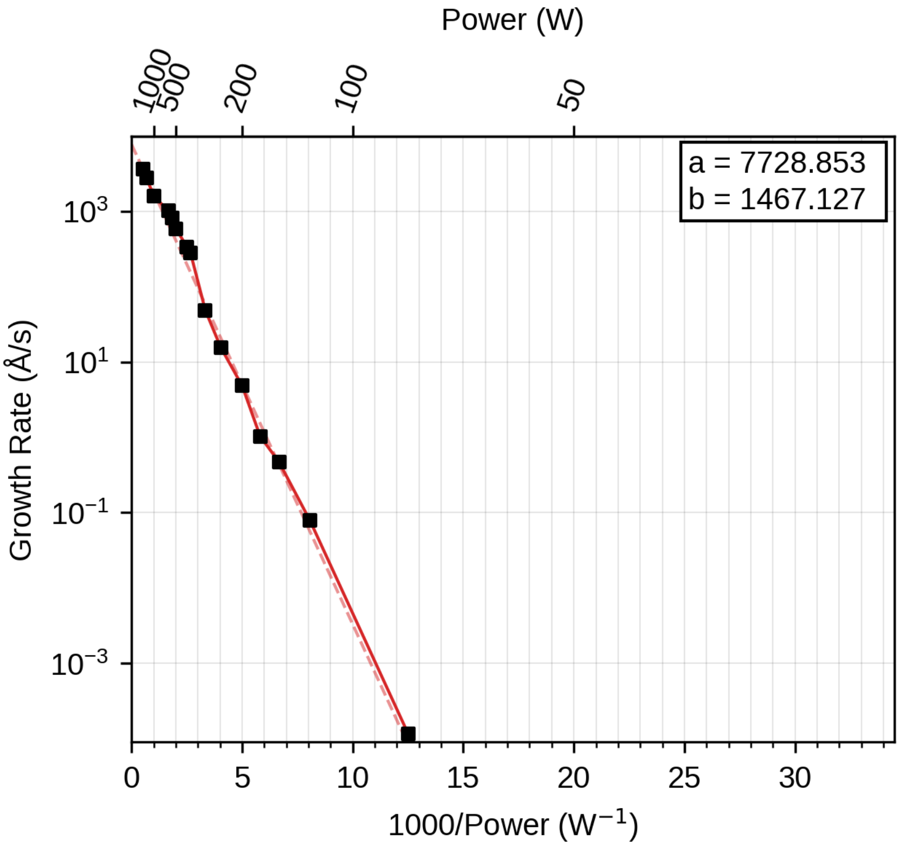

Figure B.5: Growth rate of Al as a function of incident laser power. Values of the fit parameters, a and b are quoted.Incident laser wavelength was $\lambda = 1030$ nm.

Silicon (Si)

Physical properties

Thermal Conductivity (W/mK)	149
Enthalpy of Vaporization (kJ/mol)[123]	383
Reflectivity at laser wavelength[92]	0.316
Melting point (K)	1687
Material Class	Free-standing
Source Diameter (mm)	12.7

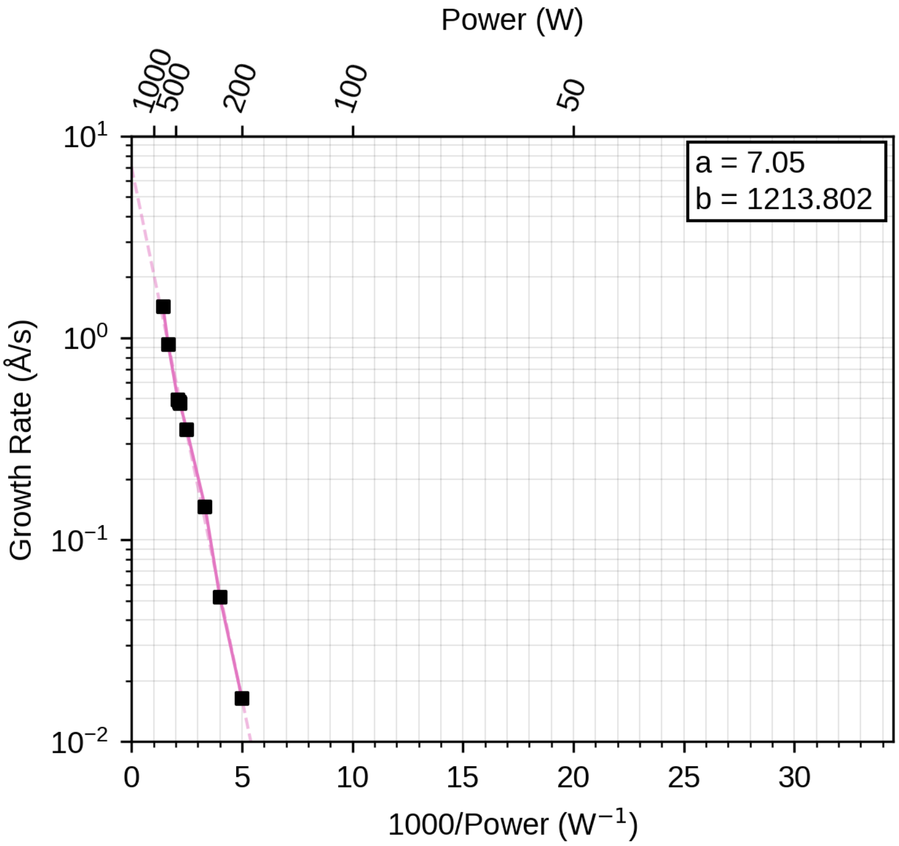

Figure B.6: Growth rate of Si as a function of incident laser power. Values of the fit parameters, a and b are quoted. Incident laser wavelength was $\lambda = 515\,\text{nm}$.

Phosphorus - red (P)

Physical properties

Thermal Conductivity (W/mK)	0.235
Enthalpy of Vaporization (kJ/mol) [123]	12.4
Reflectivity at laser wavelength	0.316
Melting point (K)	860
Material Class	Sublimating
Source Diameter (mm)	granulate

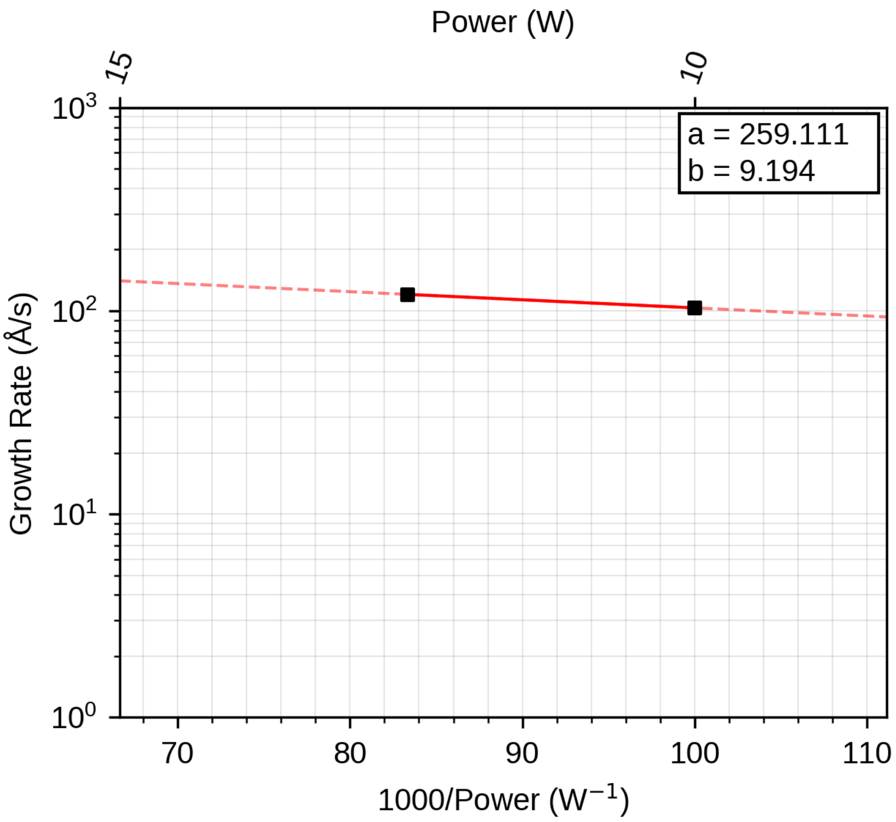

Figure B.7: Growth rate of P as a function of incident laser power. Values of the fit parameters, a and b are quoted. Incident laser wavelength was $\lambda = 1030\,\text{nm}$.

Sulfer (S)

Physical properties

Thermal Conductivity (W/mK)	0.205
Enthalpy of Vaporization (kJ/mol)[123]	45
Reflectivity at laser wavelength[124]	0.11
Melting point (K)	388.36
Material Class	Sublimating
Source Diameter (mm)	granulate

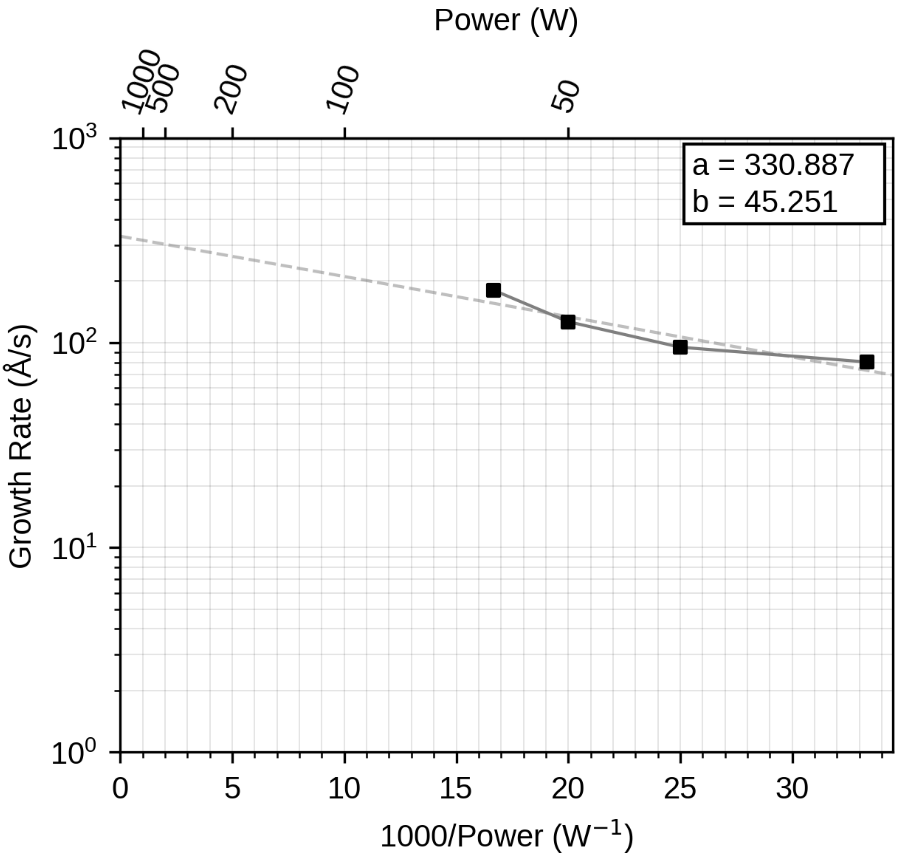

Figure B.8: Growth rate of S as a function of incident laser power. Values of the fit parameters, *a* and *b* are quoted. Incident laser wavelength was $\lambda = 1030$ nm.

Calcium (Ca)

Physical properties

Thermal Conductivity (W/mK)	201
Enthalpy of Vaporization (kJ/mol)[123]	153
Reflectivity at laser wavelength[125]	0.96
Melting point (K)	1115
Material Class	Sublimating
Source Diameter (mm)	2

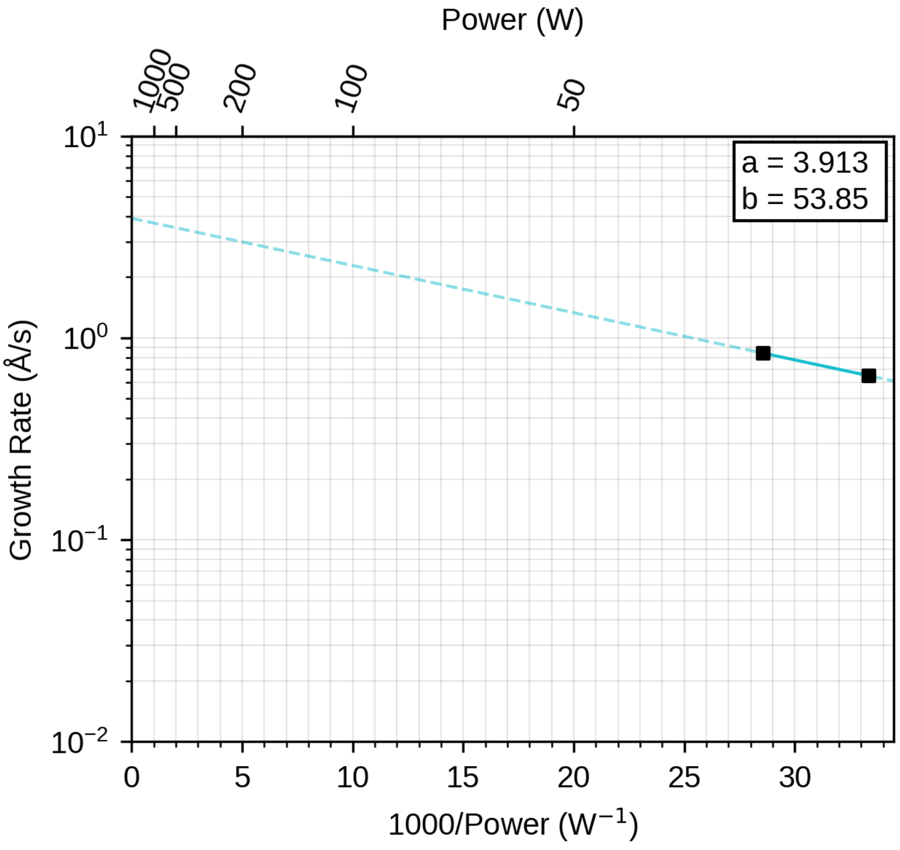

Figure B.9: Growth rate of Ca as a function of incident laser power. Values of the fit parameters, a and b are quoted. Incident laser wavelength was $\lambda = 1030$ nm.

Scandium (Sc)

Physical properties

Thermal Conductivity (W/mK)	15.8
Enthalpy of Vaporization (kJ/mol)[123]	310
Reflectivity at laser wavelength[126]	0.55
Melting point (K)	1814
Material Class	Sublimating
Source Diameter (mm)	2

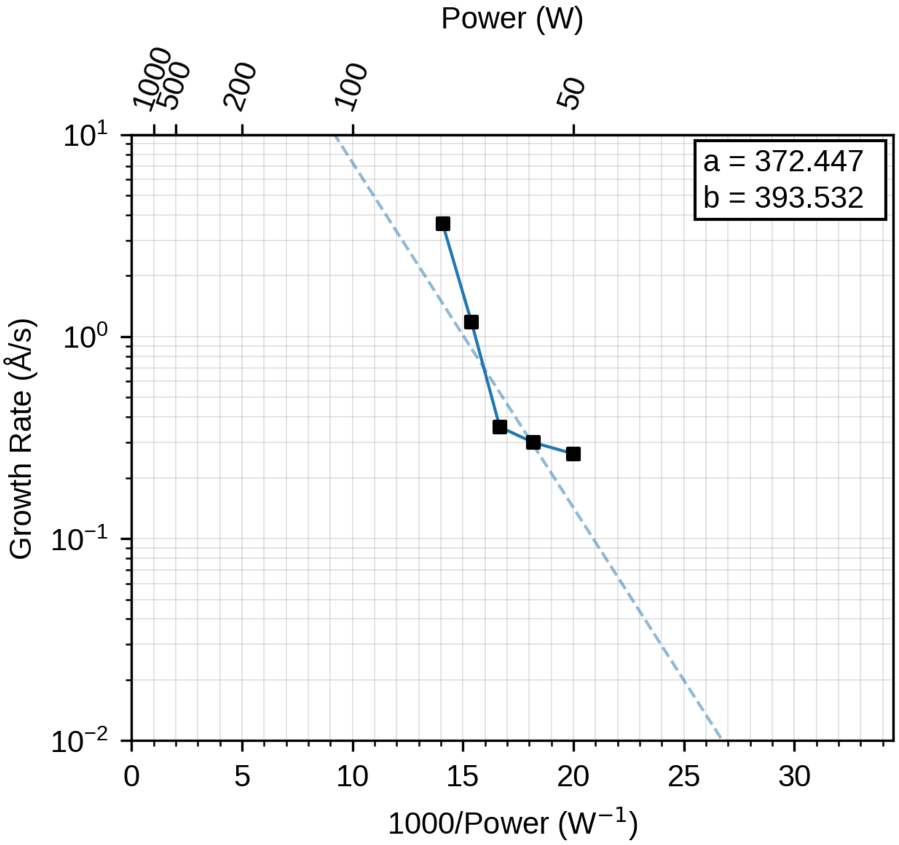

Figure B.10: Growth rate of Sc as a function of incident laser power. Values of the fit parameters, a and b are quoted. Incident laser wavelength was $\lambda = 1030\,\text{nm}$.

Titanium (Ti)

Physical properties

Thermal Conductivity (W/mK)	21.9
Enthalpy of Vaporization (kJ/mol)[123]	427
Reflectivity at laser wavelength[92]	0.57
Melting point (K)	1941
Material Class	Free-standing
Source Diameter (mm)	4, 12.7

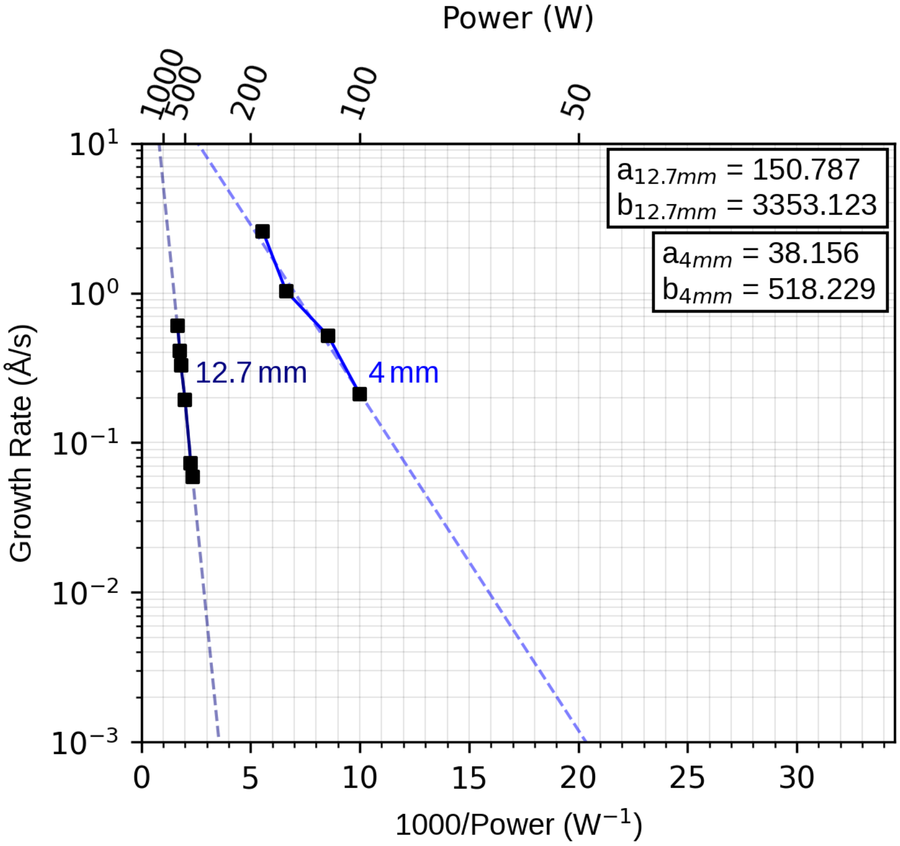

Figure B.11: Growth rate of Ti as a function of incident laser power. Values of the fit parameters, *a* and *b* are quoted. Incident laser wavelength was $\lambda = 515$ nm.

Vanadium (V)

Physical properties

Thermal Conductivity (W/mK)	30.7
Enthalpy of Vaporization (kJ/mol)[123]	451
Reflectivity at laser wavelength[92]	0.59
Melting point (K)	2183
Material Class	Free-standing
Source Diameter (mm)	3

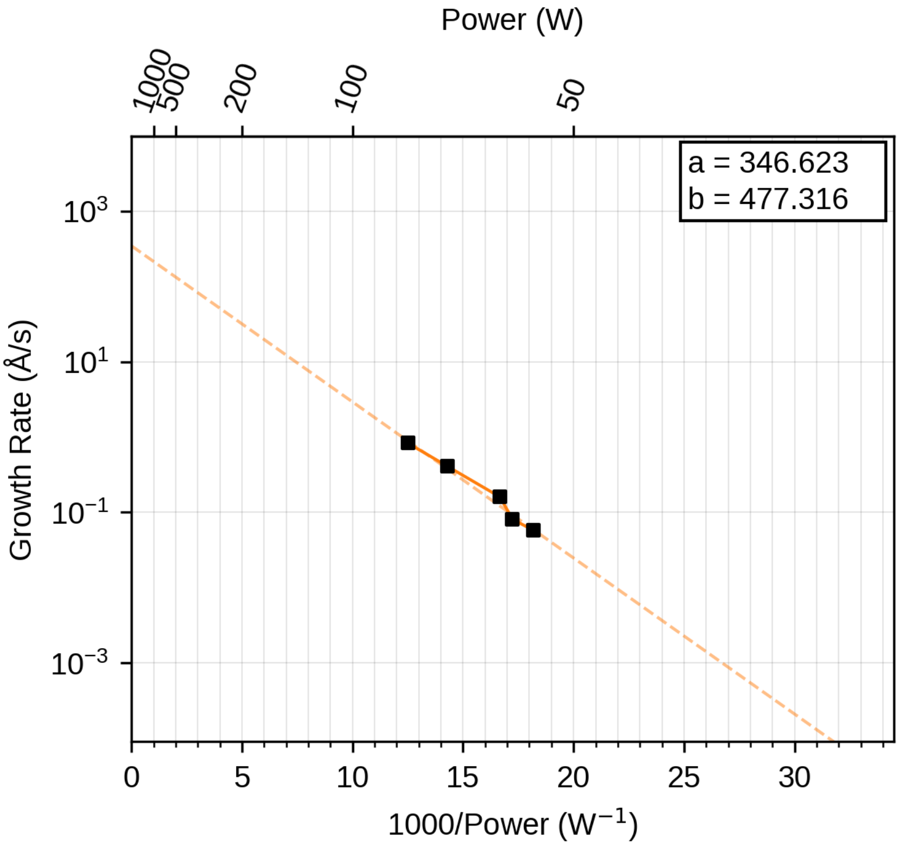

Figure B.12: Growth rate of V as a function of incident laser power. Values of the fit parameters, *a* and *b* are quoted. Incident laser wavelength was $\lambda = 1030$ nm.

Chromium (Cr)

Physical properties

Thermal Conductivity (W/mK)	93.9
Enthalpy of Vaporization (kJ/mol)[123]	347
Reflectivity at laser wavelength[92]	0.58
Melting point (K)	2180
Material Class	Sublimating
Source Diameter (mm)	3

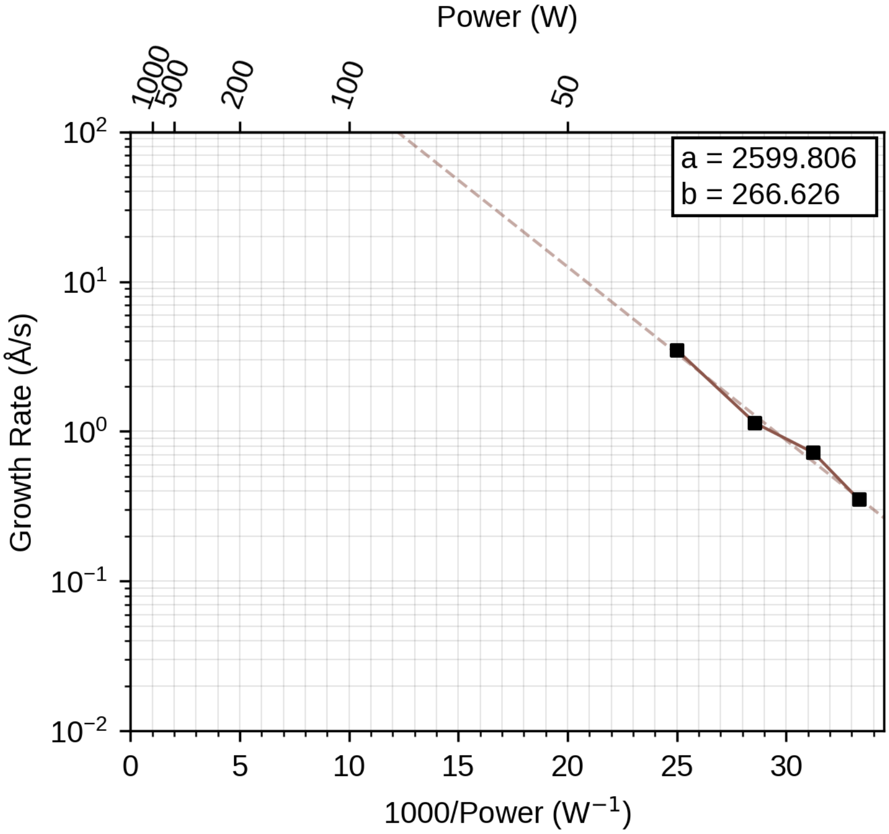

Figure B.13: Growth rate of Cr as a function of incident laser power. Values of the fit parameters, a and b are quoted. Incident laser wavelength was $\lambda = 1030\,\text{nm}$.

Manganese (Mn)

Physical properties

Thermal Conductivity (W/mK)	7.81
Enthalpy of Vaporization (kJ/mol)[123]	225
Reflectivity at laser wavelength[92]	0.66
Melting point (K)	1519
Material Class	Sublimating
Source Diameter (mm)	3

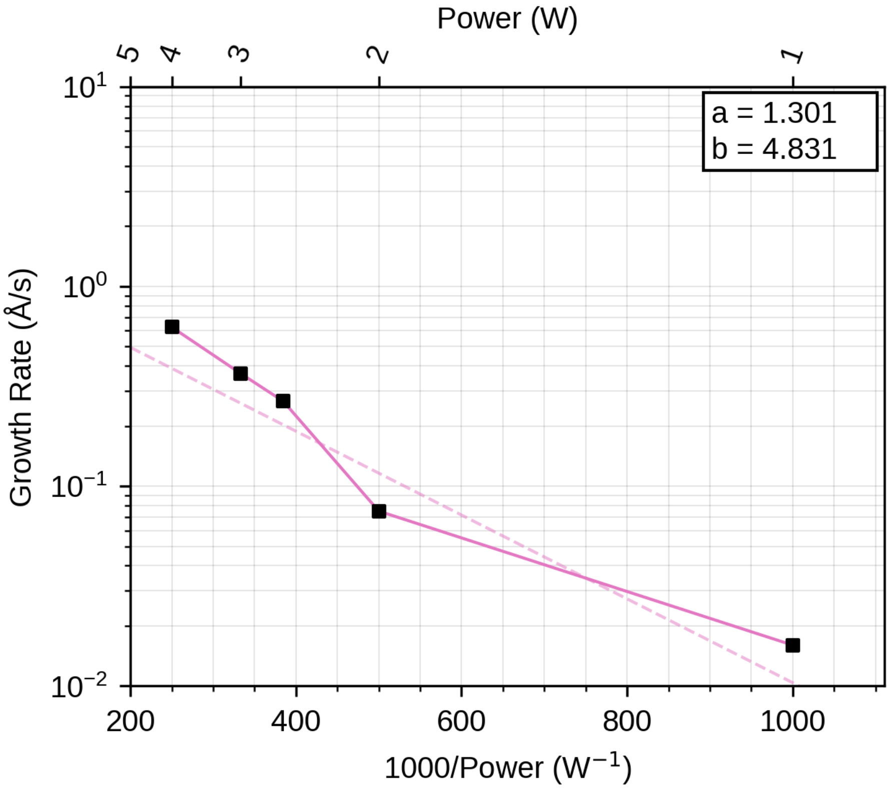

Figure B.14: Growth rate of Mn as a function of incident laser power. Values of the fit parameters, a and b are quoted. Incident laser wavelength was $\lambda = 1030\,\mathrm{nm}$.

Iron (Fe)

Physical properties

Thermal Conductivity (W/mK)	80.4
Enthalpy of Vaporization (kJ/mol) [123]	354
Reflectivity at laser wavelength [92]	0.88
Melting point (K)	1811
Material Class	Free-standing
Source Diameter (mm)	2, 3, 12.7

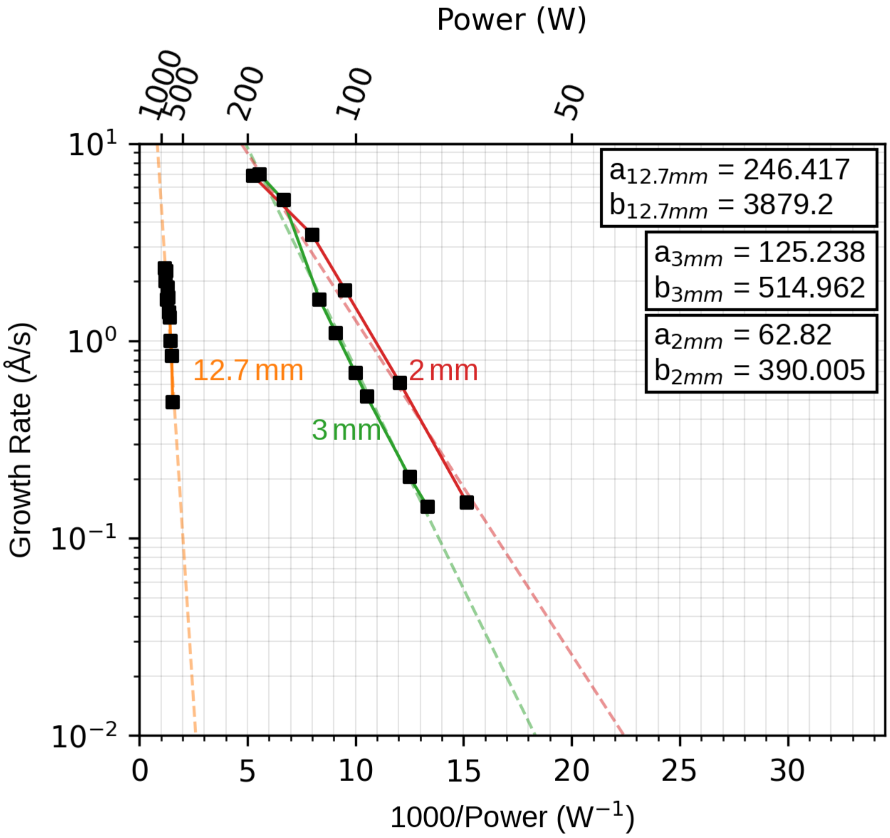

Figure B.15: Growth rate of Fe as a function of incident laser power. Values of the fit parameters, a and b are quoted. Incident laser wavelength was λ = 515 nm.

Cobalt (Co)

Physical properties

Thermal Conductivity (W/mK)	100
Enthalpy of Vaporization (kJ/mol)[123]	390
Reflectivity at laser wavelength[92]	0.76
Melting point (K)	1768
Material Class	Free-standing
Source Diameter (mm)	12.7 (4 mm length)

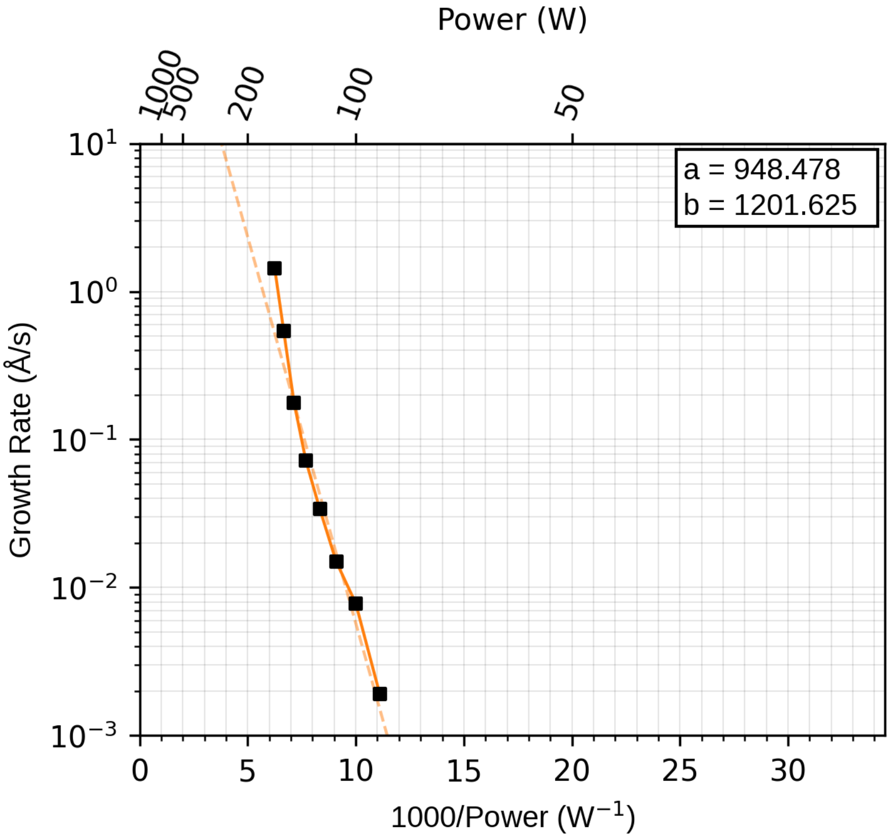

Figure B.16: Growth rate of Co as a function of incident laser power. Values of the fit parameters, a and b are quoted. Incident laser wavelength was λ = 1030 nm.

Nickel (Ni)

Physical properties

Thermal Conductivity (W/mK)	90.9
Enthalpy of Vaporization (kJ/mol)[123]	379
Reflectivity at laser wavelength[92]	0.77
Melting point (K)	1728
Material Class	Free-standing
Source Diameter (mm)	12.7 (4 mm length)

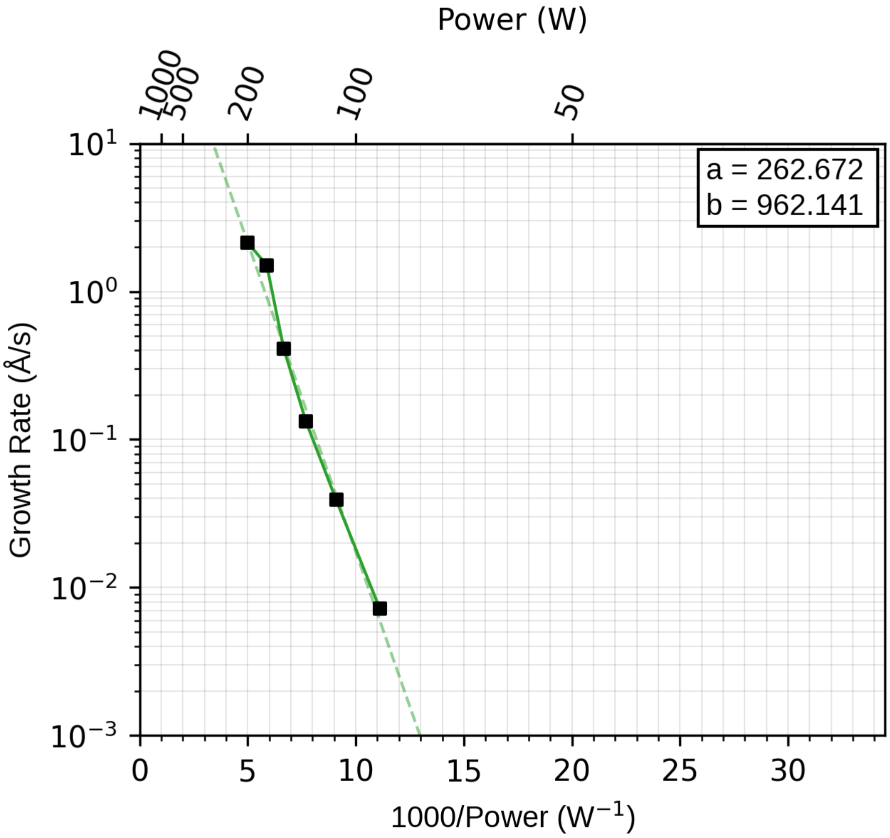

Figure B.17: Growth rate of Ni as a function of incident laser power. Values of the fit parameters, *a* and *b* are quoted. Incident laser wavelength was $\lambda = 1030$ nm.

Copper (Cu)

Physical properties

Thermal Conductivity (W/mK)	401
Enthalpy of Vaporization (kJ/mol)[123]	305
Reflectivity at laser wavelength[67]	0.97
Melting point (K)	1357.77
Material Class	Free-standing
Source Diameter (mm)	12.7

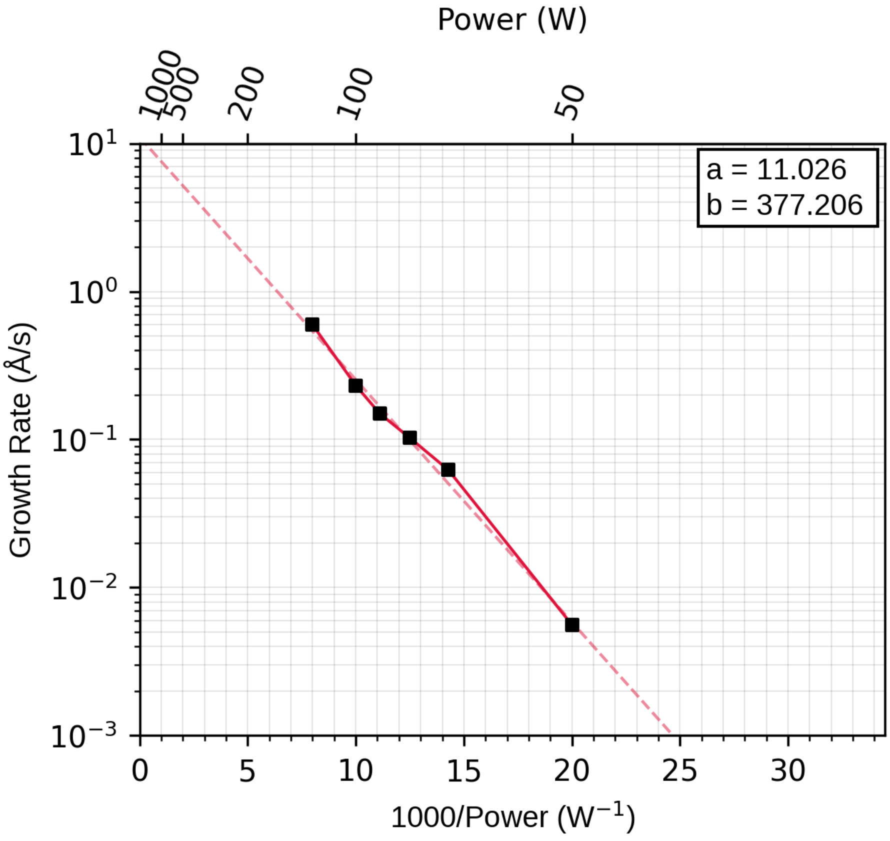

Figure B.18: Growth rate of Cu as a function of incident laser power. Values of the fit parameters, a and b are quoted. Incident laser wavelength was $\lambda = 515\,\text{nm}$.

Zinc (Zn)

Physical properties

Thermal Conductivity (W/mK)	116
Enthalpy of Vaporization (kJ/mol) [123]	115
Reflectivity at laser wavelength [67]	0.88
Melting point (K)	692.68
Material Class	Free-standing
Source Diameter (mm)	12.7

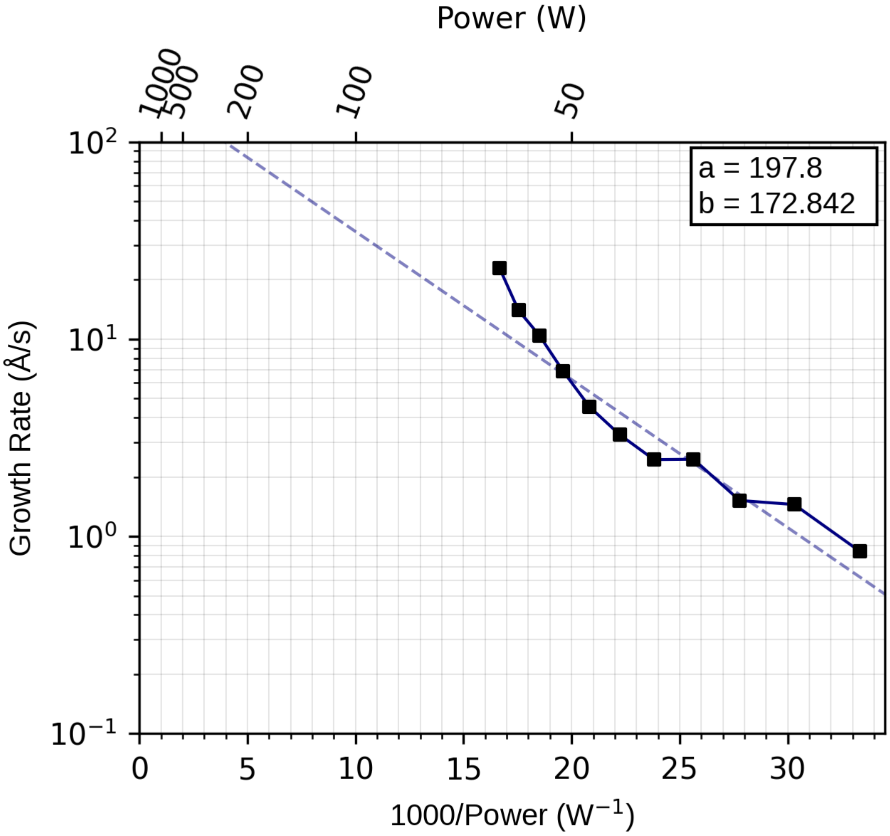

Figure B.19: Growth rate of Zn as a function of incident laser power. Values of the fit parameters, *a* and *b* are quoted. Incident laser wavelength was $\lambda =$ 515 nm.

Gallium (Ga)

Physical properties

Thermal Conductivity (W/mK)	40.6
Enthalpy of Vaporization (kJ/mol)[123]	256
Reflectivity at laser wavelength[127]	0.8
Melting point (K)	302.91
Material Class	Crucible
Source Diameter (mm)	N/A

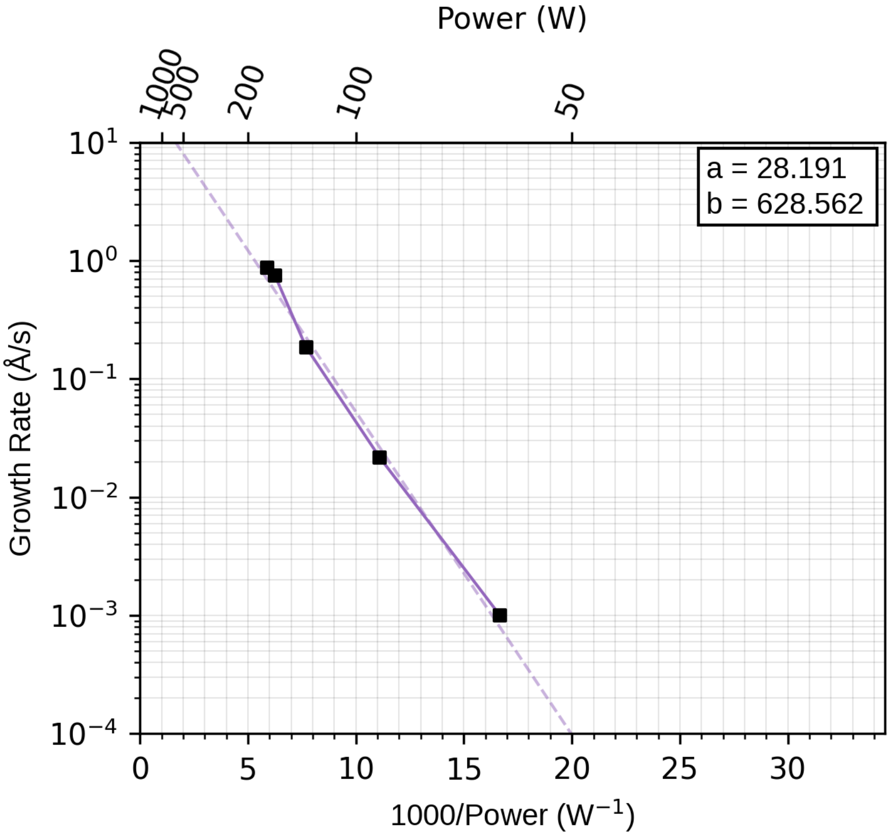

Figure B.20: Growth rate of Ga as a function of incident laser power. Values of the fit parameters, a and b are quoted. Incident laser wavelength was $\lambda = 515\,\text{nm}$.

Germanium (Ge)

Physical properties

Thermal Conductivity (W/mK)	60.2
Enthalpy of Vaporization (kJ/mol)[123]	330
Reflectivity at laser wavelength[128]	0.39
Melting point (K)	1211.4
Material Class	Crucible (Ta Crucible)
Source Diameter (mm)	N/A

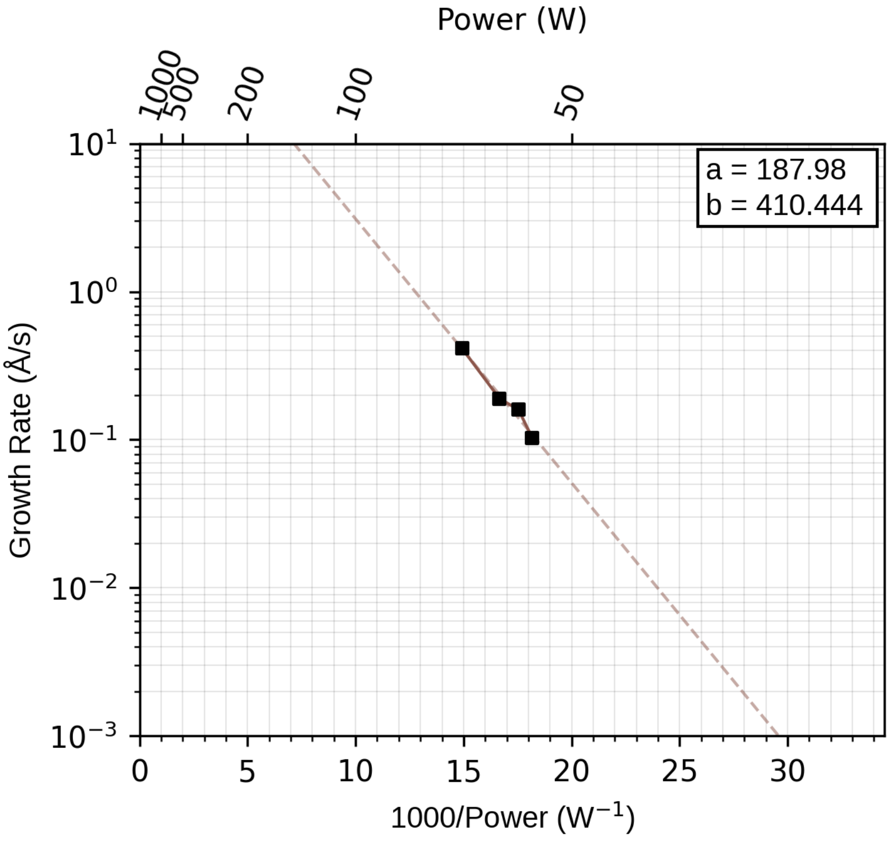

Figure B.21: Growth rate of Ge as a function of incident laser power. Values of the fit parameters, a and b are quoted. Incident laser wavelength was $\lambda = 515\,\text{nm}$.

Strontium (Sr)

Physical properties

Thermal Conductivity (W/mK)	35.4
Enthalpy of Vaporization (kJ/mol)[123]	141
Reflectivity at laser wavelength [129]	0.8
Melting point (K)	1050
Material Class	Sublimating
Source Diameter (mm)	granulate

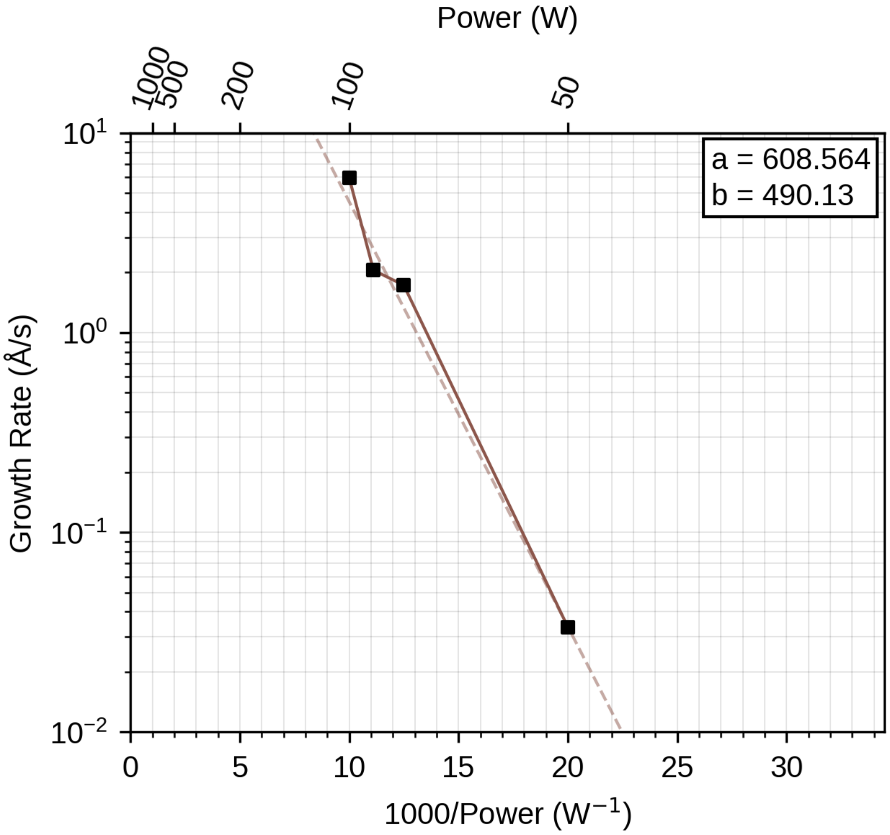

Figure B.22: Growth rate of Sr as a function of incident laser power. Values of the fit parameters, *a* and *b* are quoted. Incident laser wavelength was $\lambda = 515\,\text{nm}$.

Yttrium (Y)

Physical properties

Thermal Conductivity (W/mK)	17.2
Enthalpy of Vaporization (kJ/mol) [123]	363
Reflectivity at laser wavelength [129]	0.8
Melting point (K)	1799
Material Class	Free-standing
Source Diameter (mm)	5

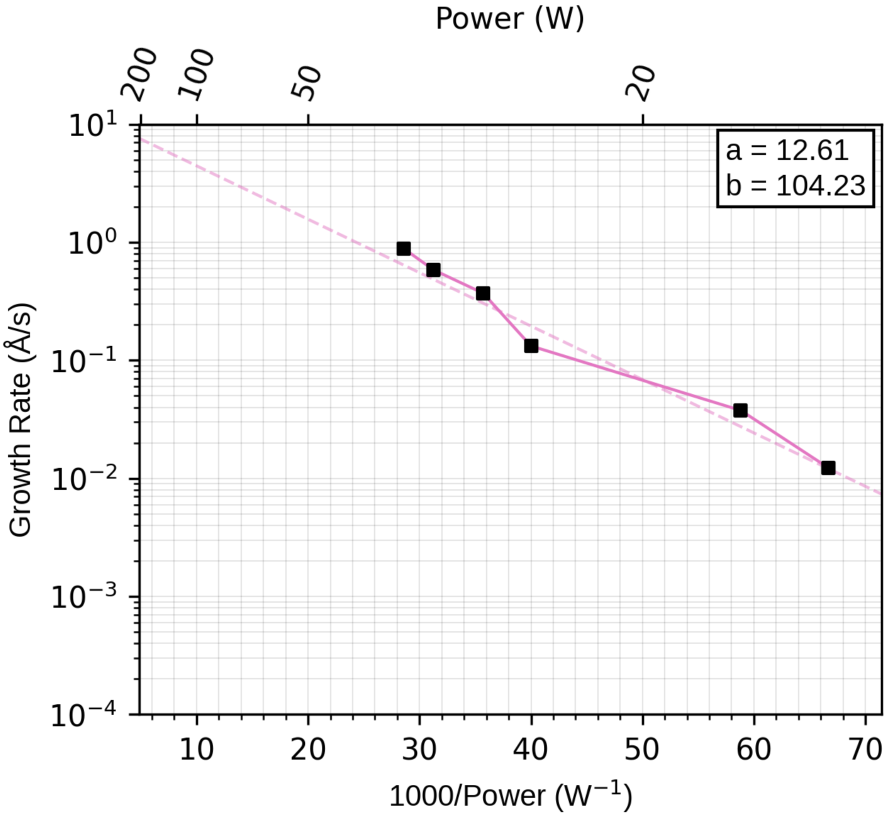

Figure B.23: Growth rate of Y as a function of incident laser power. Values of the fit parameters, *a* and *b* are quoted. Incident laser wavelength was $\lambda = 515\,\text{nm}$.

Zirconium (Zr)

Physical properties

Thermal Conductivity (W/mK)	22.6
Enthalpy of Vaporization (kJ/mol)[123]	591
Reflectivity at laser wavelength [92]	0.598
Melting point (K)	2125
Material Class	Free-standing
Source Diameter (mm)	12.7

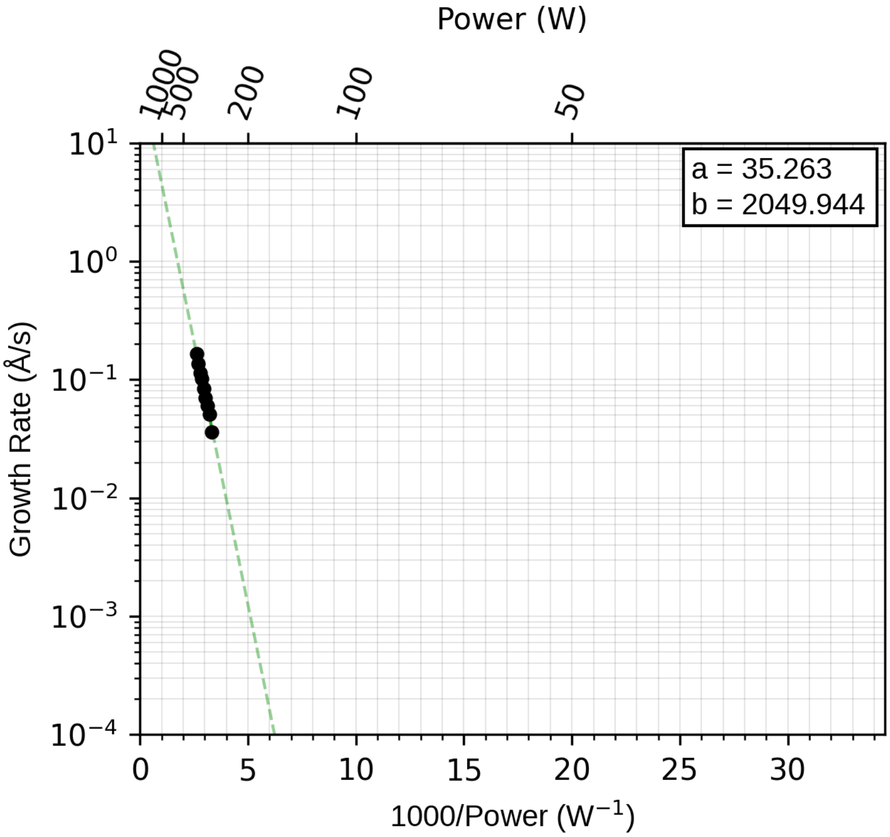

Figure B.24: Growth rate of Zr as a function of incident laser power. Values of the fit parameters, a and b are quoted. Incident laser wavelength was $\lambda = 1030\,\text{nm}$.

Niobium (Nb)

Physical properties

Thermal Conductivity (W/mK)	53.7
Enthalpy of Vaporization (kJ/mol) [123]	682
Reflectivity at laser wavelength [92]	0.809
Melting point (K)	2750
Material Class	Free-standing
Source Diameter (mm)	3

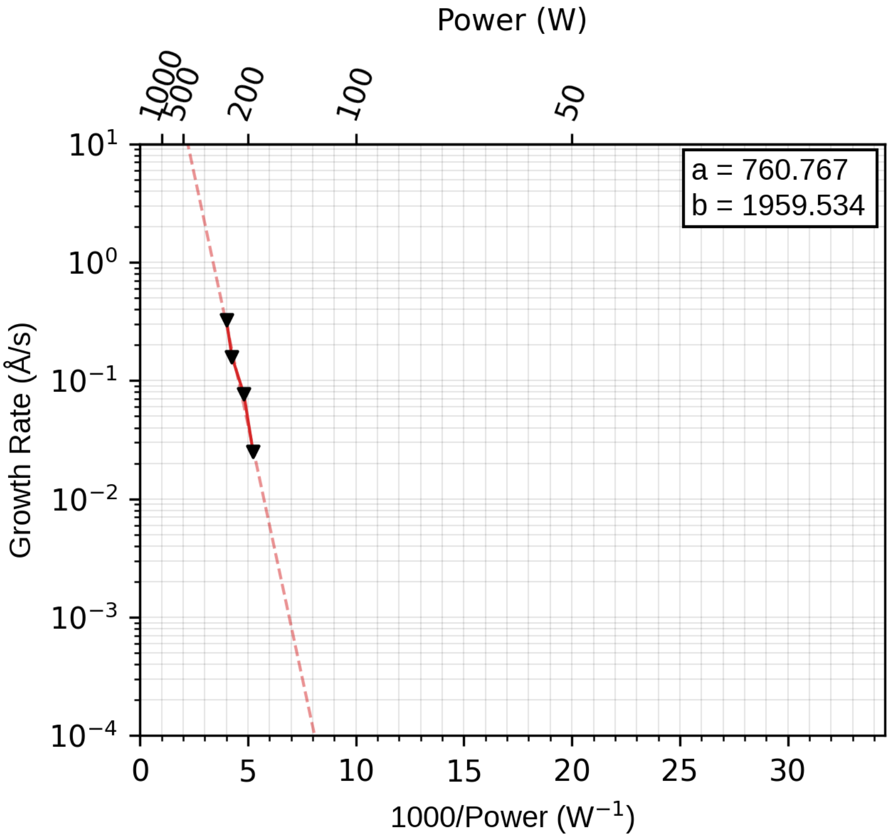

Figure B.25: Growth rate of Nb as a function of incident laser power. Values of the fit parameters, a and b are quoted. Incident laser wavelength was $\lambda = 1030\,\text{nm}$.

Molybdenum (Mo)

Physical properties

Thermal Conductivity (W/mK)	138
Enthalpy of Vaporization (kJ/mol) [123]	617
Reflectivity at laser wavelength [92]	0.92
Melting point (K)	2896
Material Class	Free-standing
Source Diameter (mm)	3, 4, 5, 12

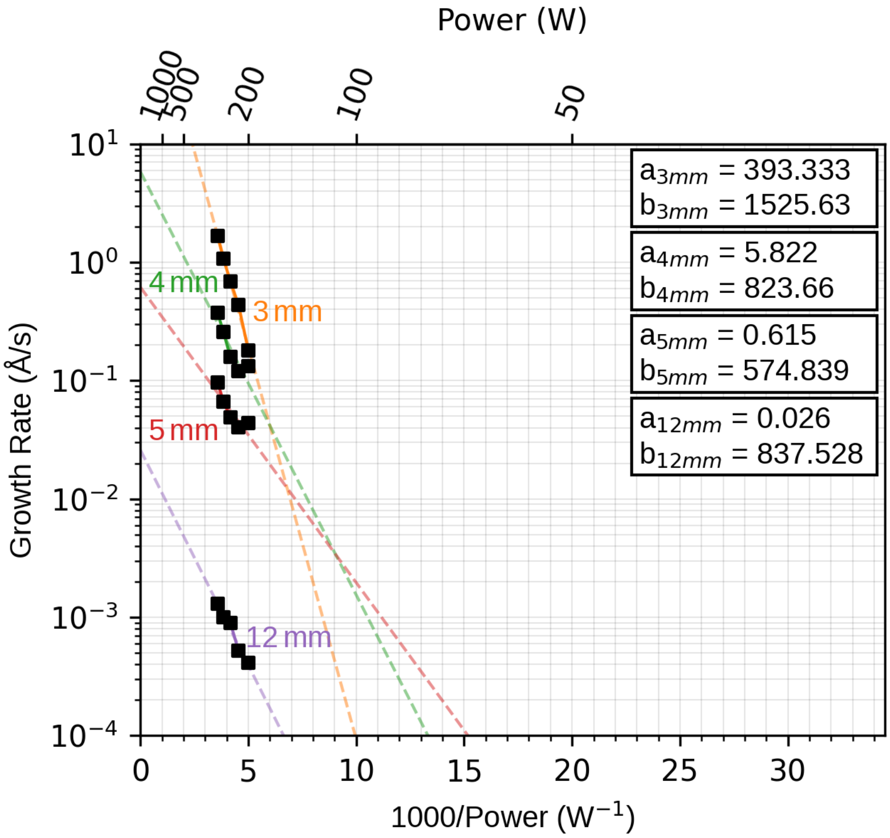

Figure B.26: Growth rate of Mo as a function of incident laser power. Values of the fit parameters, a and b are quoted. Incident laser wavelength was λ = 1030 nm.

Ruthenium (Ru)

Physical properties

Thermal Conductivity (W/mK)	117
Enthalpy of Vaporization (kJ/mol) [123]	619
Reflectivity at laser wavelength [130]	0.7
Melting point (K)	2607
Material Class	Free-standing
Source Diameter (mm)	3

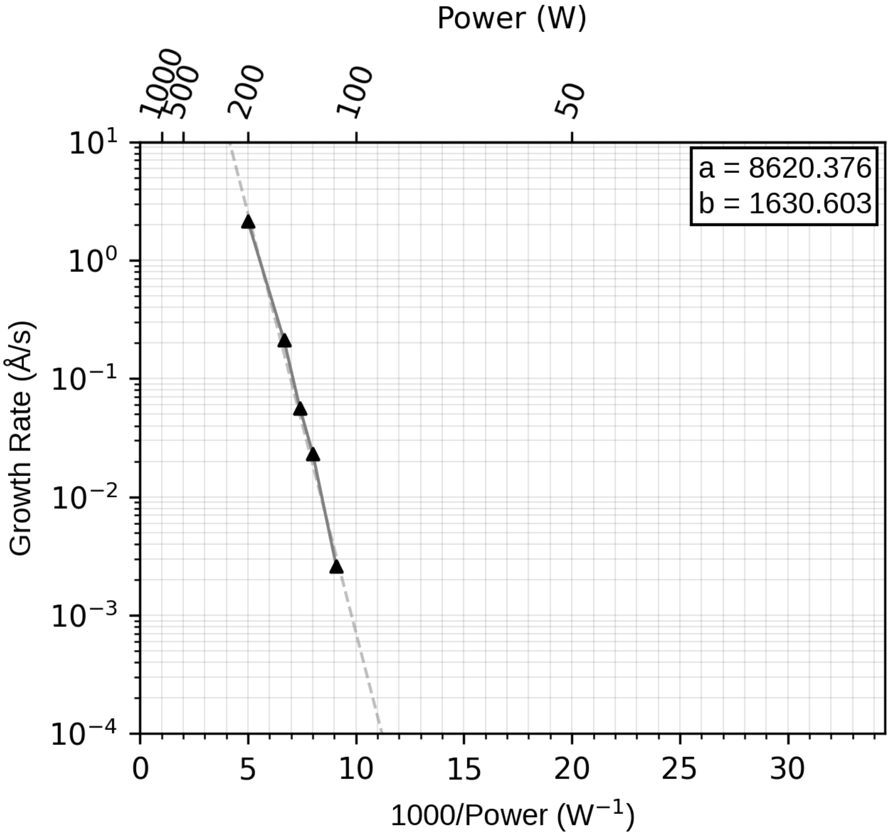

Figure B.27: Growth rate of Ru as a function of incident laser power. Values of the fit parameters, a and b are quoted. Incident laser wavelength was $\lambda = 1030\,\text{nm}$.

Rhodium (Rh)

Physical properties

Thermal Conductivity (W/mK)	150
Enthalpy of Vaporization (kJ/mol) [123]	493
Reflectivity at laser wavelength [130]	0.83
Melting point (K)	2237
Material Class	Free-standing
Source Diameter (mm)	3

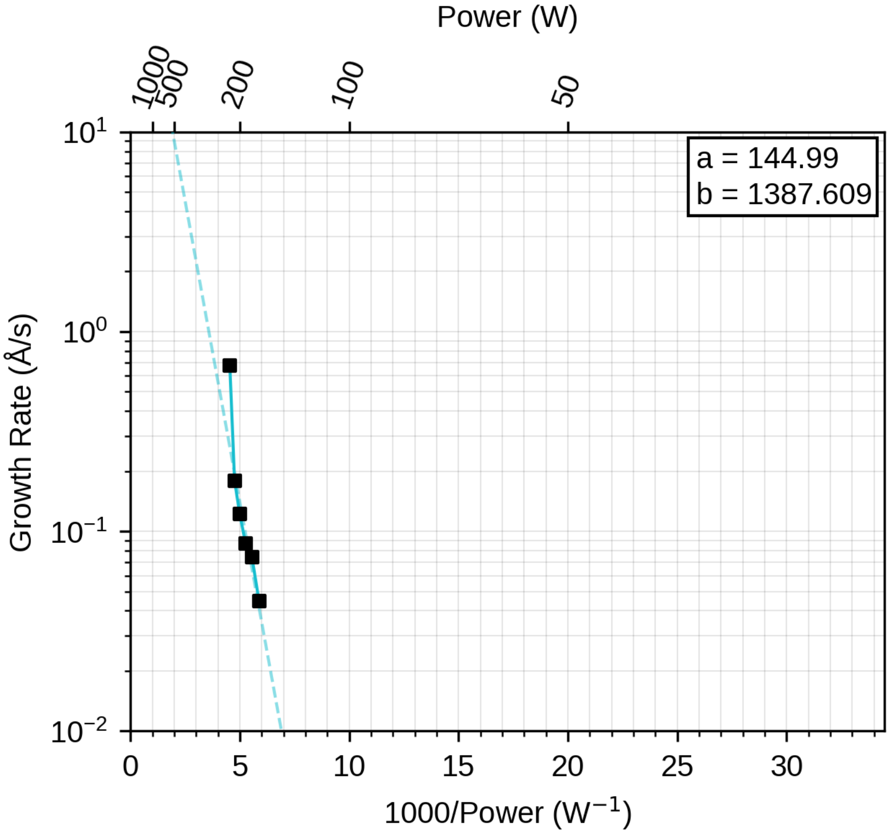

Figure B.28: Growth rate of Rh as a function of incident laser power. Values of the fit parameters, a and b are quoted. Incident laser wavelength was λ = 1030 nm.

Palladium (Pd)

Physical properties

Thermal Conductivity (W/mK)	71.8
Enthalpy of Vaporization (kJ/mol) [123]	358
Reflectivity at laser wavelength [92]	0.8
Melting point (K)	1828.05
Material Class	Free-standing
Source Diameter (mm)	6.35

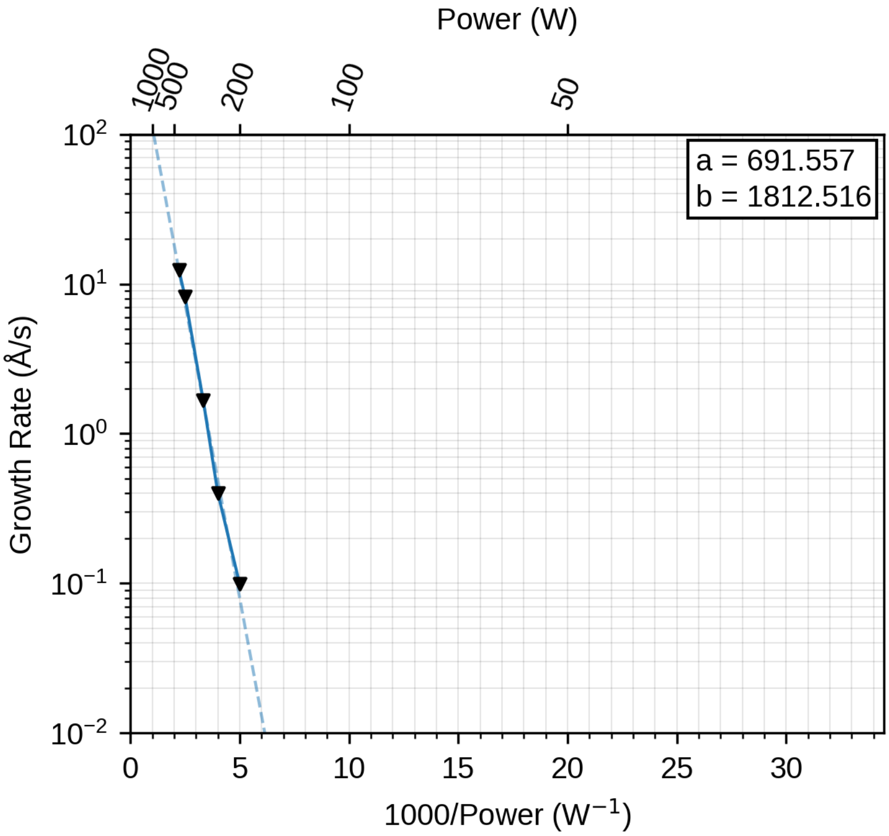

Figure B.29: Growth rate of Pd as a function of incident laser power. Values of the fit parameters, a and b are quoted. Incident laser wavelength was $\lambda =$ 1030 nm.

Silver (Ag)

Physical properties

Thermal Conductivity (W/mK)	429
Enthalpy of Vaporization (kJ/mol) [123]	254
Reflectivity at laser wavelength [92]	0.997
Melting point (K)	1234
Material Class	Crucible
Source Diameter (mm)	N/A

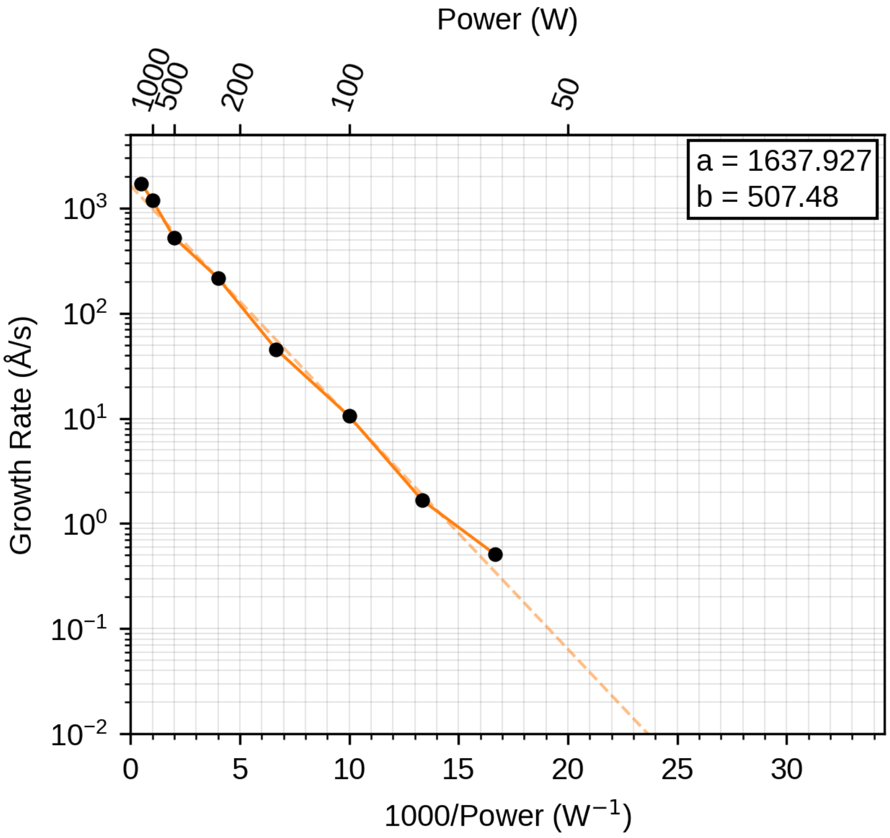

Figure B.30: Growth rate of Ag as a function of incident laser power. Values of the fit parameters, a and b are quoted. Incident laser wavelength was λ = 1030 nm.

Indium (In)

Physical properties

Thermal Conductivity (W/mK)	81.8
Enthalpy of Vaporization (kJ/mol)[123]	225
Reflectivity at laser wavelength [92]	0.876
Melting point (K)	429
Material Class	Crucible
Source Diameter (mm)	N/A

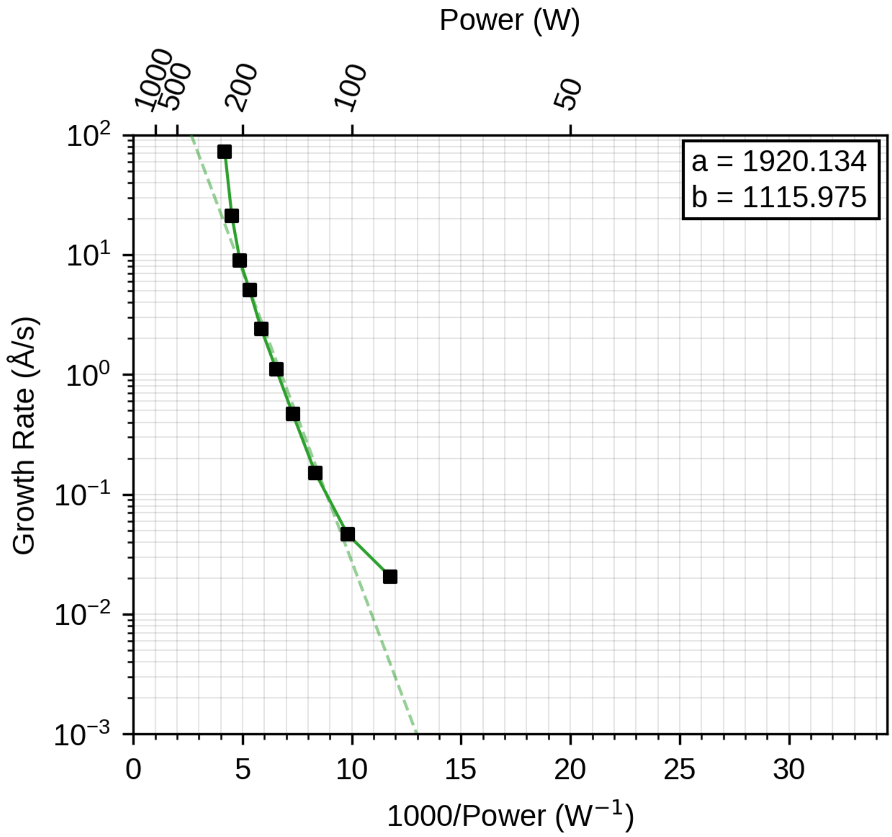

Figure B.31: Growth rate of In as a function of incident laser power. Values of the fit parameters, a and b are quoted. Incident laser wavelength was $\lambda = 515\,\text{nm}$.

Tin (Sn)

Physical properties

Thermal Conductivity (W/mK)	66.8
Enthalpy of Vaporization (kJ/mol) [123]	296
Reflectivity at laser wavelength [92]	0.813
Melting point (K)	505
Material Class	Crucible
Source Diameter (mm)	N/A

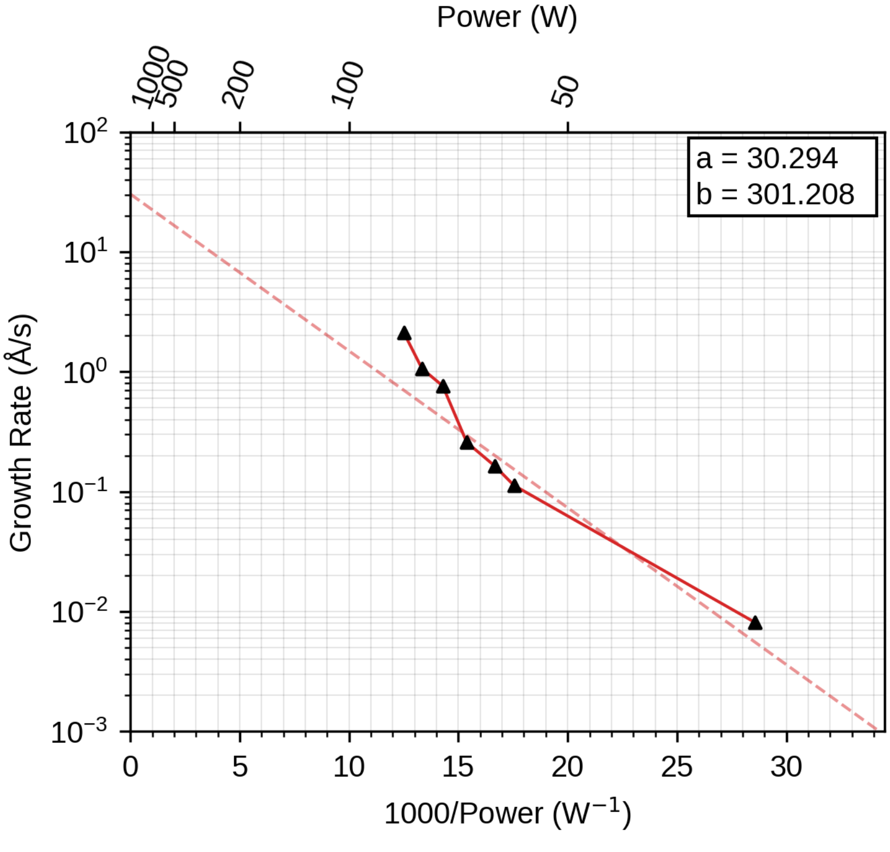

Figure B.32: Growth rate of Sn as a function of incident laser power. Values of the fit parameters, a and b are quoted. Incident laser wavelength was $\lambda = 1030\,\text{nm}$.

Antimony (Sb)

Physical properties

Thermal Conductivity (W/mK)	24.4
Enthalpy of Vaporization (kJ/mol) [123]	193
Reflectivity at laser wavelength [92]	0.813
Melting point (K)	903.8
Material Class	Sublimating
Source Diameter (mm)	granulate

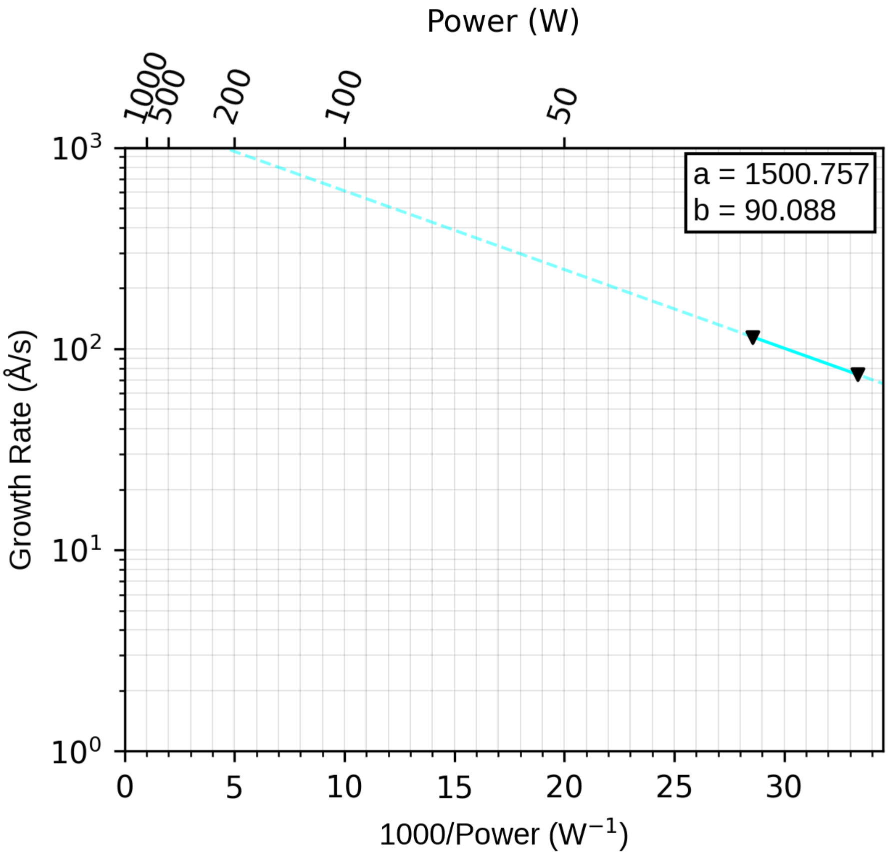

Figure B.33: Growth rate of Sb as a function of incident laser power. Values of the fit parameters, a and b are quoted. Incident laser wavelength was $\lambda = 515\,\mathrm{nm}$.

Lanthanum (La)

Physical properties

Thermal Conductivity (W/mK)	13.4
Enthalpy of Vaporization (kJ/mol) [123]	400
Reflectivity at laser wavelength [92]	-
Melting point (K)	1193
Material Class	Crucible
Source Diameter (mm)	N/A

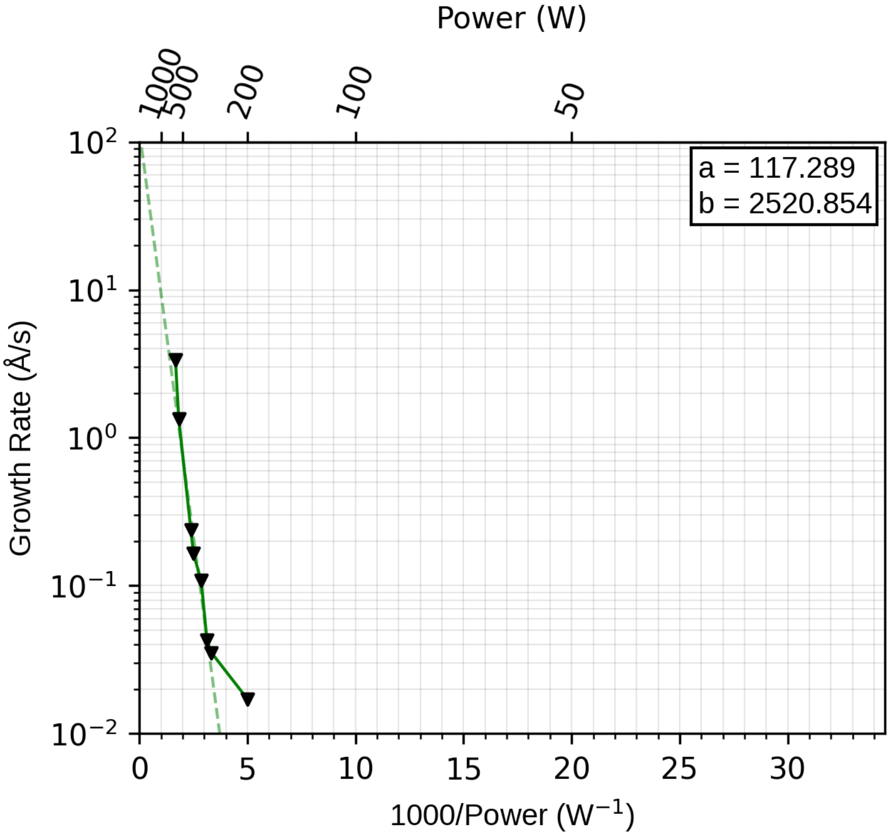

Figure B.34: Growth rate of La as a function of incident laser power. Values of the fit parameters, a and b are quoted. Incident laser wavelength was λ = 515 nm.

Cerium (Ce)

Physical properties

Thermal Conductivity (W/mK)	11.3
Enthalpy of Vaporization (kJ/mol) [123]	398
Reflectivity at laser wavelength [131]	0.87
Melting point (K)	1068
Material Class	Crucible
Source Diameter (mm)	N/A

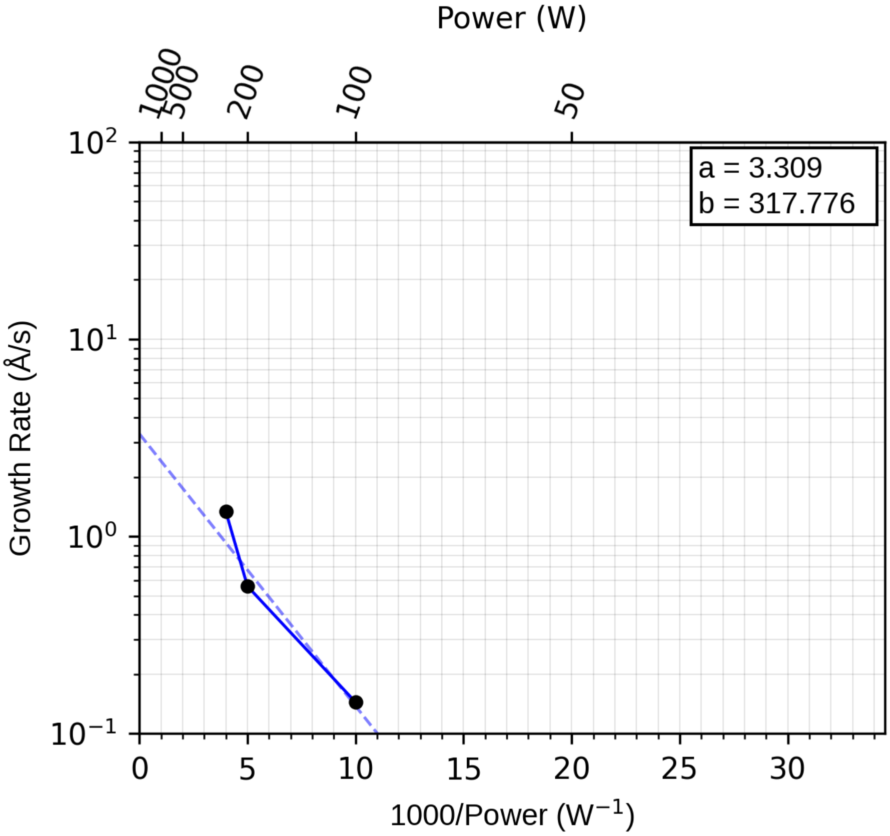

Figure B.35: Growth rate of Ce as a function of incident laser power. Values of the fit parameters, a and b are quoted. Incident laser wavelength was $\lambda = 515\,\text{nm}$.

Praseodymium (Pr)

Physical properties

Thermal Conductivity (W/mK)	12.5
Enthalpy of Vaporization (kJ/mol) [123]	331
Reflectivity at laser wavelength [132]	0.7
Melting point (K)	1208
Material Class	Crucible (Ta crucible)
Source Diameter (mm)	N/A

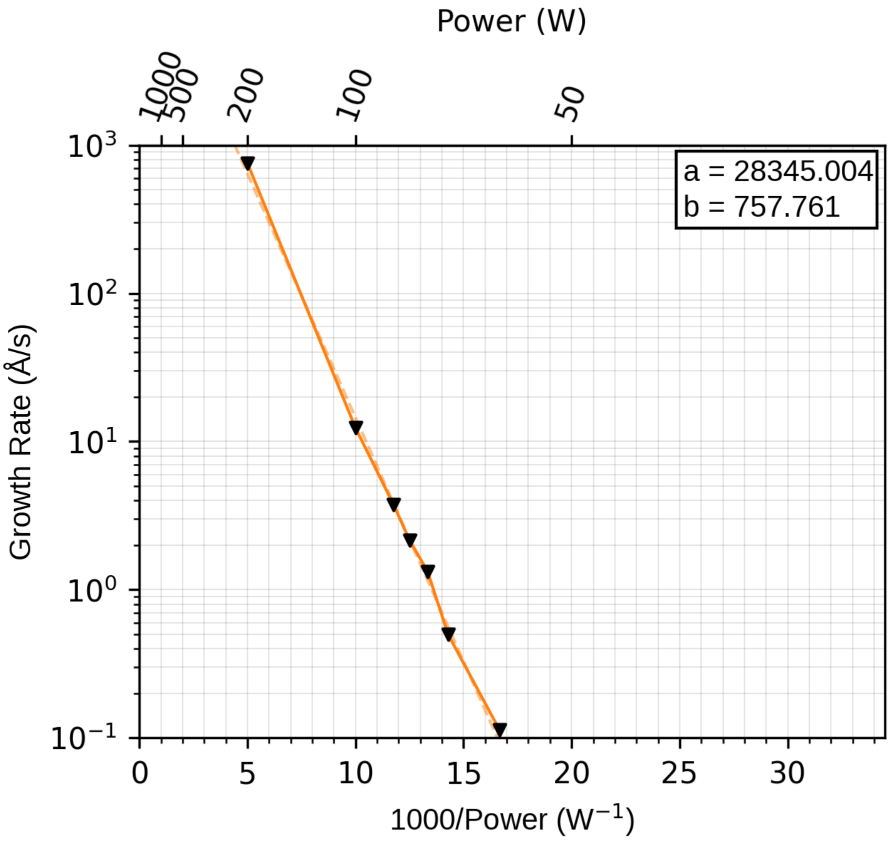

Figure B.36: Growth rate of Pr as a function of incident laser power. Values of the fit parameters, a and b are quoted. Incident laser wavelength was $\lambda = 515$ nm.

Europium (Eu)

Physical properties

Thermal Conductivity (W/mK)	12.5
Enthalpy of Vaporization (kJ/mol) [123]	176
Reflectivity at laser wavelength	-
Melting point (K)	1099
Material Class	Free-standing
Source Diameter (mm)	3

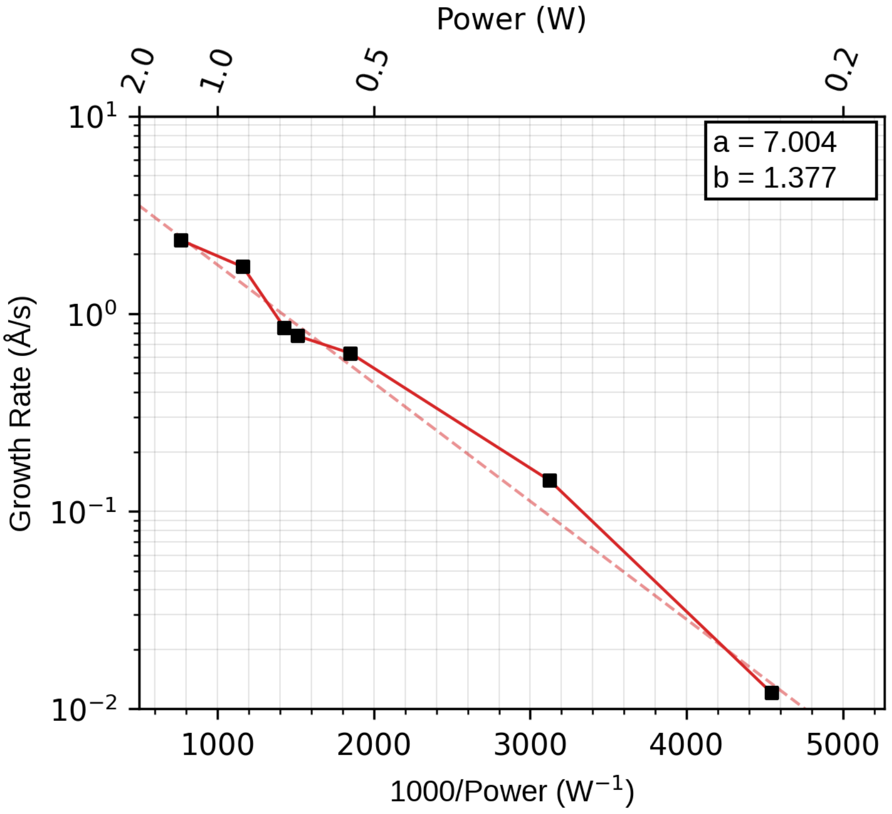

Figure B.37: Growth rate of Eu as a function of incident laser power. Values of the fit parameters, a and b are quoted. Incident laser wavelength was λ = 515 nm.

Gadolinium (Gd)

Physical properties

Thermal Conductivity (W/mK)	10.6
Enthalpy of Vaporization (kJ/mol) [123]	301
Reflectivity at laser wavelength	-
Melting point (K)	1585
Material Class	Free-standing
Source Diameter (mm)	12.7

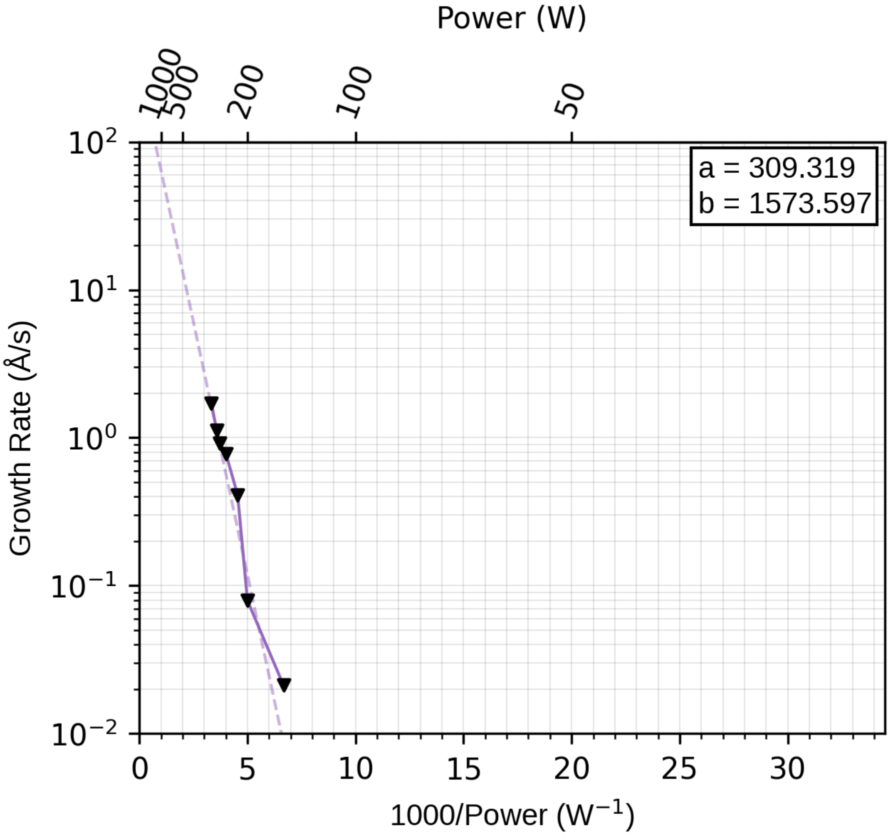

Figure B.38: Growth rate of Gd as a function of incident laser power. Values of the fit parameters, *a* and *b* are quoted. Incident laser wavelength was λ = 515 nm.

Erbium (Er)

Physical properties

Thermal Conductivity (W/mK)	14.5
Enthalpy of Vaporization (kJ/mol) [123]	280
Reflectivity at laser wavelength	-
Melting point (K)	1802
Material Class	Sublimating
Source Diameter (mm)	3

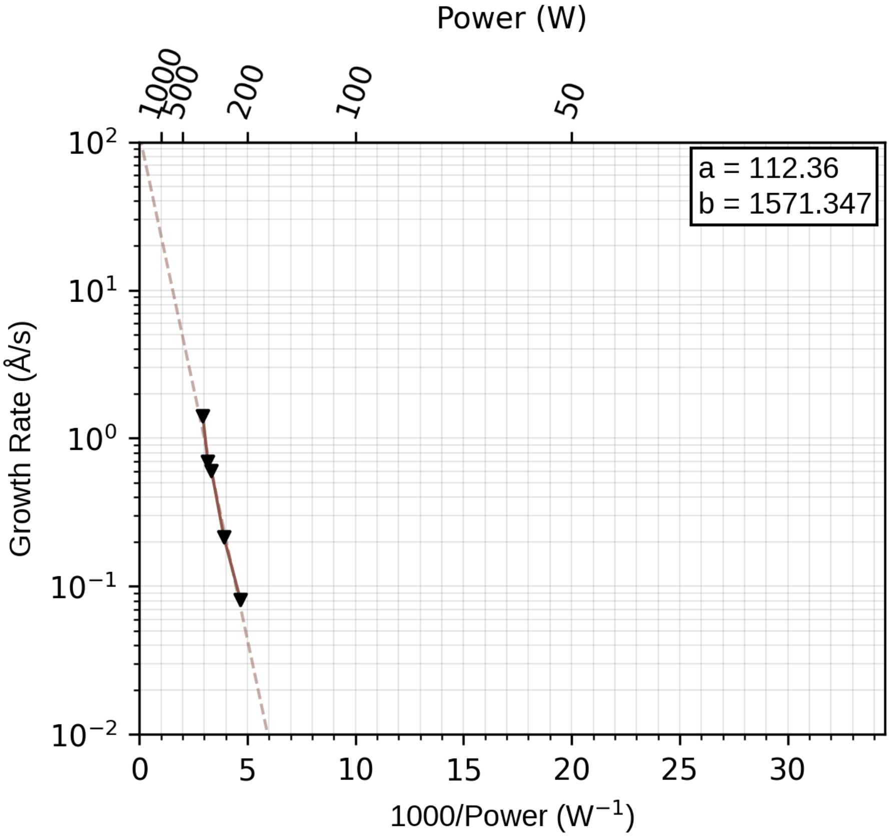

Figure B.39: Growth rate of Er as a function of incident laser power. Values of the fit parameters, a and b are quoted. Incident laser wavelength was $\lambda = 515\,\text{nm}$.

Thulium (Tm)

Physical properties

Thermal Conductivity (W/mK)	16.9
Enthalpy of Vaporization (kJ/mol) [123]	191
Reflectivity at laser wavelength	-
Melting point (K)	1818
Material Class	Sublimating
Source Diameter (mm)	3

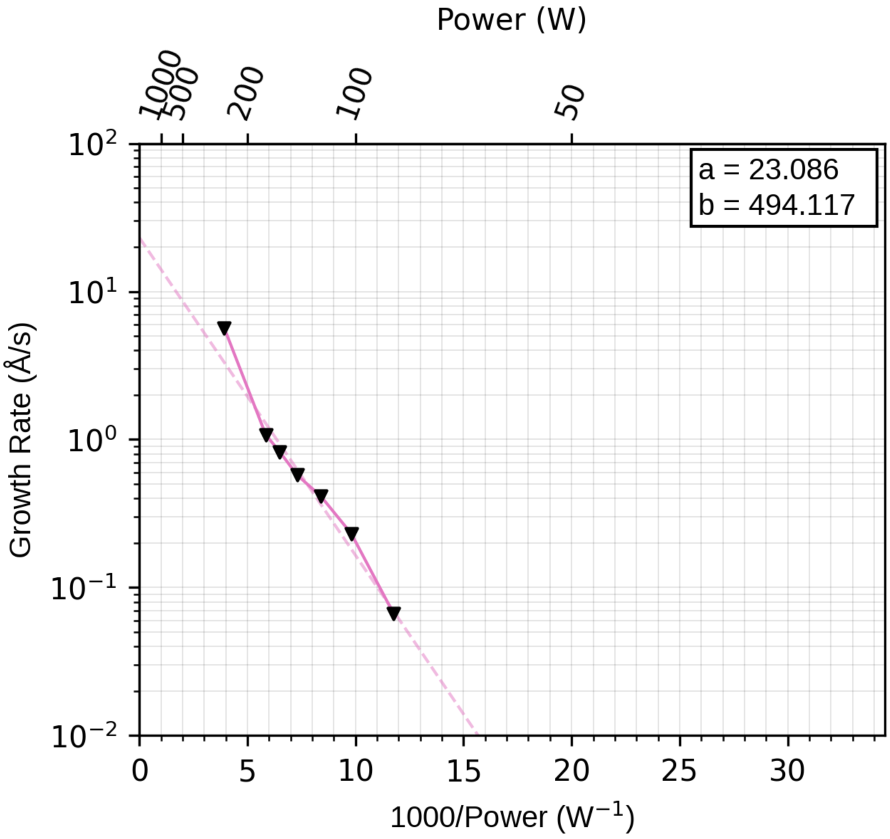

Figure B.40: Growth rate of Tm as a function of incident laser power. Values of the fit parameters, a and b are quoted. Incident laser wavelength was λ = 515 nm.

Ytterbium (Yb)

Physical properties

Thermal Conductivity (W/mK)	38.5
Enthalpy of Vaporization (kJ/mol) [123]	129
Reflectivity at laser wavelength	-
Melting point (K)	1097
Material Class	Sublimating
Source Diameter (mm)	3

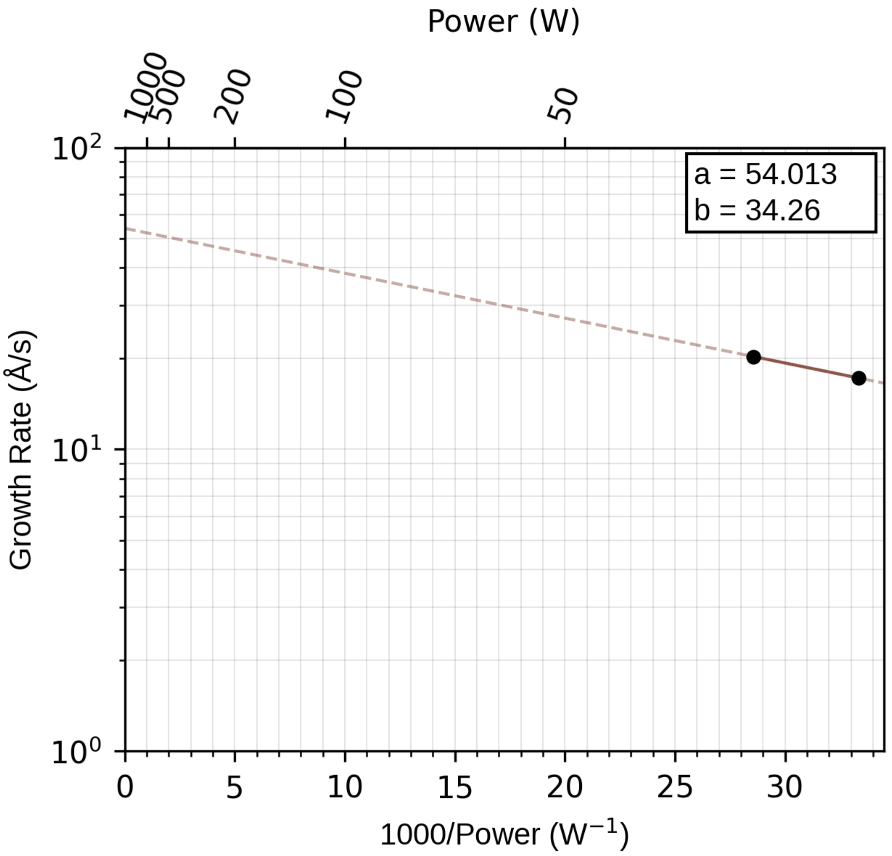

Figure B.41: Growth rate of Yb as a function of incident laser power. Values of the fit parameters, a and b are quoted. Incident laser wavelength was $\lambda = 1030\,\text{nm}$.

Lutetium (Lu)

Physical properties

Thermal Conductivity (W/mK)	16.4
Enthalpy of Vaporization (kJ/mol) [123]	414
Reflectivity at laser wavelength	-
Melting point (K)	1925
Material Class	Free-standing
Source Diameter (mm)	5

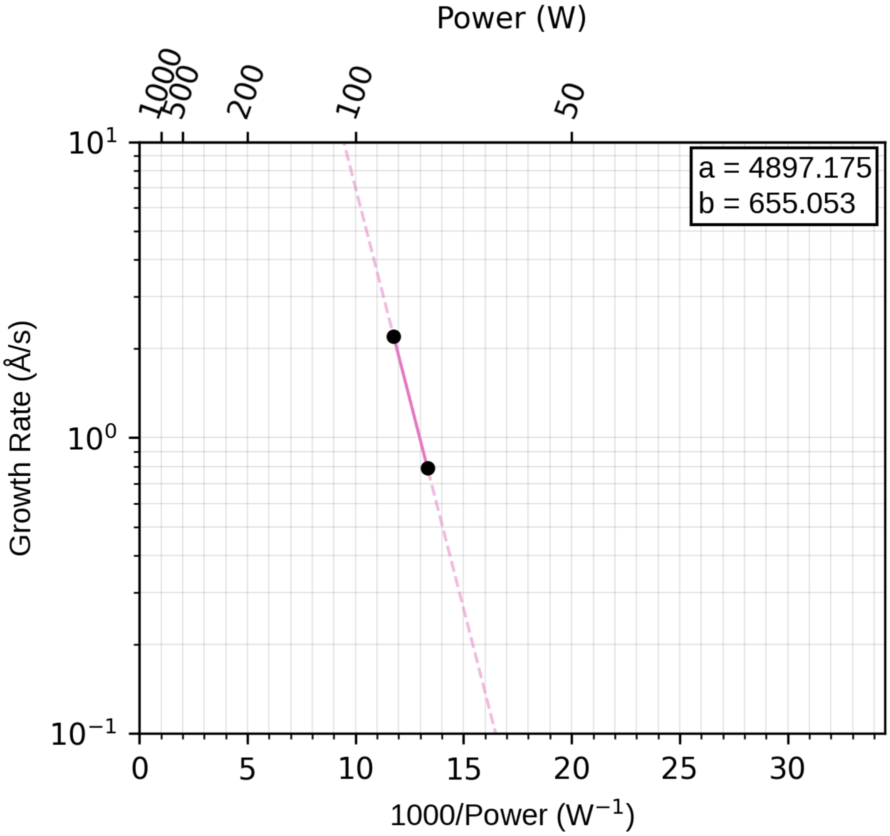

Figure B.42: Growth rate of Lu as a function of incident laser power. Values of the fit parameters, a and b are quoted. Incident laser wavelength was $\lambda = 1030\,\text{nm}$.

Hafnium (Hf)

Physical properties

Thermal Conductivity (W/mK)	23
Enthalpy of Vaporization (kJ/mol) [123]	648
Reflectivity at laser wavelength	-
Melting point (K)	2506
Material Class	Free-standing
Source Diameter (mm)	2

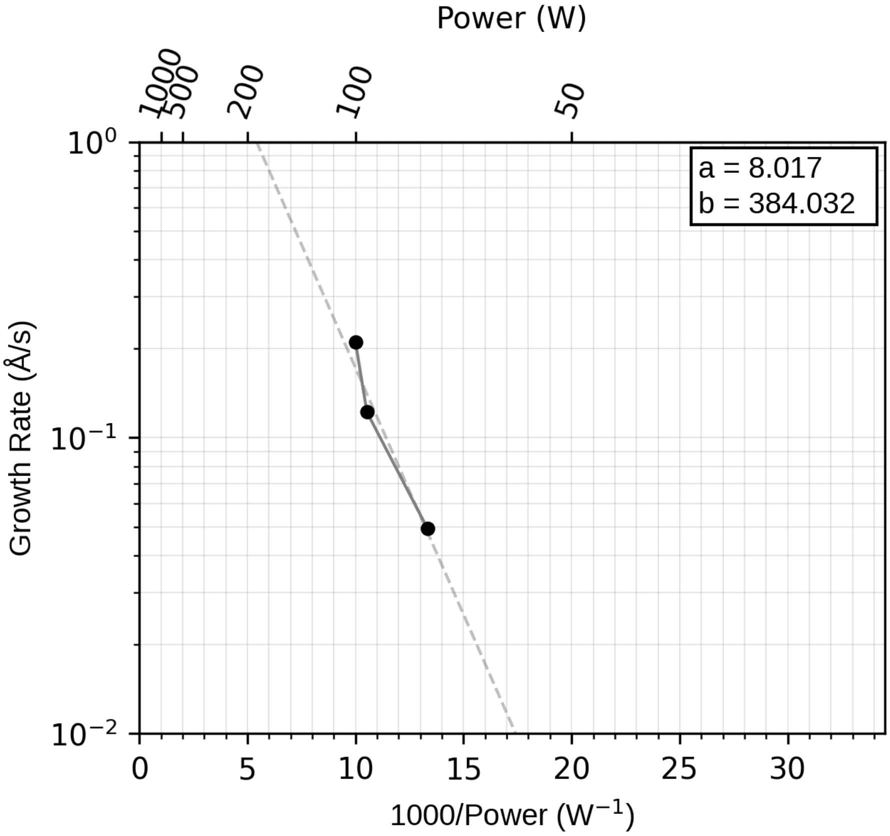

Figure B.43: Growth rate of Hf as a function of incident laser power. Values of the fit parameters, a and b are quoted. Incident laser wavelength was $\lambda = 1030\,\text{nm}$.

Tantalum (Ta)

Physical properties

Thermal Conductivity (W/mK)	57.5
Enthalpy of Vaporization (kJ/mol)[123]	648
Reflectivity at laser wavelength[92]	0.959
Melting point (K)	3290
Material Class	Free-standing
Source Diameter (mm)	2, 3, 4, 5

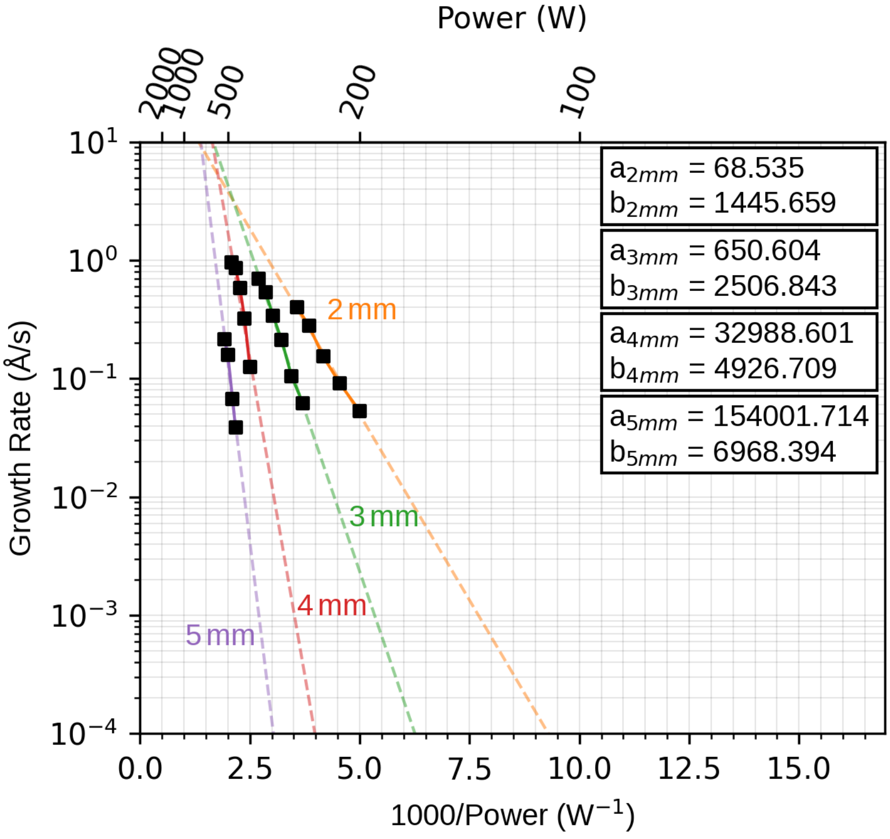

Figure B.44: Growth rate of Ta as a function of incident laser power. Values of the fit parameters, a and b are quoted. Incident laser wavelength was λ = 1030 nm.

Tungsten (W)

Physical properties

Thermal Conductivity (W/mK)	173
Enthalpy of Vaporization (kJ/mol)[123]	774
Reflectivity at laser wavelength[92]	0.94
Melting point (K)	3695
Material Class	Free-standing
Source Diameter (mm)	2, 3

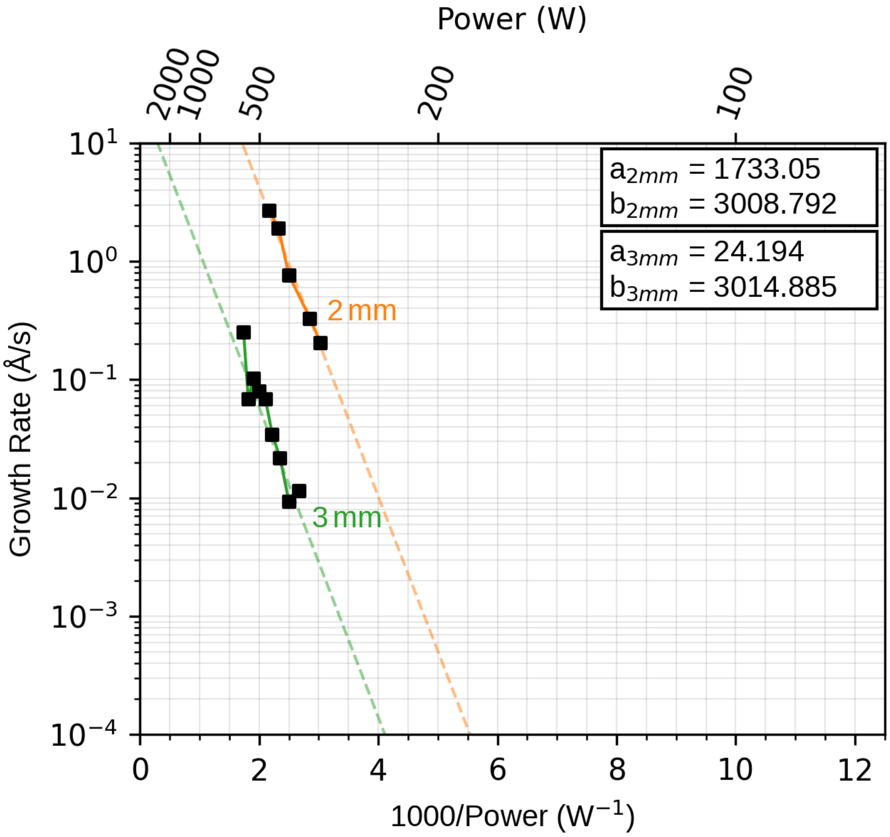

Figure B.45: Growth rate of W as a function of incident laser power. Values of the fit parameters, a and b are quoted. Incident laser wavelength was $\lambda = 1030$ nm.

Rhenium (Re)

Physical properties

Thermal Conductivity (W/mK)	48
Enthalpy of Vaporization (kJ/mol)[123]	707
Reflectivity at laser wavelength[92]	0.94
Melting point (K)	3459
Material Class	Free-standing
Source Diameter (mm)	3

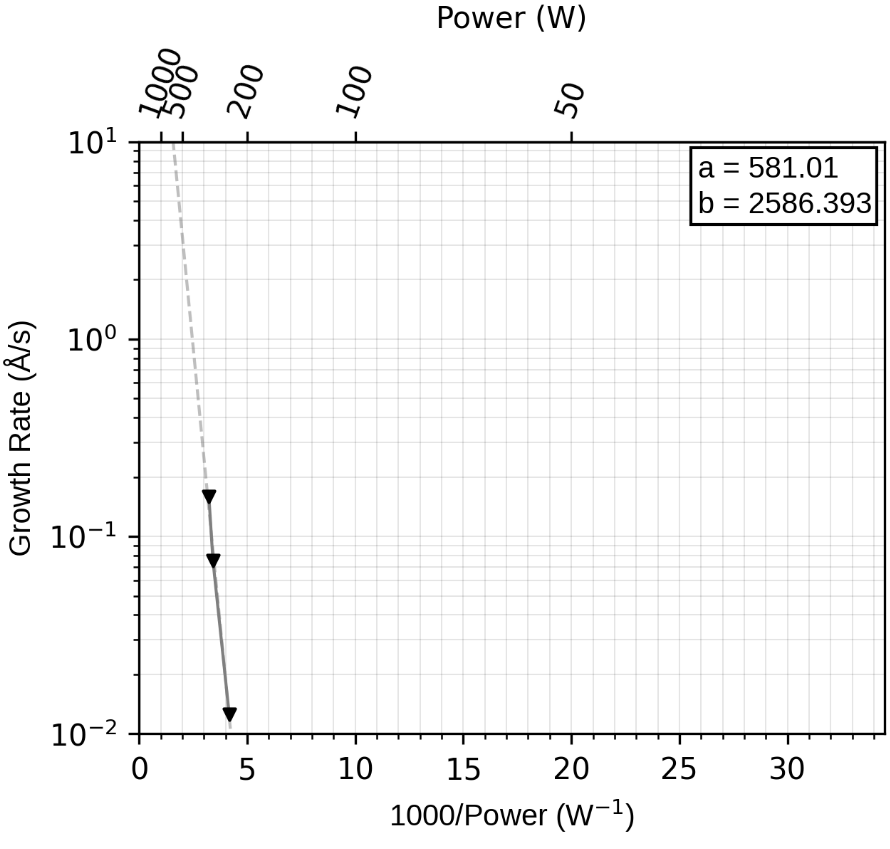

Figure B.46: Growth rate of Re as a function of incident laser power. Values of the fit parameters, *a* and *b* are quoted. Incident laser wavelength was $\lambda = 1030\,\text{nm}$.

Iridium (Ir)

Physical properties

Thermal Conductivity (W/mK)	147
Enthalpy of Vaporization (kJ/mol) [123]	564
Reflectivity at laser wavelength [92]	0.81
Melting point (K)	2719
Material Class	Free-standing
Source Diameter (mm)	3

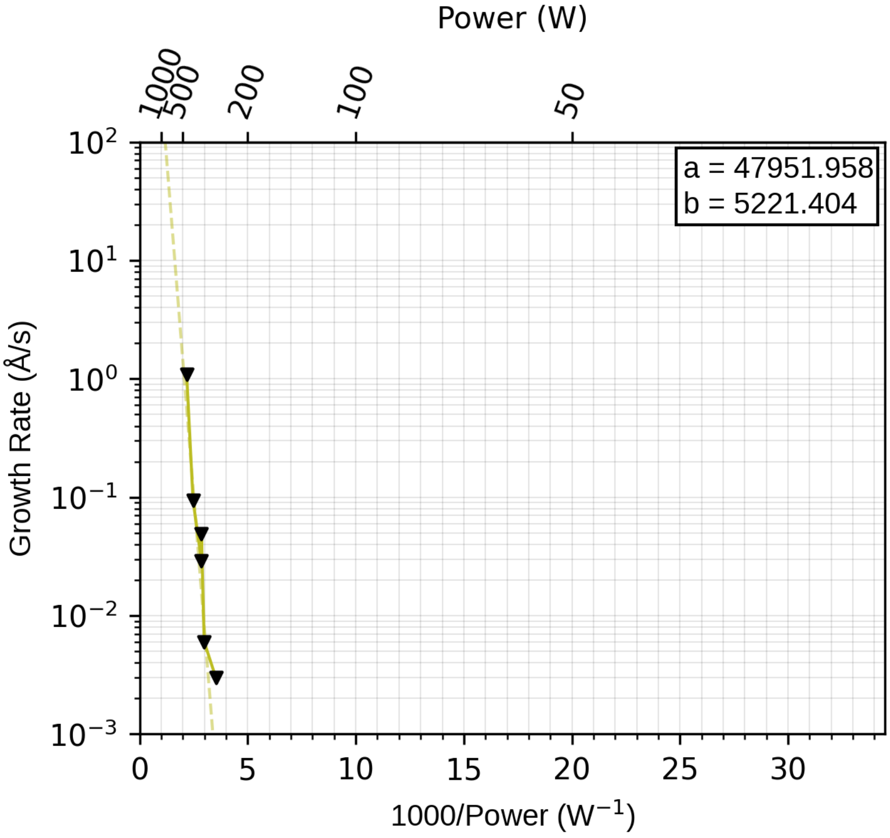

Figure B.47: Growth rate of Ir as a function of incident laser power. Values of the fit parameters, a and b are quoted. Incident laser wavelength was $\lambda = 1030$ nm.

Platinum (Pt)

Physical properties

Thermal Conductivity (W/mK)	71.6
Enthalpy of Vaporization (kJ/mol)[123]	510
Reflectivity at laser wavelength[92]	0.97
Melting point (K)	2041
Material Class	Crucible
Source Diameter (mm)	N/A

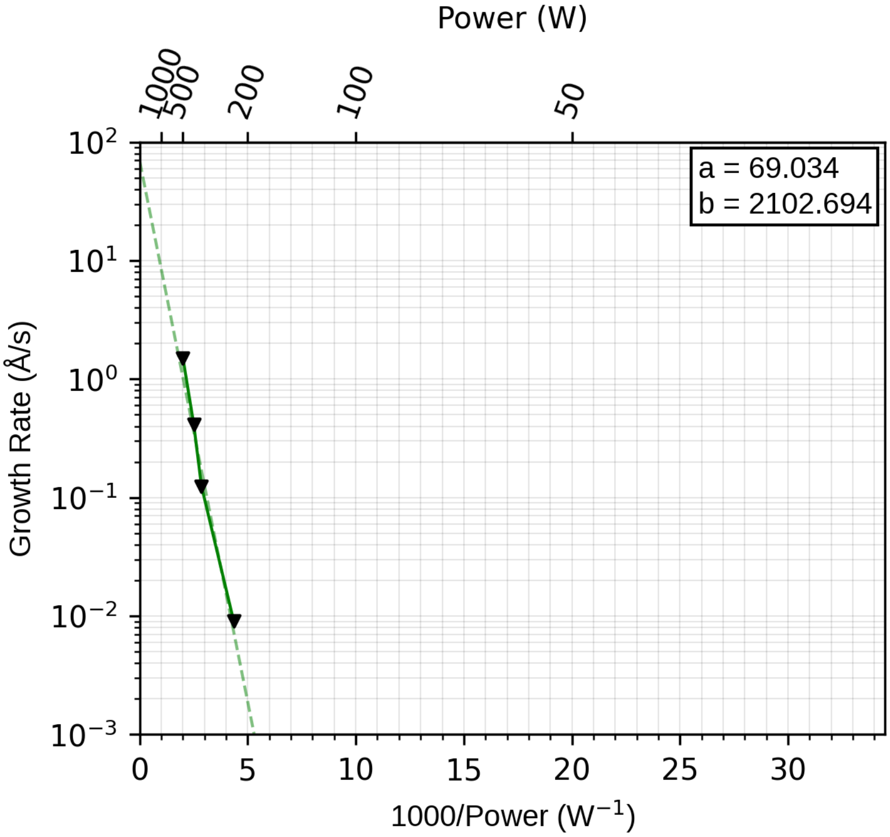

Figure B.48: Growth rate of Pt as a function of incident laser power. Values of the fit parameters, a and b are quoted. Incident laser wavelength was $\lambda = 1030$ nm.

Gold (Au)

Physical properties

Thermal Conductivity (W/mK)	318
Enthalpy of Vaporization (kJ/mol)[123]	342
Reflectivity at laser wavelength[92]	0.97
Melting point (K)	1337
Material Class	Crucible
Source Diameter (mm)	N/A

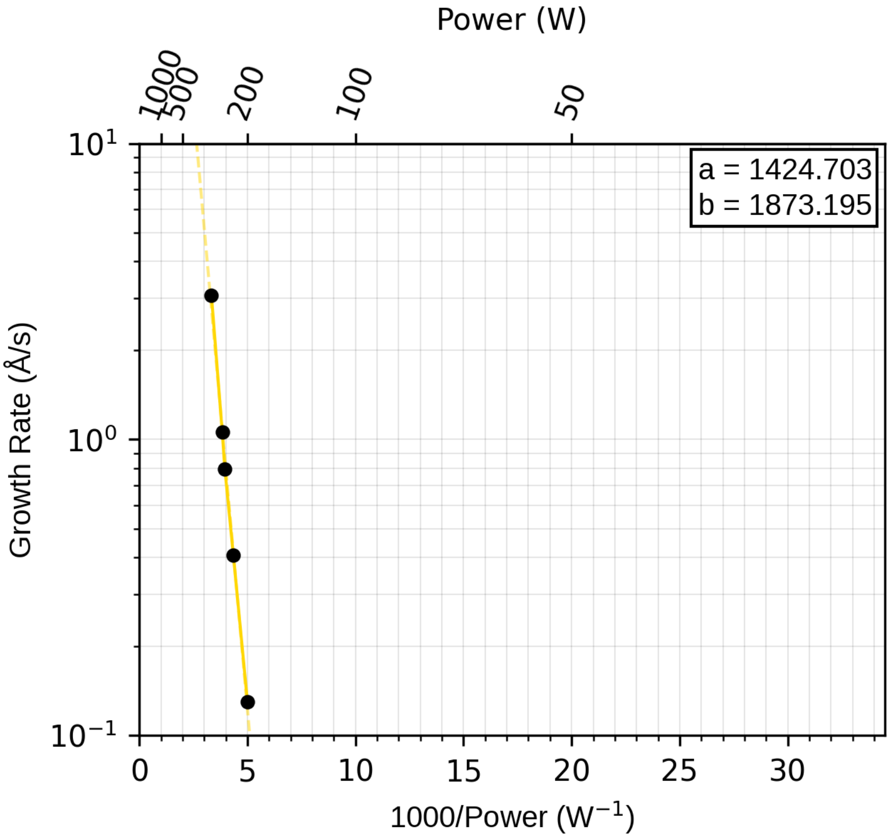

Figure B.49: Growth rate of Au as a function of incident laser power. Values of the fit parameters, a and b are quoted. Incident laser wavelength was λ = 1030 nm.

Lead (Pb)

Physical properties

Thermal Conductivity (W/mK)	35.3
Enthalpy of Vaporization (kJ/mol)[123]	177
Reflectivity at laser wavelength[92]	0.94
Melting point (K)	600
Material Class	Crucible
Source Diameter (mm)	N/A

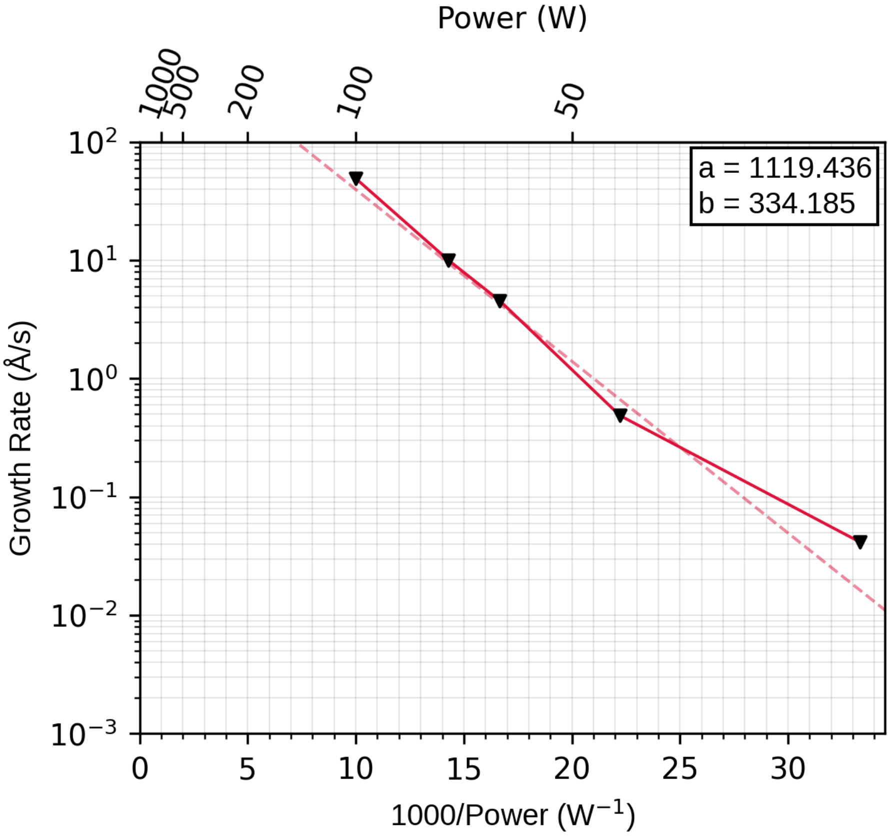

Figure B.50: Growth rate of Pb as a function of incident laser power. Values of the fit parameters, a and b are quoted. Incident laser wavelength was $\lambda = 1030\,\text{nm}$.

Bismuth (Bi)

Physical properties

Thermal Conductivity (W/mK)	7.97
Enthalpy of Vaporization (kJ/mol)[123]	179
Reflectivity at laser wavelength[92]	0.98
Melting point (K)	544
Material Class	Free-standing
Source Diameter (mm)	granulate in crucible

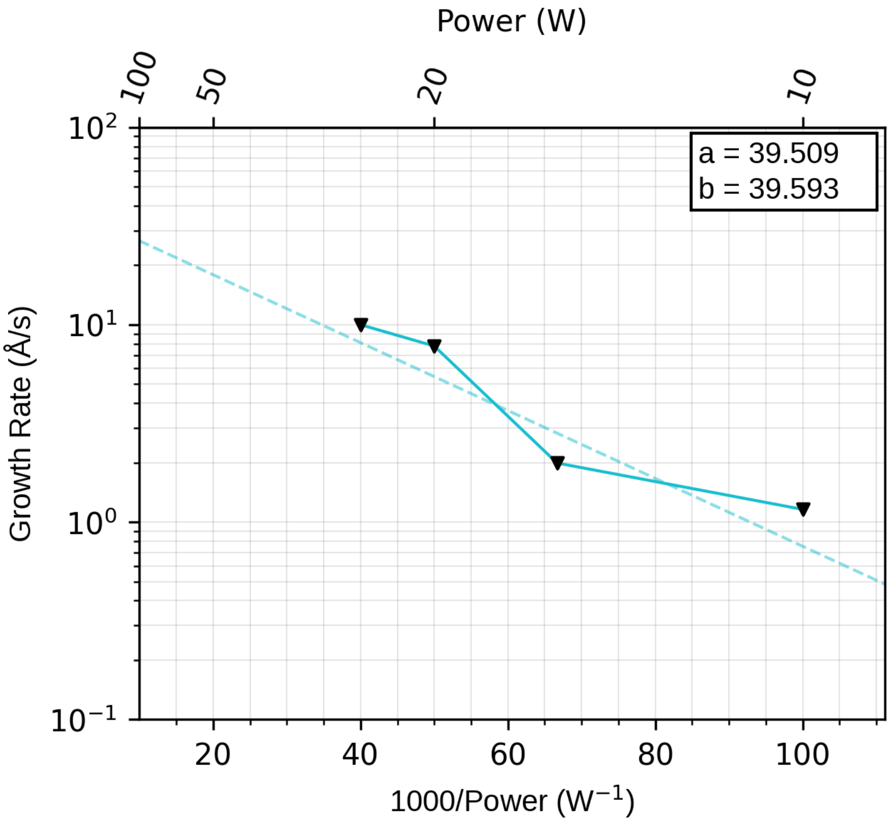

Figure B.51: Growth rate of Bi as a function of incident laser power. Values of the fit parameters, a and b are quoted. Incident laser wavelength was $\lambda = 1030$ nm.

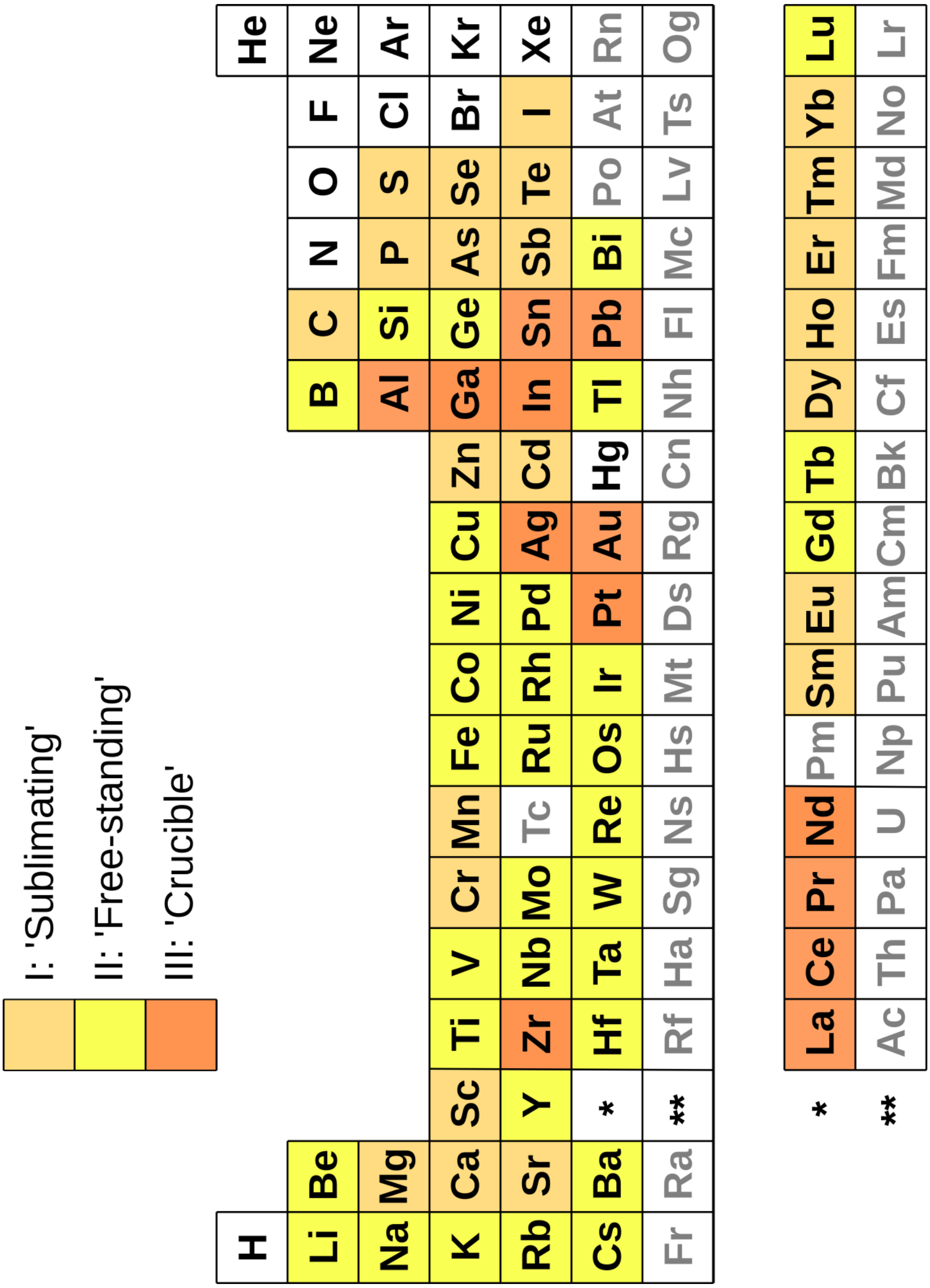

Figure B.52: Periodic table of elements showing the material class for each element: "Sublimating", "Free-standing" and "Crucible". Materials left in white are gases in UHV and the grayed-out elements are radioactive

References

[1] Tavakoli, N. *et al.* Over 65% sunlight absorption in a 1 μm Si slab with hyperuniform texture. *ACS Photonics* **9**, 1206–1217 (2022).

[2] Schmitt, T. W. *et al.* Integration of topological insulator josephson junctions in superconducting qubit circuits. *Nano Letters* **22**, 2595–2602 (2022).

[3] Günther, K. G. Aufdampfschichten aus halbleitenden III-V-Verbindungen. *Zeitschrift für Naturforschung A* **13**, 1081–1089 (1958). URL `https://doi.org/10.1515/zna-1958-1210`.

[4] Chapter 1 - Molecular beam epitaxy: fundamentals, historical background and future prospects. In *Molecular Beam Epitaxy*, 1–46 (Elsevier, Oxford, 2013).

[5] Bunshah, R. & Deshpandey, C. Evaporation processes. *MRS Bulletin* **13**, 33–39 (1988).

[6] Knudsen, M. Die Molekularströmung der Gase durch Offnungen und die Effusion. *Annalen der Physik* **333**, 999–1016 (1909).

[7] Ohring, M. *Materials Science of Thin Films* (Amsterdam: Elsevier Inc, 2002).

[8] Safarian, J. & Engh, T. Vacuum evaporation of pure metals. *Metallurgical and Materials Transactions A* **44** (2012).

[9] TU Vienna Vapor Pressure Calculator. `https://www.iap.tuwien.ac.at/www/surface/vapor_pressure`. Accessed: 2021-12-10.

[10] Obert, E. & Gaggioli, R. *Thermodynamics.* ISBN: 111417291X.

[11] Alibakhshi, A. Enthalpy of vaporization, its temperature dependence and correlation with surface tension: A theoretical approach. *Fluid Phase Equilibria* **432**, 62–69 (2017).

[12] Lide, D. R. *CRC Handbook of Chemistry and Physics, 88th Edition* (CRC Press, 2007).

[13] Verbrugghe, N., Fasquelle, D., Duponchel, B. & Députier, S. Study of tungsten films deposited by DC sputtering dedicated to integrated heaters. *Journal of Vacuum Science & Technology B* **35**, 031204 (2017).

[14] Meiners, B. M., Borchert, D., Hohage, S., Holinksi, S. & Schäfer, P. Degradation of hydrogenated amorphous silicon passivation films caused by sputtering deposition. *Physica Status Solidi (a)* **212**, 1817–1822 (2015).

[15] Linss, V., Bivour, M., Iwata, H. & Ortner, K. Comparison of low damage sputter deposition techniques to enable the application of very thin a-Si passivation films. *AIP Conference Proceedings* **2147**, 040009 (2019).

[16] Kopfermann, H. & Ladenburg, R. Experimental proof of negative dispersion. *Nature* **122**, 438–439 (1928).

[17] Kopfermann, H. & Ladenburg, R. Untersuchungen über die anomale Dispersion angeregter Gase. *Zeitschrift für Physik* **48**, 51–61 (1928).

[18] Maiman, T. H. Stimulated Optical Radiation in Ruby. *Nature* **187**, 493–494 (1960).

[19] Gordon, J. P., Zeiger, H. J. & Townes, C. H. The Maser-New Type of Microwave Amplifier, Frequency Standard, and Spectrometer. *Phys. Rev.* **99**, 1264–1274 (1955).

[20] Svelto, O. & Hanna, D. C. *Principles of Lasers* (Springer New York, NY, 2011). ISBN: 978-1-4419-1301-2.

[21] Schäfer, F. P. *Dye Lasers*, vol. 95 (Springer-Verlag, Berlin, 1990). ISBN 3-540-51558-5.

[22] Groh, G. Vacuum deposition of thin films by means of a CO_2 laser. *Journal of Applied Physics* **39**, 5804–5805 (1968).

[23] Hass, G. & Ramsey, J. B. Vacuum Deposition of Dielectric and Semiconductor Films by a CO_2 Laser. *Applied Optics* **8**, 1115–1118 (1969).

[24] Patel, C. K. N. Continuous-Wave Laser Action on Vibrational-Rotational Transitions of CO_2. *Phys. Rev.* **136**, A1187–A1193 (1964).

[25] Braun, W. *et al.* In situ thermal preparation of oxide surfaces. *APL Materials* **8**, 071112 (2020).

[26] Abate, J. A. *et al.* Active mirror: a large-aperture medium-repetition rate Nd:glassamplifier. *Appl. Opt.* 351–361 (1981).

[27] Giesen, A. *et al.* Scalable concept for diode-pumped high-power solid-state lasers. *Applied Physics B* **58**, 365–372 (1994).

[28] Trumpf GmbH + Co. KG, Ditzingen, Germany. TruDisk 2000. `https://www.trumpf.com/en_INT`.

[29] Oral Laser Abation Surgery: Step-by-Step Guide for Dentists. `https://ostrowon.usc.edu/oral-laser-ablation-surgery/`. Accessed: 2022-09-15.

[30] Ujihara, K. Reflectivity of Metals at High Temperatures. *Journal of Applied Physics* **43**, 2376–2383 (1972).

[31] Siegel, E. Optical reflectivity of liquid metals at their melting temperatures. *Physics and Chemistry of Liquids* **5**, 9–27 (1976).

[32] Brech, F. & Cross, L. Optical microemission stimulated by a ruby laser. *Applied Spectroscopy* **16**, 59 (1962).

[33] Smith, H. M. & Turner, A. F. Vacuum Deposited Thin Films Using a Ruby Laser. *Applied Optics* **4**, 147–148 (1965).

[34] Zavitsanos, P. D. & Sauer, W. E. Formation of Crystalline Films by Laser Evaporation. *Journal of The Electrochemical Society* **115**, 109 (1968).

[35] Schwarz, H. & Tourtellotte, H. A. Vacuum Deposition by High-Energy Laser with Emphasis on Barium Titanate Films. *Journal of Vacuum Science and Technology* **6**, 373–378 (1969).

[36] Ban, V. S. & Kramer, D. A. Thin films of semiconductors and dielectrics produced by laser evaporation. *Journal of Materials Science* **5**, 978–982 (1970).

[37] Dijkkamp, D. *et al.* Preparation of Y-Ba-Cu oxide superconductor thin films using pulsed laser evaporation from high Tc bulk material. *Applied Physics Letters* **51**, 619–621 (1987).

[38] Hess, M. S. & Milkosky, J. F. Vapor deposition of platinum using cw laser energy. *Journal of Applied Physics* **43**, 4680–4683 (1972).

[39] Sankur, H. Properties of thin PbF_2 films deposited by cw and pulsed laser assisted evaporation. *Appl. Opt.* **25**, 1962–1965 (1986).

[40] Trujillo, O. *et al.* CdS thin film deposition by CW Nd:YAG laser. *Thin Solid Films* **290-291**, 13–17 (1996). Papers presented at the 23rd International Conference on Metallurgical Coatings and Thin Films.

[41] Hensling, F. V. E. *et al.* UV radiation enhanced oxygen vacancy formation caused by the PLD plasma plume. *Scientific Reports* **8**, 8846 (2018).

[42] Braun, W. & Mannhart, J. Film deposition by thermal laser evaporation. *AIP Advances* **9**, 085310 (2019).

[43] Smart, T. J., Mannhart, J. & Braun, W. Thermal laser evaporation of elements from across the periodic table. *Journal of Laser Applications* **33** (2021).

[44] Lorenz, M. *et al.* Highly textured fresnoite thin films synthesized in situ by pulsed laser deposition with CO_2 laser direct heating. *Journal of Physics D: Applied Physics* **47**, 034013 (2013).

[45] Kim, D. Y., Mannhart, J. & Braun, W. Thermal laser evaporation for the growth of oxide films. *APL Materials* **9**, 081105 (2021).

[46] Kim, D. Y., Mannhart, J. & Braun, W. Epitaxial film growth by thermal laser evaporation. *Journal of Vacuum Science & Technology A* **39**, 053406 (2021).

[47] Reyren, N. *et al.* Superconducting Interfaces Between Insulating Oxides. *Science* **317**, 1196–1199 (2007).

[48] Arrhenius, S. Über die Dissociationswärme und den Einfluss der Temperatur auf den Dissociationsgrad der Elektrolyte. *Zeitschrift für Physikalische Chemie* 96–116 (1889).

[49] Langmuir, I. The vapor pressure of metallic tungsten. *Physical Review* **2**, 329–342 (1913).

[50] Paradis, P., Ishikawa, T. & Yoda, S. Surface tension and viscosity of liquid and undercooled tantalum measured by a containerless method. *Journal of Applied Physics* **97**, 053506 (2005).

[51] Rakić, A. D., Djurišić, A., Elazar, J. M. & Majewski, M. L. Optical properties of metallic films for vertical-cavity optoelectronic devices. *Appl. Opt.* **37**, 5271–5283 (1998).

[52] Ordal, M. A., Bell, R. J., Alexander, R. W., Newquist, L. A. & Querry, M. R. Optical properties of Al, Fe, Ti, Ta, W, and Mo at submillimeter wavelengths. *Appl. Opt.* **27**, 1203–1209 (1988).

[53] König, U., Kibbel, H. & Kasper, E. Si–MBE: Growth and Sb doping. *Journal of Vacuum Science and Technology* **16**, 985–989 (1979).

[54] Smink, A. E. M. *et al.* Mapping unit-cell thickness variations in thin films by post-deposition reflection high-energy electron diffraction. *Phys. Rev. Materials* **4**, 083806 (2020).

[55] Prokhorov, A. M., Ursu, I., Konov, V. I. & Mihailescu, I. N. *Laser Heating of Metals*, vol. 1 (IOP Publishing Ltd, 1990). ISBN: 0-7503-0040-X.

[56] Kuzmany, H. *Solid-State Spectroscopy: An Introduction* (Springer-Verlag Berlin Heidelberg, 2009). ISBN: 978-3-642-01478-9.

[57] Winsemius, P., van Kampen, F. F., Lengkeek, H. P. & van Went, C. G. Temperature dependence of the optical properties of Au, Ag and Cu. *Journal of Physics F: Metal Physics* **6**, 1583–1606 (1976).

[58] Reddy, H., Guler, U., Kildishev, A. V., Boltasseva, A. & Shalaev, V. M. Temperature-dependent optical properties of gold thin films. *Opt. Mater. Express* **6**, 2776–2802 (2016).

[59] Reddy, H. *et al.* Temperature-Dependent Optical Properties of Single Crystalline and Polycrystalline Silver Thin Films. *ACS Photonics* **4**, 1083–1091 (2017).

[60] Kalenskii, A. V. & Zvekov, A. A. Temperature dependences of the optical properties of aluminum nanoparticles. *Technical Physics Letters* **43** (2017).

[61] Davis, H. L., Faulkner, J. S. & Joy, H. W. Calculation of the Band Structure for Copper as a Function of Lattice Spacing. *Phys. Rev.* **167**, 601–607 (1968).

[62] Winsemus, P. *Temperature dependence of the optical properties of Au and Ag.* Ph.D. thesis (1973).

[63] Ziman, J. M. *Electrons and Phonons* (Clarendon, Oxford, 1960).

[64] Xu, M., Yang, J. Y. & Liu, L. Temperature-dependent dielectric functions of bcc transition metals Cr, Mo, and W from ultraviolet to infrared regions: A theoretical and experimental study. *Journal of Applied Physics* **123**, 155102 (2018).

[65] Winsemius, P. Temperature dependence of the optical properties Ag: The X-point. *Physica Status Solidi (b)* **59**, K55–K58 (1973).

[66] Miller, J. C. Optical properties of liquid metals at high temperatures. *The Philosophical Magazine: A Journal of Theoretical Experimental and Applied Physics* **20**, 1115–1132 (1969).

[67] Suffczynski, M. Optical properties of the noble metals. *Physica Status Solidi (b)* **4**, 3–29 (1964).

[68] Johnson, P. B. & Christy, R. W. Optical constants of the noble metals. *Phys. Rev. B* **6**, 4370–4379 (1972).

[69] Kalenskii, A. V., Zvekov, A. A. & Aduev, B. P. The Influence of Temperature on the Spectral Dependences of Aluminum's Optical Properties. *Optics and Spectroscopy* **124**, 501–508 (2018).

[70] Ren, Y., Chen, J. K. & Zhang, Y. Optical properties and thermal response of copper films induced by ultrashort-pulsed lasers. *Journal of Applied Physics* **110**, 113102 (2011).

[71] Fujioka, H. Pulsed laser deposition (PLD). In Kuech, T. F. (ed.) *Handbook of Crystal Growth (Second Edition)*, Handbook of Crystal Growth, 365–397 (North-Holland, Boston, 2015), second edition edn. ISBN: 978-0-444-63304-0.

[72] Kolasinski, K. W. Solid structure formation during the liquid/solid phase transition. *Current Opinion in Solid State and Materials Science* **11**, 76–85 (2007).

[73] Marín, A. G., Enríquez, O. R., Brunet, P., Colinet, P. & Snoeijer, J. H. Universality of Tip Singularity Formation in Freezing Water Drops. *Physical Review Letters* **113**, 054301 (2014).

[74] Snoeijer, J. H. & Brunet, P. Pointy ice-drops: How water freezes into a singular shape. *American Journal of Physics* **80**, 764–771 (2012).

[75] Grebe, G., Roussos, G. & Schulz, H. J. Cr^{2+} excitation levels in ZnSe and ZnS. *Journal of Physics C: Solid State Physics* **9**, 4511 (1976).

[76] Amin, N., Sopian, K. & Konagai, M. Numerical modeling of CdS/CdTe and CdS/CdTe/ZnTe solar cells as a function of CdTe thickness. *Solar Energy Materials and Solar Cells* **91**, 1202 (2007).

[77] Mayerhöfer, T. G., Pahlow, S. & Popp, J. The Bouguer-Beer-Lambert Law: Shining Light on the Obscure. *ChemPhysChem* **21** (2020).

[78] Theis, C. D. & Schlom, D. G. Cheap and stable titanium source for use in oxide molecular beam epitaxy systems. *Journal of Vacuum Science & Technology A* **14**, 2677–2679 (1996).

[79] Ota, Y. Silicon molecular beam epitaxy. *Thin Solid Films* **106**, 1 (1983).

[80] Latyev, L., Petrov, V. A., Čechovskoj, V. J. & Šestakov, E. N. Izlutchatelnyje svojstva tverdych materialov. *Moskva: Energia* 306–310 (1974). (in Russian).

[81] Aleshin, I. V. *et al.* The vaporization of nonlinear absorbing dielectrics under the action of light. *Zhurnal Tekhnicheskoi Fiziki* **47**, 2420–2428 (1977).

[82] Sankur, H. & Cheung, J. T. Thin-film deposition by laser-assisted evaporation. *Appl. Phys. A* **47**, 271–284 (1988).

[83] Maleeva, N. *et al.* Circuit quantum electrodynamics of granular aluminum resonators. *Nature Communications* **9**, 3889 (2018).

[84] Schörner, C., Adhikari, S. & Lippitz, M. A single-crystalline silver plasmonic circuit for visible quantum emitters. *Nano Letters* **19**, 3238–3243 (2019). PMID: 31009229.

[85] Volmer, F. *et al.* How to solve problems in micro- and nanofabrication caused by the emission of electrons and charged metal atoms during e-beam evaporation **54**, 225304 (2021).

[86] MBE Komponenten, Private Communication.

[87] Alnæs, M. S. *et al.* The FEniCS Project Version 1.5. *Archive of Numerical Software* **3** (2015).

[88] Ern, A. & Guermond, J. *Theory and Practice of Finite Elements* (Springer New York, 2004).

[89] SALOME Platform. `https://www.salome-platform.org/`. Accessed: 2022-11-10.

[90] Schoeberl, J. NETGEN: An advancing front 2d/3d mesh generator based on abstract rules. *Computing and Visualization in Science* **1**, 41–52 (1997).

[91] Knudsen, M. & Partington, J. R. The kinetic theory of gases : some modern aspects. *The Journal of Physical Chemistry* **39**, 307–307 (1934).

[92] Refractiveindex.info. `https://refractiveindex.info/`. Accessed: 2022-08-23.

[93] Harsha, K. S. *Principles of physical vapor deposition of thin films* (Elsevier, Amsterdam ; Boston, 2006), 1st ed edn.

[94] Mayo, S., Galloway, K. F. & Leedy, T. F. Radiation Dose Due to Electron-Gun Metallization Systems. *IEEE Transactions on Nuclear Science* **23**, 1875–1880 (1976).

[95] Bhattacharya, P. K., Reisman, A. & Chen, M. C. A controlled radiation source and electron/X-ray flux ratios in an electron beam metal evaporator. *Journal of Electronic Materials* **17**, 273–283 (1988).

[96] Romaniello, P., de Boeij, P. L., Carbone, F. & van der Marel, D. Optical properties of bcc transition metals in the range $0-40$ eV. *Phys. Rev. B* **73**, 075115 (2006).

[97] Brahlek, M. *et al.* Frontiers in the Growth of Complex Oxide Thin Films: Past, Present, and Future of Hybrid MBE. *Advanced Functional Materials* **28**, 1702772 (2018).

[98] The Insight Partners. `https://www.theinsightpartners.com/pr/sapphire-substrate-market/`. Accessed: 2022-07-17.

[99] Egry, I., Ricci, E., Novakovic, R. & Ozawa, S. Surface tension of liquid metals and alloys - Recent developments. *Advances in Colloid and Interface Science* **159**, 198–212 (2010).

[100] Macleod, D. On a relation between surface tension and density. *Transactions of the Faraday Society* **19**, 38–41 (1923).

[101] Copland, E. Vapor pressures in the Al(l)+Al_2O_3(s) system: Reconsidering Al_2O_3(s) condensation. *The Journal of Chemical Thermodynamics* **38**, 443–449 (2006).

[102] Cochran, C. N. Aluminum suboxide formed in reaction of aluminum with alumina. *Journal of the American Chemical Society* **77**, 2190–2191 (1955). URL `https://doi.org/10.1021/ja01613a044`. `https://doi.org/10.1021/ja01613a044`.

[103] Hoffmann, G., Cheng, Z., Brandt, O. & Bierwagen, O. Drastically enhanced cation incorporation in the epitaxy of oxides due to formation and evaporation of suboxides from elemental sources. *APL Materials* **9**, 111110 (2021).

[104] Lubin, P. *et al.* Toward directed energy planetary defense. *Optical Engineering* **53**, 025103 (2014).

[105] Takayanagi, S. Effect of oxygen pressure on the oxidation of tungsten powder. *Transactions of the Japan Institute of Metals* **3**, 100–104 (1962).

[106] Sobczak, N., Ksiazek, M., Radziwill, W., Asthana, R. & Mikulowski, B. The effect of temperature, matrix alloying and substrate coatings on wettability and shear strength of Al/Al_2O_3 couples. *Metallurgical and Materials Transactions A* **35**, 911–923 (2004).

[107] Braun, W. *Applied RHEED: Reflection High-Energy Electron Diffraction During Crystal Growth.* Springer Tracts in Modern Physics (Springer Berlin Heidelberg, 2013). ISBN: 9783662156148.

[108] Binnig, G., Quate, C. F. & Gerber, C. Atomic Force Microscope. *Phys. Rev. Lett.* **56**, 930–933 (1986).

[109] Cappella, B. & Dietler, G. Force-distance curves by atomic force microscopy. *Surface Science Reports* **34**, 1–104 (1999).

[110] Mandziak, A. *et al.* Structure and magnetism of ultrathin nickel-iron oxides grown on Ru(0001) by high-temperature oxygen-assisted molecular beam epitaxy. *Scientific Reports* **8**, 17980 (2018).

[111] Smink, S. Private Communication, 2022.

[112] Cooper, V. R. *et al.* Transparent conducting oxides: A δ-doped superlattice approach. *Scientific Reports* **4**, 6021 (2014).

[113] Zubko, P., Gariglio, S., Gabay, M., Ghosez, P. & Triscone, J. Interface physics in complex oxide heterostructures. *Annual Review of Condensed Matter Physics* **2**, 141–165 (2011).

[114] Taleb, A. A. *et al.* Ultrasmooth graphene-coated metal thin films on sapphire grown by thermal laser epitaxy. *Thin Solid Films* **758**, 139449 (2022).

[115] Wang, S. *et al.* The Hardest Superconducting Metal Nitride. *Scientific Reports* **5**, 13733 (2015).

[116] Logg, A., Mardal, K.-A., Wells, G. N. *et al.* *Automated Solution of Differential Equations by the Finite Element Method* (Springer, 2012).

[117] Abali, B. E. *Computational Reality: Solving Nonlinear and Coupled Problems in Continuum Mechanics* (Springer Singapore, 2017).

[118] Ho, C. Y., Powell, R. W. & Liley, P. E. Thermal conductivity of the elements. *Journal of Physical and Chemical Reference Data* **1**, 279–421 (1972).

[119] Leitner, M., Leitner, T., Schmon, A., Aziz, K. & Pottlacher, G. Thermophysical properties of liquid aluminium. *Metallurgical and Materials Transactions A* **48**, 1543–1940 (2017).

[120] Agheenkov, V. G. & Mihin, I. I. Calcule Metalurgice. Bucharest: Ed. Tehnica, 1964 (in Romanian).

[121] Abdullaev, R. N., Khairulin, R. A. & Stankus, S. V. Density and thermal expansion of silver in the solid and liquid states. *Journal of Physics: Conference Series* **1677**, 012161 (2020).

[122] Ramanathan, K. G. & Yen, S. H. High-temperature emissivities of copper, aluminum, and silver. *J. Opt. Soc. Am.* **67**, 32–38 (1977).

[123] Zhang, Y. Corrected Values for Boiling Points and Enthalpies of Vaporization of Elements in Handbooks. *Journal of Chemical and Engineering Data* **56** (2011).

[124] Cook, B. E. The optical properties of orthorhombic sulphur in the vacuum ultra violet (1968). University of Leicester.

[125] Hunderi, O. Optical properties of metallic calcium. *Journal of Physics F: Metal Physics* **6**, 1223–1229 (1976).

[126] Sigrist, M. *et al.* Optical properties of scandium thin films. *Phys. Rev. B* **35**, 3760–3764 (1987).

[127] Ferraton, J., Ance, C., Kofman, R., Cheyssac, P. & Richard, J. Reflectance and thermoreflectance of gallium. *Solid State Communications* **20**, 49–52 (1976).

[128] Nunley, T. N. *et al.* Optical constants of germanium and thermally grown germanium dioxide from 0.5 to 6.6ev via a multisample ellipsometry investigation. *Journal of Vacuum Science and Technology B* **34**, 061205 (2016).

[129] Endriz, J. G. & Spicer, W. E. Reflectance studies of Ba, Sr, Eu, and Yb. *Physical Review B* **2**, 1466–1492 (1970).

[130] Kress, K. A. & Lapeyre, G. J. Optical properties of molybdenum and ruthenium. *J. Opt. Soc. Am.* **60**, 1681–1684 (1970).

[131] Millhouse, A. H. & Leinhardt, T. E. Temperature dependence of the optical reflectivity of cerium metal (1965).

[132] Akashev, L. A., Popov, N. A. & Shevchenko, V. G. Optical Properties and Electronic Characteristics of Praseodymium and Neodymium in Condensed State. *Optics and Spectroscopy* **129** (2021).